The Propulsion and Trajectory Design for the Energetic Transient Array Astrophysics Mission

by
Christopher John McLain

B.S. Aeronautics and Astronautics, Unversity of Washington, 1995

SUBMITTED IN PARTIAL FULFILLMENT OF THE REQUIREMENTS FOR THE DEGREE OF

Master of Science
in
Aeronautics and Astronautics
at the
Massachusetts Institute of Technology

June 1997

Signature of Author_____
Department of Aeronautics and Astronautics
May 23, 1997

Certified by _____
Professor Manuel Martinez-Sanchez
Professor of Aeronautics and Astronautics
Thesis Supervisor

Accepted by_____
Professor Jaime Peraire
Department Graduate Committee

The Propulsion and Trajectory Design for the Energetic Transient Array Astrophysics Mission

by

Christopher John McLain

Submitted to the Department of Aeronautics and Astronautics on May 23, 1997
in partial fulfilment of the requirements for the degree of Master of Science in Aeronautics and Astronautics

Abstract

The Energetic Transient Array (ETA) is an astrophysics mission being proposed by the MIT Center for Space Research (CSR) and Group 75 at the MIT Lincoln Lab. The purpose of ETA is to provide sub-arcsecond localizations of Gamma Ray Bursts (GRBs). These localizations will facilitate the identification of a GRB source. ETA consists of two segments: a heliocentric constellation of four 'helio' satellites which provide differential time of arrival information used in the production of localizations, and a pair of Earth orbiting 'trigger' satellites which provides burst profile information. This thesis documents the propulsion and trajectory design of the helio and trigger satellites deployment and final orbits.

An analysis is carried out of the helio satellite deployment architecture. The parameters governing the deployment are described. Through simple analysis it is shown that impulsive chemical propulsion is preferable to electric propulsion. An extensive trade study of launch and chemical propulsion options is described. It is found that the most cost effective means of launching ETA is the Ariane Structure for Auxiliary Payloads (ASAP) ring on Ariane 5. The ASAP ring allows up to eight 100 kg secondary payloads which are deployed to Geosynchronous Transfer Orbit (GTO). Launch will be provided for free to ETA by CNES, the French space agency, in a cooperative agreement. Escape from GTO into heliocentric orbit will be accomplished using a Star 13A solid rocket motor. A detailed analysis of the escape burn parameters is carried out. The reliability of distributing the helio and trigger satellites among multiple ASAP launches and the integration of the Star 13A solid rocket motor are discussed.

An analysis is carried out of the trigger satellite orbit and deployment architecture. Several trigger orbits are examined. Compatibility with the helio satellites and requirements on radiation, Earth blockage, range, and continuous visibility from a single ground station led to the selection of a 20,000 km × 64,330 km radius, 7° inclined synchronous orbit (one sidereal day period) that can entered by making a single burn near apogee of GTO. The visibility of the trigger orbit from a ground station, the perturbations affecting the orbit, the required perturbation corrections, and the eclipse duration of the orbit are analyzed.

It is concluded that the work contained in this thesis significantly increased the viability of ETA over previous iterations.

Thesis Supervisor: Manuel Martinez-Sanchez
Title: Professor of Aeronautics and Astronautics, MIT

Acknowledgments

I would like to thank the great many people helped me complete this thesis:

Professor Martinez-Sanchez for securing this position for me, giving me the freedom to peruse my own ideas, and always being available and willing to listen to my ideas.

Dr. George Ricker for providing this challenging project to work on and then standing back to see what I could do with it.

Bob Dill for always being around to discuss ETA and half a dozen other space related topics and for VOLUNTEERING to read my thesis!

Nicolas Fabas for helping me with the trigger satellite work.

Francois Martel for suggesting the Ariane 5 ASAP ring and for always being helpful and encouraging.

Bob Davis, John Sultana, and Darryl Weidler at Lincoln Lab Group 75 for always for being great to work with and offering me a great position at Lincoln Lab which I was sorry to have to turn down.

Rosemary Hanlon for being the most helpful secretary at MIT and for saving me when chapter 6 of this thesis disappeared into the great bit stream of the universe.

Liz Zotos for encouraging me to come to MIT in January of 1996 and for giving me the thesis extensions necessary to get me out of MIT in June of 1997.

Professor Bruckner at University of Washington for teaching me the meaning of space systems engineering.

I also would like thank my lab mates with out whom life here would have been nearly intolerable: Greg Giffin for pool games at Tang and frequent trips to Larry's. Angie Kelic for pool games, dinner Bertucci's, and computer things. Greg Yashko for sharing my struggles with the Macs over the last few weeks. Graeme Shaw and Ray Sedwick for being the most relaxed grad students

at MIT. Finally, David Oh for getting me a job Space Systems Loral which I was sorry to have to turn down.

I must also thank Kim Mateluf for her tireless support during these last few weeks and friendship over the last seven years. Your faithful calls in lab every night at 3 AM kept me going.

No list of thank-yous would be complete without Mom, Dad, Allison who have seen me through the last 23 years.

Finally, I would like to thank the following suppliers who provided data for this thesis. Dennis Walstrom at Thiokol, Carl Stechman Kaiser Marqardt, Trip Carter at Lockheed Martin, Carry Pao at Orbital Sciences, Niel Dippery at TRW (who's offer of a job I was also sorry to have to turn down), Jim Bartron at Olin, and Mike Hersh at PSI.

"Make no little plans, they have no power to stir men's blood"
-Daniel Burnham

"I know the price of success...unremitting devotion, hard work,
and an inextinguishable love for the thing you want to happen"
-Frank Loyd Wright

Table of Contents

List of Figures

List of Tables

List of Acronyms

ASTE	All Sky Transient Explorer
AMF	Apogee Motor Firing
ASI	ArcSecond Imager
ASAP	Ariane Structure for Auxiliary Payloads
AU	Astronomical Unit
BATSE	Burst and Transient Source Experiment
BASIS	Burst ArcSecond Imaging Spectroscopy
CSR	Center for Space Research
CCD	Charged Coupled Device
COTS	Commercial Off The Shelf
CGRO	Comption Gamma Ray Observatory
DRO	Distant Retrograde Orbit
ETA	Energetic Transient Array
FY	Fiscal Year
GRB	Gamma Ray Burst
GTO	Geosynchronous Transfer Orbit
HETE	High Energy Transient Experiment
IMU	Inertial Measurement Unit
IPN	Inter-Planetary Network
LAD	Large Area Detector
LEO	Low Earth Orbit
LL 4,5	Lunar Lagrange points 4 and 5
MIT	Massachusetts Institute of Technology
MIDEX	Medium Explorer
PVO	Pioneer Venus Orbiter
RPM	Revolutions Per Minute
RTL	Round Trip time of Light
SMEX	Small Explorer
SPT	Stationary Plasma Thruster
VLBI	Very Long Baseline Interferometry

Preface

Science Marches On....

The work contained in this thesis is current as of April 1, 1997. However, in the last few weeks the ETA project has undergone considerable evolution as the result of data received from the Italian satellite Beppo SAX. This data has indicated the existence of GRB counterparts and implied that GRBs have a cosmological source. First, this resulted in the dropping of the coded aperture detectors from the trigger satellites. Latter, this resulted in the dropping of the ETA mission in favor of an entirely new mission based on the ETA trigger satellite design. The new mission known as the All Sky Transient Explorer (ASTE) will be launched from the ETA ASAP ring, inserted in to the ETA trigger orbit, and will carry a complement of gamma-ray and x-ray sensors. The trigger satellite work described in this thesis will still be of use to the ASTE team. While the author is somewhat disappointed in the outcome of ETA, rapid obsolescence is the price of working on the cutting edge. At least some of this work will live on as ASTE.

Christopher McLain
May 23, 1997

Chapter 1 Introduction

The purpose of this chapter is to describe the origin, scope, and content of this thesis. It is the author's belief that to find out where something is going it is useful to know where it has come from. To this end, the discovery of gamma-ray bursts (GRBs) and the history of the Energetic Transient Array (ETA) mission are discussed. Summaries of the previous, and current ETA proposals are presented to provide the context in which this thesis was carried out and to point out its contributions to the current proposal. Finally, the engineering nature and resulting organization of this thesis is described.

1.1 VELA and the Discovery of Gamma-Ray Bursts

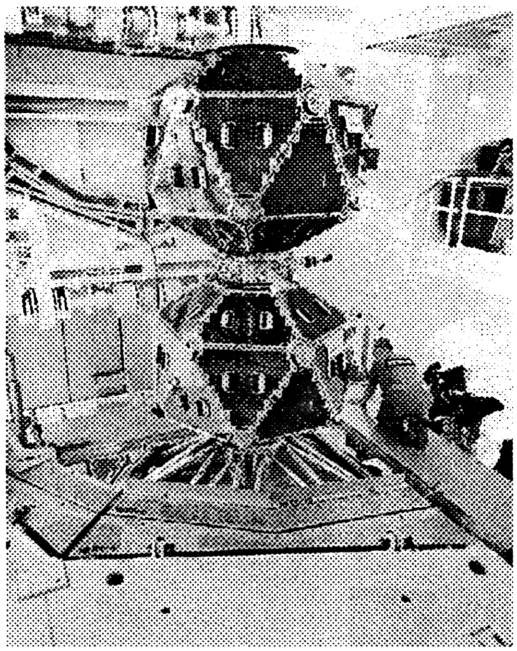

Fig. 1-1 Two advanced VELA satellites being prepared for launch.

The Air Force VELA satellites were meant to monitor violations of the then new comprehensive nuclear test ban treaty, not to discover gamma-ray bursts [1]. Launched in pairs, starting in 1963, the VELA satellites carried gamma-ray, x-ray, and neutron detectors to warn of atmospheric and space based testing of nuclear weapons. Between 1963 and 1970 six pairs of VELA satellites were launched, each succeeding generation having improved sensors. Instances of gamma-ray transients not associated with nuclear explosions were recorded for later study. In 1972 scientists at Los Alamos National laboratories discovered 16 gamma-ray transients in the VELA data between July 1969 and July 1972 which, by using the differential time of arrival at each satellite in the VELA constellation, could not have originated from either the Earth or the Sun. Shortly after these

reports of cosmic gamma-ray bursts were published in 1973, they were confirmed by sensors on the IMP-6 and OSO-7 satellites. No events of this nature had been predicted nor has any undisputed theory for their cause been forwarded. While the VELA 6a and b satellites out lived their planned three year lifetimes by a factor of five, only to be shut down in 1985, the mystery of GRBs has outlasted VELA and continues to this day.

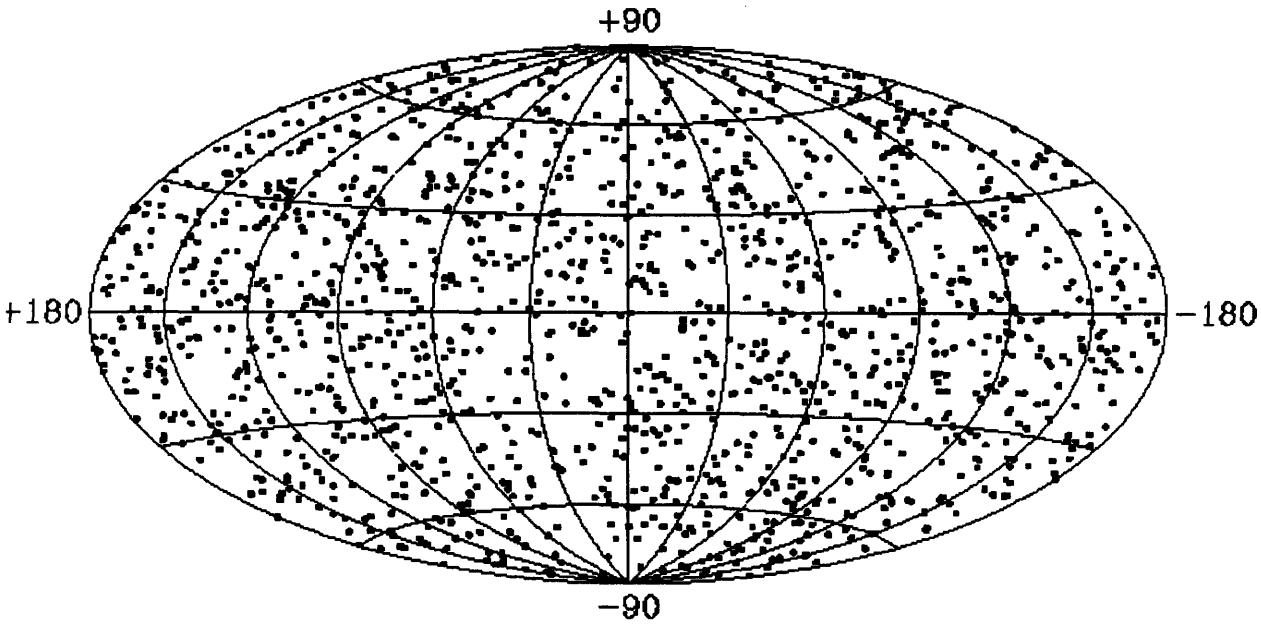

Fig. 1-2 BATSE data showing the isotropic distribution of GRB sources.

Over the past two decades numerous GRB experiments have been flown on may missions and much has been learned [2]. GRBs arrive about once a day and last for 0.01 to 1000 seconds with peak spectral intensities in the 10 keV to 100 keV range. GRBs come in two classes: type I are long (up to 1000 seconds) and consist of lower energy spectra, type II are short (0.01 to 10 seconds) and consist of higher energy spectra. Rapid time variability and absorption lines in the spectra suggest that GRBs come from compact, massive objects with intense magnetic fields. GRB sources are isotropically distributed across the sky as shown in Fig. 1-2. This rules out sources in the luminous part of the galaxy and severely limits the possible locations for GRB sources. If GRBs had the same distribution as the luminous matter in the galaxy, an anisotropic distribution corresponding to the galactic disk would be expected. To produce an isotropic distribution the Earth must be at or near the center of the source distribution. The difficulty with this is that, as Copernicus told us and modern astronomy has confirmed, Earth is not at the center of anything: not the solar system, not the galaxy, and certainly not the universe. To produce this isotropic distribution several GRB source locations have been proposed [3]:

- The Ort Cloud – A reservoir of commetary bodies is believed to exist at a distance of 100,000 AU from the Sun, so far that earth would appear at the center of the distribution. Few GRB astronomers adhere to this model because of several severe flaws. First, the Ort cloud is expected to be biased towards the ecliptic plane and therefore somewhat anisotropic. Further, even if the Ort cloud is isotropic, the Ort clouds around nearby stars are large enough that GRBs in them should be observable from Earth. This would lead to anisotropic distributions in the directions of nearby stars like Alpha Centauri. Finally, while the total energies of GRBs originating from the Ort cloud would be relatively low, no good mechanism has been suggested for how the icy bodies of the Ort cloud could produce a powerful burst of gamma radiation.

- A Galactic Halo – It is possible that GRBs originate from an as-yet-undiscovered halo of objects at a radius of several times the diameter of the luminous galaxy, a sufficiently large radius that the Earth would appear to be near the center of the distribution. The power of GRBs at this distance the observed gamma-ray spectra would suggest that GRBs are caused by highly plausible events involving neutron stars. Unfortunately, this model also has deficiencies. First, no halo of objects have been observed around our galaxy or any other. Second, if these halos exist they would have to be so large that the halos from other nearby galaxies such as the Large and Small Magalantic Clouds would be superimposed on our own halo producing anisotropies in the distribution. About half of GRB astronomers favor galactic sources for GRB.

- A Cosmological Source – Since the universe extends out nearly infinitely in every direction every point appears to be at the center. Rare objects evenly distributed over billions of light years would produce an isotropic distribution as observed from Earth. However, to produce the powers required by these distances very exotic, extraordinarily energetic events are needed such as the coalescing of black holes. Each GRB would release in a few seconds the entire energy output of the Sun over its lifetime making these among the most energetic events ever observed. About half of GRB astronomers favor a cosmological source for GRBs .

1.2 Finding the Source of GRBs

It has been said that gamma-ray bursts are among the most observed least explained phenomena known. Astronomy has developed an impressive array of tools including radio, infrared, optical, UV, x-ray, and gamma-ray telescopes over the past three hundred years. Unfortunately,

astronomers have largely been denied the use of these tools in the search for a GRB source by the nature of gamma-ray bursts. Gamma radiation precludes the use of conventional optics so that current GRB localization techniques yield error boxes from a few arcminutes to a few degrees. Within error boxes of this size powerful telescopes can find hundreds to millions of objects. Without arcsecond localizations it is impossible to pin a GRB down to a single astronomical object for observation. Further, it is impossible to tell whether GRBs repeat as would be predicted by many galactic source models.

Clearly, better localizations are required before astronomy's many techniques can be brought to bear. Two techniques have been used to produce GRB localizations: directional sensors, and arrays.

Several types of directional sensors are available but are limited by inability to use conventional optics with gamma radiation. By far the most comprehensive GRB data base has been provided by the Burst and Transient Spectrometer Experiment (BATSE) on the Compton Gamma Ray Observatory (CGRO). BATSE consists of eight large area sodium iodide scintillators distributed around CGRO. A direction can be generated from the relative strength of the burst at each scintillator with an error box of ~7°. This is far from sufficient to identify GRB counterparts.

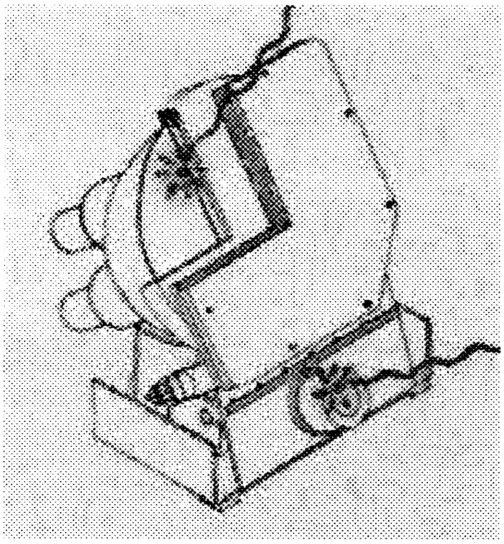

Fig. 1-3 BATSE Large Area Detector (LAD).

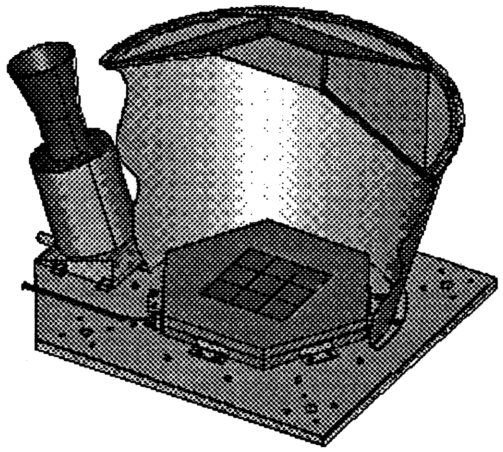

Fig. 1-4 The BASIS ArcSecond Imager (ASI).

A more sophisticated type directional sensor is a coded aperture sensor. A coded aperture sensor consists of a mask, patterned so that gamma-rays (and no other kind of light) can penetrate it in some areas and not others, positioned over a CCD imager. During a GRB the mask casts a

gamma-ray shadow pattern that can be detected using the CCD. From the relative position of the mask and its gamma-ray shadow the direction of the GRB can be determined. By using a fine enough CCD and spacing the mask a sufficient distance from the CCD the proposed Burst Arc-Second Imaging and Spectroscopy mission (BASIS), an ETA competitor, believes it can achieve the sub-arcsecond accuracy to find GRB counterparts [4]. ETA, as described later, will include a less sophisticated coded aperture sensor with arcminute accuracy to fulfill a secondary science objective.

The advantage of a directional sensor is that only a single spacecraft is required in Low Earth Orbit (LEO). LEO is easily reached and has a short Round-trip Time of Light (RTL) so that preliminary localizations can be sent to the ground during a burst. These burst warnings can be used by fast reaction telescopes to catch GRBs in the act. The disadvantage of directional sensors are that the sensor and satellite required are much more sophisticated. Directional sensors of this accuracy have not yet been built, the satellite itself must have a sub-arcsecond attitude determination system, and considerable and costly redundancy is required because the loss of the satellite results in loss of the mission.

The second method of providing GRB localizations is an array. An array consist of simple gamma-ray sensors distributed over long baselines. By correlating the different times of arrival of a GRB at three or more sensors, localizations can be produced. VELA was used as an array of several satellites with a baseline of ~240,000 km. By fitting simple gamma ray sensors to a number of planetary spacecraft including Venara, PVO, and Solar Maxim a series of arrays called Interplanetary Networks (IPNs) were created with a baseline of ~2 AU. The IPNs have yielded the best localizations yet (~ 15 arcminutes). Unfortunately, the accuracy of the IPNs is limited by the inconsistency in sensor types and mountings, the time resolution of the sensors, and the position knowledge of the spacecraft. The primary science of ETA is provided by a rationalized purpose-built version of the IPNs, as described later.

The advantages of an array localization scheme are that simple sensors of proven designs can be used and that the mission can easily be made resistant to single or multiple satellite failures. The sensors used in an array need only determine the time of arrival and profile of a GRB. This can be accomplished with a simple sodium iodide scintillator of which may similar designs have flown. No precise attitude knowledge is necessary. Further, if many sensors are provided in the array, the failure of one degrades the performance of the array but does not end the mission. As a result, the spacecraft can be of a low cost, single string design. The disadvantages of an array are that more numerous space craft are required in more difficult to reach orbits, and that the RTL across a

~2 AU constellation is 32 minutes precluding the availability of a preliminary localization during the burst for use by fast reaction telescopes. While achieving the heliocentric orbits necessary from a ~ 2 AU baseline is more difficult than LEO these orbits have been accomplished by numerous planetary spacecraft.

It is believed by the ETA science team that because every component necessary to create a sub-arcsecond GRB localization array has been demonstrated, a dedicated array provides the lowest risk and therefore lowest cost approach to sub-arcsecond GRB localization. This belief led to the ETA concept.

1.3 The ETA Concept

The ETA concept [5] was first proposed by Dr. Ricker of the MIT Center for Space Research (CSR). ETA consists of two parts: a set of Earth orbiting "trigger" satellites, and a set of Sun orbiting "helio" satellites. Both the trigger and helio satellites are of identical or nearly identical design. Each satellite has identical large area sodium iodide detectors pointed at North and South ecliptic poles and a precision clock. When a GRB is detected, the trigger satellites are able transmit a detailed burst profile to the ground at high data rate because of their close proximity to the Earth. This profile is then uplinked using a high gain antenna to the helio satellites which are distributed around the Sun in approximately Earth's orbit. Each helio satellite then compares its record to the uplinked profile using a signal processor and determines the precise arrival time of the burst. This time is then downlinked to Earth so that localization can be computed. By uplinking the burst profile and only downlinking the time of arrival the power required for the helio satellites can be greatly reduced. Very Long Baseline Interferometery (VLBI) is periodically used to provide precise orbit determinations for the trigger and helio satellites. By including redundant trigger and helio satellites the system accuracy can be increased and a graceful degradation allowed. Because ETA does not depend upon any single satellite lower individual satellite reliabilities can be tolerated. This, in turn, allows the use of a lower cost, lower complexity, single string design for each of the satellites.

With the concept defined, Professor Martinez-Sanchez of MIT and a Master's student, Bavesh Patel, were brought in to determine the best method of deploying the ETA constellation. The work of Dr. Ricker, the science team, Professor Martinez-Sanchez, and Bavesh Patel in conjunction with Orbital Sciences to lead the ETA Medium Explorer (MIDEX) proposal.

1.4 The ETA MIDEX Proposal

The ETA MIDEX proposal objectives were to provide continuous high accuracy localizations (sub-arcsecond under the best conditions) in order to answer the following questions: Do GRB counter parts exist? Do type I and II GRBs originate from the same source? Do GRBs repeat? Does gravitational microlensing occur as predicted by cosmological models? The primary constraints on the mission were: to fit on to a Medlite class launch vehicle and to have a system cost of less than $70 million (FY 94) [6].

The ETA MIDEX mission would have been launched on a DetlaLite, a proposed launch vehicle consisting of two Thiokol Castor 120s and a Delta II upper stage. An optional kick stage would then inject a stack of six micro satellites and an electric propulsion carrier into an escape trajectory. After 85 days of coasting the carrier would activate its SPT-70 xenon Hall thrusters. At the end of a 30 day insertion burn two trigger satellites would be deployed into a 3×6 million km non-Keplerian orbit around Earth with a period of 299 days. The SPT-70s would be reactivated and the stack accelerated in the retrograde direction with respect to the sun. After 68 days the first helio satellite would be released. The other three would be released after decreasing intervals giving each a progressively greater hyperbolic excess velocity with respect to the Earth. This process injected each successive helio satellite into an orbits with shorter and shorter periods. By orbiting the Sun faster than the Earth the helio satellites would appear to spread away from Earth in the prograde direction. After two years the constellation would have spread 120° around the Sun and began its useful mission.

For the purpose of this thesis the following two points should be noted. First, it was believed that the high hyperbolic excess velocities with respect to the Earth necessitated the use of the high I_{sp} SPT thrusters. The inherently low thrust of these thruster resulted in total impulse being applied over a long period of time and far from Earth. This, as explained later, caused the first assumption to be a self fulfilling prophesy. Second, the selection of the trigger orbits was made based on loose requirements about the amount of sky that could be blocked by Earth, the radiation environment of the orbit, and compatibility with the helio satellite deployment mechanism.

The ETA MIDEX proposal was submitted in June 1995 and, unfortunately, was unsuccessful. While the exact reason is unknown, several causes have been speculated. It has been suggested that the electric propulsion element of the ETA was viewed as too complex and expensive for this type of mission. However, it is unlikely that any implementation concerns were the reason for the rejection. The proposals were judged primarily on their scientific merit. The lack of ability to

produce a preliminary localization during a burst for use by fast reaction telescopes, in the way a directional sensor could, was also cited. For whatever reason, the price of ETA's science exceeded NASA's willingness to pay. However, NASA did take the unusual step of providing low level study money to continue developing the ETA concept. This study money provided the basis for the authors work, this thesis, and the genesis of the ETA Small Explorer (SMEX) proposal.

1.5 The ETA SMEX Proposal

The ETA SMEX proposal, set to be delivered in July 1997, is the result of the continuing work of Dr. Ricker, the ETA science team, the MIT Lincoln Lab Group 75, Professor Martinez-Sanchez, and the author. The objectives of the SMEX proposal remain the same as MIDEX objectives with the additional requirement to provide arcminute localizations in the first 5 seconds of a GRB. The SMEX proposal has the following tighter constraints than the MIDEX proposal: to fit on a Pegasus class or lower cost launch vehicle, and to have a system cost of less than $39 million (FY 97). To allow the SMEX ETA proposal to meet its increased requirements and more stringent constraints the following advances in the ETA design have been made:

- Impulsive Propulsion – By making an impulsive burn near Earth the ΔV required to achieve a given hyperbolic excess velocity can be greatly reduced as is described in later chapters. This low ΔV allows the use of low I_{sp} but flight proven, low cost, and inherently impulsive chemical propulsion. A solid rocket motor proved to be the best choice. Impulsive propulsion is the authors primary contribution to the current form of the ETA proposal.

- Ariane 5 ASAP – The compact impulsive nature of chemical propulsion allows the use of secondary payload slots on the Ariane 5 Auxiliary Structure for Secondary Payloads (ASAP). The ASAP ring allows the mounting of up to eight, 90 to 100 kg, $60 \times 68 \times 80$ cm payloads underneath the primary Ariane 5 payload [7]. For a cost of ~$1 million a piece, payloads are delivered to Geosynchronous Transfer Orbit (GTO), an energetic orbit from which escape is relatively easy. The disadvantage of the ASAP ring is that the US government will not pay for launches on foreign vehicles. To counter this, a cooperative agreement with the French space agency CNES has been worked out. ETA will purchase its primary sensors from the French and in exchange CNES will provide the launch for free. Francios Martel is responsible for suggesting the ASAP ring and the author is responsible for working out the details of this concept.

- Coded Aperture Detectors – In response to the criticism that ETA cannot provide preliminary localizations during the burst, a set of coded aperture directional sensors have been added to the trigger satellites. These sensors will provide ~5 arcminute localizations instantly for transmission to the ground in the form of a burst warning which can be used by fast reaction telescopes. The desire to minimize the RTL in order to speed delivery of the burst warnings and requirement to provide continuous burst warnings and has led to changes in the trigger orbits.

- Synchronous Trigger Orbits – Changes in requirements have resulted in changes in the trigger orbits. In order to reduce the RTL from 20 - 40 seconds to less than 1 second, to ensure that each trigger satellite is visible from one ground station continuously, and to remain compatible with the helio satellite deployment mechanism, a synchronous (one sidereal day period) trigger obit has been selected. The original requirements on blockage due to the Earth and radiation environment were reduced facilitating this change.

These changes have resulted in the following mission plan. The SMEX ETA will be launched in two batches of three satellites (two helio satellites and one trigger satellite) nominally separated by 60 days. Even in the event of a launch failure a minimal constellation will be formed. After being released into GTO and checked out in 3 axis stabilized mode, the helio satellites will assume their burn orientation and spin up to 120 RPM. At a preset point near perigee the helio satellites will make a 1101 m/s burn using their Star 13A solid rocket motor allowing them to escape Earth. By inserting with a hyperbolic excess velocity parallel to the velocity vector of Earth each satellite will enter a heliocentric orbit with a period greater then that of Earth. As the helio satellites orbit the sun slower than Earth they will appear to spread away from Earth in the retrograde direction. The trigger satellites will hold in 3 axis mode for 8 to 12 orbits until an opportunity to insert into their final orbit, a 20,000 × 64,330 km radius synchronous orbit that is continuously visible from the Haystack Massachusetts ground station. The insertion will be accomplished by assuming their burn orientation, spinning up to 120 RPM, and making a 1247 m/s burn near apogee using their Star 13A solid rocket motor. Over the next two years the helio satellite constellation will spread 120° around the sun in a direction retrograde at which point it will enter full operation.

1.6 This Thesis

As described above, three of the major changes between the MIDEX and SMEX proposals involve changes to the propulsion and trajectory for ETA. This thesis describes the propulsion and trajectory design for the SMEX proposal and how it was arrived at. This is primarily an

engineering document. The previous thesis spent considerable time discussing the systems engineering of ETA. It believed that this work sufficiently cover the systems engineering of ETA so that this material will not be repeated here.

This document is organized to be as terse and direct as possible. In many cases, results were obtained using complicated orbital mechanics codes written by the author. These codes are generally not unique to this project and similar codes are commonly commercially available. The detailed description these codes is left to appendices in order to maintain the flow of the work.

This thesis is divided into the following chapters.

- Chapter 2 First Order Helio Satellite Orbits – This chapter describes how the helio satellites are deployed and why impulsive propulsion is superior to electric propulsion for this mission type. The trade study leading to the choice of the Ariane 5 ASAP ring and solid rocket prolusion is developed in detail.

- Chapter 3 Detailed Helio Satellite Orbits – This chapter describes how realistic burn parameters and final orbital elements are developed for the helio satellites. Constellation development and propulsion system is also described.

- Chapter 4 First Order Trigger Satellite Orbits – The evolution of the trigger satellite orbit in response to changing mission requirements over the course of the design process is described. The selection and properties of the current trigger orbit are described. The ground track and sky track of the trigger orbit are developed.

- Chapter 5 Detailed Trigger Satellite Orbits – The calculation of insertion opportunities is developed. The effect of and corrections required by the perturbations on the trigger orbit are also described.

- Chapter 6 Conclusion

Of these chapters the most important are chapter 2 and 4. These describe most directly how the current ETA propulsion and trajectory design were developed. Finally, the following codes are included in the appendices:

- Appendix A - Cowell's Method Propagator

- Appendix B - 2-D GTO Escape
- Appendix C - 3-D GTO Escape
- Appendix D - Keplerian Propagator
- Appendix E - Sky Track Plots
- Appendix F - Encke's Method
- Appendix G - Eclipsing

Chapter 2 First Order Heliocentric Satellite Orbits

The primary science of ETA is accomplished by spreading multiple sensors around the two AU baseline of Earth's orbit. Since the intrinsic advantage of the ETA concept is that these sensors can be very simple, the challenge of the ETA concept is how to spread these sensors over a large baseline. As with most things, there are multiple ways of spreading the sensors, carried by the helio satellites, around the Sun. The purpose of this chapter is to describe the trade study used to determine the "best" method for spreading the helio satellites around the Sun.

This chapter deals with the helio satellite deployment architecture, or systems level, trade study and is therefore one of the most important in the thesis. The architecture trade studies determine *how* the system works, as opposed to the specifics of how a given subsystem works. The function and design of the subsystems flow down from the architecture. This flow down constitutes the majority of the design work. Oddly, in most cases very little manpower and money is devoted to the architecture phase of the design. However, once this phase is complete the design team develops a momentum in one direction and it becomes very hard to go back. If a fundamentally better architecture exists, it will not be found because the design team is already concentrating on the details of carrying out the original architecture. Therefore, it is important to get the architecture trade study right the first time.

The primary difference between this proposal and thesis and the previous proposal and thesis derives from a difference in helio satellite deployment architecture dictated by the work described in this chapter. The reason for this difference will be elaborated upon in the following sections.

To describe how the best mechanism for spreading the helio satellites is selected the following sections are included. First, it is necessary to describe what spreading is and how it is achieved. Second, the parameters and criteria for this segment of the mission are described. Next, the possible options and the methodology for comparing them are described. Finally, the results of the trade study are presented.

2.1 The Nature of Spreading

Since this chapter deals primarily with the task of spreading helio satellites around the sun it is appropriate to begin with a description of what spreading is, how it is achieved, and what its effects are.

Spread in this document refers to the angular distribution of a constellation of helio satellites around the Sun. The constellation shown in Figure 2-1 has a spread of ~60° after one year, ~120° after two years, and ~180° after three years. In Figure 2-1 the Earth (*) and the helio satellites (+) are shown in the inertial frame and since each snapshot is a year apart the Earth appears in the same location. The spread rate is the average rate at which the constellation spreads. The spread rate of the constellation in Figure 2-1 is 60°/yr. Both spread and spread rate can be positive or negative referring to the direction of spreading around the Sun. A constellation is said to have a *positive* spread rate when it spreads around the Sun *ahead* of Earth in a *counter clockwise* direction as shown in Figure 2-1. Conversely, a constellation is said to have a *negative* spread rate when it spreads around the Sun *behind* Earth in a *clockwise* direction as shown in Figure 2-2. This purely geometric definition of spread rate will be supplemented by a definition of the physical mechanism shortly.

The concept of spread and spread rate can also be applied to individual helio satellites. The spread and spread rate of the constellation is that of the maximum spread rate satellite. The spread rates of the other helio satellites determine the distribution of helio satellites within the constellation. In this chapter it is assumed that the satellite spread rates are evenly distributed within the constellation. In the case of a four satellite constellation with a spread rate of 60°/yr the individual satellites have spread rates of 15°/yr, 30°/yr, 45°/yr, and 60°/yr. An even distribution of spread rates does not nessecaraly produce the optimum constellation for science return but is a good approximation of the optimum distribution.

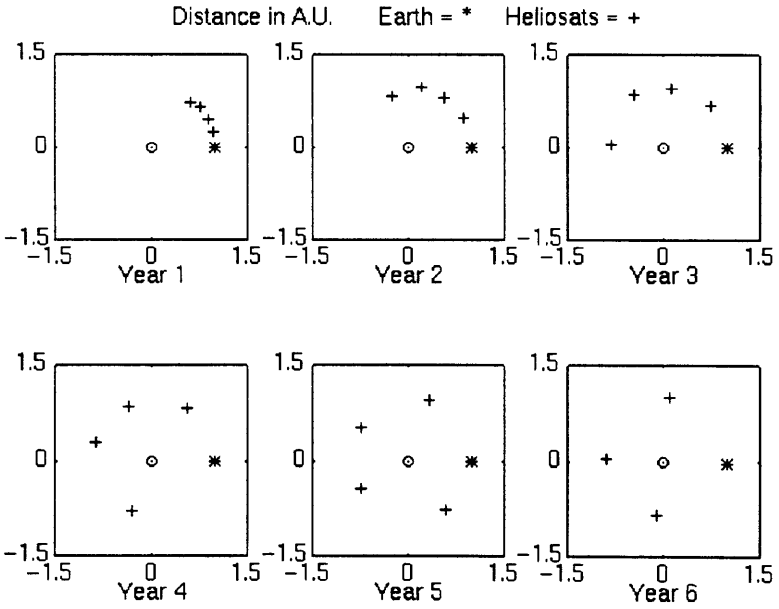

Fig. 2-1 The evolution of a satellite constellation with a positive 60°/yr spread rate.

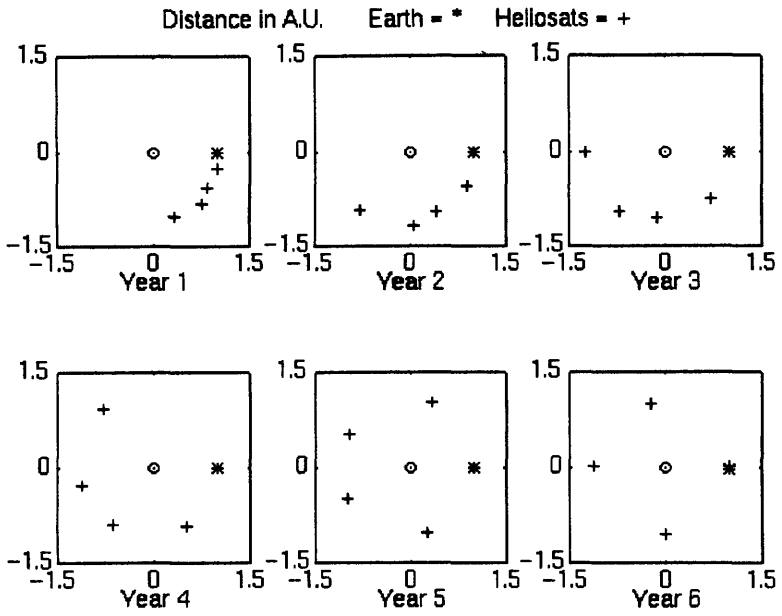

Fig. 2-2 The evolution of a satellite constellation with a negative 60°/yr spread rate.

Spread rate is the principal variable in the development of the ETA constellation. A spread of 120° is required before the constellation becomes fully operational. The spread rate, therefore, determines how long after launch it takes for the constellation reaches initial operational capability. With this in mind, the fastest spread rate possible would seem desirable. However, there are direct costs of generating higher spread rate and indirect costs associated with the effect of spread rate on the lifetime of the constellation. After the constellation spreads 360° it loops back upon itself. This produces an unfavorable distribution of helio satellites and the quality of the array begins to degrade. The higher the spread rate the faster this occurs. At a first glance it would seem desirable to "fix" the constellation once it reaches its optimum configuration rather than allowing it to loop back on it self. How this can be accomplished and why this is undesirable is described in the following sections. Knowing that fixing the constellation is undesirable, a balance must be struck between how long it take the constellation to develop and how long it takes the constellation to loop back on itself.

Given the importance of spread rate to the ETA mission, it is important to describe how spread rate is achieved.

Positive spread rate is created by injecting helio satellites with V_{inf} opposite to Earth's velocity vector as shown in Figure 2-3a. This places the satellites into heliocentric orbits with aphelions at Earth's radius, perihelions within the radius of Earth's orbit, and periods shorter than Earth's. A

helio satellite with a period shorter than Earth will orbit the Sun faster than Earth and therefore appear to spread away from Earth in the counter clockwise direction, giving it a positive spread rate.

Negative spread rate is created by injecting helio satellites with V_{inf} parallel to Earth's velocity vector as shown in Figure 2-3b. This places the satellites into heliocentric orbits with perihelions at Earth's radius, aphelions outside the radius of Earth's orbit, and periods longer than Earth's. A helio satellite with a period longer than Earth will orbit the Sun slower than Earth and therefore appear to spread away from Earth in the clockwise direction, giving it a negative spread rate.

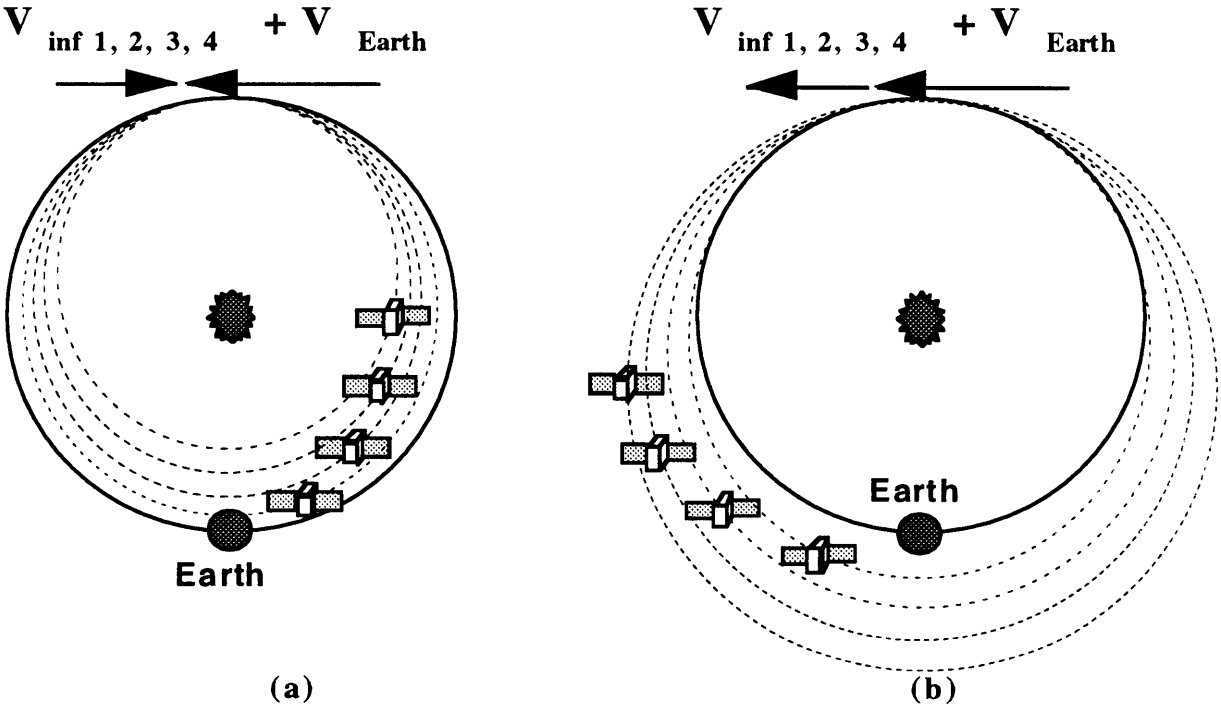

Fig. 2-3 Positive and negative spread rates.

The spread rate of a helio satellite is given as a function of the period of the satellite's and Earth's orbit by:

$$S = 2\pi\left(\frac{P_{Earth}}{P_{Sat}} - 1\right) \tag{2-1}$$

Where P_{Earth} is the period of Earth and P_{sat} is the period of the helio satellite. The period of an orbit is given by:

$$P = 2\pi\sqrt{\frac{a^3}{\mu}} \tag{2-2}$$

Where a is the semi-major axis of the orbit and μ is the gravitational parameter. The semi-major axis is given in terms of the energy, ε, of the orbit by:

$$a = -\frac{\mu}{2\varepsilon} \tag{2-3}$$

By substituting equation 2-3 into equation 2-2 and the results into equation 2-1 the follow equation for spread rate can obtained in terms of the energies of the orbits:

$$S = 2\pi\left(\left(\frac{\varepsilon_{sat}}{\varepsilon_{Earth}}\right)^{3/2} - 1\right) \tag{2-4}$$

The energy of the satellite's orbit is given by the by the vis-viva integral:

$$\varepsilon_{sat} = \frac{\left(V_{Earth} + V_{inf}\right)^2}{2} - \frac{\mu}{a_{Earth}} \tag{2-5}$$

Where V_{Earth}, the velocity of Earth, is given by $\sqrt{\mu / a_{Earth}}$. By substituting equation 2-5, and equation 2-3, for ε in terms of a, into equation 2-4 the following equation for spread rate in terms of V_{inf}, a_{Earth}, and μ is produced:

$$S = 2\pi\left(\left(\frac{a_{Earth}\left(\sqrt{\mu / a_{Earth}} + V_{inf}\right)^2}{\mu} + 2\right)^{3/2} - 1\right) \tag{2-7}$$

The calculation of spread rate can be simplified by linearizing the change in orbital energy around the Sun with respect to a small change in orbital velocity. This linearization, performed in the previous thesis, yields [8]:

$$S \approx \frac{3V_{inf}}{a} \tag{2-8}$$

Where S is the spread rate, a is the semi-major axis of Earth's orbit, and V_{inf} is parallel to the velocity vector of Earth. If V_{inf} is not parallel to the velocity vector of Earth the result can be approximated by multiplying V_{inf} by the cosine of the angle between the two vectors. For hand calculations the constant $a/3$ is equal to 27.5 when S is in °/yr and V_{inf} is in m/s. Equation 2-8 closely approximates the full Keplerian solution, as shown in Figure 2-4, and only breaks down at exit velocities approaching solar escape (above spread rates of 300°/yr). Because of the accuracy and simplicity of equation 2-8 it is used as the definition of spread rate in this chapter.

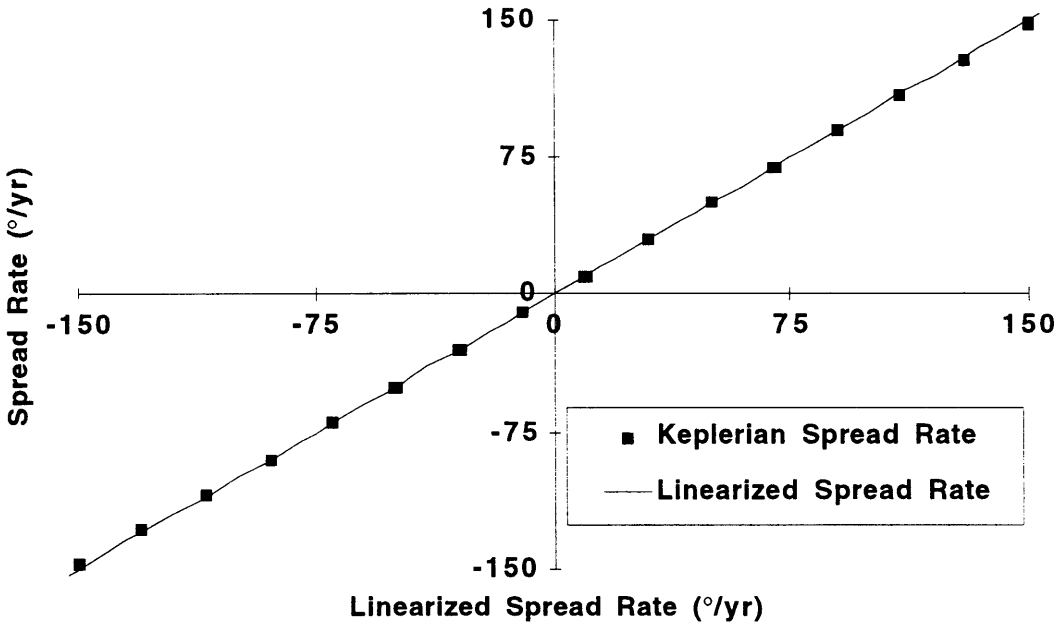

Fig. 2-4 Linearized vs. Keplerian spread rate.

Spread rate also has a strong effect on the environment experienced by a given helio satellite. The mechanism for creating spread rate changes the aphelion or perihelion of the satellite's final orbit considerably, as shown in Figure 2-5. For spread rates over ±100°/year a satellite will be going inside the orbit of Venus for positive spread rates and outside the orbit of Mars for negative spread rates. The higher the spread rate the greater the variation in environmental conditions over one orbit. The variation of solar flux with spread rate is shown in Figure 2-6, and the variation in black body temperature with spread rate is shown in Figure 2-7. Figure 2-7 assumes a cube of perfect conductivity, emissivity equal to one, and absorptivity equal to one, with one face pointed towards the Sun.

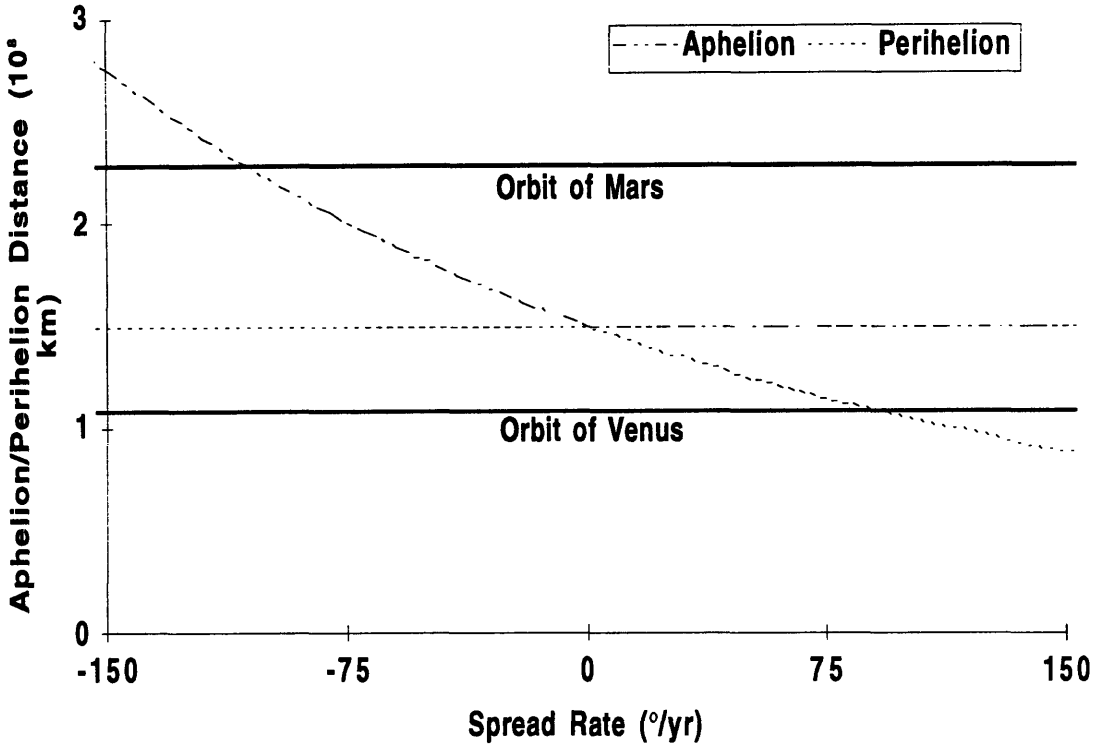

Fig. 2-5 Aphelion and perihelion vs. spread rate.

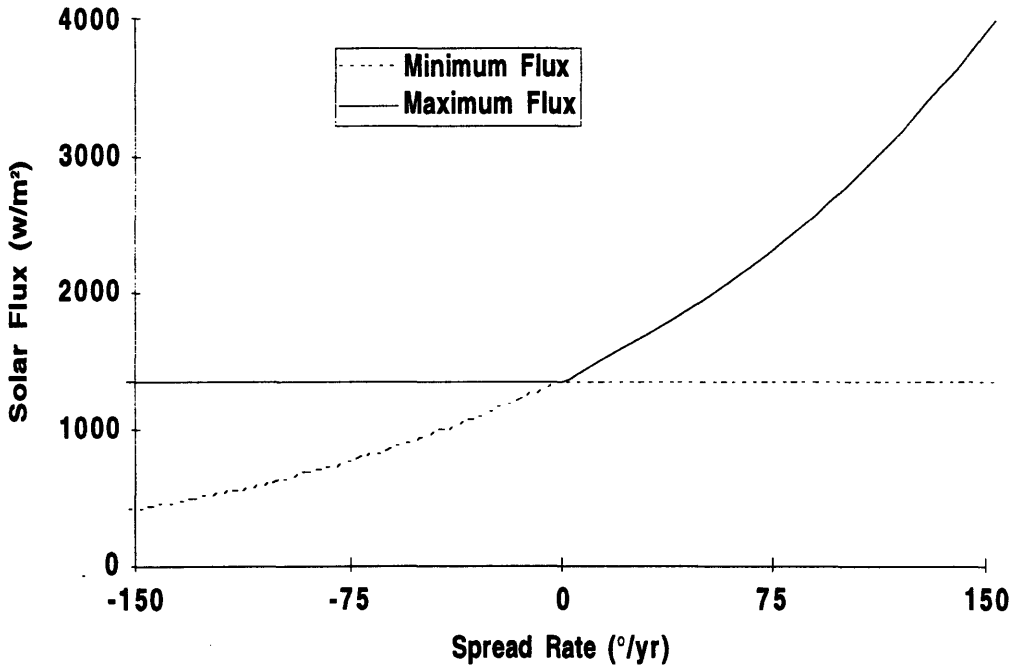

Fig. 2-6 Minimum solar flux vs. spread rate.

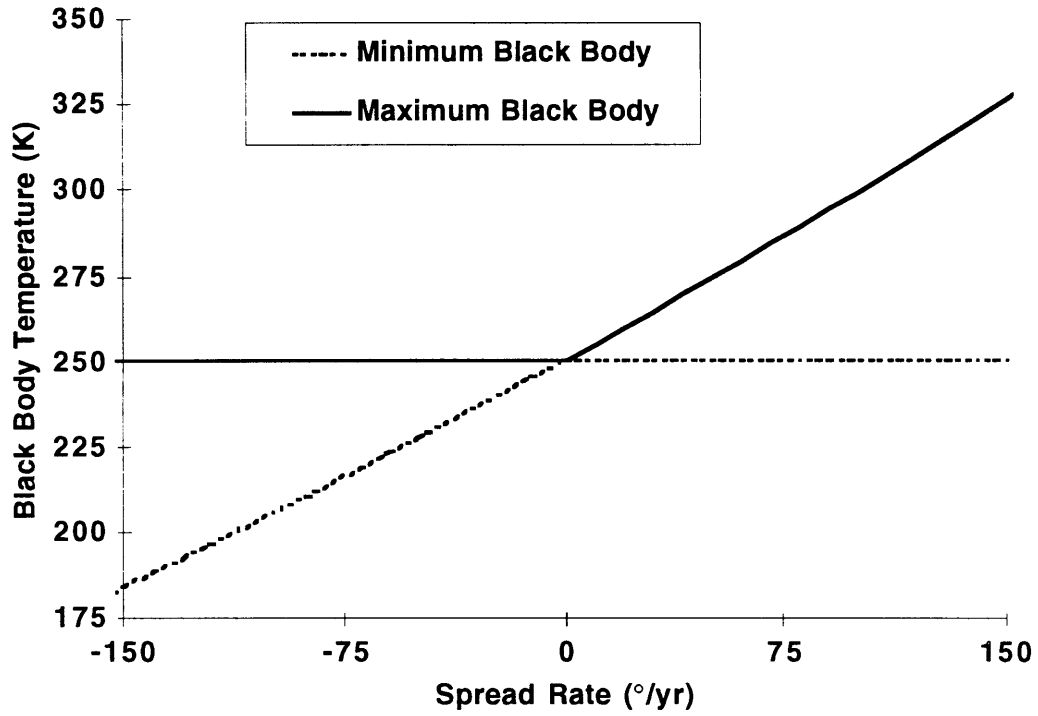

Fig. 2-7 Black body temperature of a cube.

2.2 Parameters and Criteria

With spreading defined, the remainder of this chapter is dedicated to considering the possible helio satellite deployment architectures. It is should be noted at this phase of the design the requirements were still general and flexible. In order to accommodate this each option was considered over a range of the following parameters:

- **Spread Rate** - A spread of at least 120° is required within two years of launch. However, it was not yet clear whether the minimum spread rate of 60°/yr was acceptable or whether a higher spread rate might be desirable. A range of spread rates from 30°/yr to 120°/yr was considered with a baseline of 90°/yr.

- **Number of Helio Satellites** - A minimum constellation can be formed with two helio satellites and one trigger satellite. However, increasing the number of helio satellites allows for a graceful degradation but increases the mass and the cost of the mission. A range of constellation sizes from 2 to 8 was considered with a baseline of 4 helio satellites.

In selecting between a number of options criteria are required. The following criteria were used:

- **Launch Vehicle** - It is desirable to minimize the launch mass in order to allow ETA to be proposed as a SMEX class mission and to minimize the system cost. In the first iteration, ETA required a Medlite launch vehicle and was therefore proposed as a MIDEX class mission. However, it is desirable to fit ETA into the constraints of a SMEX class mission which requires a Pegasus class or smaller launch vehicle. More SMEX class mission are available so that fitting ETA into the SMEX class increases the chances that ETA will be selected. Further, the launch vehicle is one of the most expensive components of any mission. Minimizing the launch vehicle needed helps minimizes the cost of mission.

- **Cost** - The primary constraint on all space mission is cost. Unfortunately, cost is often very difficult to estimate. Judgment can be used to differentiate between options. For example, monopropellant propulsion systems are generally less expensive than bipropellant propulsion systems.

- **Reliability** - NASA looks very favorably on missions that inherently have a higher probably of success. Again, the reliability of a system is often hard to quantify and judgment is required to differentiate between options. In general complex systems and systems with single point failures are less reliable.

2.3 Mission Options

This section outlines which helio satellite deployment options were considered.

The relationship between the options considered is shown in Figure 2-8. The options considered can be divided into two primary groups: Electric propulsion, and Impulsive propulsion. Electric propulsion offers high I_{sp} but is inherently low thrust. It is demonstrated in section 2.5 that electric propulsion is unfavorable for this mission class. Chemical propulsion, while having a lower I_{sp} than electric propulsion, is inherently impulsive and can therefore take advantage of the high velocities just after injection to greatly reduce the required ΔV. Chemical propulsion can itself be broken into two categories: missions that are launched on dedicated launch vehicles, and missions that are launched as secondary payloads. Dedicated launch vehicle missions, the traditional way of launching a mission, are considered in section 2.6. Within the dedicated launch vehicle category two sub categories exist based on where the propulsion system is located: concentrated in a single

propulsion bus, or distributed among the helio satellites. For each sub-category several propulsion types are considered (bipropellant, monopropellant, etc.). The option of launching as a secondary payload to GTO is discussed in section 2.7. Again, within the secondary payload category several propulsion types are considered. Ultimately, one of the secondary payload options was selected.

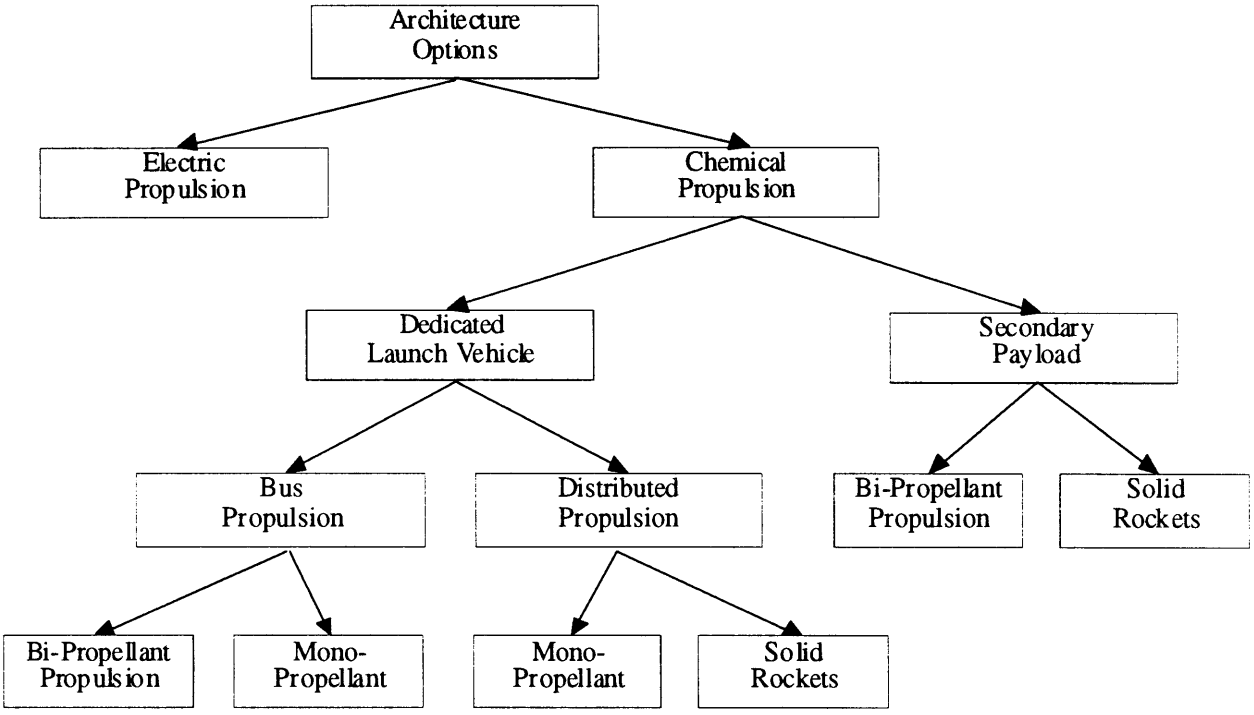

Fig. 2-8 Helio satellite deployment options.

2.4 Methodology

This section describes the methodology for analyzing the performance of the options considered. To the degree possible, the same methodology was applied to each option. However, the considerable variability in the options made it necessary to adjust the following methodology to the given circumstances.

First order analyses using Keplerian orbital mechanics and the rocket equation were applied to each class of options. The first order analysis of electric propulsion and dedicated launch vehicles is carried out in section 2.5 resulting in the elimination of electric propulsion. The first order analysis of secondary payload missions is described in the beginning of section 2.7.

Second order models of each option as a function of constellation spread rate, constellation size, and thrust acceleration were then created as shown in Figure 2-9. A 50 kg microsatellite (Table 2-1) scaled from the pervious proposal was used to determine the payload mass. The initial propellant mass was estimated using the Keplerian ΔVs computed in the first order section. A tank mass and propulsion system mass appropriate for the given propulsion type was then estimated. Finally, the deployment sequence was then numerically modeled using a Cowell's method propagator described in Appendix A. Numerical modeling allowed finite burn duration effects, wait times between satellite deployments, and time variable thrust and I_{sp} to be accounted for. The Keplerian estimates of ΔV generally produced low estimates of the propellant required so the results of the numerical model were used to adjust the propellant required. In the case of solid propellants numerical modeling was neglected because solid propellants produce such high accelerations that the Keplerian estimates are very accurate.

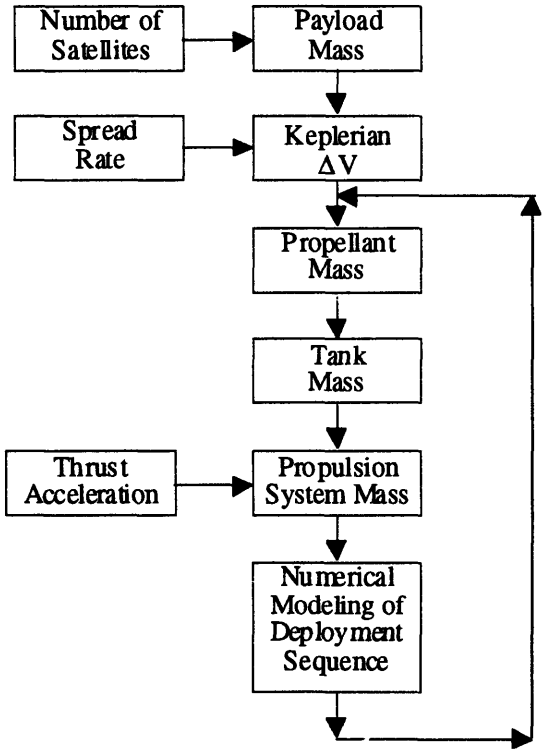

Fig. 2-9 Second order modeling of deployment options

Once the model for an option was constructed two sets of parametric data were generated. First, thrust acceleration and number of satellites was varied for 90°/yr spread rate constellations. These data yielded an optimum thrust acceleration. This thrust acceleration was then used to generate the second set of parametric data where the number of satellites and the spread rate were varied. Finally, these data were then used to compare the launch mass of each option.

Table 2-1 Assumed Helio Satellite Mass

Item	Mass (kg)
Structure / Thermal	12.0
Sensor(s)	10.0
Attitude Control	8.0
Power	7.0
RF Communications	3.5
Computer	1.2
Sub Total	41.7
20% Margin	8.3
Total	50.0

2.5 Chemical Versus Electric

Two very different propulsion systems can be used to achieve a V_{inf} with respect to Earth and thus a spread rate: impulsive, low I_{sp}, chemical propulsion such as solids, liquid propellants, or low thrust, high I_{sp}, electrical propulsion such as arcjets, Hall thrusters, and ion engines. This section will explain why impulsive propulsion's ability to use the presence of Earth at injection gives it greater performance for the mission types considered.

Consider the mission low thrust electric architecture used in the MIDEX proposal and an equivalent impulsive architecture. Both the impulsive and low thrust versions of the mission start when the satellites are injected at or above escape velocity. Next, each satellite must be provided with a different ΔV, corresponding to a different V_{inf} and spread rate, so that a constellation is formed. This ΔV is the primary propulsion for the mission. Without it the satellites might spread with respect to Earth, depending upon their injection velocity, but not with respect to each other. The problem then is to use the least ΔV to create a given V_{inf}. The relation between ΔV and V_{inf} can be found from energy conservation:

$$\frac{1}{2}V_{inf}^2 = \frac{1}{2}V^2 - \frac{\mu}{r}, \text{ or}$$

$$V_{inf}^2 = V^2 - V_{esc}^2 \tag{2-9}$$

Where V is the velocity of the satellite, μ is the gravitational parameter of Earth, r is the radius of the satellite from earth, and $V_{esc} = (2\mu/r)^{1/2}$ is the local escape velocity from Earth. Assuming that

the satellite is launched at escape and is provided a ΔV to spread itself with respect to Earth and any other satellites launched with it equation 2-9 becomes:

$$V_{inf}^2 = (V_{esc} + \Delta V)^2 - V_{esc}^2 \tag{2-10}$$

solving for ΔV:

$$\Delta V = \sqrt{V_{esc}^2 + V_{inf}^2} - V_{esc} \tag{2-11}$$

ΔV can be minimized in equation 2-11 for a given V_{inf} by maximizing V_{esc}. V_{esc} is at its maximum just after injection when the satellites are closest to Earth and drops off rapidly as the satellites leave the Earth frame. When V_{esc} is zero ΔV is equal to V_{inf}. Impulsive propulsion can take advantage of the high V_{esc} near Earth by making its ΔV over a course of minutes or seconds immediately after injection. Low thrust propulsion must make its ΔV over weeks or months when the satellites are far from Earth and V_{esc} is nearly zero.

The reduction in required ΔV by applying thrust near Earth can be explained in terms of basic physics. The purpose of a ΔV is to change the energy of an orbit in the Earth frame in order to give it a V_{inf}. The rate at which the energy of a satellite's orbit is changed is the force acting on the satellite multiplied by the velocity of the satellite with respect to Earth. Therefore a given impulse (force times time) will create the greatest change in orbital energy when the impulse is applied at the highest velocity relative to Earth. An impulse applied to a satellite at V_{esc} near Earth where V_{esc} is high will change the energy of the satellite's orbit far more than if the impulse is applied when the satellite is far from Earth where V_{esc} is approaching zero.

To quantify the advantage of high thrust propulsion consider a spread rate of 90°/yr. This spread rate requires a V_{inf} of 2475 m/s from equation 2-8. If the ΔV is made at a 300 km altitude just after injection to the escape transfer orbit, the required ΔV is 277 m/s. If the ΔV is made far from Earth, the required ΔV is 2475 m/s. Impulsive propulsion, in this case, requires nearly an order of magnitude less ΔV than low thrust propulsion. Figure 2-10 shows the required ΔV versus spread rate assuming the ΔV is made at a 300 km altitude and escape velocity.

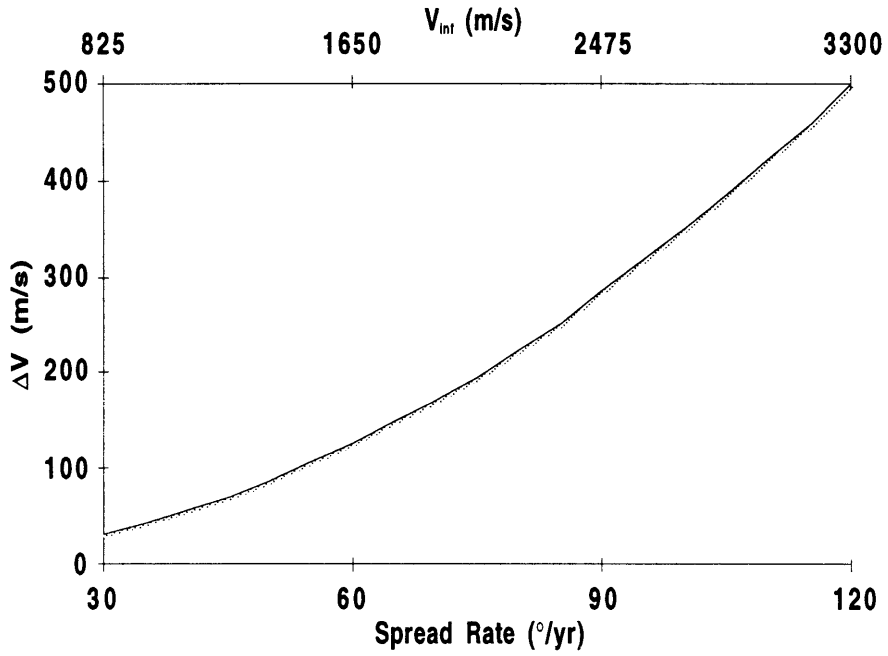

Fig. 2-10 ΔV vs. spread rate and V_{inf}.

To include the effect of the difference in I_{sp} between impulsive and low thrust propulsion it is assumed that to be equivalent, both types of propulsion must have the same wet mass to dry mass ratio. This assumption makes electric propulsion appear better than it is since the solar arrays and power converters needed for electric propulsion will make it heavier at the same mass ratio. While the assumption of similar mass ratios is poor, it saves delving into the specifics of each technology. The ratio of I_{sp}'s to yield the same mass ratio is simply the ratio of the ΔVs:

$$\frac{I_{sp\ electric}}{I_{sp\ chemical}} = \frac{V_{inf}}{\sqrt{V_{esc}^2 + V_{inf}^2} - V_{esc}} \tag{2-12}$$

Figure 2-11 shows the low thrust I_{sp} needed to produce the same mass ratio as several different types of chemical propulsion versus spread rate. Impulsive propulsion has a clear advantage over low thrust propulsion for the spread rates considered. Even at the same mass ratios and weights chemical propulsion is preferable because it is simpler and more flight proven.

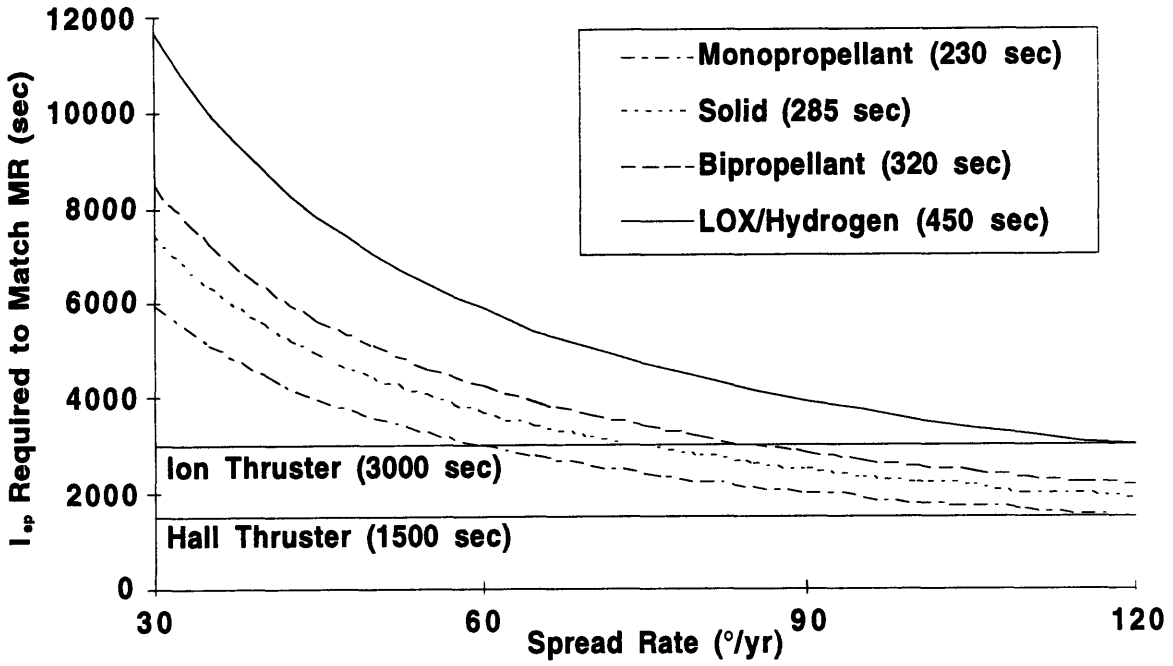

Fig. 2-11 Low thrust I_{sp} needed to match impulsive I_{sp}.

The difference in outcome between this thesis and the previous one results from the analysis in this section. The equivalent analysis in chapter 4 of the previous thesis makes no distinction between V_{inf} and ΔV. This put chemical propulsion at an extreme disadvantage since it is required to produce a vastly greater ΔV than it should have had to. Since only one method of applying ΔV is considered, far from Earth, only one architecture is considered. Because this thesis recognizes the difference between V_{inf} and ΔV and consequently considers multiple architectures a much different result was obtained.

The analysis in this section shows why "fixing" the helio satellite constellation in its optimum position is undesirable. In order to fix the constellation the spread rate of each satellite must be eliminated. This requires eliminating the difference in period between the helio satellites and Earth. To do this a ΔV equivalent to the original $\sim V_{inf}$ must be applied. However, as explained above the V_{inf} can be up to an order of magnitude higher than the spreading ΔV. Thus, fixing the constellation requires an order of magnitude more ΔV than the original spreading ΔV.

2.6 Dedicated Launch Vehicle Missions

This section analyzes dedicated launch vehicle options. A dedicated launch vehicle is the simplest way of placing a payload onto an escape trajectory. Many launch vehicles and their variants are

available in the class needed to launch a constellation of helio satellites, as is shown in Table 2-2. Since a large number of similar competitive launchers exist it is reasonable to assume that launch cost will be proportional to launch mass. Therefore, all dedicated launch vehicle propulsion systems should be optimized for minimum launch mass. This section contains four sub-sections: an analysis of the optimum position of perigee for dedicated launch vehicle missions, an analysis of propulsion options using a single propulsion bus, an analysis of propulsion options where the propulsion is distributed between the helio satellites, and, finally, a comparison of the bus and distributed propulsion options.

Table 2-2 Launch vehicles capabilities to $C_3 = 0$ [9,10,11]

Launch Vehicle	Launch Mass (kg)
Pegasus XL / Star 27	127
Taurus / Star 37	315
Taurus / Orion 38 / Star 37	340
Taurus XL / Star 37	360
Taurus XL / Orion 38 / Star 37	380
Taurus XLS / Star 37	400
Taurus XLS / Orion 38 / Star 37	425
LMLV 2	425
Taurus XL / AUS-51	430
Taurus XL / Orion 38 / AUS-51	445
Taurus XLS / AUS-51	515
Taurus XLS / Orion 38 / AUS-51	530
LMLV 3 (2 strap on)	590
LMLV 3 (6 strap on)	700

2.6.1 Position of Perigee

Position of perigee is the location of the escape trajectory perigee (for secondary payloads the location of the GTO perigee) measured as the clockwise angle from the the velocity vector of Earth as shown in Figure 2-12. The ability of a dedicated launch vehicle, as opposed to a secondary payload mission, to choose its launch time of day, and thus the position of perigee, is one of its primary advantages. The optimum position of perigee for a single satellite results in a V_{inf} parallel to the velocity vector of Earth.

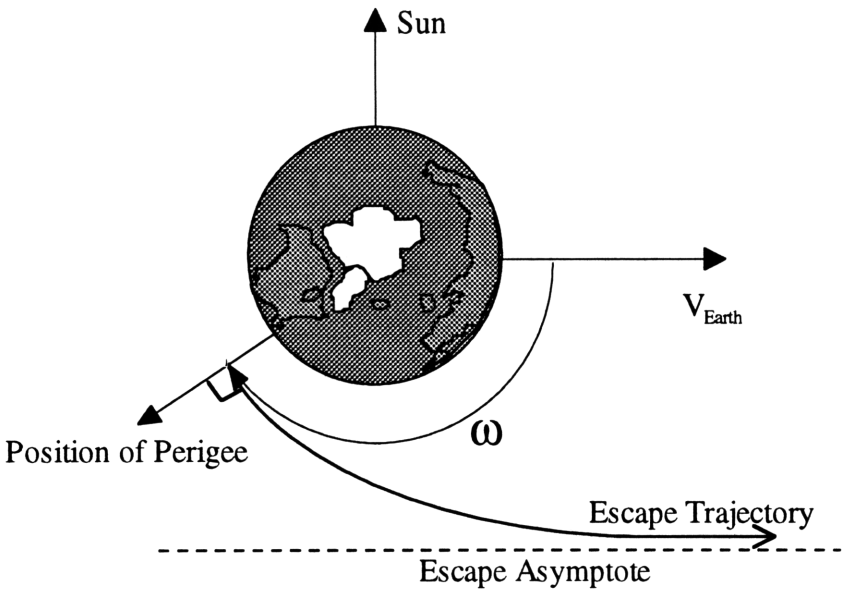

Fig. 2-12 The definition of position of perigee used in this chapter.

To derive an equation for the optimum position of perigee for a single satellite, the perigee that yields an escape velocity vector parallel to the Earth's velocity vector, note that the position of perigee for the satellite shown in Figure 2-12 is equal to the limiting true anomaly for the escape trajectory given by:

$$\omega = \sin^{-1}\left(\frac{1}{e}\right) + \frac{\pi}{2} \tag{2-13}$$

Where e is the eccentricity given by:

$$e = \sqrt{1 + \frac{2\varepsilon h^2}{\mu^2}} \tag{2-14}$$

Where ε is the specific mechanical energy of the orbit, h is the specific mechanical energy, and both are given by:

$$\varepsilon = \frac{V_{\inf}^2}{2}$$
$$h^2 = V_{perigee}^2 R_{perigee}^2 = (V_{\inf}^2 + V_{esc}^2) R_{perigee}^2 \tag{2-15}$$

Where $V_{perigee}$ and $R_{perigee}$ are the velocity and radius at perigee and $V^2_{perigee}$ can be substituted with equation 2-9 to produce the second form of h^2. Substituting 2-15 into 2-14, remembering that $V_{esc} = (2\mu/r)^{1/2}$, and simplifying yields:

$$e = \sqrt{1 + 4\frac{V_{inf}^2}{V_{esc}^2}\left(1 + \frac{V_{inf}^2}{V_{esc}^2}\right)} \tag{2-16}$$

Substituting 2-16 into 2-13 yields:

$$\omega = \sin^{-1}\left(\left(1+4\frac{V_{inf}^2}{V_{esc}^2}\left(1+\frac{V_{inf}^2}{V_{esc}^2}\right)\right)^{-\frac{1}{2}}\right)\mp\frac{\pi}{2} \qquad (2\text{-}17)$$

Where ω is the position of perigee. The second term in equation 2-13 is negative for positive spread rates and positive for negative spread rates. Unfortunately, all of the satellites in a constellation will be given the same position of perigee if launched on the same vehicle. The optimum position of perigee for a constellation minimizes the average ΔV of all satellites. It is necessary to find the V_{inf}, and from that the ΔV, for each satellite to yield a component of V_{inf} parallel to Earth's velocity vector corresponding to the desired spread rate. The V_{inf} needed is found by solving:

$$V_{\text{inf } component} = V_{\text{inf}}\cos\left(\omega-\sin^{-1}\left(\left(1+4\frac{V_{inf}^2}{V_{esc}^2}\left(1+\frac{V_{inf}^2}{V_{esc}^2}\right)\right)^{-\frac{1}{2}}\right)\pm\frac{\pi}{2}\right) \qquad (2\text{-}18)$$

Where the second term in the cosine is positive for positive spread rates and negative for negative spread rates. Using equation 2-18 to optimize position of perigee for the minimum average ΔV for all satellites in constellations of different sizes and spread rates yields Figure 2-17. The positions of perigee versus spread rate for constellations of 4 to 8 satellites can be fit by the line ω = -0.2141S - 0.8740 without significant error, where ω is in degrees and S is in degrees per year. Errors in position of perigee of three to four degrees result in changes in required ΔV of less than a 0.1%. For negative spread rates the position of perigee is the one shown Figure 2-13 plus 180°.

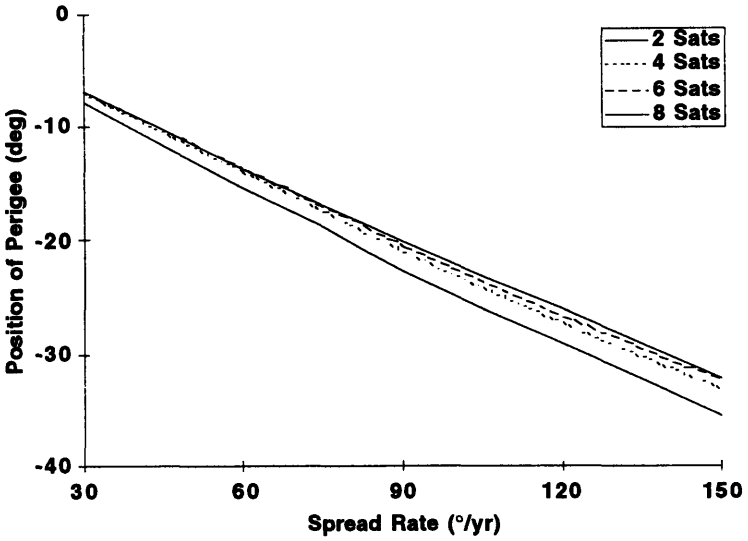

Fig. 2-13 Position of perigee vs. positive spread rate.

2.6.2 Bus Propulsion

In a bus propulsion system the spreading ΔV for each satellite is provided by a single propulsion bus. A bus / satellite stack is injected with the V_{inf} of the maximum spread rate satellite. After the maximum spread rate satellite is released, the bus decelerates the stack to the V_{inf} required by the next highest spread rate satellite and releases that satellite. The process of decelerating and releasing satellites continues until all of the satellites are released. The satellites are decelerated from the maximum spread rate so that the stack is left at or near escape wich facilitates inserting the trigger satellites. A wait time is required between each ΔV for releasing a satellite and performing a collision avoidance maneuver.

The advantage of a bus propulsion system is that it requires purchasing only one propulsion system and is therefore lighter and lower cost than a distributed propulsion system which requires purchasing multiple propulsion systems. The disadvantage of a bus propulsion system is that it must be more reliable than a distributed propulsion system. If a bus propulsion system fails the entire mission may be lost.

For performance calculations the bus is considered an augmented satellite. Because the bus is placed into a solar orbit with the satellites it makes sense to include a set of sensors on the bus and make continued use of its attitude control, communications and power system after its initial task is done. The mass budget for the bus will be the mass of the propulsion system plus the mass budget in Table 2-1. The wait time between burns is assumed to be 10 minutes.

2.6.2.1 Bus Monopropellant

The monopropellant system for the dedicated launch vehicle bus monopropellant propulsion option is modeled in this section and all later sections with the following assumptions. The monopropellant system is assumed to have a nominal I_{sp} of 230 sec at an inlet pressure of 200 psi. Thrust is assumed to be proportional to tank pressure. The tank pressure is modeled with a 4 to 1 adiabatic isentropic expansion starting at 400 psi and 300 K. The adiabatic isentropic expansion is justified because all of the propellant is used over a short period of time preventing significant heat transfer. The effect of inlet pressure on I_{sp} is given by [12]:

$$I_{sp} = I_{sp\,nominal}\left(1 - 0.005\frac{P_{nominal}}{P}\right) \tag{2-19}$$

Where P is inlet pressure. In addition to the nominal propellant, 10% more propellant is included as trapped propellant and flight performance reserve. The mass of the propellant tank is assumed to be 10% of the mass of the propellant. The mass of the thruster is modeled by [12]:

$$M_{thruster} = 0.068745\ F^{0.55235} \tag{2-20}$$

Where mass is in kg and force is in N. Equation 2-20 is a fit to existing monopropellant thrusters but produces low estimates for very low thrusts (<50 N). Finally, the mass of the latch valves, filters, pressure transducers, lines, line heaters, and fittings is assumed to be 5 kg.

The results of modeling the primary payload bus monopropellant propulsion system are shown in Figures 2-14 and 2-15. Launch mass versus initial acceleration based on nominal thrust is shown in Figure 2-14 for a 90°/yr spread rate. The optimum is caused by the superposition of two competing processes: decreasing thrust leads to higher finite burn duration losses, and increasing thrust leads to increased thruster mass. This optimum, however, is relatively wide. Using the optimum acceleration of 0.05g the launch mass versus spread rate is shown in Figure 2-15.

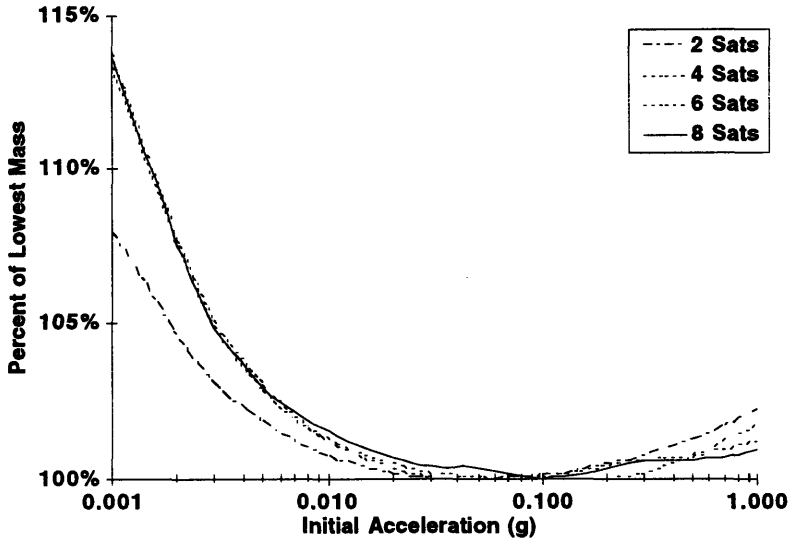

Fig. 2-14 Launch mass vs. initial acceleration for bus monopropellant at a 90°/yr spread rate.

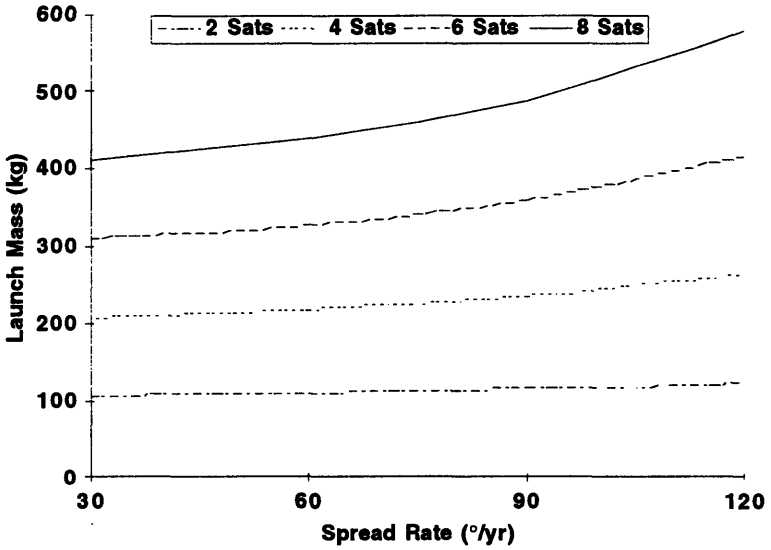

Fig. 2-15 Launch mass vs. spread rate for bus monopropellant.

2.6.2.2 Bus Bipropellant

The bipropellant propulsion system for the dedicated launch vehicle bus bipropellant propulsion option is modeled in this section and all later sections with the following assumptions. The bipropellant thruster is assumed to have a nominal I_{sp} of 290 sec at an inlet pressure of 220 psi. Higher performance dual mode engines are being developed but are not generally available in the thrust range required and are expensive to qualify so are not considered. A pressure regulated

nitrogen pressurant system is assumed. In addition to the nominal propellant, 10% more propellant is included as outage and flight performance reserve. The mass of the propellant tank is assumed to be 10% of the mass of the propellant. The mass of the thruster is modeled by:

$$M_{thruster} = 0.18989\ F^{0.48667} \qquad (2\text{-}21)$$

Where mass is in kg and force is in N. Equation 2-21 is a fit to the masses of the 4 to 800 N bipropellant thrusters manufactured by Kaiser Marquardt [13]. Finally, the mass of the latch valves, check valves, filters, pressure transducers, pressure regulators, lines, line heaters, and fittings is assumed to be 10 kg.

The results of modeling the primary payload bus bipropellant propulsion system are shown in Figures 2-16 and 2-17. Launch mass versus initial acceleration is shown in Figure 2-16 for a 90°/yr spread rate. Using the optimum initial acceleration of 0.02g, launch mass versus spread rate is shown in Figure 2-17.

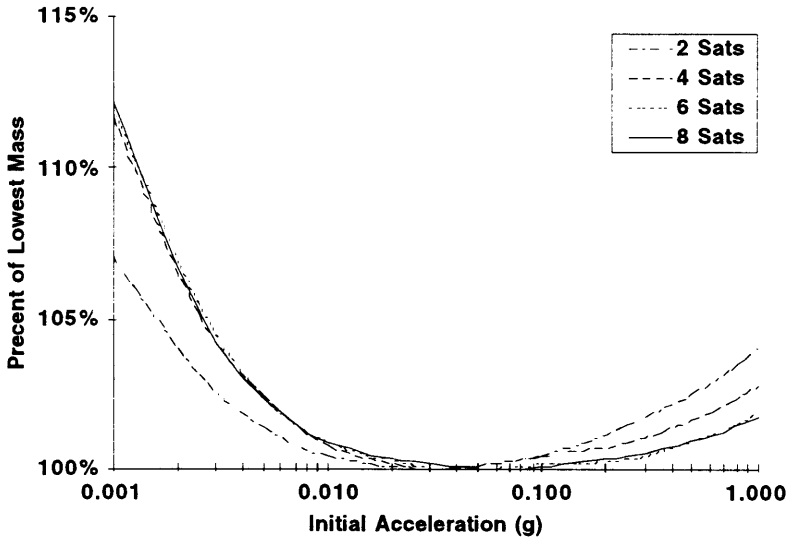

Fig. 2-16 Launch mass vs. initial acceleration for bus bipropellant at a 90°/yr spread rate.

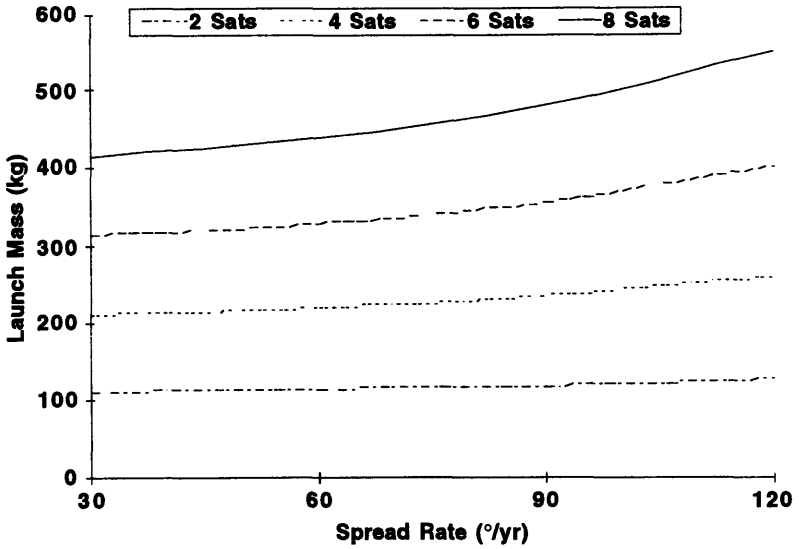

Fig. 2-17 Launch mass vs. spread rate for bus bipropellant.

1.6.3 Distributed Propulsion

In a distributed propulsion system the spreading ΔV for each satellite is provided by the satellite's own propulsion system. The satellite stack is injected with the V_{inf} of the lowest spread rate satellite. Starting with the maximum spread rate satellite, each satellite in turn separates from the stack and makes its spreading ΔV. As with the bus propulsion system, the satellite release order is arranged so that the largest ΔVs are made closest to Earth. Again, a wait time is required between releasing satellites but it will be shorter than for the bus propulsion option because no collision avoidance maneuver is necessary.

The advantage of a distributed propulsion system is that the failure of one satellite propulsion system does not prevent the deployment of the other satellites. In addition, burns can be made in parallel reducing finite burn loss. The disadvantage of a distributed propulsion system is that it costs more than a bus propulsion system because more propulsion systems must be purchased and the launch mass will be higher for a distributed propulsion system.

The mass of the satellites is assumed to be the mass of the propulsion system plus the mass budget in Table 2-1. Monopropellant and solid propulsion are considered in the following sections. However, bipropellant propulsion is neglected because hand calculations showed that it will yield no performance advantage at this size while incurring significant cost and complexity. The wait time between releases is assumed to be 5 minutes.

2.6.3.1 Distributed Monopropellant

All of the assumptions made for the monopropellant propulsion system in the bus monopropellant section are retained in this section.

The results of modeling the primary payload distributed monopropellant propulsion system are shown in Figures 2-18 and 2-19. Launch mass versus initial acceleration based on nominal thrust is shown in Figure 2-18 for a 90°/yr spread rate. Using the optimum initial acceleration of 0.05g, the launch mass versus spread rate is shown in Figure 2-19.

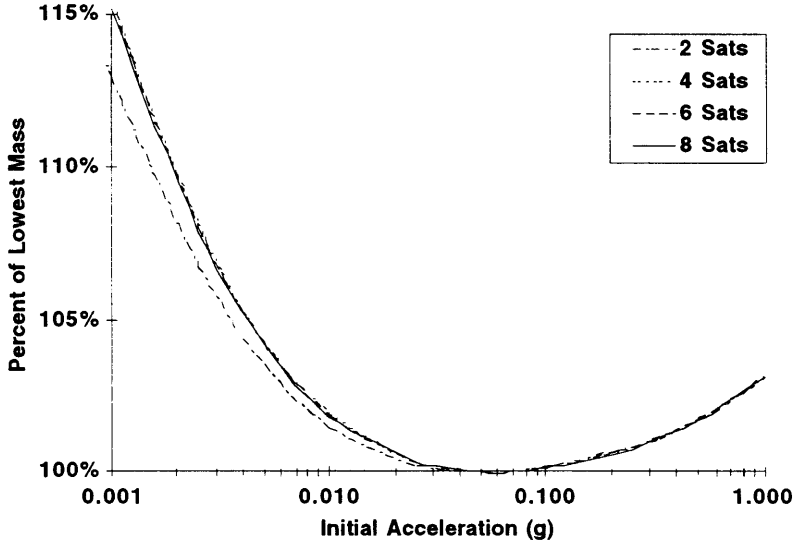

Fig. 2-18 Launch mass vs. initial acceleration for distributed monopropellant at a 90°/yr spread rate.

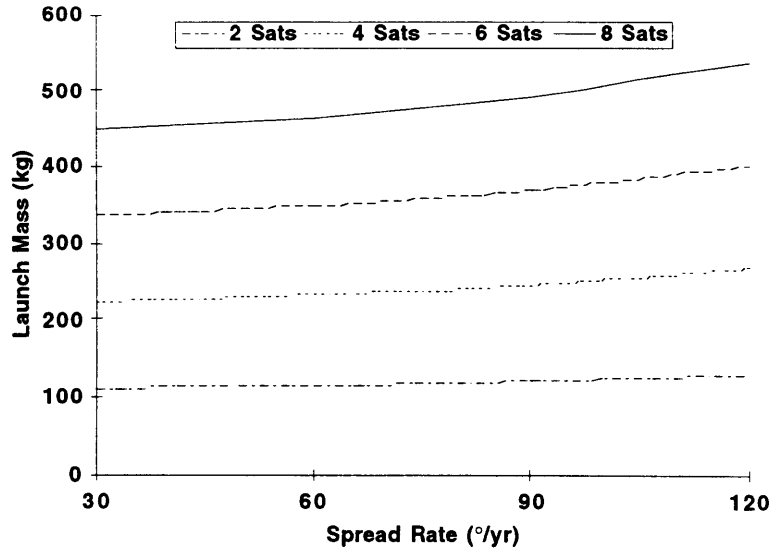

Fig. 2-19 Launch mass vs. spread rate for distributed monopropellant.

2.6.3.2 Distributed Solid

A simple way of providing distributed propulsion is through small solid motors such as the Star 5, a solid rocket motor originally developed for stage separation purposes. For performance calculations a generic solid in the Star 5 class is assumed with a mass fraction of 50% and an effective I_{sp} of 265 sec. Since the action time of a solid is very rapid the performance can be modeled as Keplerian. The solid motors are sized for the ΔV of the largest spread rate satellite. For lower spread rates the satellites are allowed to coast to a higher altitude where their spreading ΔV is the same as that of the maximum spread rate satellite. Coasting to a higher altitude saves the complexity of off loading or off pointing the solid motors. Even if the motors were off loaded this maneuver would still be necessary because most solid motors can only be off loaded 20%. The launch mass versus spread rate is shown in Figure 2-20.

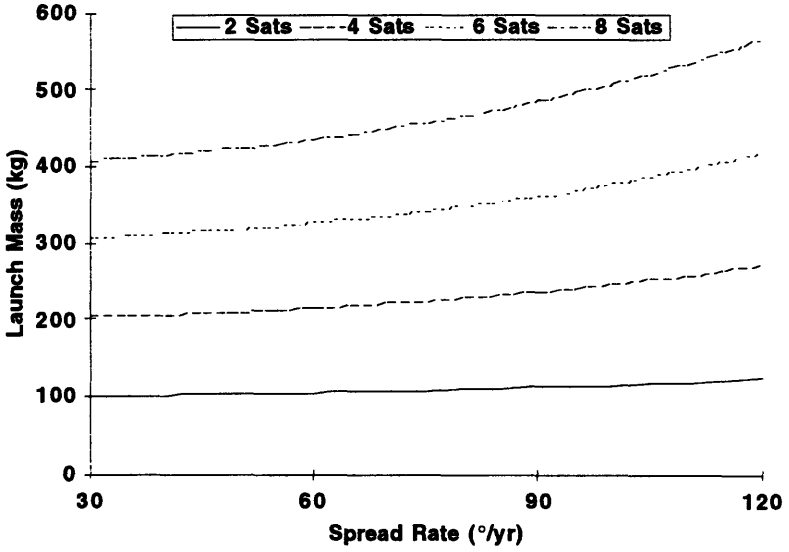

Fig. 2-20 Distributed solid launch mass vs. number of satellites and spread rate.

2.6.4 Comparison of Dedicated Launch Vehicle Options

Figure 2-21 compares bus monopropellant and bipropellant propulsion by superimposing Figures 2-15 and 2-17. Over most of the range shown monopropellant and bipropellant propulsion are nearly equivalent. Bipropellant propulsion has an increasing advantage at high spread rates and large constellation sizes because of its high I_{sp}. Monopropellant has an advantage at lower spread rates and smaller constellation sizes because its fewer components result in a lower dry mass. Monopropellant propulsion is always preferable to bipropellant when the two are nearly equivalent because of monopropellant propulsion's low cost (1/3 to 1/4 of bipropellant propulsion) and simplicity.

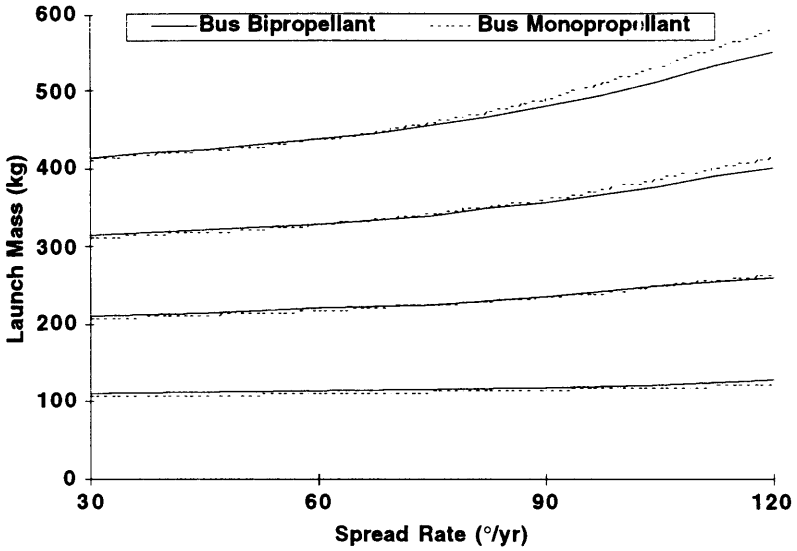

Fig. 2-21 Comparison of bus bipropellant and monopropellant.

Figure 2-22 compares distributed monopropellant and solid propulsion by superimposing Figures 2-19 and 2-20. At lower spread rates solid propulsion has an advantage due to its high I_{sp} and low mass fraction. This advantage is lost at high spread rates because it is assumed that the solid motors are not off loaded for the lower spread rate satellites in a constellation. Even if off loading is assumed it has a minor effect on the launch mass since most solids can only be off loaded 20%. When monopropellant and solid propulsion are nearly equivalent solid is preferable because of its low cost and simplicity.

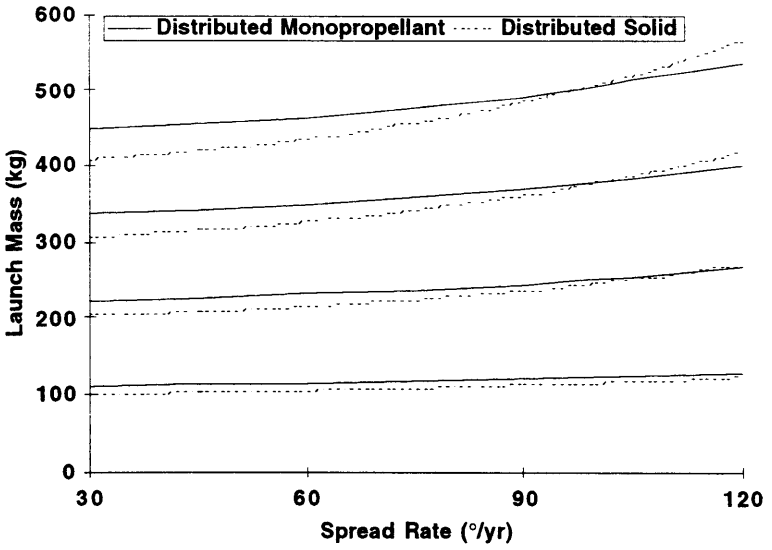

Fig. 2-22 Comparison of distributed monopropellant and solid.

Finally, Figure 2-23 compares the best bus option, bus monopropellant, and the best distributed option, distributed solid, by superimposing Figures 2-15 and 2-20. Over the spread rates shown both are nearly equivalent so a decision between the two must be made on different criteria. Bus monopropellant offers lower cost at higher complexity and risk of a single point failure. Distributed solid offers simplicity and lower risk at higher cost. It is felt that the additional cost of the distributed solid option is more than offset by its simplicity and reduced risk.

Before continuing to the secondary payload section it is useful to compare the best dedicated launch vehicle option, distributed solids, to the previous iteration ETA. The launch mass of the previous iteration was 498 kg. This mission was subject to single point failure of the electric propulsion bus and required relatively untested (at least in the west) SPT thrusters. The launch mass of the distributed solid option is ~330 kg (220 kg for a four satellite constellation to 60°/yr and 110 kg for two trigger satellites), a 33% improvment over the original. The distributed solid option is not subject to the single point failure of a propulsion bus and uses well proven (old) propulsion technology. Distributed solid propulsion is a significant improvement over the previous design. Unfortunately, the distributed solid is not enough of an improvement to fit on to any Pegasus class or less expensive dedicated launcher. This provides motivation for investigating secondary payload options.

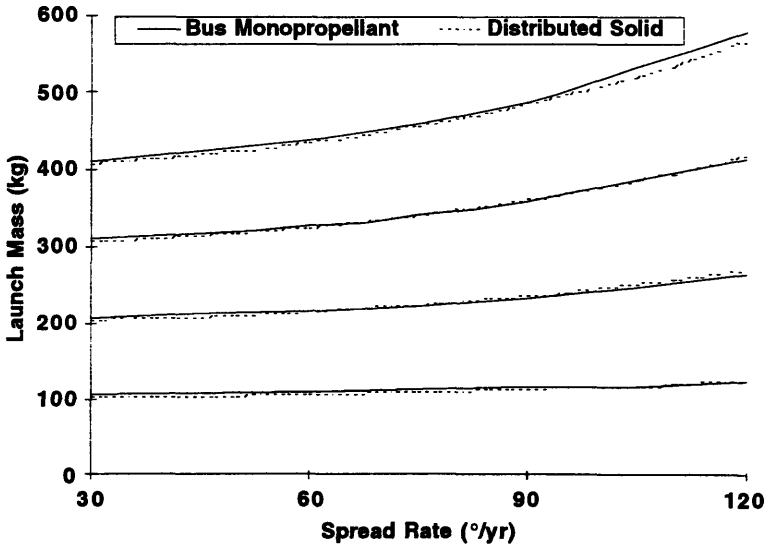

Fig. 2-23 Comparison of bus monopropellant and distributed solid.

2.7 Secondary Payload Missions

Frequently, commercial missions are injected into GTO with a small amount of excess capacity. This excess capacity can provide a very economical way of launching ETA. Unfortunately, this capacity is rarely used because no standard procedure exists for purchasing and utilizing it, with the exception of the Ariane Structure for Auxiliary Payloads (ASAP). The Ariane 4 ASAP ring can launch several 50 kg payloads simultaneously while the Ariane 5 ASAP ring is even more capable. The Ariane 5 ASAP ring is designed to launch up to eight 80 kg[1], 60×60×80 cm payloads for a ~$1 million documentation fee [14]. This is less than half the commercial rate and even less for small launchers like Pegasus. Thus, the Ariane 5 ASAP ring can loft an entire constellation at a great cost savings. The Ariane 5 ASAP capabilities will be assumed for the remainder of this paper.

A further advantage of the ASAP slot is that ETA satellites can be divided between multiple launches for the same price. To do this with dedicated launch vehicles would be prohibitively expensive. If two helio satellites and one trigger satellite are launched in each of two batches, even in the event of a launch failure a minimal ETA constellation can be established. This minimal constellation could then be augmented in the future by refurbishing and launching the prototype helio and trigger satellites. Dividing the launches greatly increases the reliability of mission success.

While ASAP payload slots are inexpensive and offer a higher probability of mission success, they have three disadvantages. First, Ariane is a foreign launch vehicle. NASA is barred from purchasing space on foreign a launcher. To deal with this, it is believed that an arrangement can be worked out with CNES, the French space agency. ETA would purchase it primary sensors from CNES and CNES would provide a free launch for ETA on the ASAP ring.

The second disadvantage is the cost of getting from GTO to escape: 776 m/s (assuming a 300 km × 35,786 km transfer orbit)[2] in addition to the spreading ΔV. Under ideal conditions a 90°/yr spread rate would require 1053 m/s. While this is substantially higher than the spreading ΔV required for

---

[1] Ariane later incresed this number to 100 kg. This number is still used in this chapter but the updated number is used in later chapters.

[2] Ariane later changed its GTO to 600 km × 35,786 km. Again, this number is still used in this chapter but the updated number is used in later chapters.

dedicated launch vehicle missions, it will be shown that the ETA helio satellites will still fit comfortably within the ASAP slot.

The third disadvantage arises from the secondary nature of ASAP slots. Secondary payloads do not choose the launch window; the primary payload does. Depending on the time of launch the position of perigee of the transfer orbit can be very different from the optimum position of perigee for the desired spread rate. An off optimum position of perigee will result in a V_{inf} that is not parallel to the velocity vector of Earth. Correcting for a non-parallel V_{inf} requires a larger V_{inf} or making the ΔV at a true anomaly off perigee, both of which require a larger than ideal ΔV. A code, which is described in Appendix B, was written that models the escape from GTO and yields the spread rate as a function of position of perigee, burn true anomaly, and ΔV. Optimizing this function for ΔV versus position of perigee to yield a constant ±90°/yr spread rate by varying the burn true anomaly results in Figure 2-24. The optimum true anomaly versus position is shown in Figure 2-25. If a specific direction of spreading is required, either positive or negative, then the worst possible ΔV, assuming no control over position of perigee, is the worst point on the curve in Figure 2-25 corresponding to that specific spreading direction. This can cost up to 3.40 km/s. However, if either positive and negative spread rates are acceptable (bi-directional spreading), so that the spreading direction with the lower cost at any given point is selected, the cost can be reduced to a maximum of 2.23 km/s. The bi-directional spreading cost versus position of perigee is shown in Figure 2-26 for several spread rates.

Fortunately, Ariane 5 GTO launches are restricted to a 45 minute launch window per day [15]. The start of this window varies slightly with time of year. The range of launch times during a year translates to positions of perigee from approximately 90° to 120°, as show in Figures 2-24, 2-25 and 2-26. This range of positions of perigee is nearly ideal for negative spread rates. For -90°/yr the maximum cost in this range is 1.35 km/sec or only 300 m/s greater than ideal. With holding orbits an ideal ΔV can be achieved, as discussed in the next section.

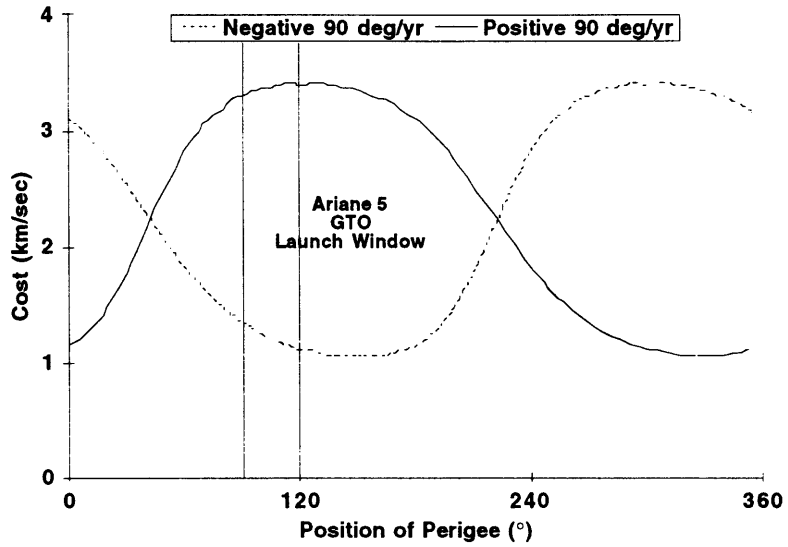

Fig. 2-24 Cost vs. position of perigee for a ±90°/yr spread rate.

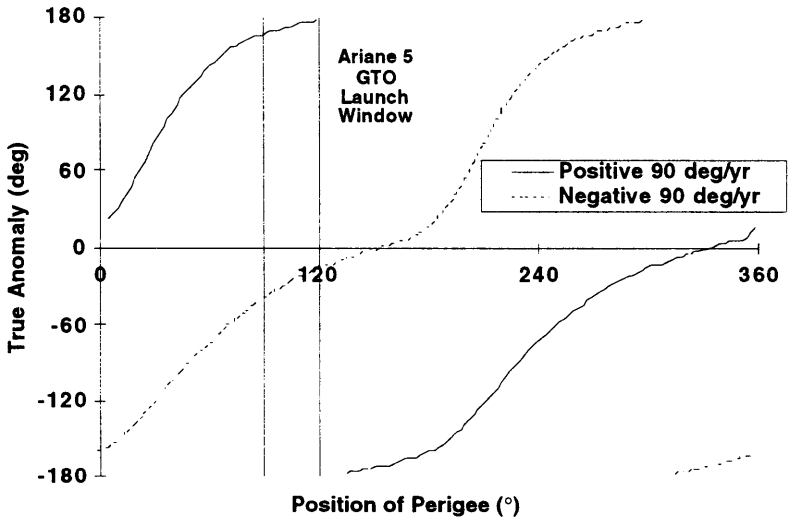

Fig. 2-25 True anomaly vs. position of perigee for a ±90°/yr spread rate.

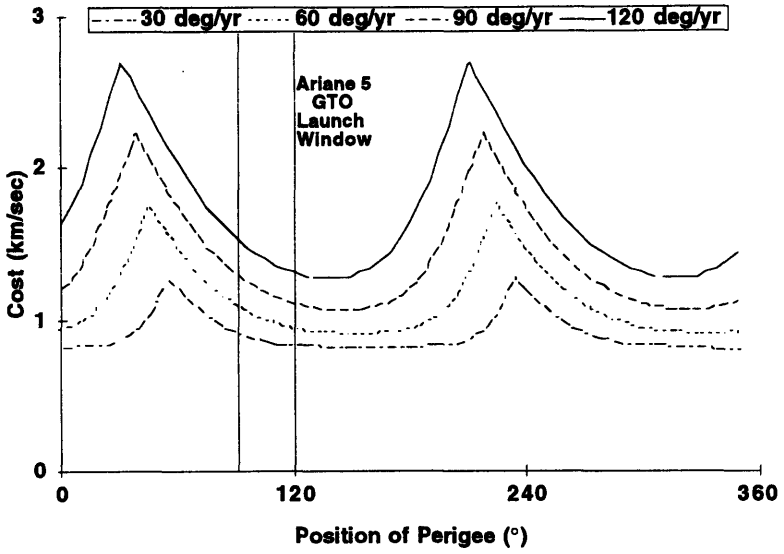

Fig. 2-25 Cost vs. position of perigee for several spread rates.

2.7.1 Holding

The purpose of a holding is to move a sub-optimum position of perigee to an optimum position of perigee using of the motion of Earth around the Sun, as shown in Figure 2-27, to rotate the apsides of GTO relative to Earth's velocity vector. After deploying the primary payload, the ASAP ring releases the helio satellites. The helio satellites wait in GTO until the position of perigee moves to the optimum point and then make their escape ΔV.

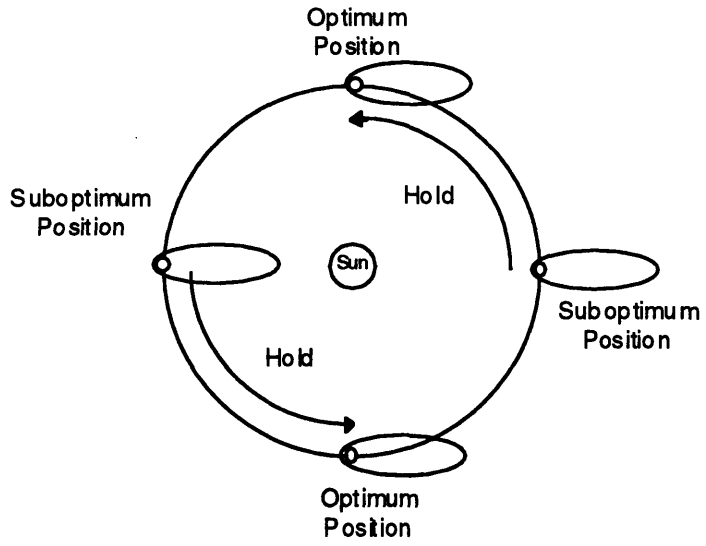

Fig. 2-27 Holding orbit concept.

The motion of Earth around the sun alone would produce a change in position of perigee of ~1°/day. However, oblateness of the Earth causes the holding orbit to precess in the inertial frame reducing the rate of change in position of perigee to ~0.66°/day. The cost versus hold time in GTO for a 90°/yr spread rate is shown in Figure 2-28. A wait of no more than 65 days yields the ideal ΔV for a -90°/yr spread rate.

The primary disadvantage of holding in GTO is radiation exposure. A satellite in GTO will spend a significant fraction of its time in the Van Allen radiation belts. It is assumed in this analysis that performance is the primary mission driver and that the radiation exposure from holding in GTO is acceptable. Therefore, the performance calculation made in the following sections assume that holding in GTO will be used to achieve the ideal ΔV. At a later date, radiation concerns resulted in holding being dropped from the ETA plan.

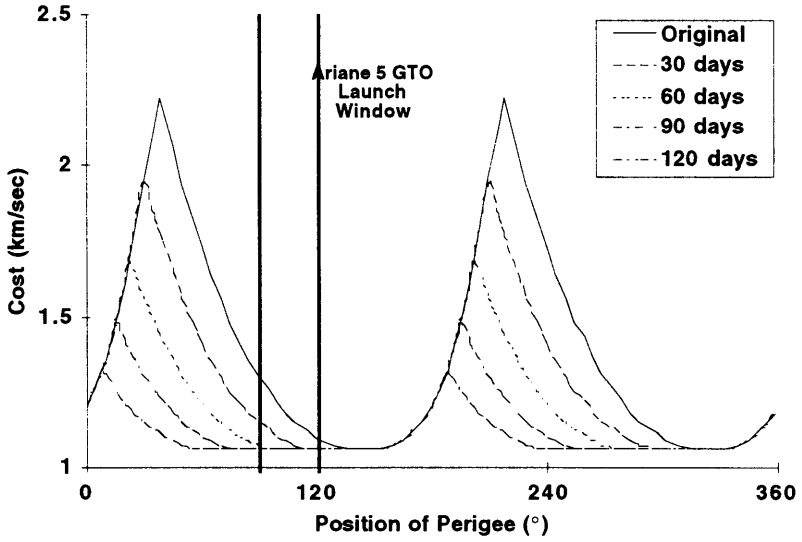

Fig. 2-28 Cost vs. hold time and starting position of perigee for a ±90°/yr spread rate.

Assuming the worst case, the cost of immediate departure from GTO will be an increase of no greater than 30% in ΔV. At a 90°/yr spread rate this will cost ~6 kg of payload. At a 60°/yr spread rate this will cost ~4.5 kg of payload. Another option is to design for the average ΔV in the launch window and accept a slightly higher or lower spread rate depending upon the actual position of perigee. The average ΔV will cost less than ~3 kg at a 90°/yr spread rate. Finally, if some hold time is acceptable, the greatest decreases in ΔV derive from the earliest part of the holding time.

Bipropellant and solid propulsion systems are considered in the following sections for producing the required ΔV. Monopropellant is neglected because it is not capable of significant payload at these ΔVs.

2.7.2 Liquid Propulsion

The secondary payload bipropellant propulsion system is modeled in the same way as the previous bipropellant propulsion system was modeled. The only exception is that the mass of valves and lines is assumed to be 5 kg due to the small size of this system. The mass of each satellite is assumed to be the mass of the propulsion system plus the mass budget in Table 2-1.

The results of modeling the secondary payload bipropellant propulsion systems are shown in Figures 2-29 and 2-30. Because the total mass is limited to 80 kg, payload mass is used as a performance metric. The payload mass will be limited by the highest spread rate satellite so only it needs to be modeled. Payload mass versus initial acceleration is shown in Figure 2-29 for a 90°/yr spread rate. Using the optimum initial acceleration of 0.1g the payload mass versus spread rate is shown in Figure 2-30. These results are conservative because of the high outage and flight performance reserve assumed earlier.

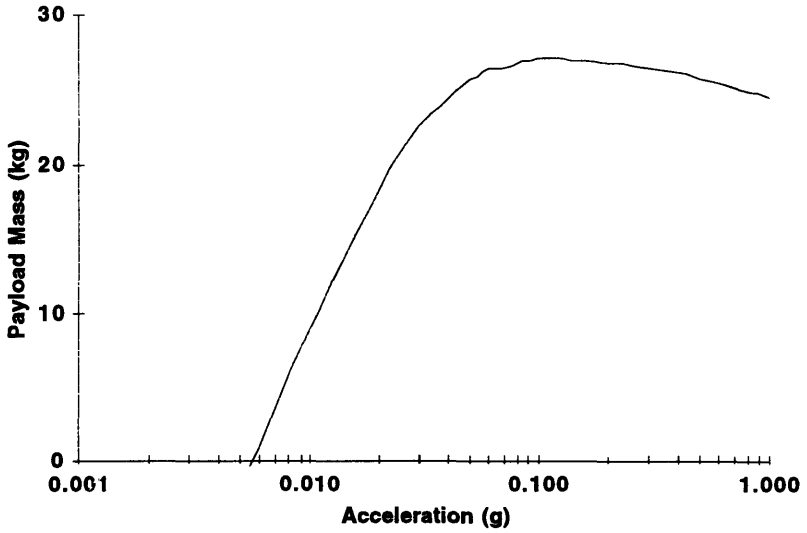

Fig. 2-29 Payload mass vs. initial acceleration for secondary bipropellant at a 90°/yr spread rate.

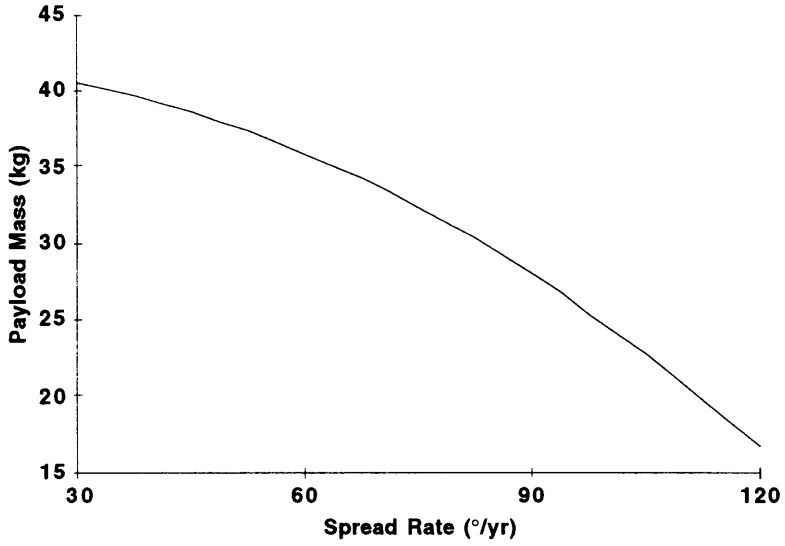

Fig. 2-30 Payload mass vs. spread rate for secondary bipropellant.

2.7.3 Secondary Payload Solid Propulsion

With its inherent simplicity and low cost, solid propulsion is an attractive option. The analysis of the secondary payload solid propulsion system is easier than that of the secondary payload liquid propulsion system because the high thrust and short action time of solids make finite burn losses negligible. Assuming a generic solid with a mass fraction of 0.9 and an I_{sp} of 285 sec yields the payload mass versus spread rate shown in Figure 2-31. Figure 2-31 also shows the capability of the Star 13A using up to 20% off loading to achieve different spread rates. The Star 13 motors manufactured by Morton Thiokol are low cost and ideal for this mission class. The real payload may be somewhat smaller than shown in Figure 2-31 due to additional structure resulting from the high burn out accelerations (≥10 g) of small solid motors.

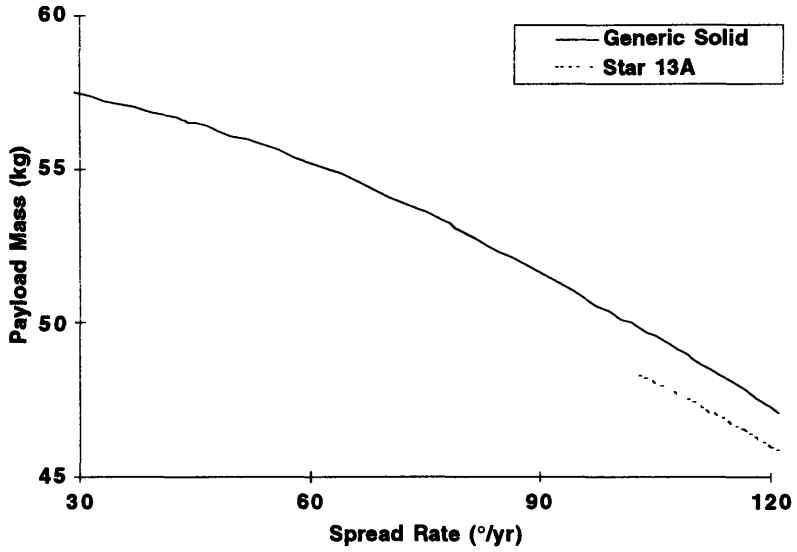

Fig. 2-31 Payload mass vs. minimum spread rate for secondary payload solid propulsion.

2.7.4 Comparison of Secondary Payload Options

Figure 2-32 compares secondary payload bipropellant and solid propulsion by superimposing Figures 2-30 and 2-31. Solid propulsion has an advantage due to its high mass fraction and short action time which minimizes finite burn duration losses. Solids are also simpler and more economical than bipropellants. The only disadvantages of solid propulsion are its lack of flexibility and high accelerations.

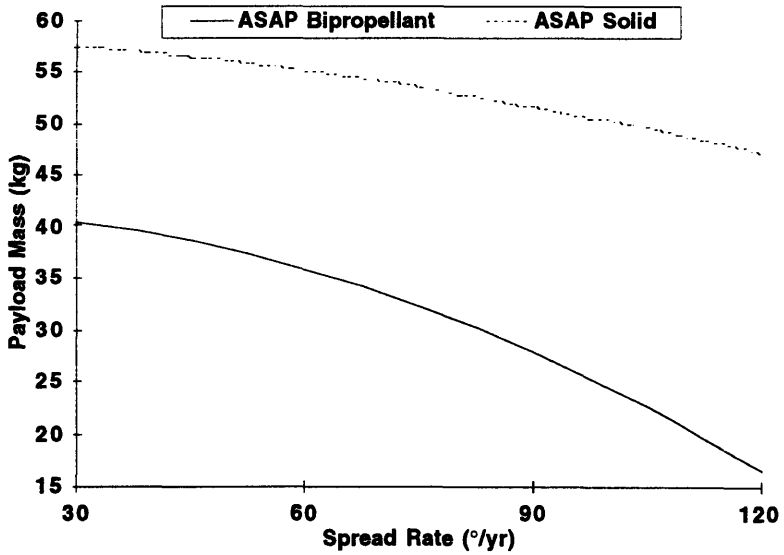

Fig. 2-32 Comparison of secondary payload bipropellant and solid.

2.8 Conclusions

Finally, it is necessary to compare dedicated launch vehicles and secondary payload slots. Secondary payload solid propulsion offers a significant advantage over dedicated launch vehicle distributed solid propulsion. Secondary payload solid propulsion retains the advantage of dedicated launch vehicle distributed solid propulsion in that it uses the same well proven low cost technology and is not subject to a single point failures. Further, the ability to divide ETA into more than one launch increases the reliability of secondary payload solid propulsion. Finally, because secondary payload solid propulsion does not require a Medlite class launch vehicle it allows ETA to be proposed as a SMEX class mission. For these reasons, secondary payload solid propulsion was selected for the current iteration of ETA.

The rest of this thesis deals with the implications of this choice. The following chapter describes the details of secondary payload solid propulsion. Chapter 4 describes the search for a trigger orbit and method of deploying the trigger satellites compatible with secondary payload solid propulsion. Chapter 5 describes the details of this trigger orbit.

In retrospect, the second order numerical modeling of each option was overkill. In engineering the simplest solution is often the best solution. First order arguments could have been used to establish that secondary payload solid propulsion was the best choice.

Chapter 3 Detailed Heliocentric Orbits

The purpose of this chapter is to develop the details of the helio satellite orbits and their required propulsion system. This flows down from the helio satellite deployment architecture determined in the last chapter and the requirements outlined in section 3.1 of this chapter. A 3-Dimensional Keplerian model is optimized to provide an upper bound on the required ΔV. Next, a burn strategy is developed to deal with the fixed ΔV provided by the solid rocket motor. Final orbital elements are generated as a function of spread rate and launch date. An analysis is carried out on the probability of mission success of distributing the satellites over several launches. Finally, the Star 13 propulsion system for ETA is described.

3.1 Requirements

The requirements solidified in the time between the architecture trade study and the detailed design work contained in this chapter. The following requirements and constraints were used in the preparation of the detailed design:

- **60°/yr Spread Rate** - This was felt by the science team to be the best balance between time that it takes the constellation to develop, the direct propulsive cost, and the indirect cost from the helio satellite environment . This is the minimum spread rate in order to produce an operational constellation in two years.

- **4 Helio Satellites** - This is the minimum number of satellites to provide a redundant constellation capable of cross checking its own localizations (three operating helio satellites even in the event of a helio satellite failure and at least one trigger satellite). Further, this is the minimum number of helio satellites necessary to provide a minimal working constellation (two helio satellites and one trigger satellite) in the event of a launch failure if the helio satellites are divided into two launches .

- **Distributed Launches** - The helio satellites will be divided into two launches in order to increace the probability of mission success.

- **GTO** - Between the architecture trade studies and the detailed design it was learned that Ariane had changed the GTO for Ariane 5 to 6,978 km × 42,165 km [16]. Further, the ASAP payload mass has increased in steps from 80 kg to 100 kg [7]. This was fortunate because the dry mass of the microsatellites also increased during this time.

3.2 Minimum ΔV

This section describes how minimum ΔV burn parameters are generated as a function of launch date and desired spread rate. Since there are an infinite set of ΔVs and burn parameters that will yield a given spread rate on a given day, it is necessary to chose criteria to optimize the burn parameters by. The simplest choice is to optimize the burn parameters for the minimum ΔV as is done in this section. While this yields the minimum necessary ΔV, it does not yield realistic burn parameters because the solid propulsion system for each helio satellite is only capable of the same fixed ΔV which must be selected far in advance of launch. The fixed ΔV case is treated in section 3.3 by introducing the additional criterion of minimizing the effect on the final spread rate of an error in the burn parameters. However, the minimum ΔV case can be used to provide and upper bound on the ΔV required.

The process of generating the minimum ΔV burn parameters as a function of desired spread rate and launch date is summarized in Figure 3-1. As described in Appendix C, spread rate and the final heliocentric orbital elements are generated as a function of launch date, ΔV, burn true anomaly, f, and the burn angles θ, and ϕ shown in Figure 3-2. The multivariable optimizer routine FMIS in MATLAB is used to generate the burn parameters f, θ, ϕ that maximize spread rate for a given ΔV and launch date and time. At each date an array of maximum spread rates and burn parameters is produced corresponding to constant increments of ΔV from 900 to 1500 m/s (900, 1000, ... , 1500). From this array the burn parameters for fixed increments of spread rate from -10 to -120 °/yr (-10, -15, -20, ..., -120) are linearly interpolated. These data are recorded, the date is incremented, and the process is repeated at the new date until the end of the year is reached.

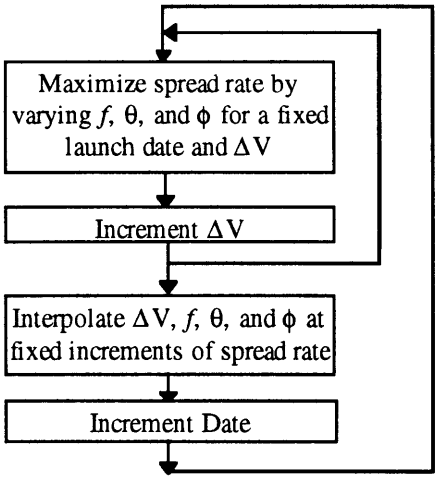

Fig. 3-1 Generating minimum ΔV burn parameters.

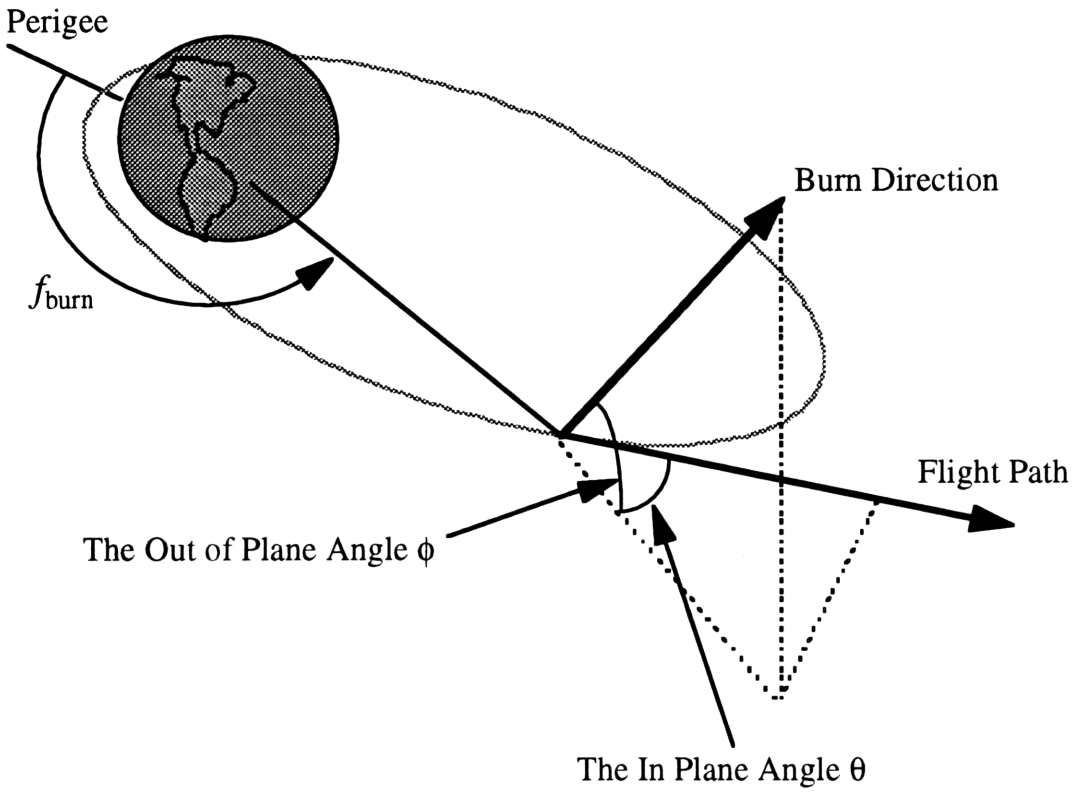

Fig. 3-2 Burn angles.

The Ariane 5 launch window is shown in Figure 3-3. The window definition is based on Arianespace's assumption that all primary payloads are spun stabilized during transfer and have their solar panels mounted perpendicular to their spin axis. In order to ensure sufficient illumination of the solar panels it is necessary to specify a minimum angle between the spin axis and the Earth to Sun vector. The opening of the Ariane 5 launch window is defined by a minimum angle of 65° between a reference Apogee Motor Firing (AMF) attitude and the Earth to Sun vector. The reference AMF attitude is the direction vector of the burn necessary to transfer from Ariane 5 GTO to a zero inclination Geosynchronous orbit on the sixth apogee after launch. The reference AMF attitude is perpendicular to the position vector on the sixth apogee with a -7.45° declination angle with respect to the equatorial plane. The close of window is defined as occurring 45 minutes after the opening. The variation in window opening is caused by the variation in the Earth to Sun vector over the course of the year with respect to Earth's tilted spin axis which is fixed in space which causes the inclination of GTO to vary with respect to the ecliptic even though it is fixed with respect to the equatorial plane.

It is assumed that launch occurs at the end of the Ariane 5 launch window and that the helio satellites spend four orbits in GTO prior to escape to allow for check out. For every four minutes

later the launch occurs the position of perigee decreases by 1° increasing the required ΔV as shown in Figure 3-25. The later the launch time the higher the ΔV required. Assuming and end of window launch produces the highest and most conservative minimum required ΔV for a given spread rate. The minimum required ΔV as a function of spread rate and launch date is shown in Figure 3-4. The variation minimum required ΔV over the year is caused by the variation in the variation of the inclination of GTO to the ecliptic and the variation of the Ariane 5 launch window (which itself is caused by the same variation in inclination). The burn parameters f, the burn true anomaly, and θ, the in plane flight path angle are shown in Figure 3-5, and Figure 3-6. The optimum burn true anomalies occur just before perigee (slightly negative fs) and the optimum in plane flight path angles are small but positive. It was found that ϕ, the out of plane flight path angle, is zero at all points to within the accuracy of the optimization.

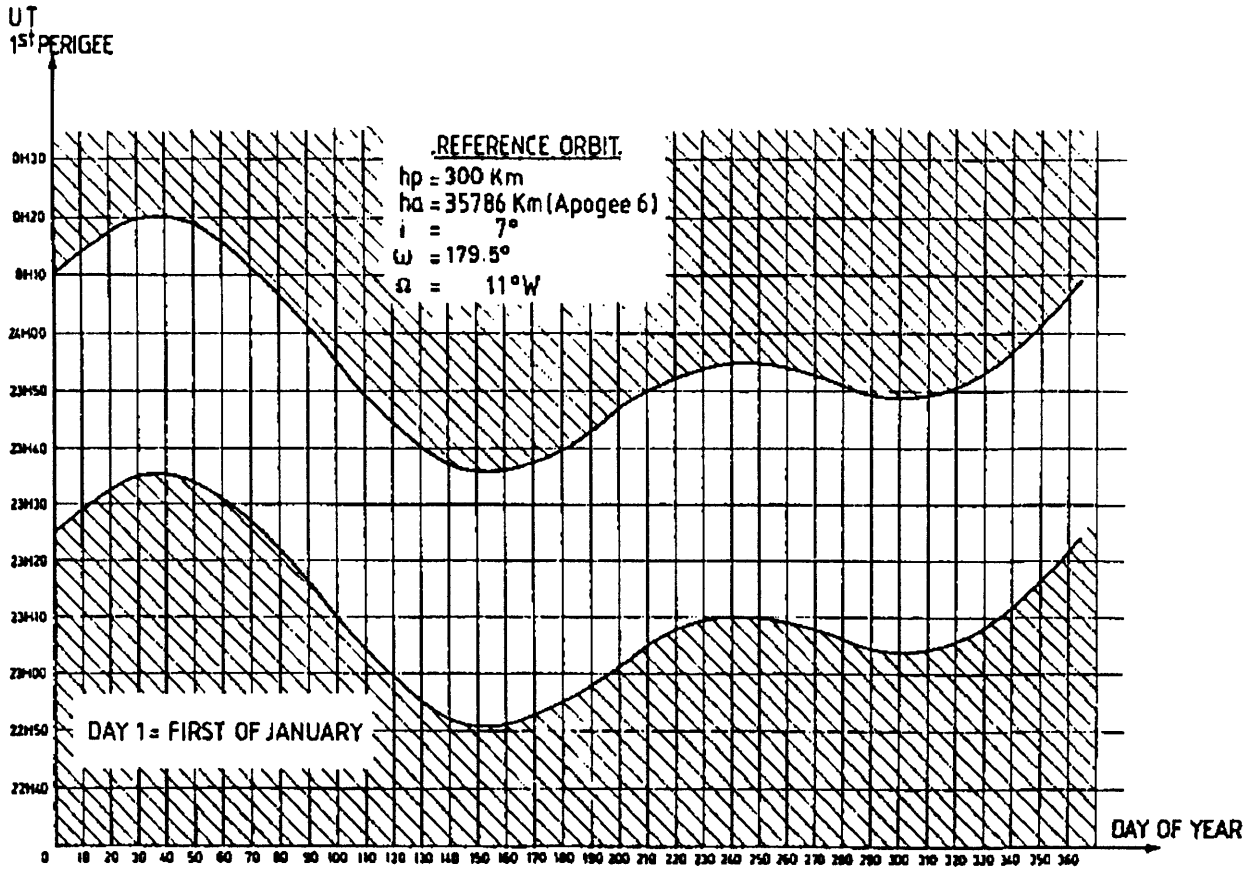

Fig. 3-3 Ariane 5 GTO Launch Window [15].

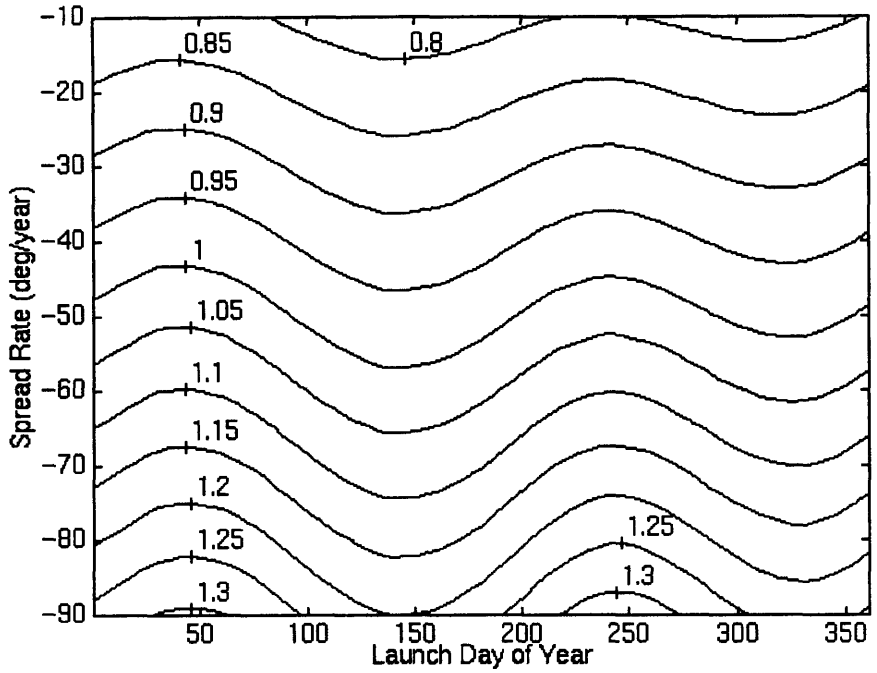

Fig. 3-4 Minimum ΔV (km/sec) required for a given spread rate and launch date.

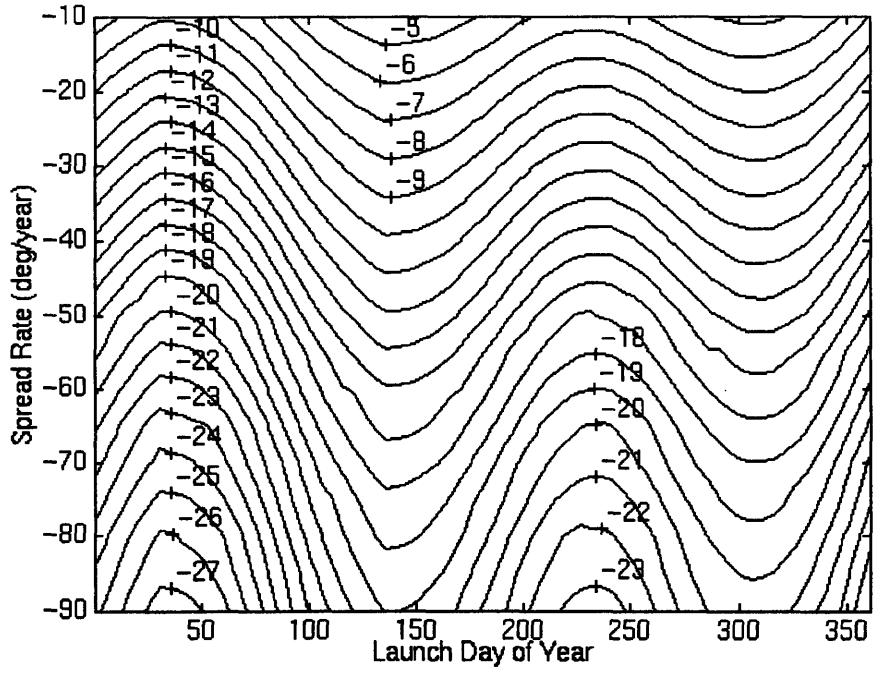

Fig. 3-5 Burn true anomaly, f, (°) for minimum required ΔV.

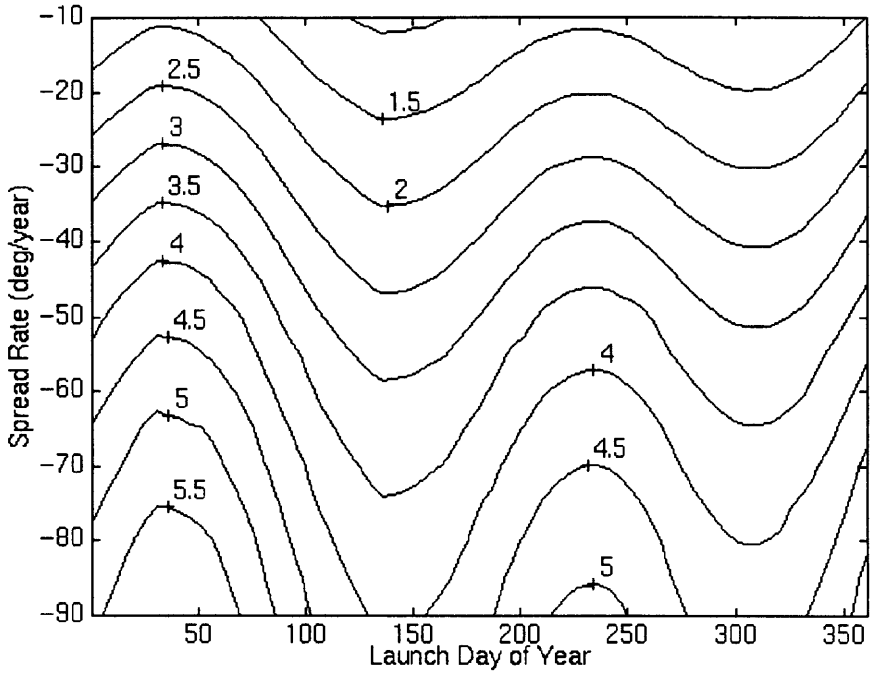

Fig. 3-6 In plane burn angle, θ, (°) for minimum required ΔV.

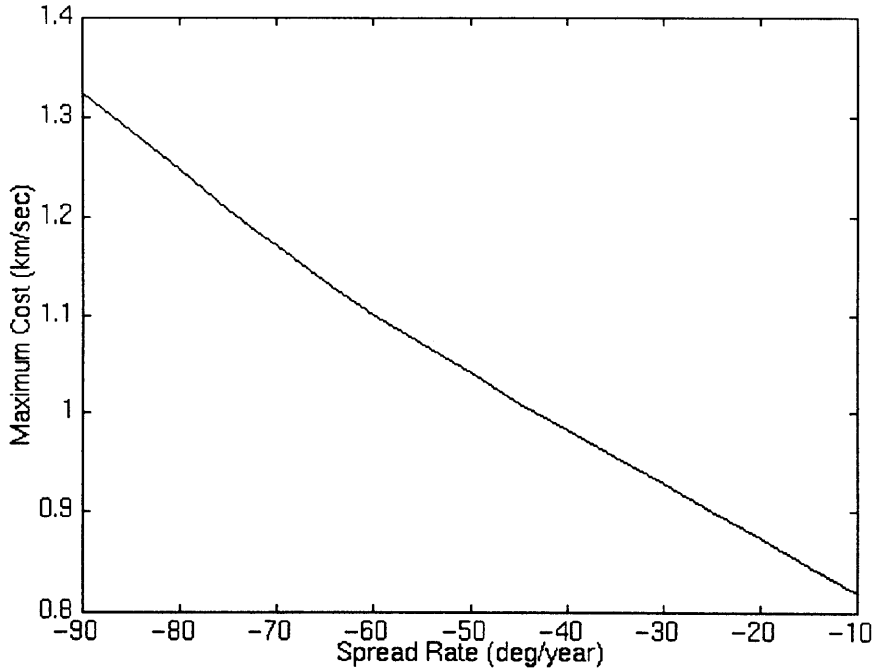

Fig. 3-7 The maximum minimum ΔV during the year to produce a given spread rate.

As can be seen in Figure 3-4 the ΔV required for a given spread rate varies by up to ~75 m/s over the course of a year. The maximum minimum ΔV required to achieve a desired spread rate during a year is shown in Figure 3-7. This result provides a upper bound for the helio satellite ΔV. For a 60 deg/yr spread rate the required ΔV is 1101 m/s.

3.3 Fixed ΔV

It is unlikely that a helio satellite will ever be injected with the exact minimum required ΔV for its launch date and spread rate. Both the trigger and helio satellites use the same solid rocket motor in order to reduce the mission cost through commonality. The solid rocket motor selection is driven by the greater mass and ΔV requirement of the trigger satellites. While the trigger and helio satellites will use different propellant loads, solid rocket motors are limited to a maximum off load of 20%. In some cases a fully off loaded motor of the type required by the trigger satellites will provide vastly more ΔV than required by the helio satellites. Even in the case that the motor can be off loaded to provide the maximum ΔV required by the maximum spread rate helio satellite, this ΔV will exceed the minimum required ΔV for that satellite at most times of the year. Further, since all of the helio satellites will use the same propellant load, even if the maximum spread rate helio satellite is provided with exactly its minimum required ΔV, all of the other helio satellites will exceed their required ΔVs. It is inevitable that most or all of the helio satellites will be injected with greater ΔV than their minimum required.

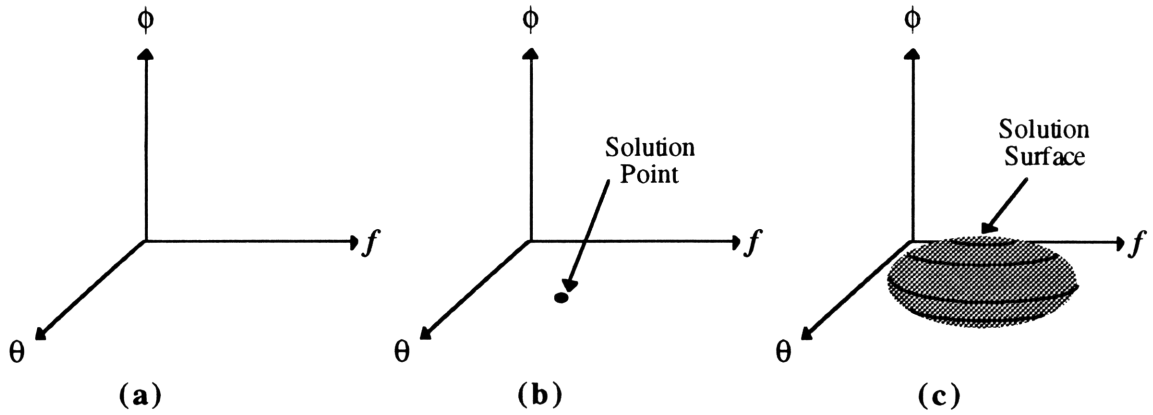

Fig. 3-8 Burn parameter space and solution surface.

In the likely event that a helio satellite exceeds its minimum required ΔV for its desired spread rate an infinite set of burn parameters will produce the desired spread rate. To visualize this it is useful to define two items: the burn parameter space, and the solution surface. The burn parameter space is a three dimensional space with f, θ, and ϕ as orthogonal axes as shown in Figure 3-8a. Every point in burn parameter space for a fixed ΔV and launch date specifies a set of burn parameters

which yield a corresponding spread rate. The solution surface is the locus of all points in the burn parameter space that yield the desired spread rate. For a ΔV less than the minimum required to produce the desired spread rate the solution surface will contain no points as shown in Figure 3-8a. All points in the burn parameter space correspond to a spread rate lower than the desired spread rate. For a ΔV exactly equal to the minimum required to produce the desired spread rate the solution surface will consist of a single point as shown in Figure 3-8b. Only that point in the burn parameter space corresponds to the desired spread rate. All other points correspond to lower spread rates. Finally, if the ΔV is greater than the minimum required to produce the desired spread rate the solution surface is a three dimensional surface in burn parameter space as shown in Figure 3-8c. Every one of the infinite number of points on the solution surface will produce the desired rate. Points outside of the surface will produce a lower spread rate, and points inside of the surface will produce a higher spread rate.

While any of the infinite number of points on the solution surface will produce the desired spread rate, it is possible to introduce "nice to have" criteria to narrow the selection of burn parameters. These "nice to have" criteria should enhance the mission by decreasing the cost, increasing the probability of success, or increasing the operability of the system. Possible criteria include: selecting the burn parameters so as to minimize the effect of errors in the burn parameters which increases the probability of mission success, selecting the burn parameters so the burn takes place in view of a ground station which increases operability, and selecting the burn parameters so that the burn takes place at a time convenient for the ground controllers which also increases operability. Of these, selecting the burn parameters so as to minimize the effect of errors in the parameters has been chosen since mission success is more important than operability and the same operability effects can be achieved by selecting the appropriate number of holding orbits in GTO.

In order to minimize the effect of errors in the burn parameters it is best to minimize the effect of pointing errors. True anomaly, once the initial elements of GTO are calculated after launch, is simply a function of time which can be measured with great precision. The pointing of the satellite, however, is a function of the attitude determination system, the IMU, the spin balancing of the satellite, and thrust misalignment of the engine. Since pointing errors are larger and harder to control than errors in burn true anomaly the most can be gained by minimizing their effects.

The effects of pointing error can be minimized by minimizing the partial derivatives of spread rate with respect to θ, and ϕ on the solution surface. These partial derivatives are minimized at the points on the solution space with largest and smallest true anomalies provided that the partial derivatives are smooth. This can be seen by looking at a two dimensional slice through the

solution surface as shown in Figure 3-9. Consider points A, B, and C where A and B correspond to the points with the largest and smallest true anomalies on the solution surface and C is another point on the solution surface. Points A, B, and C are perturbed by a small change in θ to become points A', B', and C'. Points A' and B', while no longer on the solution surface, remain much closer to the solution surface than does point C' and thus have spread rates much closer to the desired rate. Therefore, in order to reduce the effect of a pointing error chose either the largest or smallest true anomaly at which the desired spread rate can be achieved.

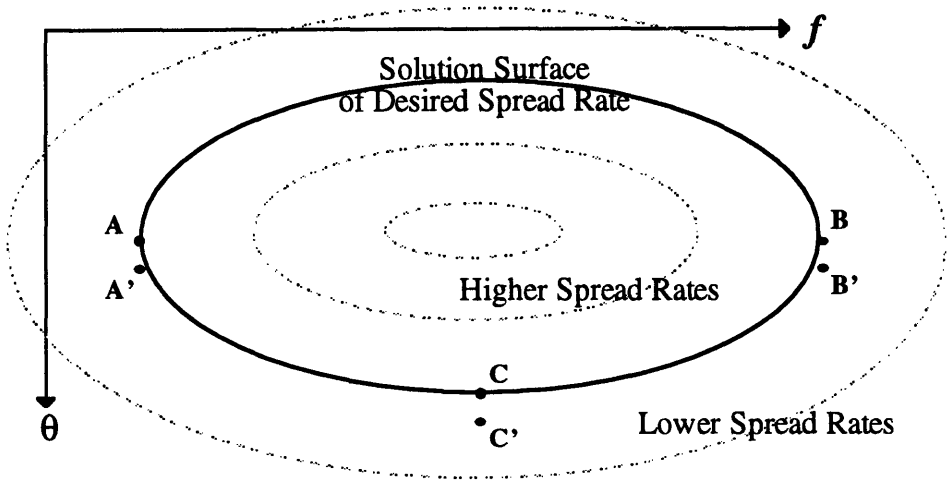

Fig. 3-9 The effect of a small change in flight path angle

The process of generating the fixed ΔV burn parameters and elements as a function of the desired spread rate and launch date is summarized in Figure 3-10. The multivariable optimizer routine FMIS in MATLAB is used to generate the burn angles θ and ϕ that maximize spread rate and final elements for a given true anomaly, f, and fixed ΔV. At each date an array of maximum spread rates, burn angles, and final elements is produced corresponding to constant increments of true anomaly as shown in Figure 3-11. From this array the burn parameters f, θ, and ϕ and final elements are linearly interpolated for fixed increments of spread rate from -10 to -90 °/yr (-10, -15, -20, ..., -90). Two sets of data are produced as shown in Figure 3-11. Class I corresponds to the largest true anomaly (usually positive) that produces the desired spread rate. Class II corresponds to the smallest true anomaly (usually negative) that produces the desired spread rate. These data are recorded, the date is incremented, and the process is repeated for the new date until the end of the year is reached.

The burn parameters and final elements for a 1101 m/s fixed ΔV are shown in Figures 3-12 to 3-27. It is assumed that the launch takes place at mid window as shown in Figure 3-3 and injection occurs after four obits in GTO for check out. Assuming a middle of window launch results in

average elements. The burn parameters burn true anomaly, f, and inplane flight path angle, θ, are shown in Figures 3-12 to 15 for class I and II injections. Again, it was found that the out of plane flight path angle, ϕ, is zero at all points to within the accuracy of the optimization. The final orbital elements a, e, i, Ω, ω and f are shown in Figures 3-16 to 3-27 for class I and II injections. Figures 3-16 and 3-17, which show final semi-major axis, are identical and constant with time of year because all orbits with the same spread rate have the same period and therefore the same semi-major axis. The dark regions in Figures 3-22 to 3-25 are caused by 180° jumps in plotted quantities.

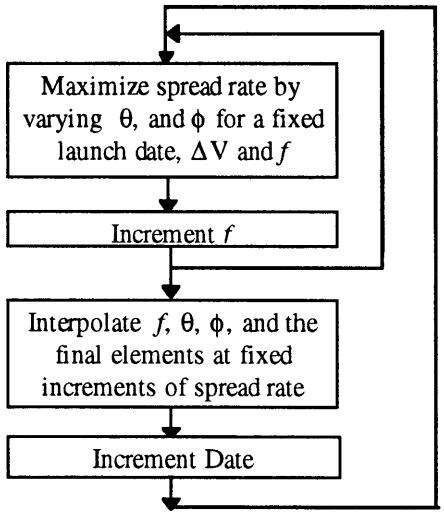

Fig. 3-10 Generating fixed ΔV burn parameters and elements.

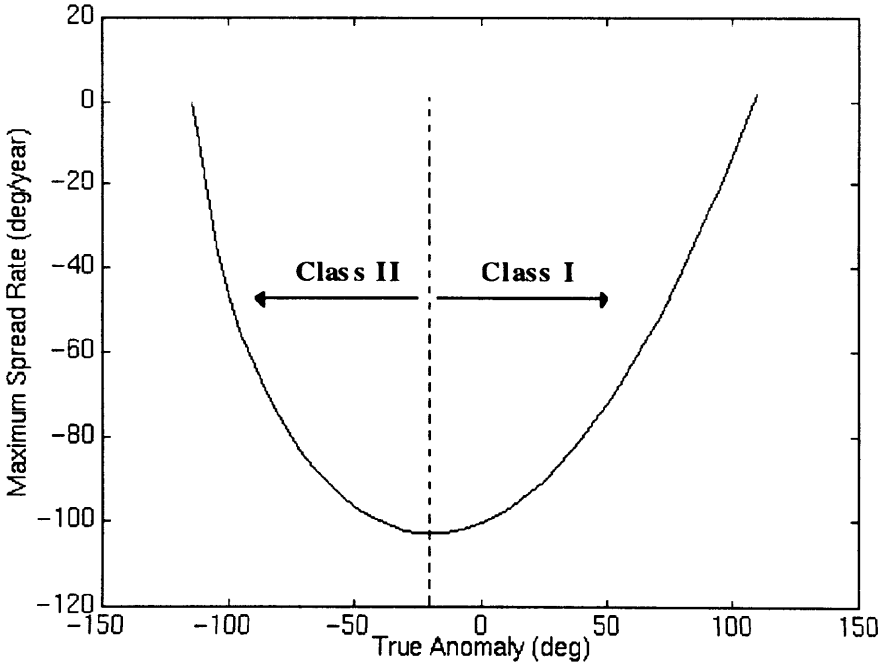

Fig. 3-11 Class I and Class II injections for fixed ΔV.

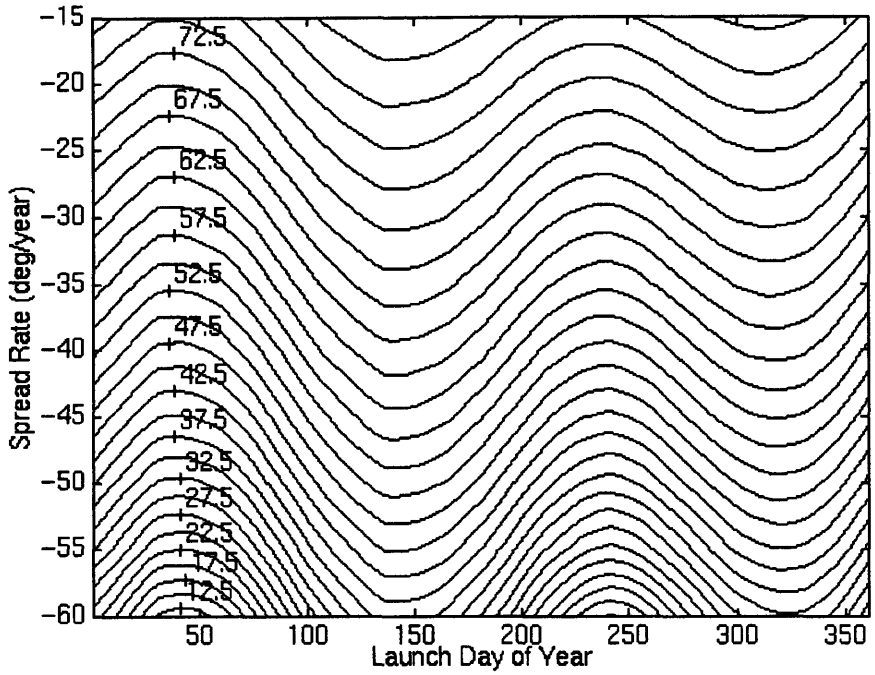

Fig. 3-12 Burn true anomaly, f, for fixed 1101 m/s ΔV Class I injection.

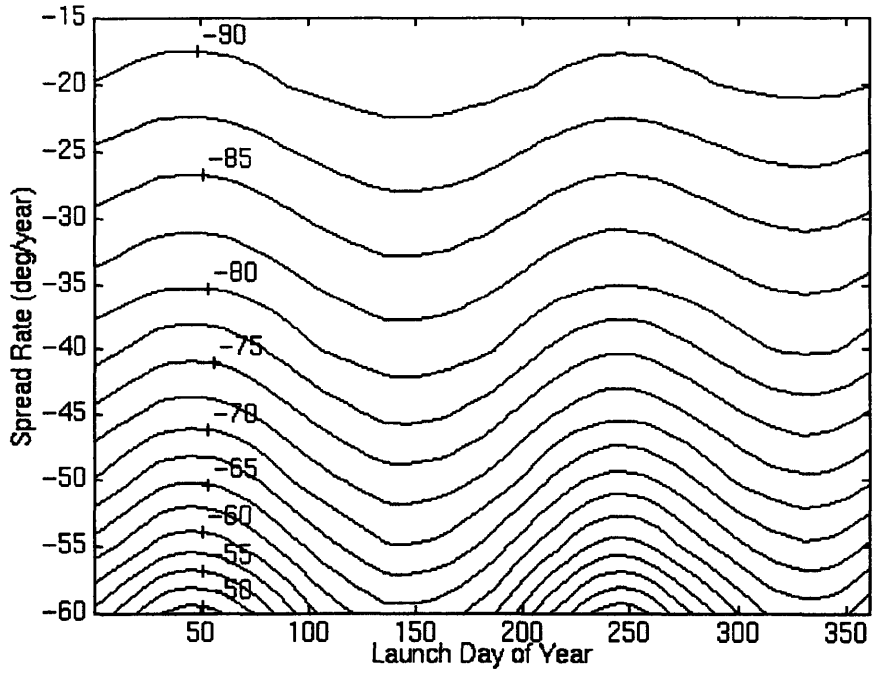

Fig. 3-13 Burn true anomaly, f, for fixed 1101 m/s ΔV Class II injection.

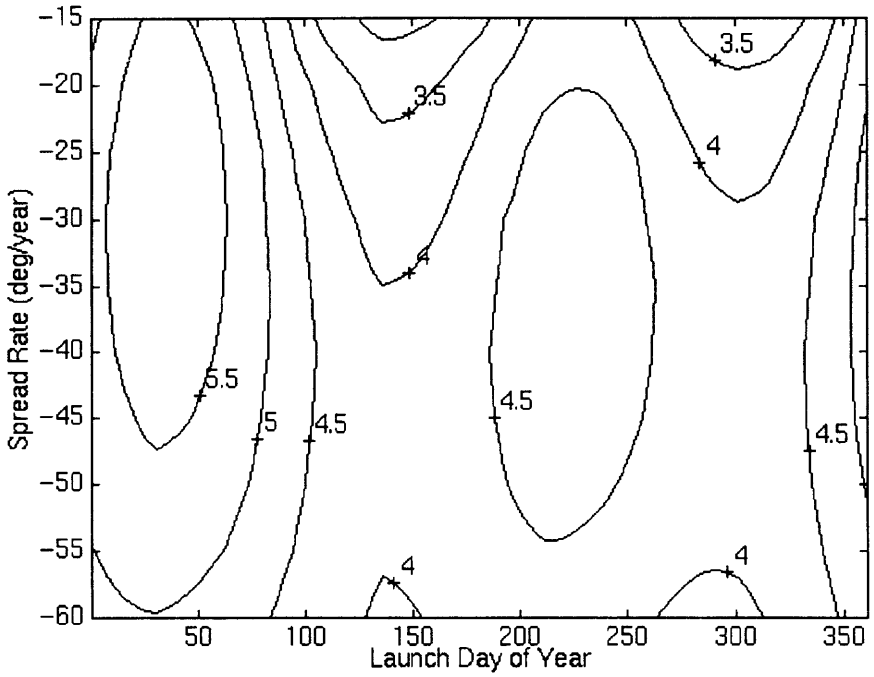

Fig. 3-14 In plane burn angle, θ, for fixed 1101 m/s ΔV Class I injection.

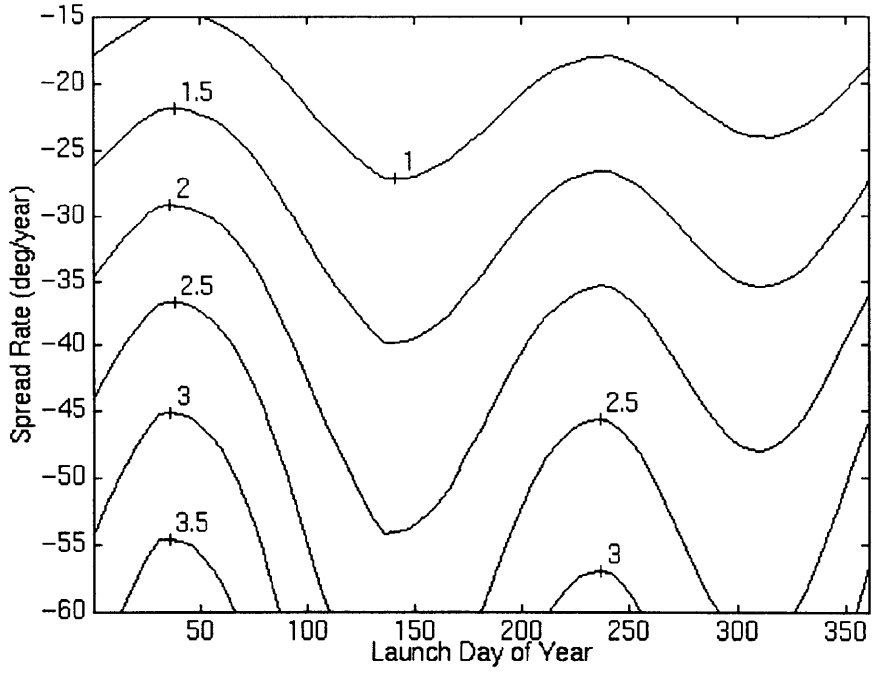

Fig. 3-15 In plane burn angle, θ, for fixed 1101 m/s ΔV Class II injection.

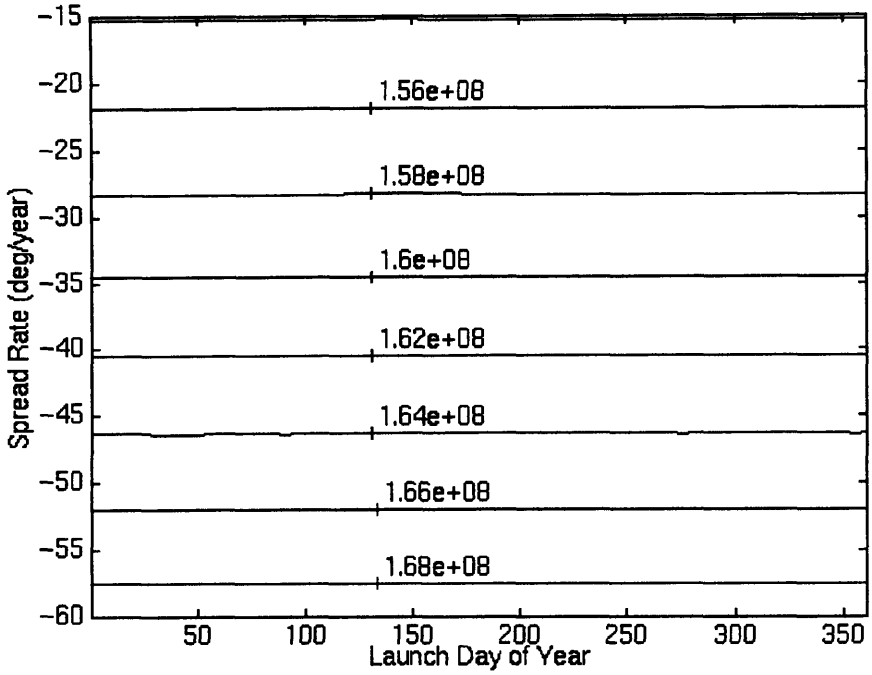

Fig. 3-16 Helio satellite semi-major axis, a, for fixed 1101 m/s ΔV Class I injection.

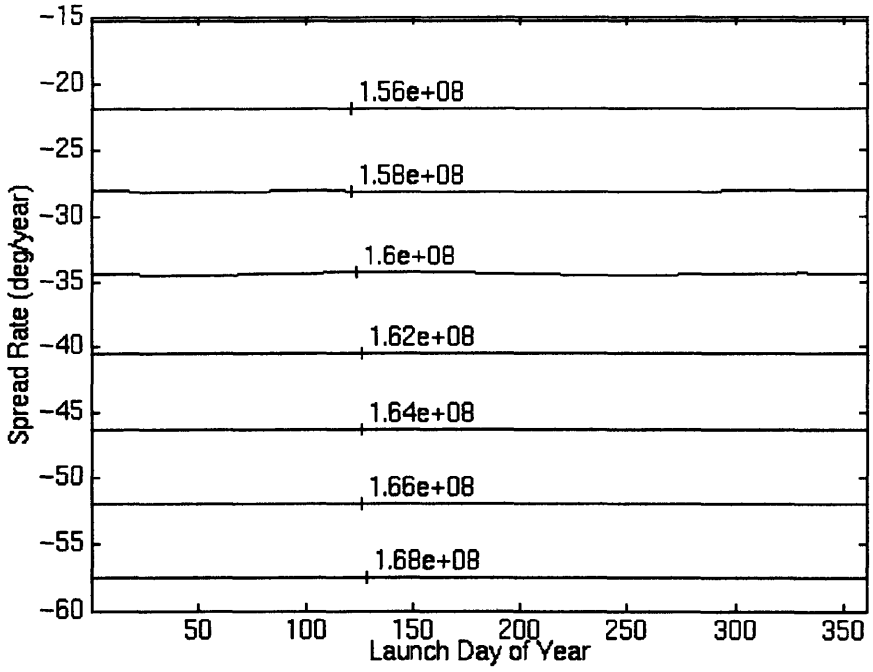

Fig. 3-17 Helio satellite semi-major axis, a, for fixed 1101 m/s ΔV Class II injection.

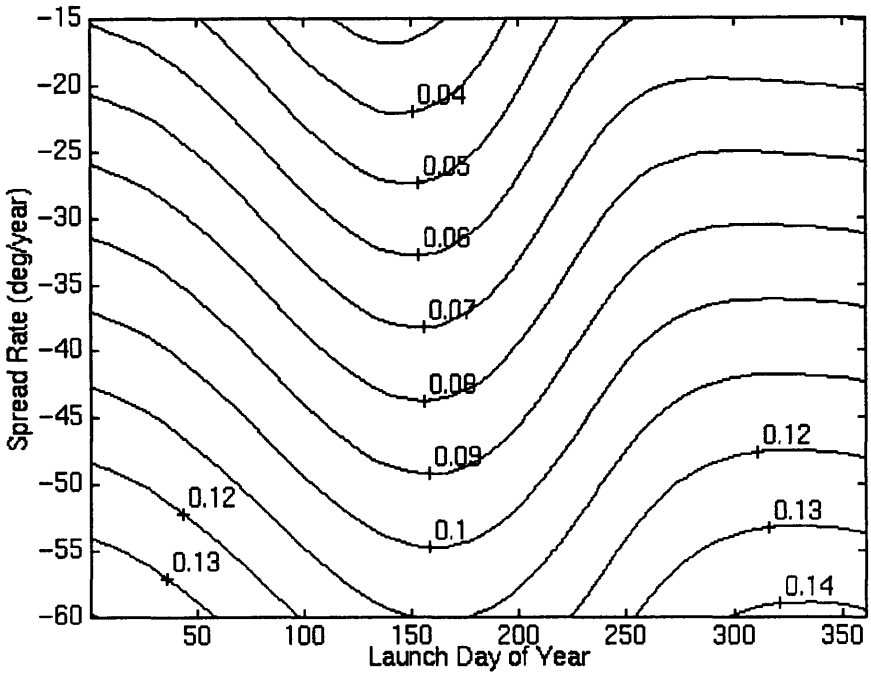

Fig. 3-18 Helio satellite eccentricity, e, for fixed 1101 m/s ΔV Class I injection.

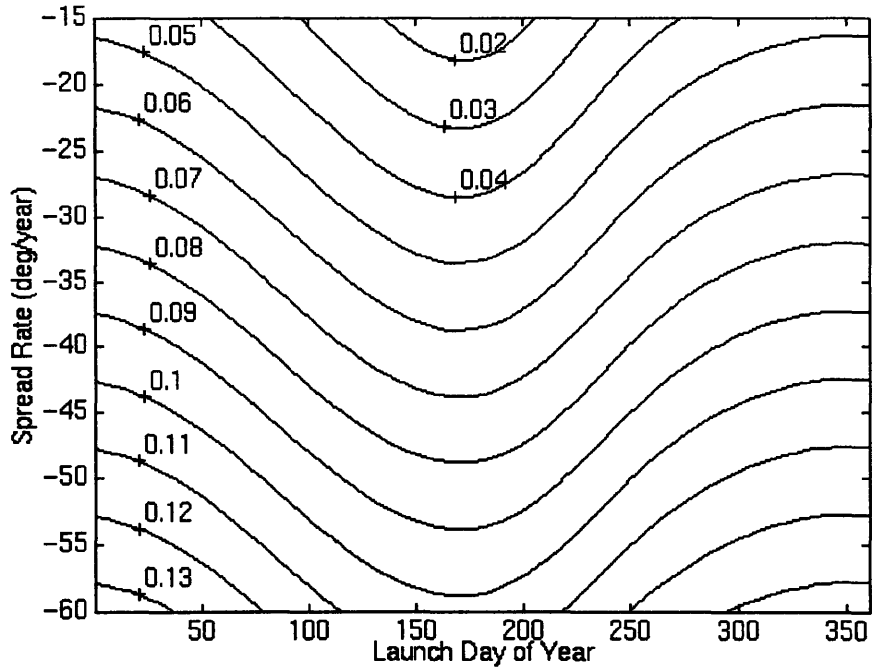

Fig. 3-19 Helio satellite eccentricity, e, for fixed 1101 m/s ΔV Class II injection.

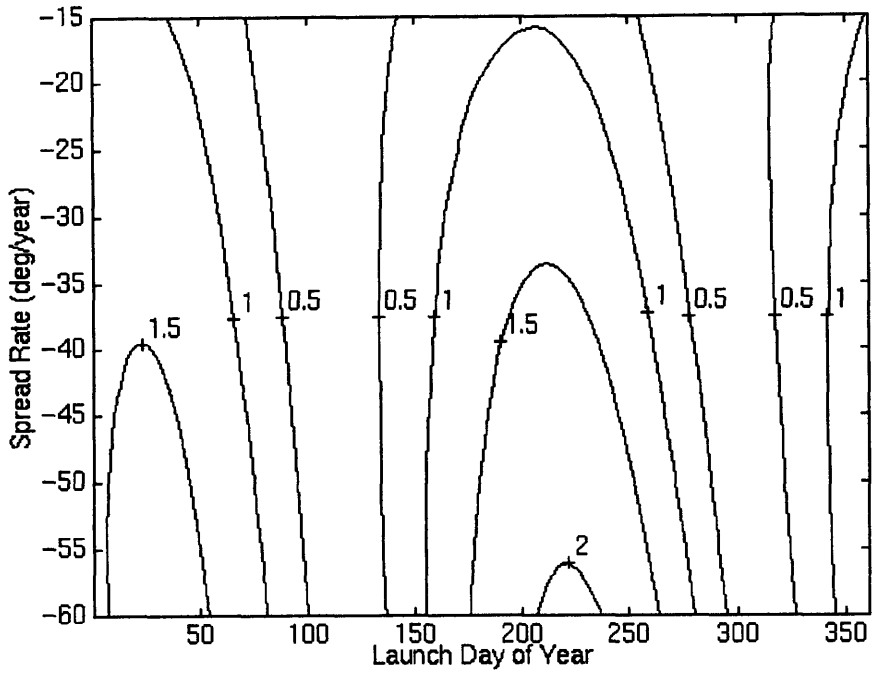

Fig. 3-20 Helio satellite inclination, i, for fixed 1101 m/s ΔV Class I injection.

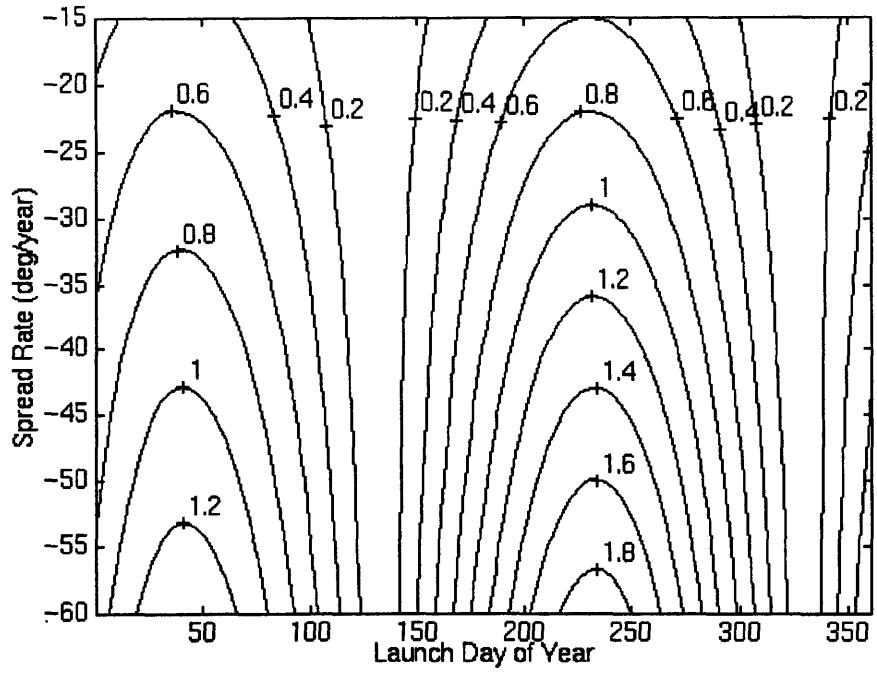

Fig. 3-21 Helio satellite inclination, i, for fixed 1101 m/s ΔV Class II injection.

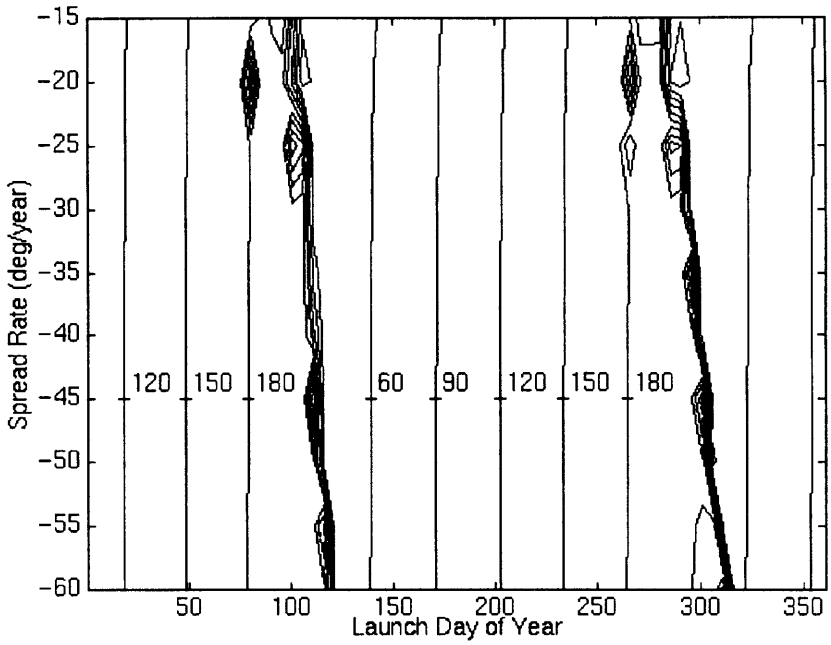

Fig. 3-22 Helio satellite longitude of the ascending node, Ω, for fixed 1101 m/s ΔV Class I injection.

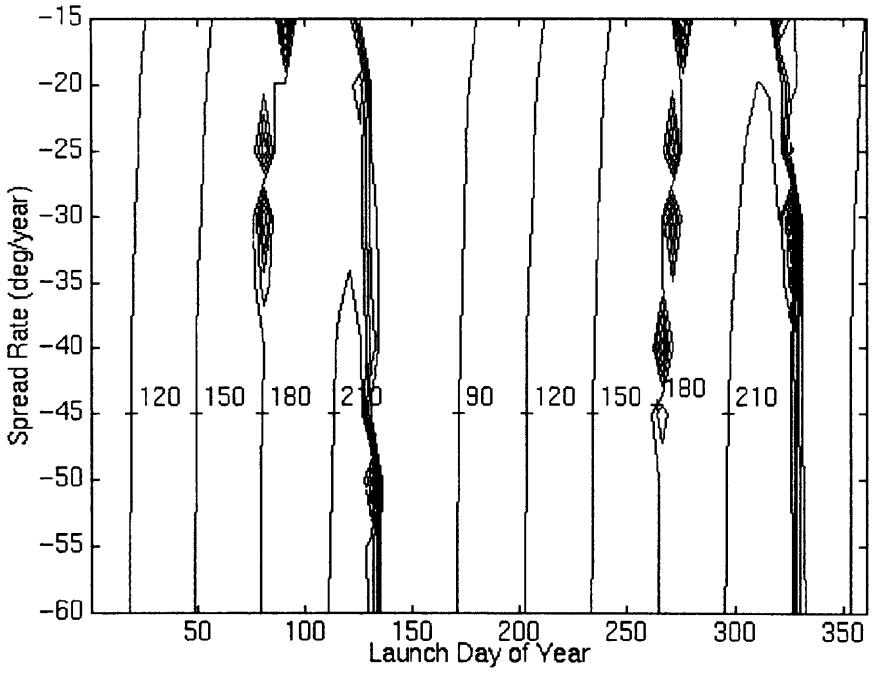

Fig. 3-23 Helio satellite longitude of the ascending node, Ω, for fixed 1101 m/s ΔV Class II injection.

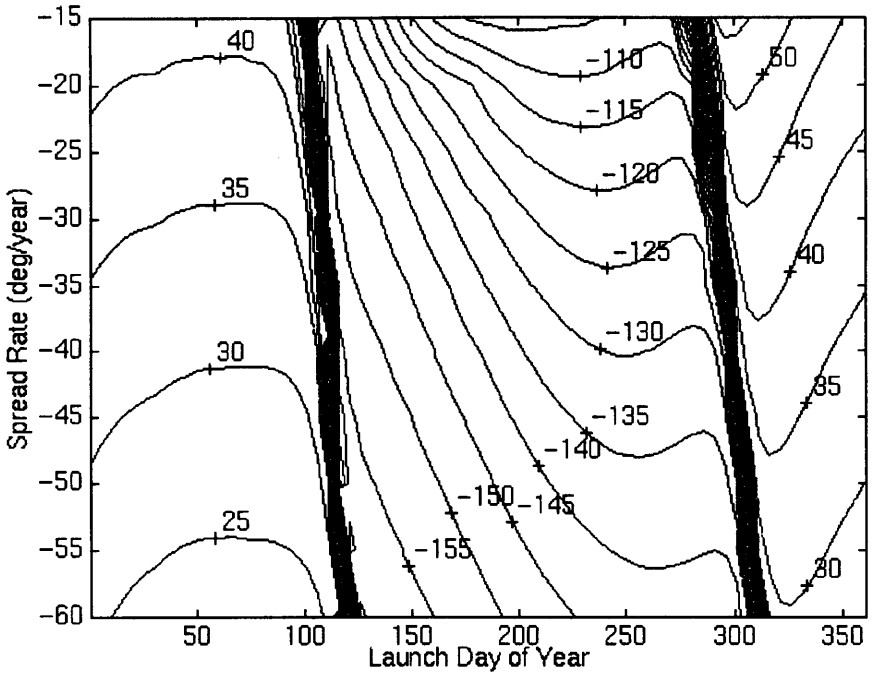

Fig. 3-24 Helio satellite argument of perigee, ω, for fixed 1101 m/s ΔV Class I injection.

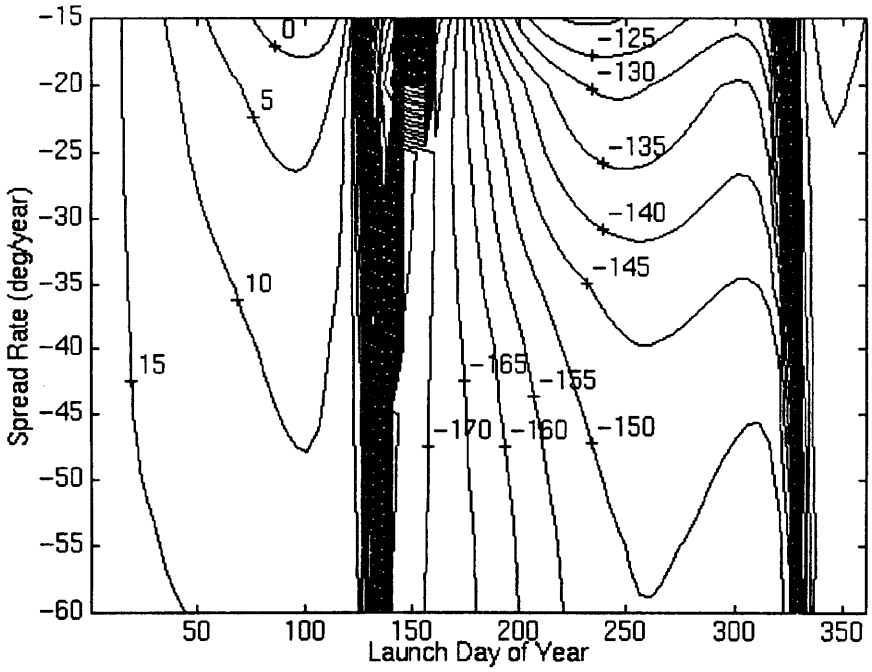

Fig. 3-25 Helio satellite argument of perigee, ω, for fixed 1101 m/s ΔV Class II injection.

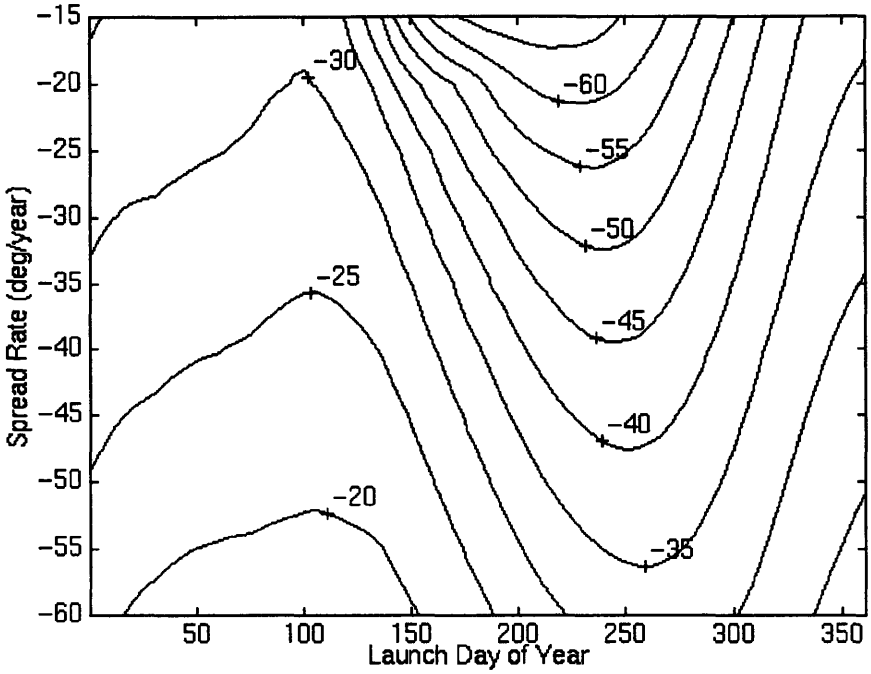

Fig. 3-26 Helio satellite true anomaly, f, for fixed 1101 m/s ΔV Class I injection.

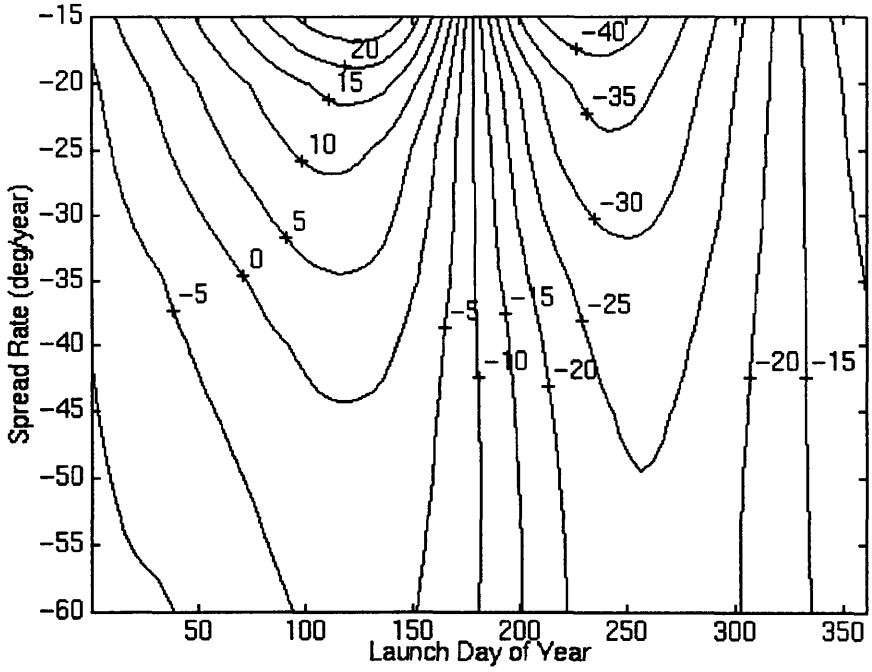

Fig. 3-27 Helio satellite true anomaly, f, for fixed 1101 m/s ΔV Class II injection.

3.3 Constellation Reliability

This section contains an analysis of the probability of mission success. For the purpose of this section mission success is defined as one trigger satellite and two helio satellites being operational after five years. This provides the minimal working constellation. The probability of 3 and 6 satellites surviving launch was also tracked. The reliability results are shown in table 3-1.

Options using one to three launch vehicles and various groupings of trigger and helio satellites were considered. The manifest of each launch is listed in brackets. Launches with an "o" before them are optional and only take place when a prior launch fails. For example, "(1 trig, 2 heo), (1 trig, 2 heo), o(1 trig, 1 heo)" means that one trigger and two helio satellites will be launched on each of the first two launches and in the event that one of these launches fails a third launch containing one trigger and one helio satellite will be made. The "option probability" in table 1 is the probability that an optional launch will take place. With the exception of the single launch option, all options allow a minimal constellation to be established by the second launch if the first fails.

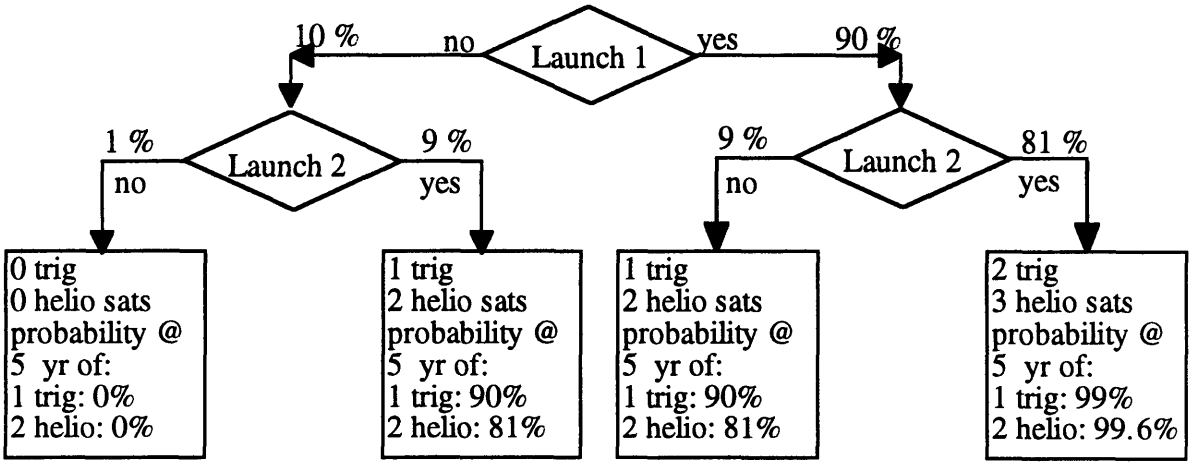

Fig. 3-28 Example failure tree.

For each option a launch failure tree was constructed. An example failure tree for (1 trig, 2 heo), (1 trig, 2 heo) is shown in Figure 3-28. The probability of each launch outcome and, given the number of trigger and helio satellites that survive launch in that outcome, the probabilities of having one trigger and two helio satellites operational at the end of five years is computed. The probability of mission success is the sum over all of the possible launch outcomes of the probability of that outcome multiplied by the probability for that outcome of having one trigger and two helio satellites at the end of five years. The launch reliability was assumed to be 90%, equal to

the reliability of Ariane 4 over its first 10 flights. The probability of each trigger and helio satellite of surviving five years once in orbit was assumed to be 90%.

Table 3-1 Deployment Options

	(2 trig, 4 heo)	(1 trig, 2 heo), (1 trig, 2 heo)	(2 trig, 2 heo), (1 trig, 2 heo)	(1 trig, 3 heo), (1 trig, 2 heo)	(1 trig, 2 heo), (1 trig, 2 heo), O(1 trig, 1 heo)	(1 trig, 2 heo), (1 trig, 2 heo), (1 trig, 1 heo)	(1 trig, 2 heo), (1 trig, 2 heo), O(1 trig, 2 heo)	(1 trig, 2 heo), (1 trig, 2 heo), (1 trig, 2 heo)
Total Sats	6	6	7	7	8	8	9	9
Trigger Sats	2	2	3	2	3	3	3	3
Heo Sats	4	4	4	5	5	5	6	6
Optional Sats					2		3	
3 Sats after 5 years	88.8%	93.0%	94.0%	94.6%	94.6%	95.3%	97.8%	98.8%
6 Sats after launch	90.0%	81.0%	81.0%	81.0%	81.0%	81.0%	97.2%	97.2%
3 Sats after launch	90.0%	99.0%	99.0%	99.0%	99.0%	99.0%	99.9%	99.9%
Option Probability					18.0%		19.0%	

This analysis shows that dividing the satellites into two launches produces a significant increase in the probability of having three satellites after launch and a significant increases in the probability of mission success. Launching seven and eight satellites marginally increases reliability over six satellites divided between two launches. Greatly increased reliability can be achieved by launching nine satellites in three batches. In general increased reliability comes at increased cost.

3.4 Star 13 Propulsion System

This section describes the Morton Thiokol Star 13 solid rocket motor used to provide the primary propulsion for ETA [17, 18]. The Star 13 will be procured as an existing commercial-off-the-shelf (COTS) component eliminating the need for a detailed design of this subsystem and saving a great amount of money. The selection, basic characteristics, off loading, grain design, thermal pulse, and handling of the Star 13 family are discussed in this section.

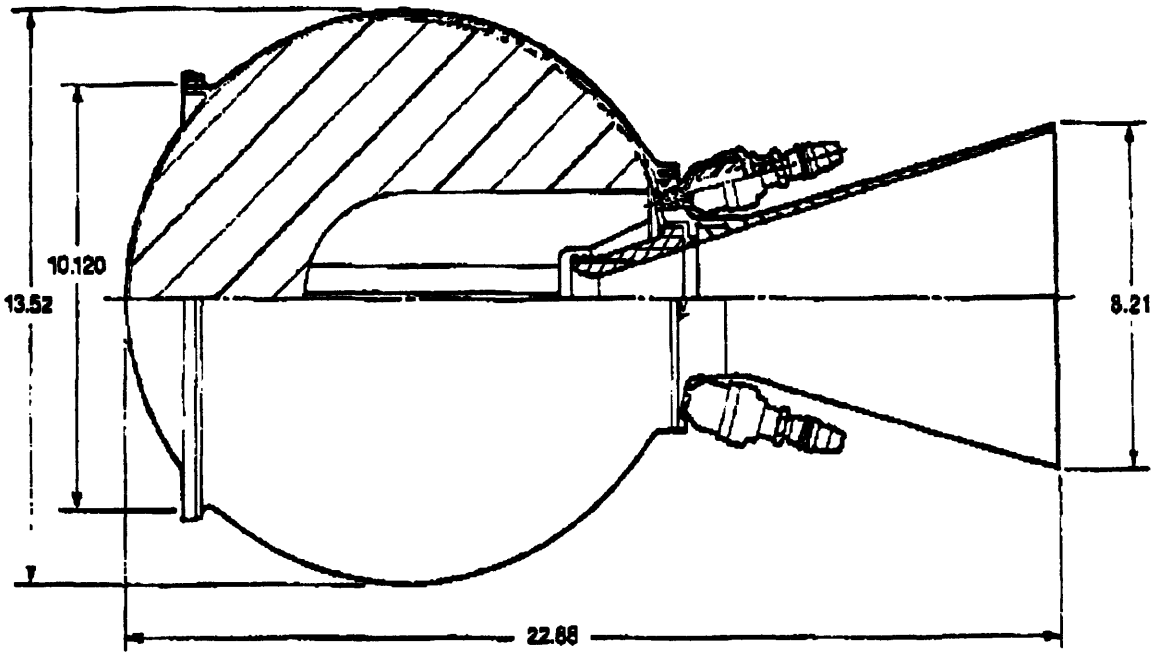

Fig. 3-28 Morton Thiokol Star 13A [17].

Table 3-2 Star 13A and B Characteristics [17]

Item	Star 13A	Star 13B
Max Thrust	7560 N	9790 N
Effective I_{sp}	286.5 sec	285.7 sec
Max Propellant	33.1 kg	41.2 kg
Burn Out	4.5 kg	5.6 kg
Other Expendables	0.4 kg	0.2 kg
Max Total	38.0 kg	47.0
Maximum Off Loading	20%	20%
Diameter	343 mm	343 mm
Length	581 mm	638 mm
Expansion Ratio	17	17

The Star 13 family, consisting of the A and B variants, was selected because its performance fit the required impulse for ETA and is relatively low cost. Other choices were constrained by the lack of other engines in this class. The Star 13A consists of a spherical titanium case and a vitreous silica phenolic nozzle with a graphite throat insert. The Star 13B is identical with the exception of an

additional 57 mm barrel section. The Star 13A will be used in most cases except in the event of extreme mass growth (approaching ~100 kg total mass) when the Star 13B will be needed. If necessary, identical interfaces and diameters should allow the relatively easy substitution of the B variant for the A variant early in the design program. The characteristics of the Star 13A and B are shown in table 3-2. Both are space qualified.

Propellant off loading will be used for impulse control. The trigger satellites and the helio satellites will use different propellant off loadings in order to save mass. The propellant off loading is limited to 20%. That is, up to 20% of the propellant can be removed without affecting the stability of the engine. The total impulse is accurate to ±0.5%. Off loading costs ~$10,000 per engine and must be specified well in advance of delivery. Propellant load and total mass versus ΔV and non-propulsive mass (everything except the Star 13) for the Star 13A and B are shown in Figures 3-29 and 3-30 respectively. Each of these figures can be divided into three regions. First, in the upper right corner of the chart there is a region which is not reachable. The propellant required exceeds the maximum load of the engine. Second, in the center of the chart there is a region where the required propellant load is between 80% and 100% and total mass and off loading is a function of ΔV and non-propulsive mass. Finally, in the lower left hand corner of the chart there is a region where the propellant loaded is limited by the maximum off load and not the ΔV. In this region total mass is only a function of non-propulsive and the propellant loading is a minimum 80%. The mission suffers a mass penalty due to unneeded propellant and requires off pointing to spoil the additional ΔV provided by this excess propellant. Only at total masses exceeding 92 kg for the limiting trigger ΔV (1247 m/s) is a Star 13B required.

Grain redesign will be used to tailor the thrust versus time curve in order to hold burn out acceleration below a desired level. The limiting loads on the ETA micro-satellites will be determined by the Star 13 burn. If unmodified the burn out acceleration of the ETA micro-satellites will be as high as 17 g's. For a nominal cost (~50,000 per design) Thiokol can redesign the propellant grain so that the burn profile becomes regressive rather than slightly progressive and the burn out acceleration is reduced to as low as 10 g's. This requires a small amount of off loading and a small amount of additional insulation which will slightly increase the burn out mass.

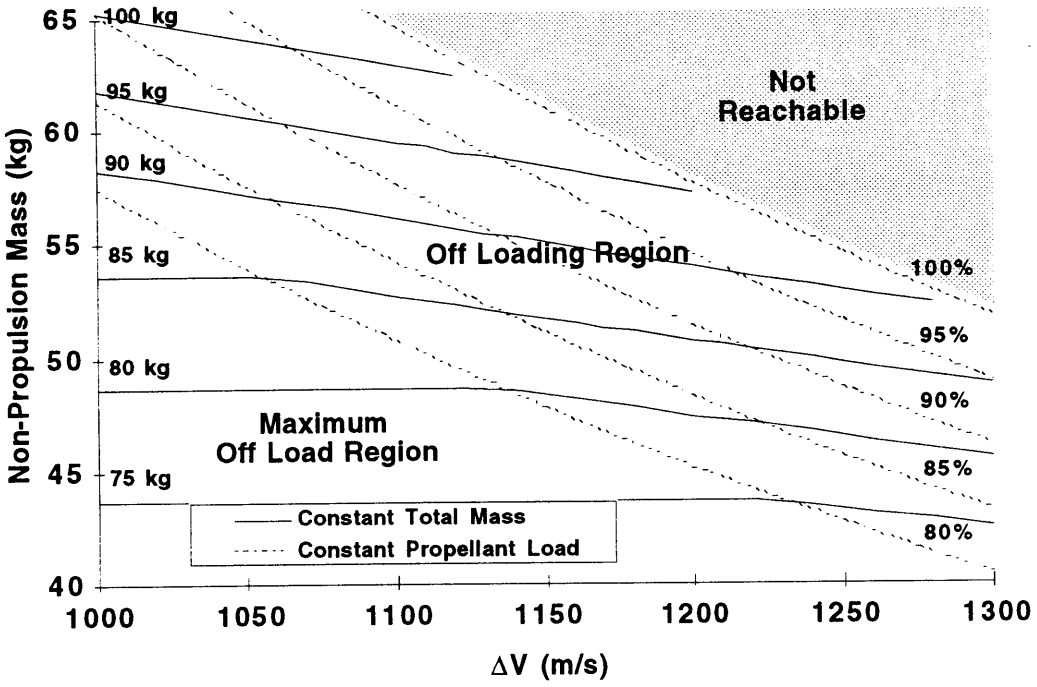

Fig. 3-29 Propellant load and total mass vs. non-propulsive mass and ΔV for the Star 13A

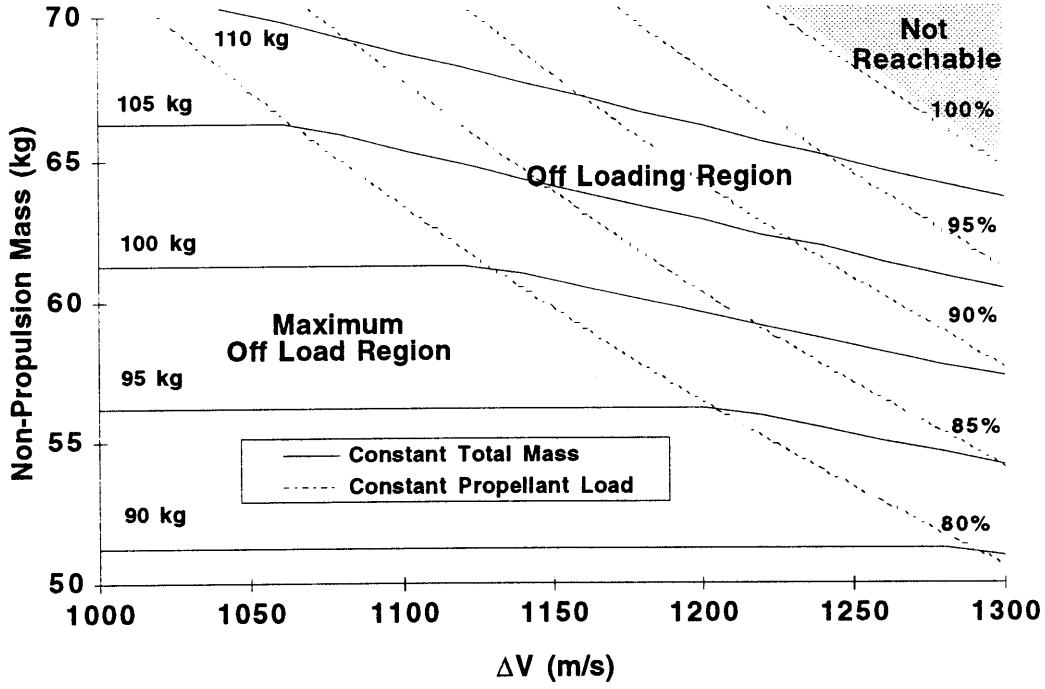

Fig. 3-30 Propellant load and total mass vs. non-propulsive mass and ΔV for the Star 13B

Since the ETA micro-satellites will be built around the Star 13, the thermal pulse into the satellites from the engine is of great concern. The during the burn the ~15 second burn the exterior of the Star 13 case will not exceed 100° C. However, within two minutes after the burn the case around the interface plane will rise to 370° C. While the nozzle will reach considerably higher temperatures, it is external to the micro-satellites and radiates directly to space. First order analysis has shown that by providing thermal standoffs for the interface planes, and radiation shielding in the engine cavity consisting of several layers of reflective metal foil, the total change in the temperature of the micro-satellite structure can be held to a few degrees. In this case the majority of the thermal energy of the energy is radiated out the aft end of the engine cavity to space. While more detailed computations should be done in the future, the thermal pulse from the engine seems manageable.

The handling of the Star motors, while non-trivial, is substantially easier than the handling of an equivalent bipropellant system. The Star motor is monolithic and only integrated with the micro-satellites at the launch site just before integration with the launch vehicle. During construction of the micro-satellites only inert mass models are needed for fit checking. This contrasts to a bipropellant system where a complex assembly of tanks, valves, pipes, and a thruster must be built, tested, and integrated with the micro-satellites. Integration at the launch site will likely be supervised by a Thiokol engineer. While integration will require care, it will be considerably easier than fueling and charging a bipropellant system.

The Star 13 by far provides the cheapest and simplest means of propulsion for ETA. It is certainly an enabling factor for the ETA design.

3.5 Conclusion

This chapter contains a detailed description of the operation, burn parameters, final elements, and propulsion system for the ETA helio satellites. While this level of detail exceeds what is normal for this stage of the design process, it does lend realism to the project and decreases the chances that an unforeseen detail will hinder the project in the future. As the design progresses, software should be developed to automatically plan the burns as a function of the real launch time and constraints placed by operability and the release of the primary payload. All changes to GTO made by Arianespace should be carefully noted as they will have extreme effects on the required ΔV. Of particular importance are changes in the launch window. This concludes the detailed discussion of the helio satellites. The next two chapters will deal with the details of the trigger satellites.

Chapter 4 First Order Trigger Satellite Orbits

This chapter describes the architecture trade studies used to determine the "best" trigger orbit and means of reaching that orbit. This chapter traces the evolution of the trigger orbit from the Distant Retrograde Orbit (DRO) used on the previous iteration of ETA into the synchronous orbit used in this iteration. The primary drivers for this evolution were the changing requirements on the trigger orbits and the need to remain compatible with the helio satellite launch and propulsion mechanisms.

This chapter starts with a description of the requirement and how and why they evolved over the course of the preliminary design process. Next, a series of sections will discuss each option considered. These options included DRO, Lunar Lagrange Point 4,5 (LL 4,5) orbit, high circular orbits, and synchronous orbits.

The work on the DRO and LL 4,5 orbits was heavily assisted by Nicolas Fabas, a student from Sup'Aero in France, who interned for CSR during the summer of 1996. Fabas's work on the DRO orbits confirmed the author's work. The author's work on the LL 4,5 confirmed Fabas's more extensive work. This extensive cross-checking was necessitated by the often non-intuitive results produce by the nature of these orbits. Since Fabas's work is thoroughly documented in his project report [19], the details of his analysis will not be repeated here. The description of the DRO and LL 4,5 will concentrate on their basic properties and how the changing requirements led to their consideration and rejection.

4.1 Requirements

This section describes the requirements on the trigger orbits and their evolution. The great changes in the trigger orbits between this iteration and the previous can be traced to the changing trigger orbit requirements and the need to maintain commonality with the changing helio satellite deployment mechanism.

It is widely understood that design is an iterative process, however, it is less widely understood that requirements are iterative. Requirements can change during the preliminary design phase of a program for three reasons. First, changes can result from changing top level requirements. As a program progresses its goals are reassessed, new goals added, and old ones dropped. In the case of ETA, feed back on the previous proposal led to the inclusion of a new secondary mission objective, the instantaneous reporting of arcminute localization burst warnings. Second, conflicts in requirements can lead to re-prioritizing of requirements. Often cost and performance requirements conflict. As a program progresses the true cost of certain requirements becomes

known. In order to meet cost requirements, performance requirements are frequently relaxed. In the case of ETA, the cost in complexity of achieving an orbit completely outside the Van-Allen trapped radiation belts exceeded the benefit of doing this, leading to relaxed requirements of trapped radiation. Finally, improved understanding of problems leads to changes in requirements. In the case of ETA, the realization that ETA has its best sensitivity out of the ecliptic plane reduced the requirement to minimizing the blockage of Earth in the ecliptic plane.

The following list includes all of the requirements that have applied to the ETA trigger orbits and explains how and why each changed over time.

- **Compatibility** - In order to minimize cost, the trigger satellites will be the same as, or slight modifications of, the helio satellites. The trigger satellite propulsion system and launch mechanism must therefore be similar or identical to those on the helio satellite. The evolution of the helio satellite deployment architecture trade study described in chapter 3 was one on the primary drivers for the trigger satellite design.

- **Radiation** - Initially the trapped radiation environment was to be minimized. The radiation environment affects the quality of the data produced by, and the cost and mass of, the trigger satellites. First, energetic particles striking the primary detectors will register as gamma ray events. Background radiation increases the noise and decreases the sensitivity of the GRB detectors. Second, radiation degrades electronic components and solar arrays. Radiation can also cause single event upsets and latches in flight computers. To protect against radiation, increased shielding, radiation hardened components, and thicker cover glasses on the solar panels are required which increases the cost and mass of the satellite.

  The radiation from cosmic rays and solar flares can not be controlled through the selection of the trigger orbit. However, the radiation dose from trapped particles in the Van Allen radiation belts varies substantially with the orbit selected.

  No quantitative information on the effect of radiation on the trigger satellite data was available to the author. The significance of the radiation in a given orbit was determined entirely by the science team. The relative importance of radiation changed substantially over the course of the architecture trade studies. Initially no trapped radiation was acceptable, however, as the design progresses this requirement was eased substantially.

- **Earth Blockage** - Initially Earth blockage was to be minimized. GRBs occurring in parts of the sky blocked by the Earth as seen from the position of the trigger satellite will not be detected. If a burst is not detected by the trigger satellites, even if it is by the helio satellites, no template can be constructed and uploaded to the helio satellites so no localization can be produced. The relative importance of blockage decreased with the realization that the blockage of Earth is mostly near the ecliptic plane where ETA has its least sensitivity due to the configuration of the constellation and the mounting of the sensors.

- **Eclipsing** - Initially Eclipsing was to be minimized. Eclipsing necessitates the inclusion of batteries and results in thermal transients in the space craft. The batteries needed to run critical components during eclipse add mass and complexity. In addition, when the space craft enters eclipse it is cut off from solar radiation but continues to radiate itself causing the space craft to cool. The NaI crystals used in the GRB detectors can shatter during rapid cooling. The importance of eclipsing decreased when it was pointed out that the satellites would experience eclipsing during the deployment sequence of most of the architectures under consideration, particularly secondary payload missions. First order calculation showed that if the GRB detectors were isolated and insulated sufficiently eclipsing would not cause rapid decreases in the in temperature. It was also pointed out that HETE, which would have experienced very frequent eclipsing, had NaI crystals in its sensors and was able to deal with the eclipsing in a similar manner.

- **Range** - The maximum tolerable range from Earth decreased substantially over time. Range determines the Round Trip time of Light (RTL) and effects the data rate and communications system necessary. Midway through the design process the requirement to provide rapid arcminute localization burst warnings was added. To facilitate the use of rapid reaction telescopes on the ground, total response times of a few seconds were required. This resulted in a requirement that the trigger satellites be within one light second of earth. This also helped fulfill an increasing demand for raw data from the trigger satellites by reducing the path losses and increasing the data rate.

- **Availability** - The requirement to provide rapid arcminute localization burst warnings resulted in a requirement that the trigger satellite be continuously available. In the previous iteration of ETA down linking all of the helio satellites could take up to 12 hours depending on the configuration of the constellation and the time of day that the burst occurred. Given this, the trigger satellites needed only be in view of the ground once in a 12 hour period. However, if a burst warning is to be disseminated in a few seconds the satellites must always be in view

of a ground station. This along with the next two requirements necessitated a synchronous orbit.

- **Ground Stations** - The first iteration of ETA contained only one ground station at Haystack. It was sufficient to see the trigger satellites at least once every 12 hours. When the requirement for continuos availability was introduced the number of ground stations was increased to three. These ground station were based on the HETE ground stations and distributed around the world to provide continuous contact. Later, in order to minimize cost, this was reduced to one pair of ground stations located at Haystack. This also contributed to the selection of the synchronous orbit.

- **Reliability** - Finally, the requirement to provide a minimal constellation in the event of a launch failure clinche the need to for a synchronous orbit. In the event that the trigger satellites are distributed among two launches and one launch fails, in order to provide continuous burst warning the remaining trigger must remain visible from the single ground station at all times. This dictates a synchronous orbit (thought not necessarily a geostationary orbit). The requirement to provide a minimal constellation in the event of a launch failure also confirms that a minimum of two trigger satellites are required.

The following sections describe how the above requirements apply to each orbit considered.

4.2 Distant Retrograde Orbit

The distant retrograde orbit was originally used by the last iteration of ETA. This orbit was selected for the following reasons:

- **Compatibility** - The insertion could be made over 30 days with an electric propulsion system. The trigger satellites were identical to the helio satellites.
- **Earth Blockage** - At its nearest approach the DRO selected was 3×10^6 km from Earth so little or no blockage occurred.
- **Radiation** - 3×10^6 km is also well out side of the Earth's radiation belts. The environment experience is equivalent to the helio satellite environment.
- **Eclipsing** - Once on station no eclipsing occurs.

Initially these same requirements remained in effect so this was the first trigger orbit considered for this iteration of ETA during the spring and early summer of 1996. The following subsections consider the nature of the DRO, the transfer to the DRO, and why the DRO was rejected.

4.2.1 Properties of the DRO

The DRO orbit is closely related to Hill orbits. The Hill, or Clohessy-Wiltshire, equations are the linearized equations of motion for a body relative to a reference body (here taken as Earth) which is in a circular orbit. The Hill acceleration is given by [20, pg. 142]:

$$\mathbf{a} = \begin{bmatrix} 3n^2 & 0 & 0 \\ 0 & 0 & 0 \\ 0 & 0 & -n^2 \end{bmatrix} \mathbf{r} + \begin{bmatrix} 0 & 2n & 0 \\ -2n & 0 & 0 \\ 0 & 0 & 0 \end{bmatrix} \mathbf{v} \tag{4-1}$$

Where n is the rotation rate, or mean motion, of the reference body around another body, $\mathbf{r}$ is the position, and $\mathbf{v}$ is the velocity relative to the Hill frame. The Hill frame is centered on the reference body with the **x**-axis pointed away from the body being orbited and the **y**-axis parallel to the velocity vector of the reference body as shown in Figure 4-1.

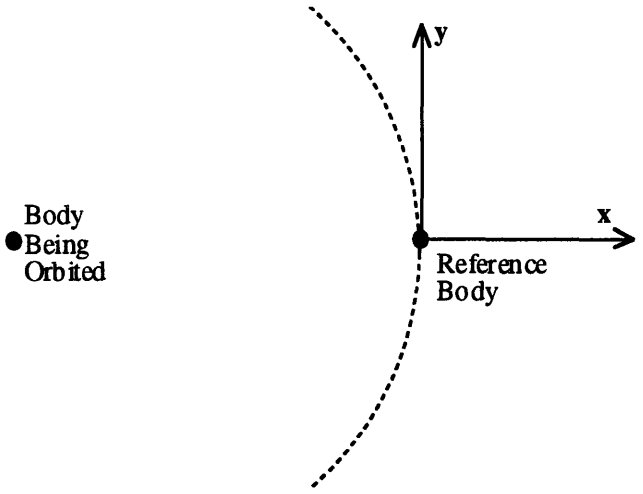

Fig. 4-1 The Hill frame.

Hill's equations admit a periodic solution given by:

$$\mathbf{r} = \begin{bmatrix} A\sin(nt+\psi) \\ 2A\sin(nt+\psi) \\ 0 \end{bmatrix} \tag{4-2}$$

Where A is the (arbitrary) nearest approach the Hill orbit makes to Earth, t is time, and ψ is an angle that determines the initial condition. In the Hill frame this orbit appears as and ellipse with its

line of apsides along the y-axis as shown in Figure 4-2. The semi-major axis of the ellipse is twice the semi-minor axis. The Hill orbit has a period equal to the reference body's and moves in a retrograde direction. In an inertial frame the Hill orbit is an elliptical orbit with the same semi-major axis and line of apsides as the reference orbit as shown in Figure 4-3. The only difference between the Hill orbit and the reference orbit is that the Hill orbit has a non-zero eccentricity. Despite the fact the Hill orbit is prograde in the inertial frame, the Hill orbit has a higher velocity at perihelion than Earth and a lower velocity than Earth at aphelion causing the apparent retrograde motion in the Hill frame.

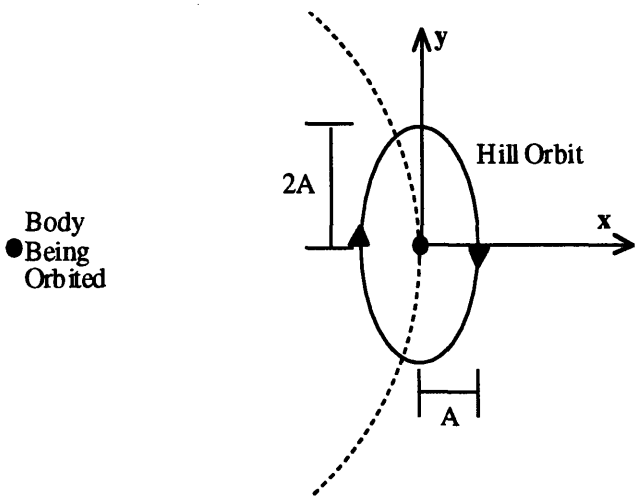

Fig. 4-2 Hill orbit viewed in the Hill frame.

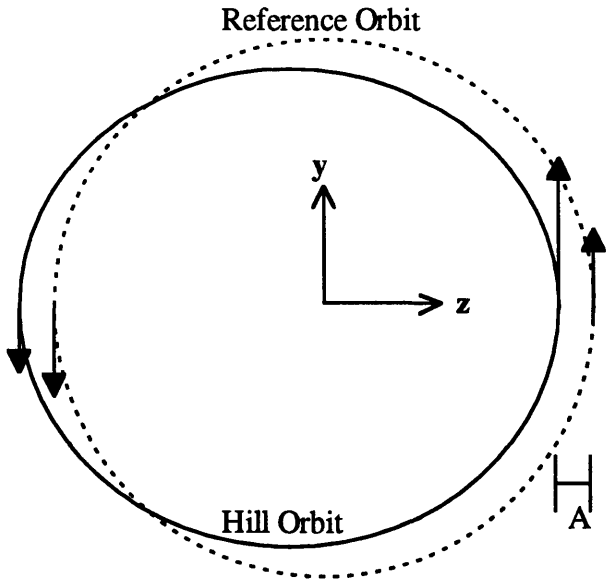

Fig. 4-3 Hill orbit viewed in the inertial frame.

The difference between the DRO and the Hill orbit is the gravitational influence of Earth. Hill's equations assume that the reference body has no mass. The gravitational influence of Earth reduces the period and the ratio of semi-minor axis to semi-major axis from that of a Hill orbit. The DRO considered has a period of 299 days (as opposed to 365 for a true Hill orbit), a semi-minor axis of 3×10^6 km, and a semi-major axis of 5.1×10^6 km (as opposed to 6×10^6 km for a true Hill orbit) as shown in Figure 4-4.

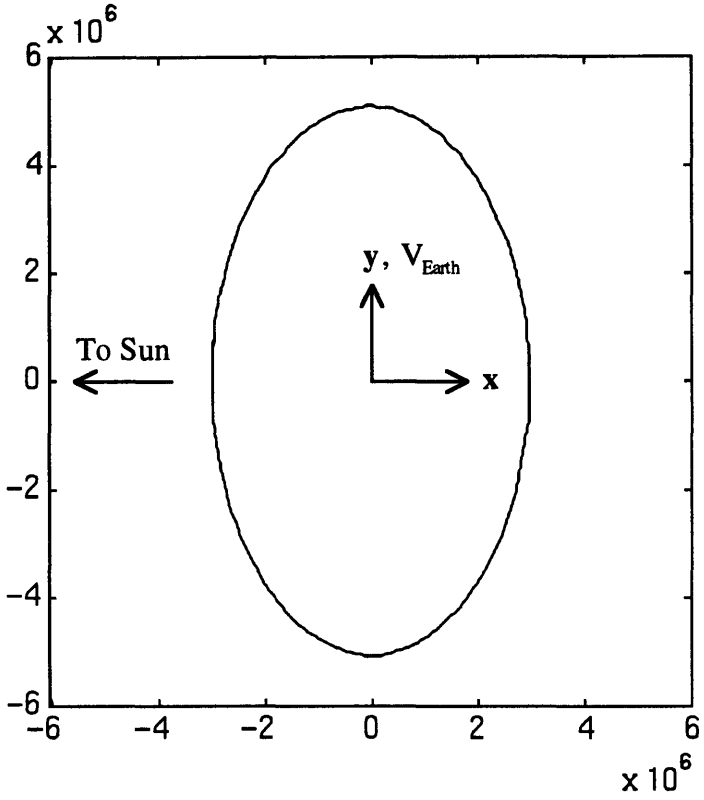

Fig. 4-4 The 3×10^6 km semi-minor axis DRO considered for ETA.

The particular DRO used by ETA was selected for its stability and resistance to lunar perturbations. It was observed that DROs passing in the vicinity of Earth-Sun L1,2 (located at $\sim\mp1.5\times10^6$ km on the x-axis) showed instability, became chaotic, and often escaped. DROs with semi-minor axes of 3×10^6 km or greater did not show instability. Orbits above 3×10^6 km were not considered because of increasing RTL and decreasing data rates. Orbits significantly lower than 1.5×10^6 km suffered from lunar perturbations.

4.2.2 Transfer to the DRO

The nature of the transfer to DRO determines the type and cost of propulsion system needed. In the previous iteration of ETA the stack consisting of the bus, the helio satellites, and the trigger

satellites injected to a near escape orbit and allowed to coast for 85 days before the SPT thrusters were started. After 30 days the SPT thrusters were shut down and the triggers were released into the DRO. This maneuver is not fully described in the previous thesis and was never fully duplicated by the author. The limited number of published works on transfer to DRO are also sketchy [21]. Electric propulsion was eliminated early so little consideration was given to this type of transfer. At this point in the design process both dedicated launch vehicle and secondary payload options were still under consideration so data for each were generated.

Transfers to DRO were optimized through numerical modeling using a code summarized in Figure 4-5. First, a position and velocity history for DRO is created by modeling the orbit in the Hill frame using the Cowell's method code described in appendix A. Next, a transfer trajectory for a given near escape injection velocity and position of perigee is computed. At the intersection of the transfer trajectory and the DRO the velocity history is used to compute a necessary insertion ΔV. The insertion velocity, recorded as a difference, Δ, from escape, is then varied to minimize the insertion ΔV. Finally, once an optimum ΔV for a given position of perigee is found the position of perigee is incremented and the process repeated to produce the minimum ΔV as a function of position of perigee.

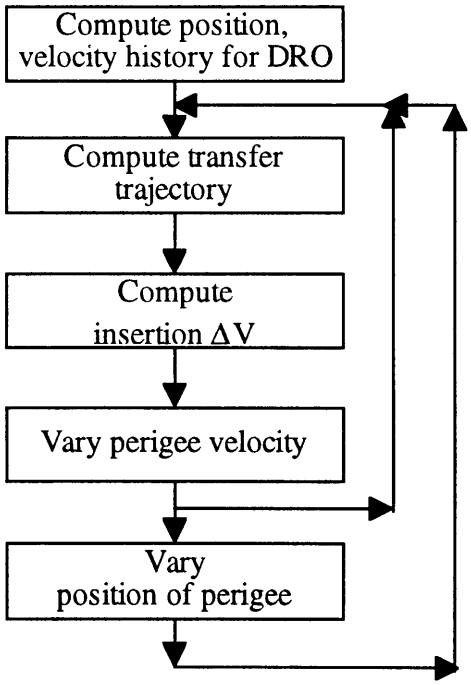

Fig. 4-5 Optimization of transfer to DRO.

The results of this optimization are shown in Figure 4-6 and 4-7 and were confirmed by Fabas. Figure 4-6 shows the final insertion cost versus position of perigee and Figure 4-7 shows the

difference, Δ, between the transfer injection velocity and escape at perigee. A sharp minimum in insertion ΔV exists at a position of perigee of ~120°. The sharpness of this minimum is a third body effect and was also present in Fabas's data.

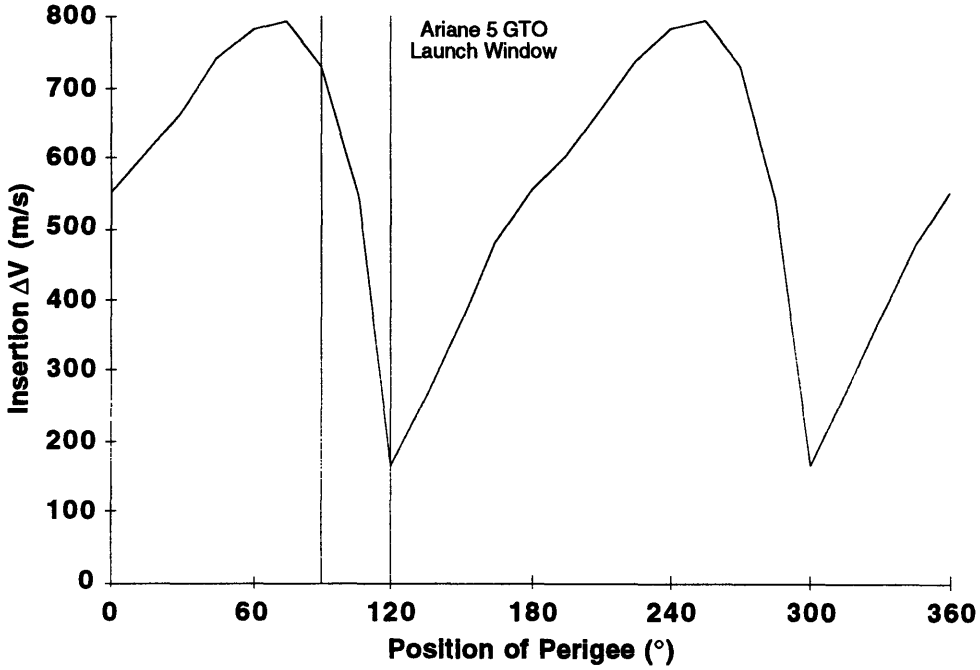

Fig. 4-6 Insertion cost to DRO.

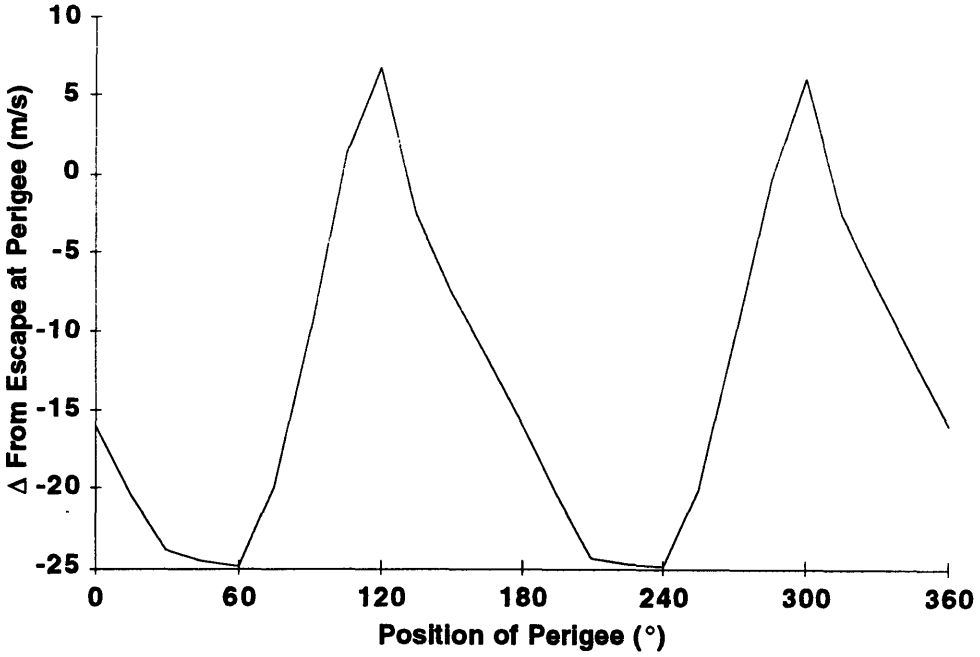

Fig. 4-7 Δ from escape velocity at perigee for transfer to DRO.

Fortunately, the minimum insertion ΔV fell near the optimum position of perigee for the helio satellites and was similar to the spreading ΔV required for ETA. This allowed for good compatibility with the dedicated launch vehicle options which could be launched with the ideal position of perigee for the trigger satellites at little cost. The bus was to be injected with the velocity of the highest spread rate helio satellite, then make burns to slow itself and release each of the remaining helio satellites. After the last helio satellite was deployed the bus could make a small burn to place itself into the transfer to DRO. Once the bus had coasted to the DRO injection point it could make an insertion burn and deploy the trigger satellites. For the distributed propulsion option the trigger satellites could be injected into the DRO transfer and then the helio satellite could make their spreading burns. The triggers would then coast to the DRO injection point and make their own insertion burns. Only the distributed solid option would have had problems with the DRO. It was unclear whether the solid rocket motors would have the accuracy needed for inserting into the DRO.

The secondary payload option had more problems with transfers to the DRO. While the trigger ΔV required for escaping GTO and inserting to the DRO is similar to the ΔV required for the helio satellites, the narrow optimum in position of perigee was problematic. Since the secondary payload options have no control over position of perigee it was very unlikely that they would ever be launched with the optimum position of perigee. Fortunately, the optimum did fall at the end of the Ariane 5 launch window as shown in Figure 4-6. By holding in GTO for no more than 45 days the trigger satellites could shift their positions of perigee to the optimum position of perigee if the radiation does is tolerable. Unfortunately, the secondary payload solid propulsion option had more problems with transfer to DRO than the dedicated launch vehicle distributed solid propulsion option did. The helio satellite propulsion system for the secondary payload solid propulsion option could only produce a single impulse, while the trigger satellites require two impulses (escape from GTO and insertion to DRO). In addition to accuracy concerns, the secondary payload solid propulsion would have required a secondary propulsion system to insert to DRO. In this case the trigger satellite would have been significantly different from the helio satellite increasing the cost of the mission. This represented a serious conflict between the optimum helio satellite deployment mechanism and the DRO orbit. However, the DRO was eliminated as a trigger orbit more because of changes in the requirements than because of the conflict with the secondary payload solid propellant option.

4.2.3 The Elimination of the DRO

The DRO was dropped from consideration because of the requirement to provide rapid arcminute localization burst warnings in order to facilitate the use of rapid reaction telescopes for observing

GRBs. Trigger satellites in DRO are between 10 and 16 light seconds from Earth. Ideally burst warning would be provided within 1 light second. This led to the consideration of the Lunar L4,5 point orbits.

4.3 Lunar Lagrange Point 4,5 Orbit

With introduction of the arcminute localization burst warning requirement and the elimination of the DRO a new trigger orbit was needed. While the Earth blockage and radiation requirements had been loosened, orbits closer than lunar orbit were considered by the science team to have too much Earth blockage and too high of a trapped radiation dose. Orbits higher than lunar orbit had RTLs that were too long to meet the rapid response criteria. Finally, orbits in the immediate vicinity to the Moon suffered form instability due to the perturbation of the Moon. The only stable orbit that could be found in this vicinity was the LL4,5 orbit.

By this time, the task of analyzing the transfer was simplified by the selection of the secondary payload options over the dedicated launch vehicle options. The choice between liquid propulsion systems and solid rocket motors had not yet been made so both are considered here.

The primary work on LL4,5 orbits was done by Fabas and the data included in this section was produced by Fabas. The author's working in parallel confirmed these analyses. The LL4,5 orbit was considered for the current iteration of ETA over the summer of 1996.

4.3.1 The Nature of the LL4,5 Orbits

The five Lagrange points, as shown in Figure 4-8, are periodic solutions to the restricted three body problem. The restricted three body problem concerns the motion of two finite mass bodies (the Earth and the Moon in this case) and one infinitesimal mass (the trigger satellite). If the two finite mass bodies are in circular or elliptical orbits around their common center of gravity, an infinitesimal mass body placed at the Lagrange points will remain fixed relative to the two massive bodies as seen from a frame rotating about the center of mass of the system at the rate of the massive bodies. The three co-linear Lagrange point are unstable. Without station keeping a trigger satellite placed at L1, L2, or L3 will drift away and so were rejected as trigger orbits. The L4 and L5 points, located at the vertices of equilateral triangles formed by the three bodies, are stable and require no station keeping.

The LL4,5 orbit as viewed in inertial coordinates is has the same semi-major axis (384,000 km or 1.28 light seconds) and the same eccentricity (0.0549) as the Moon's orbit. The period of the

LL4,5 orbit is ~27.3 days. The LL4,5 orbit will eclipse one to two times a year with a maximum pen-umbra duration of 270 minutes and a maximum umbra duration of 150 minutes. This eclipsing rate was considered to be low enough that the triggers could be shut down during the eclipse with out significant loss of data. The Earth blockage from LL4,5, while much larger than from DRO, is still negligible. The radiation environment is also comparable to DRO except when the LL4,5 points sweep through the Earth's geo-tail once a month.

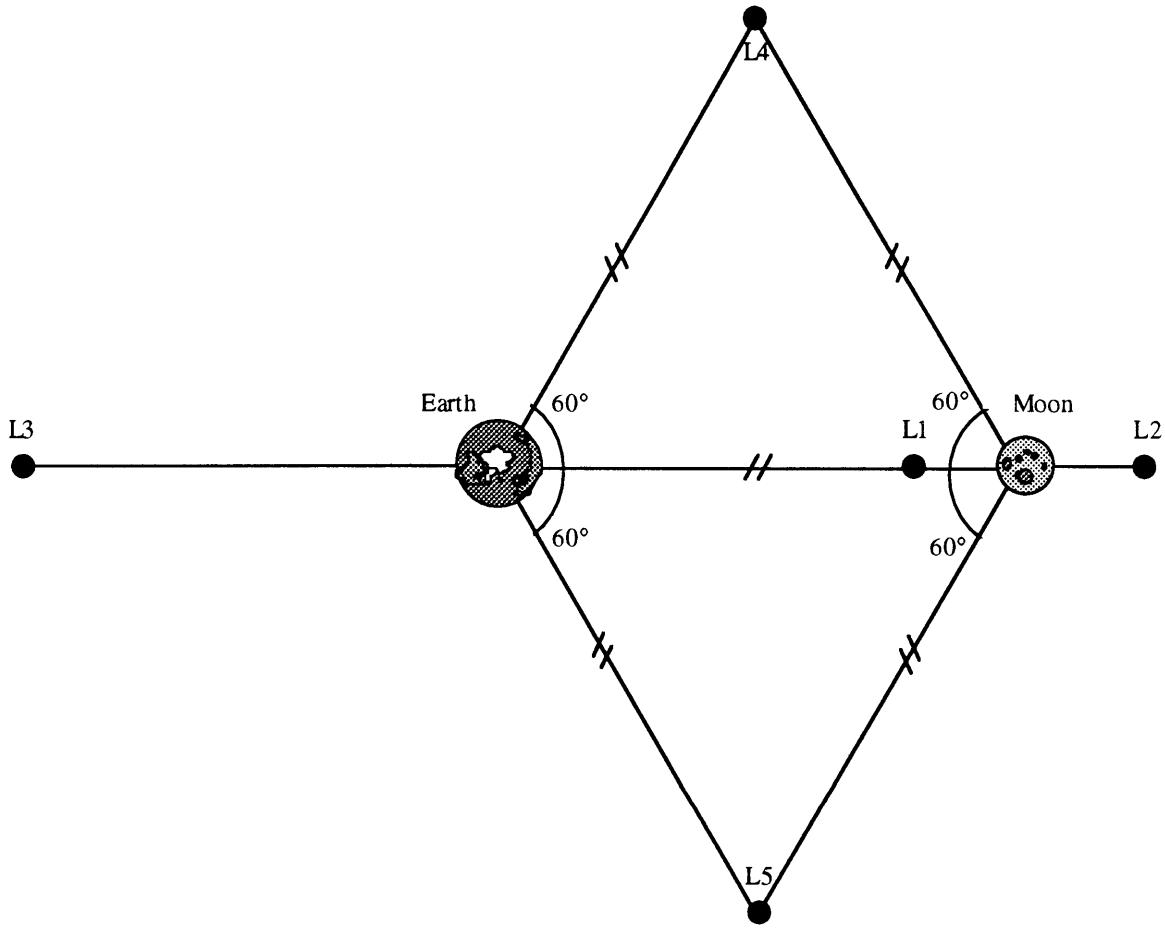

Fig. 4-8 Lunar Lagrange points.

4.3.2 Transfers to LL4,5 Orbits

Transfers consisting of two and three or more burns were considered. It was assumed that transfers would be made to the LL4,5 orbit and then re-phased with small burns to the actual LL4,5 point. Initially, Fabas considered a two burn quasi-Hohman transfer as shown in Figure 4-9. The two burn cost of inserting to LL4,5 orbit is shown in Figure 4-10 as a function of the angle, θ, between the lines of apsides of GTO and the LL4,5 orbit. The total cost was only a weak function of θ so for simplicity LL4,5 was modeled as a circular obit in later analyses. The

maximum cost was 1,550 m/s. This was significantly higher than the ~1000 m/s to escape GTO and achieve a reasonable spread rate raising compatibility concerns. The high cost of this transfer motivated the search for other transfers

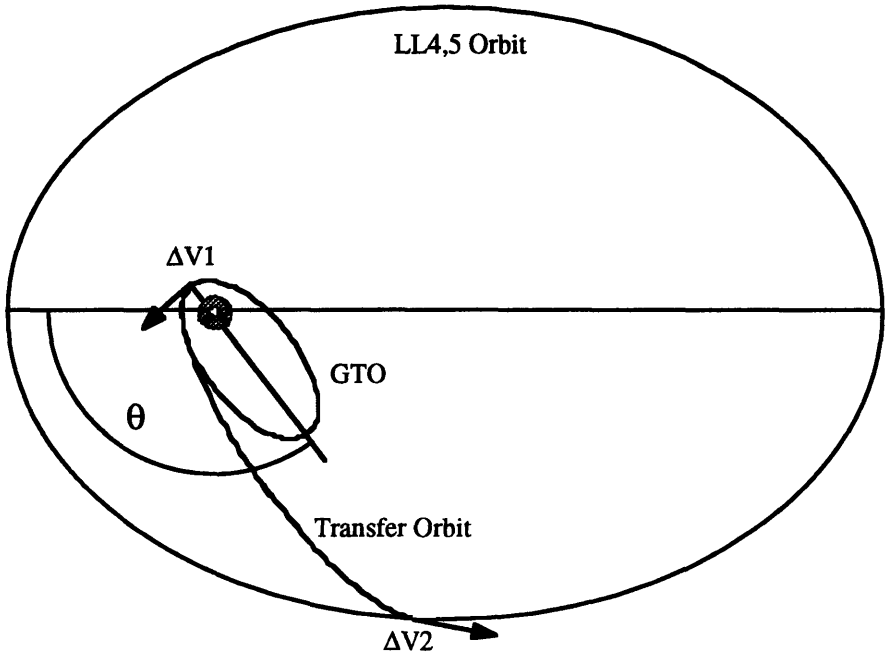

Fig. 4-9 Two burn transfer to LL4,5 orbit.

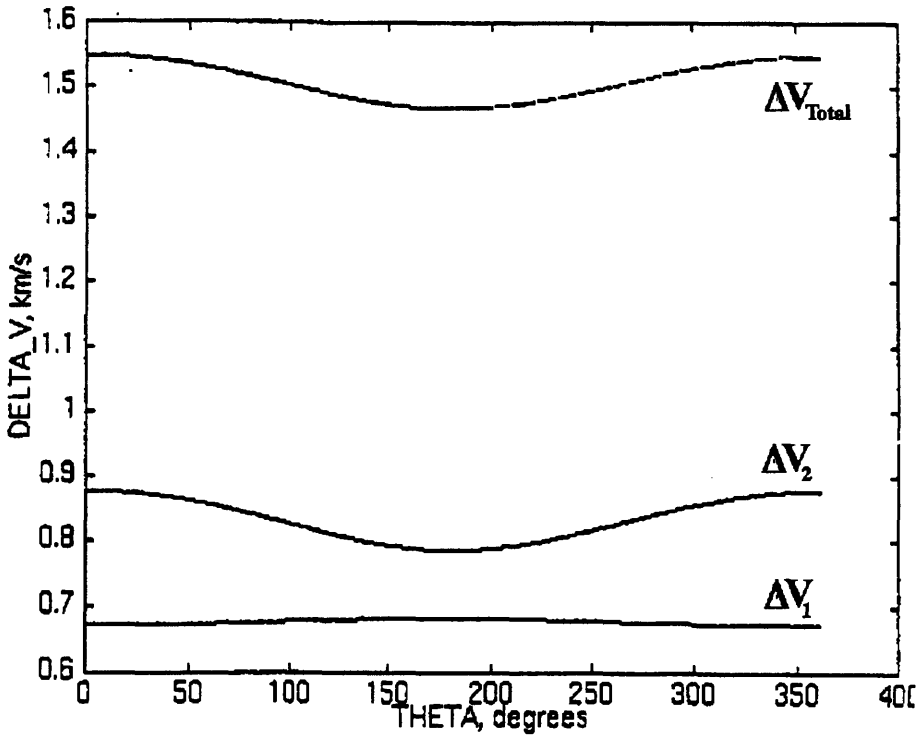

Fig. 4-10 Cost of a two burn transfer to LL4,5 orbit.

Next, a three burn transfer was considered by Fabas as shown in Figure 4-11. First, a burn was made to inject the trigger satellite into a transfer orbit with an apogee much higher than 384,000 km. At apogee a second burn was made to raise the perigee to 384,000 km. Finally, a third burn is made at the new perigee to circularize into the final orbit. It was found that as the initial apogee was increased the third body effect of the Sun became greater and greater as shown in Figure 4-12, 4-13, and 4-14. Above 1×10^6 km apogees often did not exist and the triggers simply escaped. Initial apogees of twice the radius of LL4,5 (768,000 km) and 1×10^6 km were considered. The total cost for these transfers is shown in Figures 4-15 and 4-16. Relative to the two burn transfer, the maximums are much higher (1.8 km/s for 1×10^6 km) the minimums are much lower (1.1 km/s for 1×10^6 km).

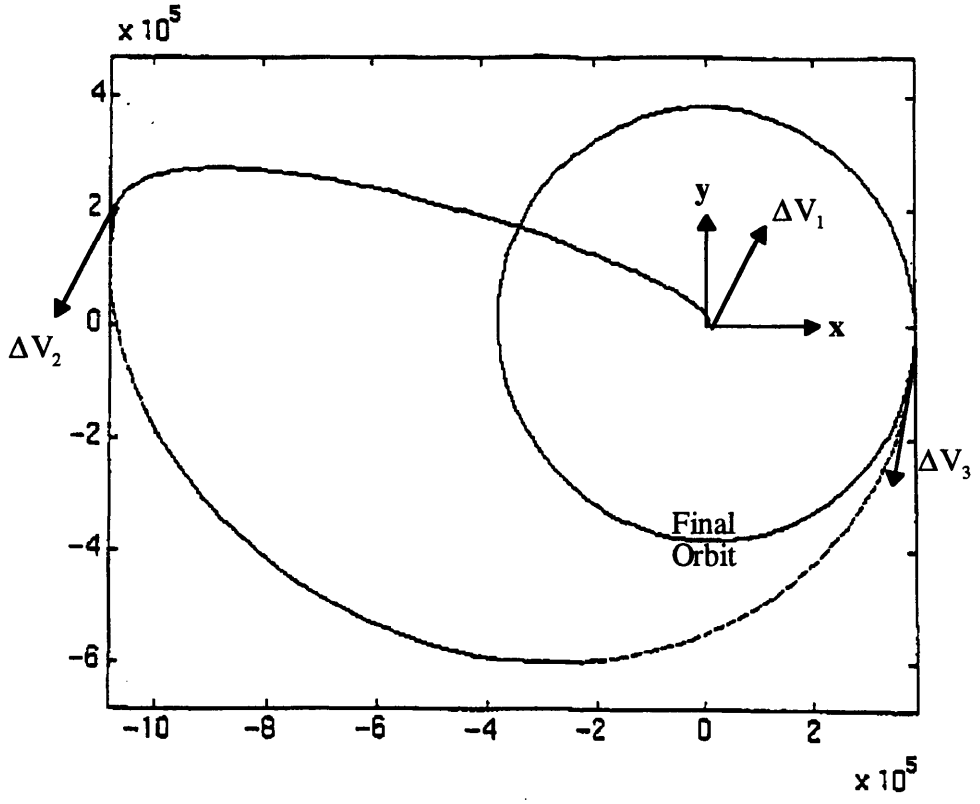

Fig. 4-11 Three burn transfer to LL4,5 orbit with initial apogee of 1×10^6 km.

By holding in GTO it was believed that the minimum could always be achieved, providing that the radiation exposure in GTO was acceptable. As an alternative, if the trapped radiation in the Van Allen belts was found to be too great, the triggers could be boosted into a holding orbit with a much greater apogee that spends very little time in the radiation belts. For holding orbits of this type small apogee correction would be needed to account for the perturbation of the Sun. The cost

of these corrections was never more than ~75 m/s so that a total cost of 75 m/s above of the minimum (1,175 m/s) could be achieved.

A total cost of 1,100 to 1,175 m/s, depending on the type of holding orbit used, was much closer to the helio satellite ΔVs than was the two burn cost. The LL4,5 transfer was compatible with the bipropellant secondary payload option. Unfortunately, the requirement for multiple accurate burns made the LL4,5 transfer incompatible with the solid propellant secondary payload option.

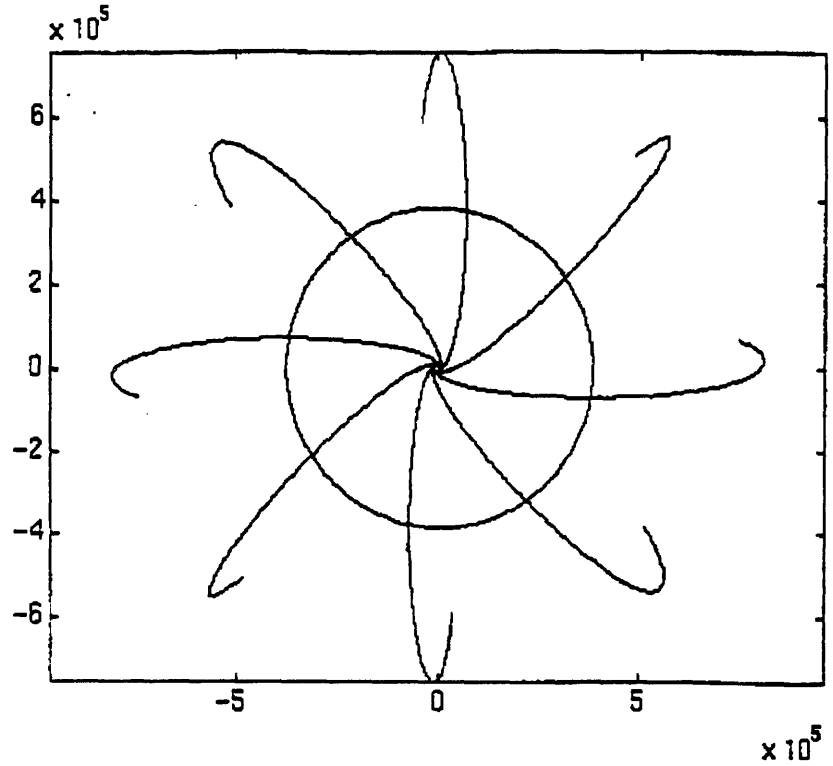

Fig. 4-12 Transfer orbits with expected initial apogee of 768,000 km and the final LL4,5 orbit.

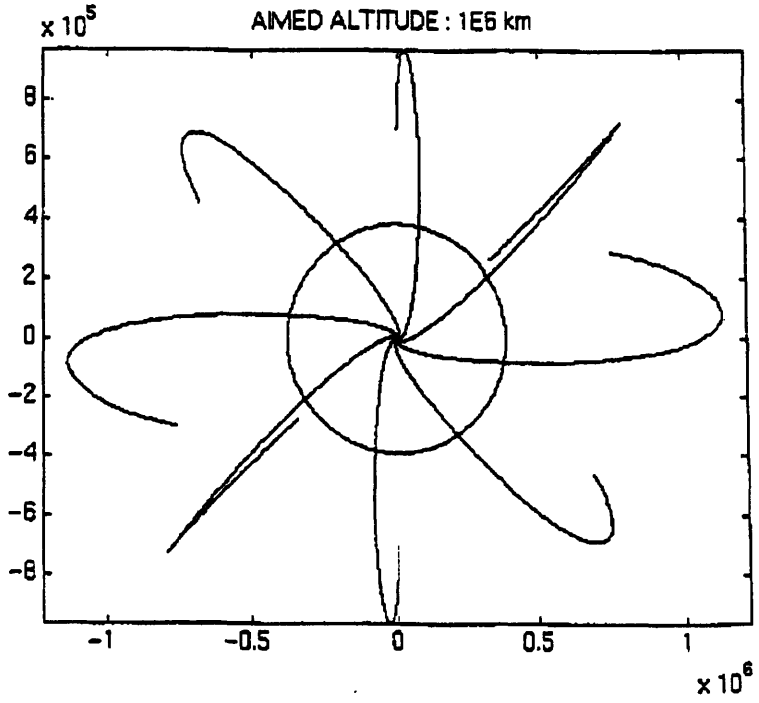

Fig. 4-13 Transfer orbits with expected initial apogee of 1×10^6 km and the final LL4,5 orbit.

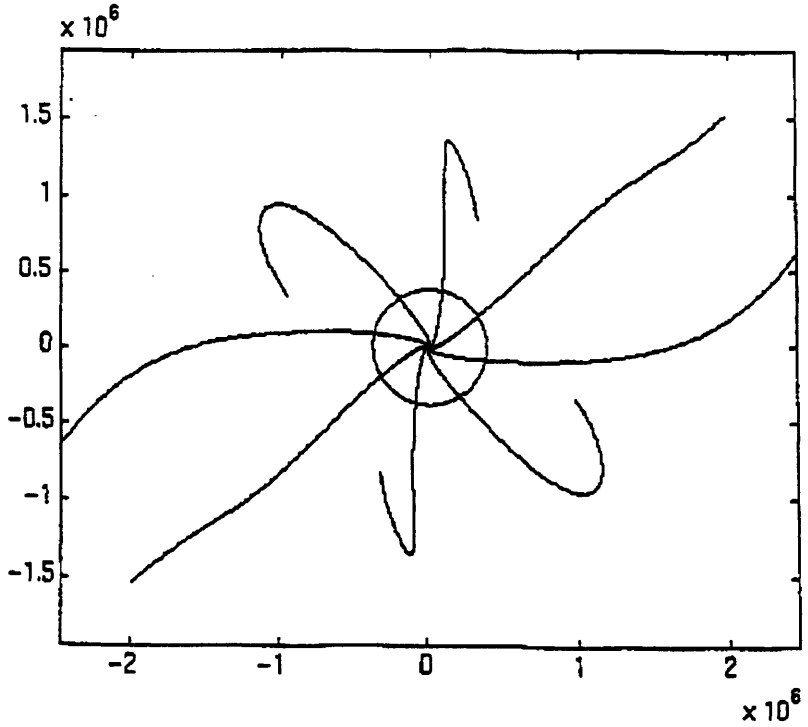

Fig. 4-14 Transfer orbits with expected initial apogee of 1.5×10^6 km and the final LL4,5 orbit.

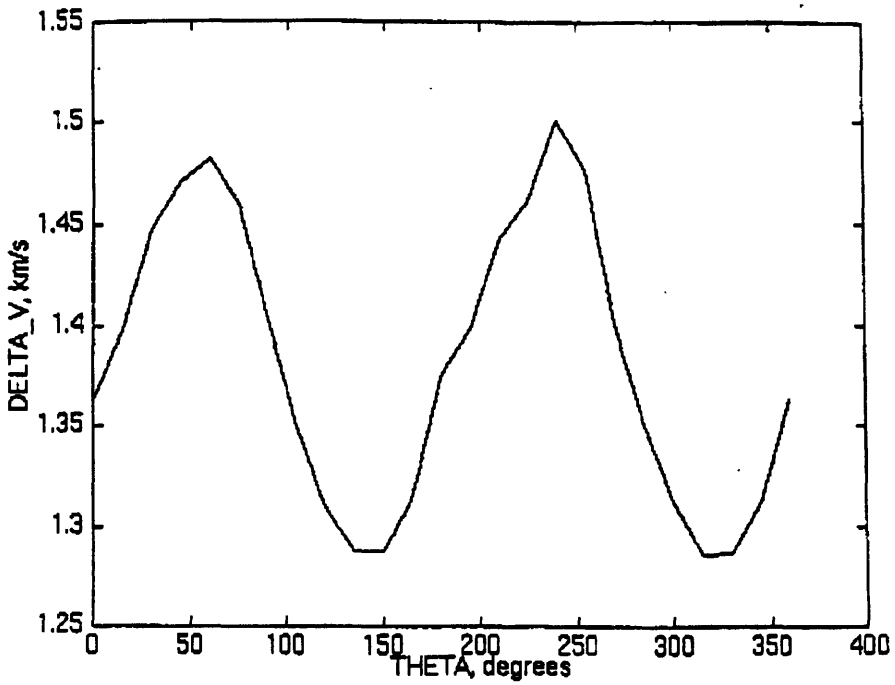

Fig. 4-15 Cost of a three burn transfer to LL4,5 orbit with initial apogee of 768,000 km.

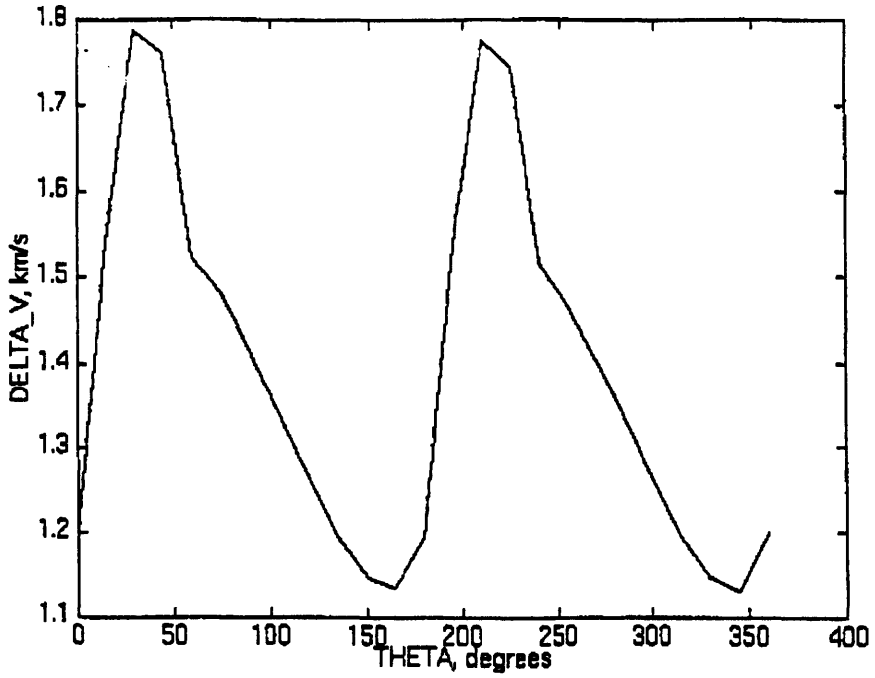

Fig. 4-16 Cost of a three burn transfer to LL4,5 orbit with initial apogee of 1×10^6 km.

4.3.3 The Elimination of the LL4,5 Orbits

By the time Fabas had completed his work the solid propellant secondary payload option had emerged as the best choice for the helio satellites. This option would have required a substantial and expensive secondary propulsion system to perform the multiple precision burns to enter LL4,5 orbit. Additional concerns were raised with the radiation exposure of holding in GTO and the complexity of holding in a high apogee orbit. Facilitated by a further relaxation of the requirements on Earth blockage and trapped radiation environment, the LL4,5 orbits were dropped from consideration and orbits were considered that could be reached from GTO with one or two solid rocket motor burns.

4.4 High Circular Orbit

By the end of summer, 1996, the science team had relaxed its requirements on Earth blockage and trapped radiation to the point that they considered a 60,000 km circular orbit to be acceptable. Considering the compatibility problems of the chosen secondary payload solid propulsion option with the LL4,5 orbit, circular trigger orbits above 60,000 km were sought that could be reached using the helio satellite solid rocket motor and one other small solid rocket motor. The Hohman transfer cost from GTO to circular orbits of this type are shown in Figure 4-17.

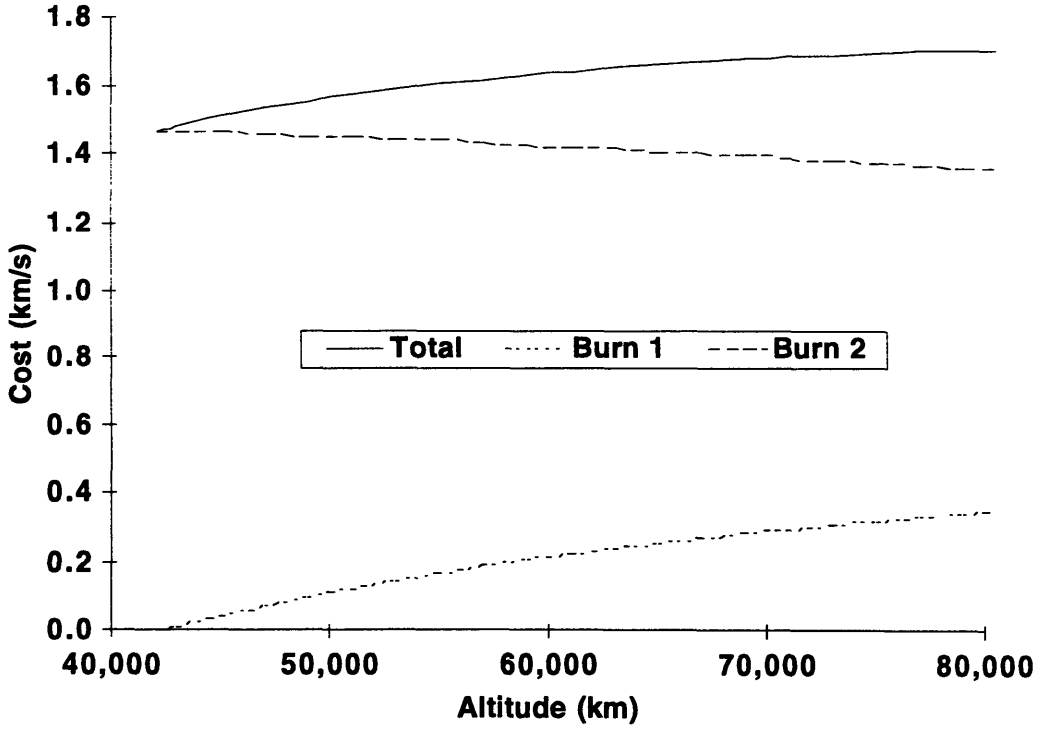

Fig. 4-17 Cost of a two burn transfer to circular orbit.

These high circular orbits offered several advantages. The transfers required were entirely Keplerian so no consideration was required for third body effects and position of perigee. This eliminated any need for additional radiation exposure and operational complexity incurred by holding orbits. The delicate three body nature of the DRO and LL4,5 trigger orbits required high accuracy insertion to produce stable orbits. Without three body effects, small pointing and total impulse errors have proportionately small effects on the final high circular orbits. This enabled the use of solid rocket motors which inherently have less controllability.

Thiokol makes a number of smaller solid rocket motors capable of providing the first, and smaller, apogee raising burn. Of these the Star 6B is shown in Figure 4-18 and described in table 4-1 was the best engine for this task [17]. For ETA, the Star 13A and Star 6B could be mounted back to back as was done on the Swedish research satellite Freja. In this configuration the trigger satellites could be aligned for the perigee burn, spun up, the perigee burn made, and then the apogee burn made without despining or reorienting between burns as shown in Figure 4-19. The performance of this combination of motors in terms of useful mass (non-propulsive mass) is shown in Figure 4-20 as a function of apogee radius assuming an 80 kg ASAP slot[3]. At 60,000 km circular the useful mass is 37.2 kg. The maximum perigee is limited by the propellant load of the Star 6B to ~65,000 km radius. Even if higher perigees could be achieved they would not be desirable since the useful mass is declining rapidly with perigee radius.

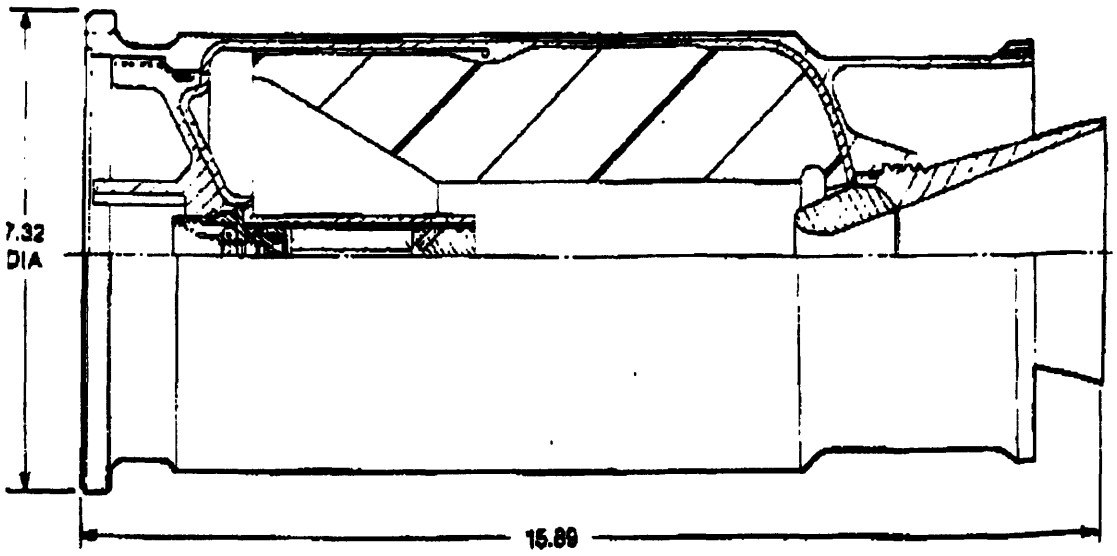

Fig. 4-18 The Star 6B [17].

[3] Ariane later incresed this number to 100 kg. This number is still used in this chapter but the updated number is used in later chapters.

Table 4-2 Star 6B Characteristics [17]

Item	Star 6B
Max Thrust	2820 N
Effective I_{sp}	273 sec
Max Propellant	6.10 kg
Burn Out	4.05 kg
Other Expendables	0.20 kg
Max Total	10.35 kg
Loading	42% to 117%
Diameter	186 mm
Length	403 mm
Expansion Ratio	28

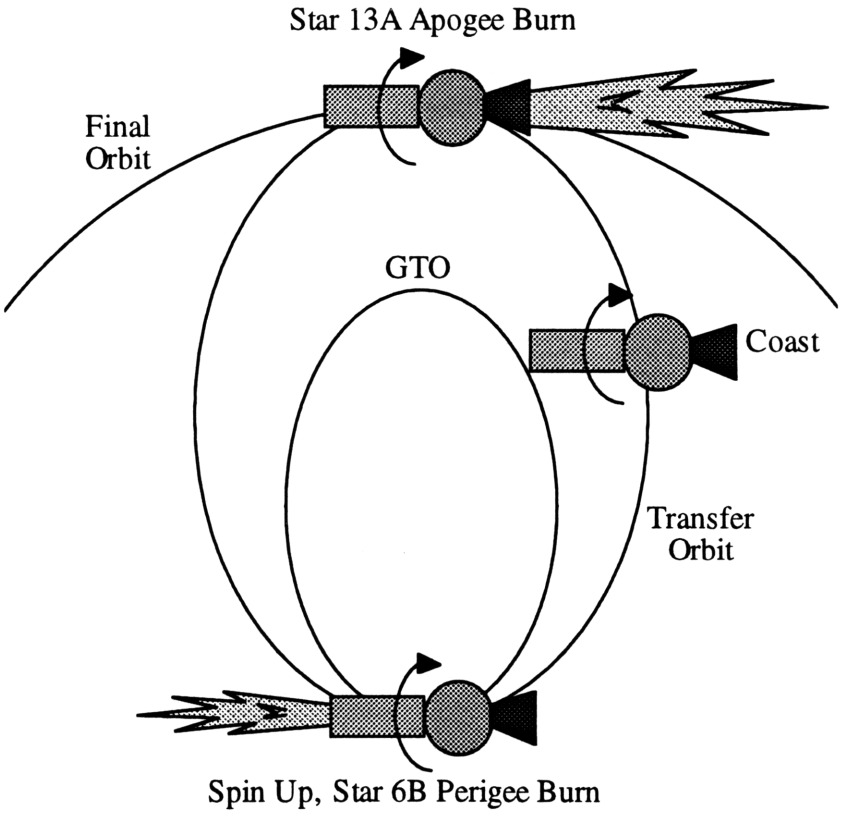

Fig. 4-19 The deployment sequence for a back to back pair of a Star 6B and a Star 13A .

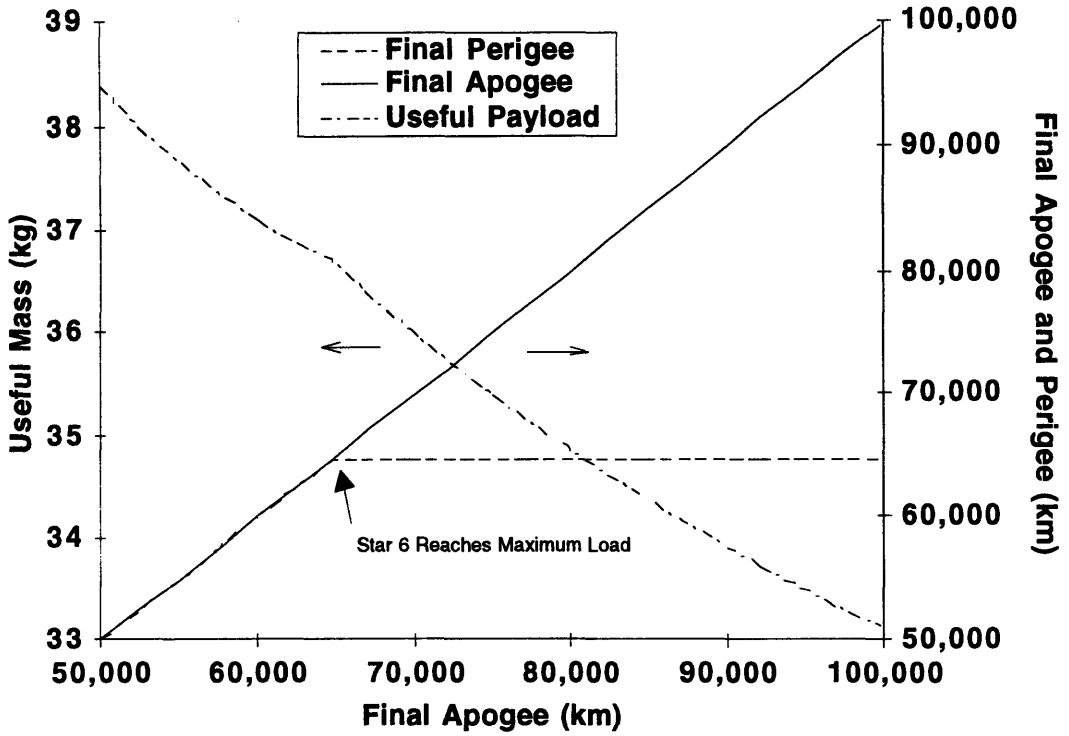

Fig. 4-20 Useful mass, final trigger apogee, and final trigger perigee vs. final apogee for Star 6B / Star 13A combination.

Unfortunately, several problems with this arrangement of engines led to its rejection. First, a useful mass of 37.2 kg was not sufficient for the non-propulsive trigger satellite mass. Second, the addition of the Star 6B to the standard helio satellite configuration, while much less of a modification than adding a liquid secondary propulsion system as required by the DRO and the LL4,5 orbit, was considered too complex and expensive. Third, the total length of the Star 6B and Star 13A was 984 mm which exceeded the 800 mm maximum dimension of the ASAP slot[4]. While waivers are sometimes obtainable, relying on getting one did not seem wise. Finally, a further reduction in the requirements on Earth blockage and trapped radiation and the desire to move to a single ground station allowed and necessitated a move to a synchronous orbit.

4.5 Synchronous Orbits

The synchronous orbit was the final orbit considered and the orbit selected. Synchronous orbits are characterized by a one sidereal day period (23 hrs 56 min 4.091 sec) and a semi-major axis of 42,165 km. Synchronous orbits can be entered from GTO with a single burn which costs less than the insertion into a high circular orbit as will be described in section 4.5.1. Synchronous

[4] Ariane later incresed this number to 885 mm, 800 mm above the separation plane and 85 mm below.

orbits with high enough perigees can be made continuously visible from a given point on the surface of the Earth. The perigee required to provide continuously visibility is computed in section 4.5.2. A trigger satellite in a continuously visible orbit can provide continuous burst warnings to a single ground station even in the event that the other trigger satellite is lost due to launch failure. The consideration of synchronous orbits was allowed by a final reduction in the requirements on Earth blockage and trapped radiation so that orbits with perigees higher than 20,000 km were acceptable. Further, synchronous orbits were required by the shift to a single ground station at Haystack in order to reduce cost. Given the trapped radiation requirements, a 20,000 km × 64,330 km synchronous orbit is the baseline orbit.

4.5.1 Insertion Mechanism and Cost

The family of synchronous orbits reachable from GTO have perigees from 6,678 km to 42,165 km. For all but the limiting synchronous orbit perigees, each final perigee can be reached by making a burn at two true anomalies: one before apogee, and one after apogee as shown in Figure 4-21. Insertions occurring before apogee will be defined as type I insertions and insertions occurring after apogee will be defined as type II insertions. In the case of off perigee and off apogee insertions both the perigee and the apogee are raised and the argument of perigee is shifted from the original GTO argument of perigee, ω, by an amount $\Delta\omega$. Type I insertions produce a positive change in argument of perigee and type II insertions produce a negative change in argument of perigee. This change in argument of perigee causes a difference in the sky tracks of type I and type II orbits, as is described in section 4.5.2, and will be used in the next chapter to produce a desired angular separation in the lines of apsides between the two trigger satellites in the ETA constellations. The type of insertion does not change its cost.

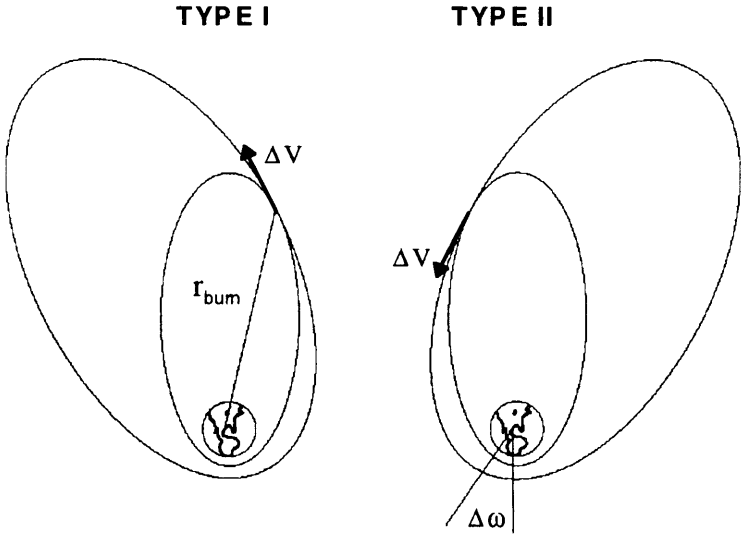

Fig. 4-21 Type I and II transfers to one day orbits.

The cost of insertion can be derived starting with the square of the specific angular momentum, h^2, of a an orbit given by:

$$h^2 = v^2(r\cos\phi)^2 \tag{4-3}$$

Where v is the local velocity, r is the local radius, and ϕ is the local flight path elevation angle. At the co-tangential insertion point between GTO and the synchronous orbit both r and ϕ are the same resulting in the following relation ship between GTO and the synchronous given by:

$$\frac{h_{GTO}^2}{v_{GTO}^2} = \frac{h_{Sync}^2}{v_{Sync}^2} \tag{4-4}$$

The velocity of an object in orbit is given as a function of radius and the specific mechanical energy, ε, of the orbit by a form of the Vis-Viva integral:

$$v^2 = 2\varepsilon + \frac{2\mu}{r} \tag{4-5}$$

Where μ is the gravitational parameter. Inserting equation 4-5 into equation 4-4 and solving for the burn radius, r_{burn}, gives:

$$r_{burn} = \frac{\mu h_{GTO}^2 - \mu h_{Sync}^2}{h_{Sync}^2\varepsilon_{GTO} - h_{GTO}^2\varepsilon_{Sync}} \tag{4-6}$$

Of the variables in equation 4-6 only h_{Sync} is a function of synchronous orbit perigee radius, $r_{Sync\ Peri}$, given by:

$$h_{Sync}^2 = 2e_{Sync}r_{Sync\ Peri}^2 + 2\mu r_{Sync\ Peri} \tag{4-7}$$

The other variables in equation 4-6 are h_{GTO} equal to 69086.38 km²/sec, ε_{GTO} equal to -8.11103 km²/sec[25], and ε_{Sync} equal to -4.72667 km²/sec². The burn radius as a function of perigee radius is shown in Figure 4-22. With these values and the burn radius the ΔV can be computed using the Vis-Viva integral:

$$\Delta V = \left(2\varepsilon_{Sync} + \frac{2\mu}{r_{burn}}\right)^{\frac{1}{2}} - \left(2\varepsilon_{GTO} + \frac{2\mu}{r_{burn}}\right)^{\frac{1}{2}} \tag{4-8}$$

The required ΔV as a function of synchronous orbit perigee radius is shown in Figure 4-23. The ΔV required for entering a 20,000 km perigee radius synchronous orbit is 1247 m/s. This is reasonably compatible with the helio satellite propulsion system.

---

[5] This uses the most curent data for the Ariane 5 GTO (6978 km × 42165 km).

The type I pre and post burn true anomalies, f_I, can be computed in terms of pre and post burn specific mechanical energy, ε, and specific angular momentum, h, as given by:

$$f_I = \cos^{-1}\left(\frac{1}{\sqrt{1+\frac{2\varepsilon h^2}{\mu^2}}}\left(\frac{h^2}{\mu r_{burn}}-1\right)\right) \tag{4-9}$$

The pre and post burn type I true anomalies are shown in Figure 4-24. The type II true anomalies, f_{II}, are given by 360-f_{II},. The change in argument of perigee, Δω, is given by f_{post}-f_{pre} as shown in Figure 4-25. For a 20,000 km perigee radius synchronous orbit Δω is 50.96°.

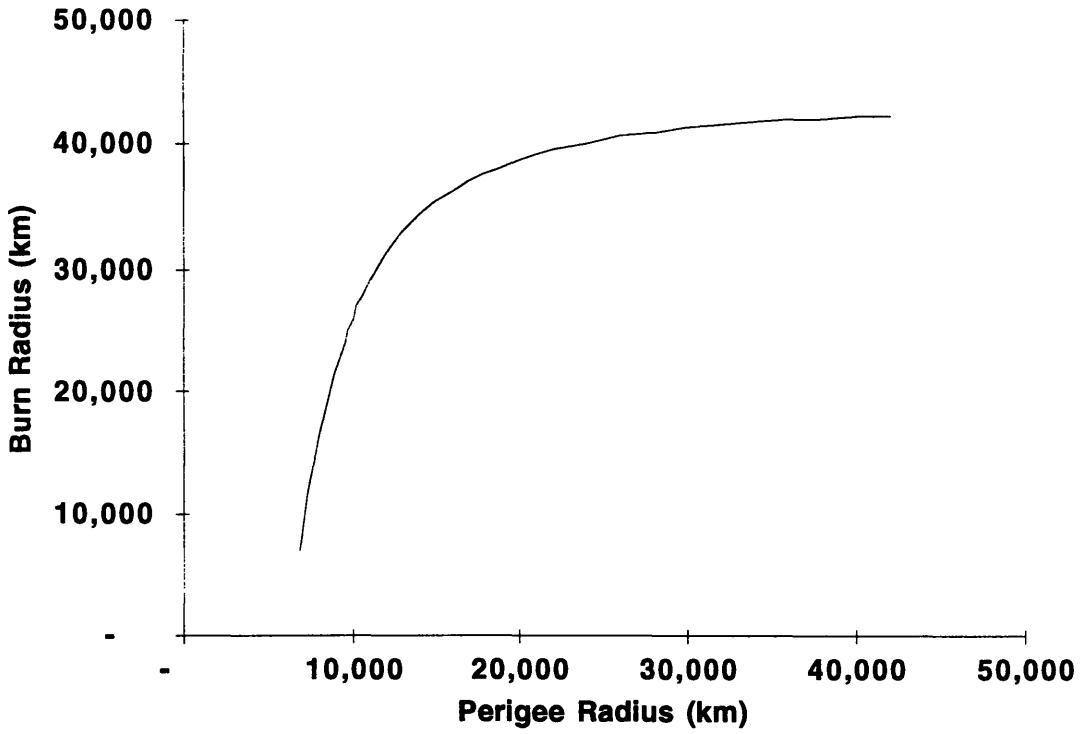

Fig 4-22 Burn radius.

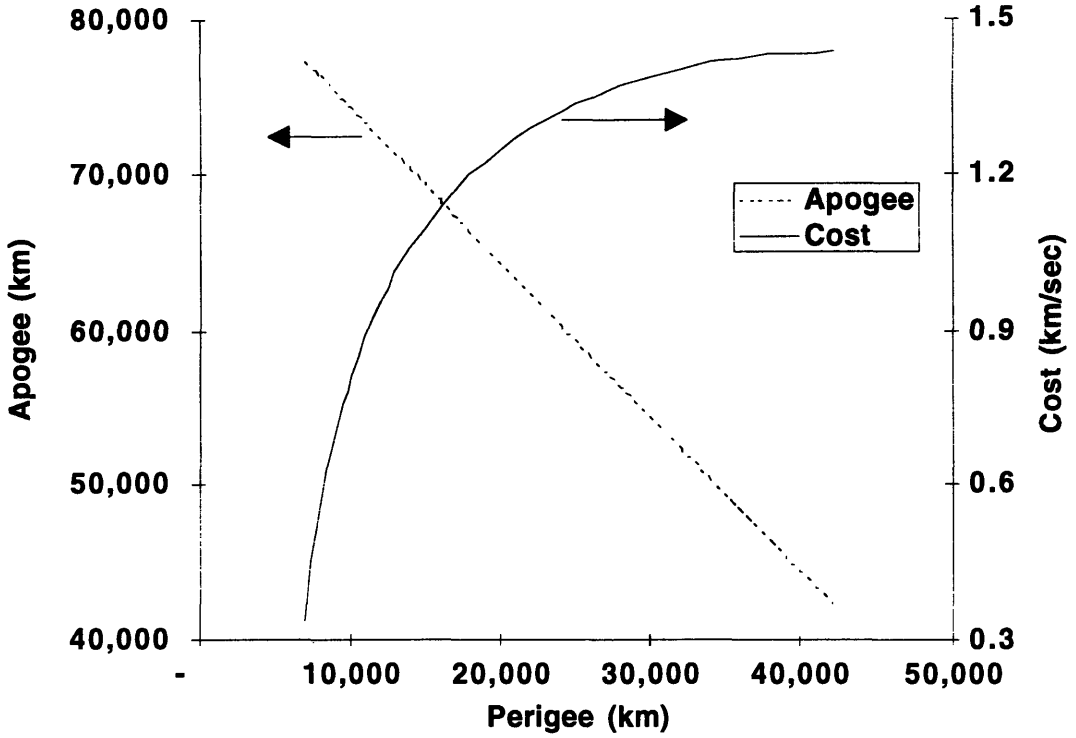

Fig. 4-23 Apogee and insertion cost vs. perigee radius for insertion to synchronous orbit from GTO.

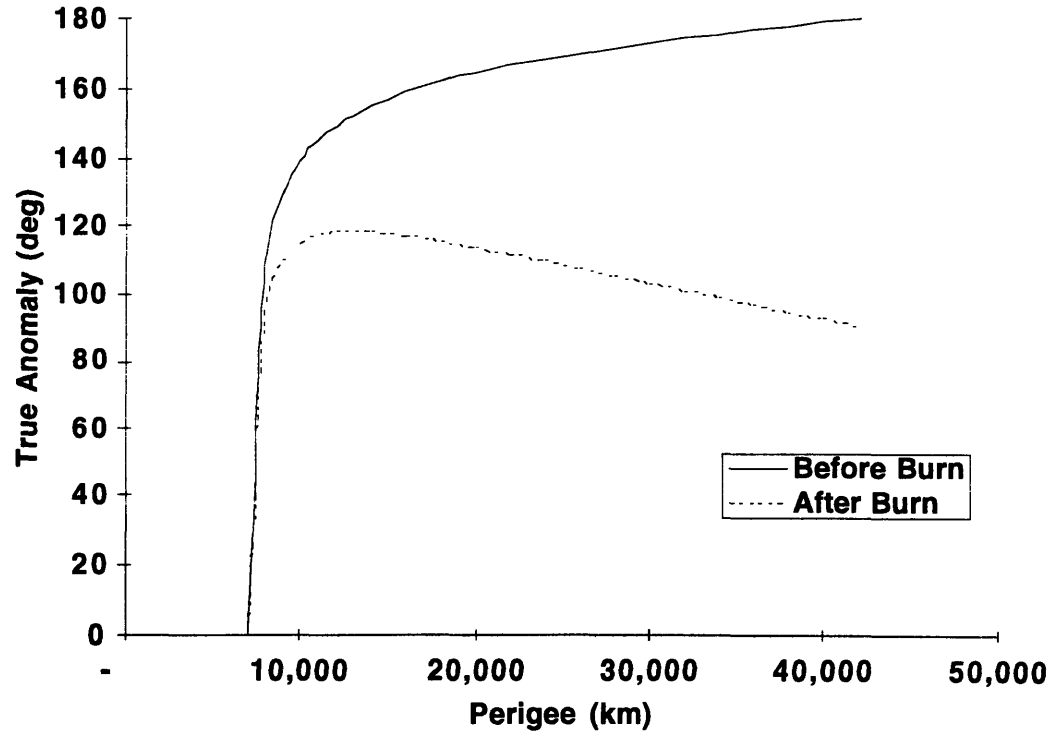

Fig. 4-24 Pre and Post burn true anomaly for insertion to synchronous orbit from GTO.

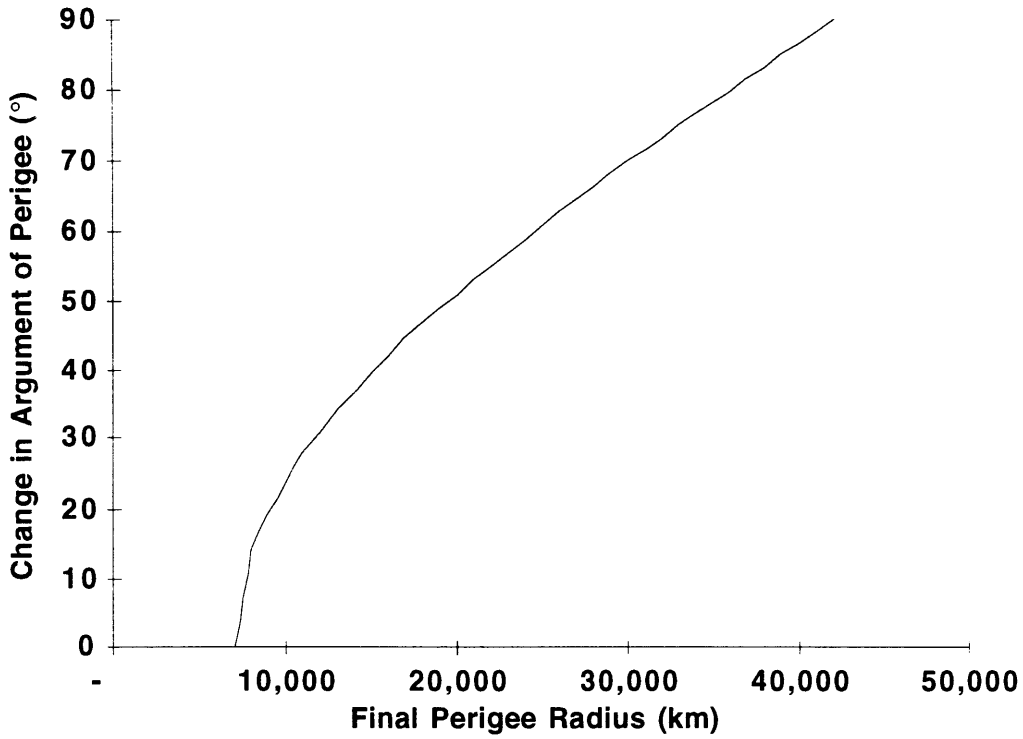

Fig. 4-25 Change in argurment of perigee, $\Delta\omega$, vs. perigee radius.

4.5.2 Visibility of Synchronous Orbits

Continuos visibility from a single point on the surface of the Earth is a property of many, but not all, synchronous orbits. This can be seen by observing the effect of perigee radius on the space track of a synchronous orbit. The space tracks for 0° inclination synchronous orbits with perigees of 10,000 km, 20,000 km, 30,000 km, and 40,000 km are shown in Figure 4-26 as viewed looking down from the north pole in a frame rotating with the Earth. A geostationary orbit in this frame would appear as a point. As the perigee radius decreases the space track spreads over a larger and larger region. At some critical altitude the figure of the orbit becomes so large as to be not visible form one point on Earth at all times. This section determines the critical perigee radius above which synchronous orbits are always visible.

The codes that generate the sky tracks used in this section are described in appendices D and E. The first code is a Keplerian propagator used to produce a position history for an orbit. The second code produces the sky tracks and requires as input the position history plus the longitude and latitude of a view point at the beginning of the position history.

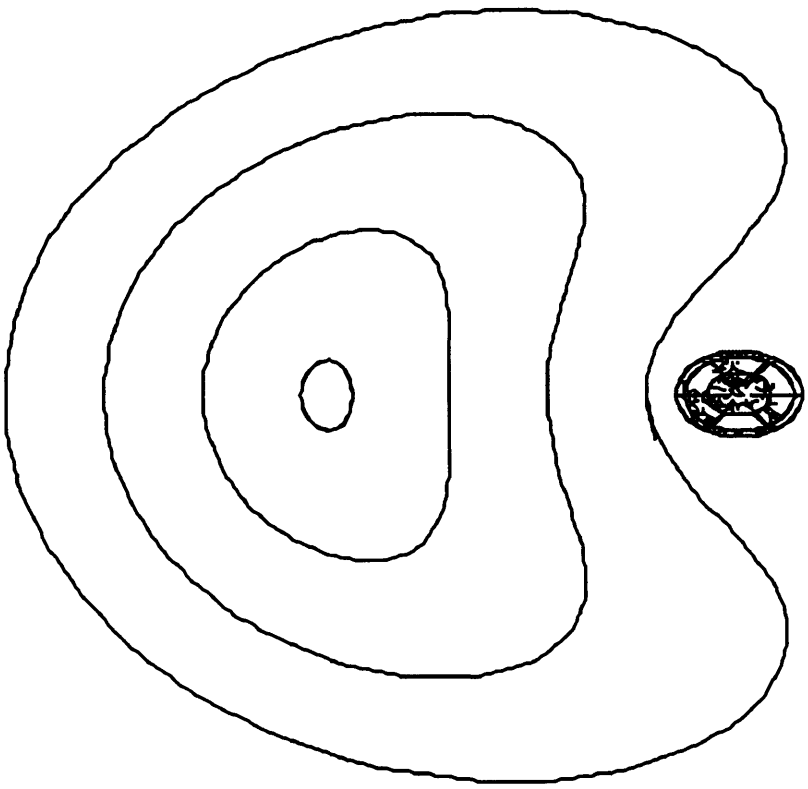

Fig. 4-26 Space tracks 10,000 km, 20,000 km, 30,000 km, and 40,000 km perigee radius synchronous orbits.

First, it is necessary to model the synchronous trigger orbit. The inclination, i, is taken to be 7°. To simplify the problem it is assumed that the orbit has a longitude of the ascending node, Ω, of zero with respect to an arbitrary coordinate system. The argument of perigee is taken to be the 189.5° of the Ariane 5 GTO plus or minus $\Delta\omega$, as computed in the last section, depending upon the type of injection. The trigger orbit is them propagated from perigee through one full day.

Next, it is necessary to chose a viewing point. The latitude is assumed to be that of Haystack, 42.5°. For the purpose of this work the optimum longitude is the one that produces the highest minimum elevation possible. It is first assumed that the longitude of the view point at the beginning of the orbit propagation is equal to the argument of perigee of the orbit being propagated. In the case of a zero inclination orbit this assumption produces the optimum view point. For non-zero inclinations this assumption approximates the optimum location. From the view point produced by the first assumption the sky track appears skewed as shown in Figure 4-27. The optimum view point for non-zero inclination orbits is a small difference in longitude, *Δlong*, from the first assumed view point. This *Δlong* can be found by varying the initial longitude until a highest minimum elevation is found. This new view point produces the sky track shown in Figure 4-28. The *Δlong* for type I and II orbits is shown in Figure 4-29. The highest

minimum elevation for type I and II orbits is shown in Figure 4-30. The maximum change in the line of apsides from the optimal position that is tolerable while still staying continuously above the horizon is shown in Figure 4-31. This will be used in the next chapter for determining insertion windows to the final trigger orbit. Finally, the sky tracks for type I and II orbits with perigees from 10,000 km to 42,000 km every 2,000 km are shown in Figure 4-32 and 4-33. Above a 15,000 km radius perigee the type I orbit will always be visible and above a 16,000 km radius perigee the type II orbit will always be visible.

Several properties of the synchronous orbit sky tracks should be noted before continuing. The tick marks in Figure 4-28 denote one hour increments from perigee passage. At the lowest corners of sky track the hour ticks are closely spaced and the satellite has a lowest apparent velocity. The trigger satellites spend 6 hours in the bottom 5° of elevation of the sky track. Considerable observation time will be lost if both the lower tips are cut off by having too low of a perigee radius or one tip is cut off by not having the orbit properly centered over the view point resulting in a skewed sky track like shown Figure 4-25. A margin of 5° to 10° must be kept between the horizon and the minimum elevation of the sky track in order to account for obstructions such as buildings and trees, and the East-West drift between corrections.

This section has assumed an ideally located view point. To center an orbit over a given view point requires inserting into a synchronous orbit with the correct phasing. The windows for inserting into synchronous orbits with the correct phasing are described in detail in the next chapter.

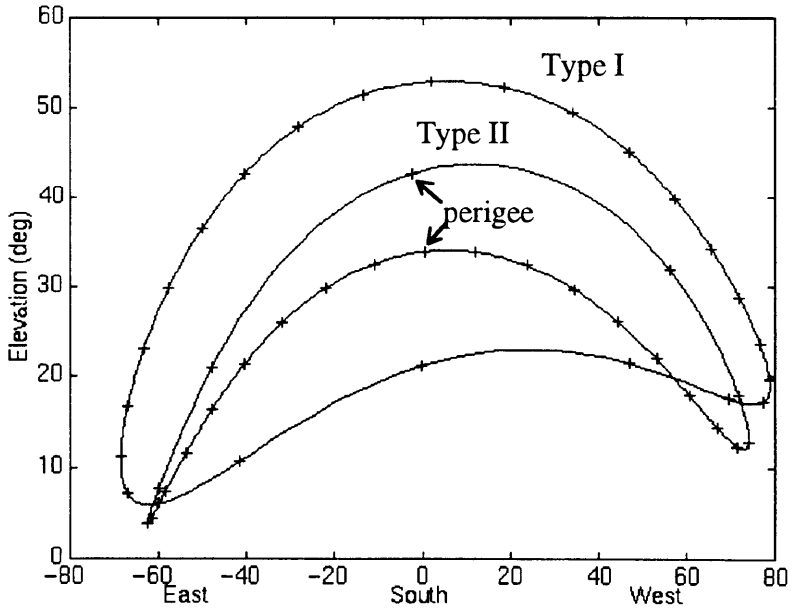

Fig. 4-27 Un-optimized 20,000 km perigee type I and II.

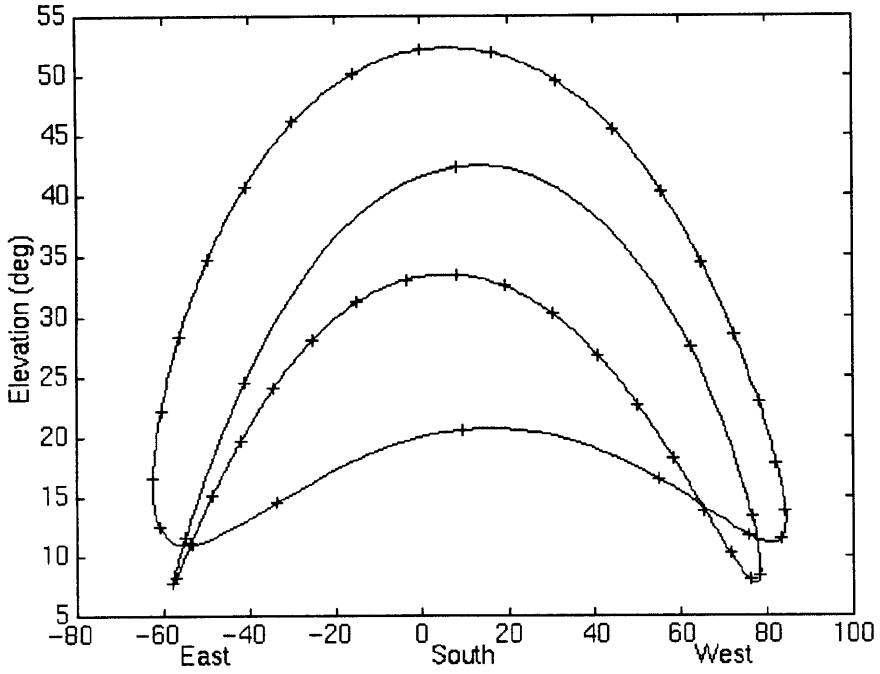

Fig. 4-28 Optimized 20,000 km perigee type I and II.

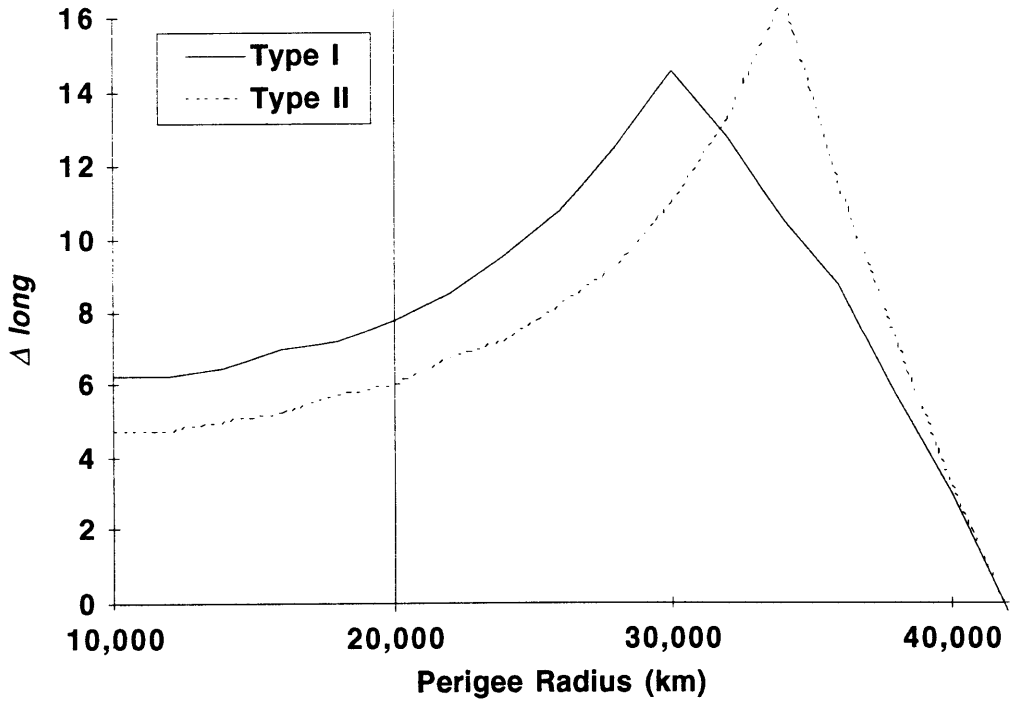

Fig. 4-29 *Δlong* for type I and II orbits.

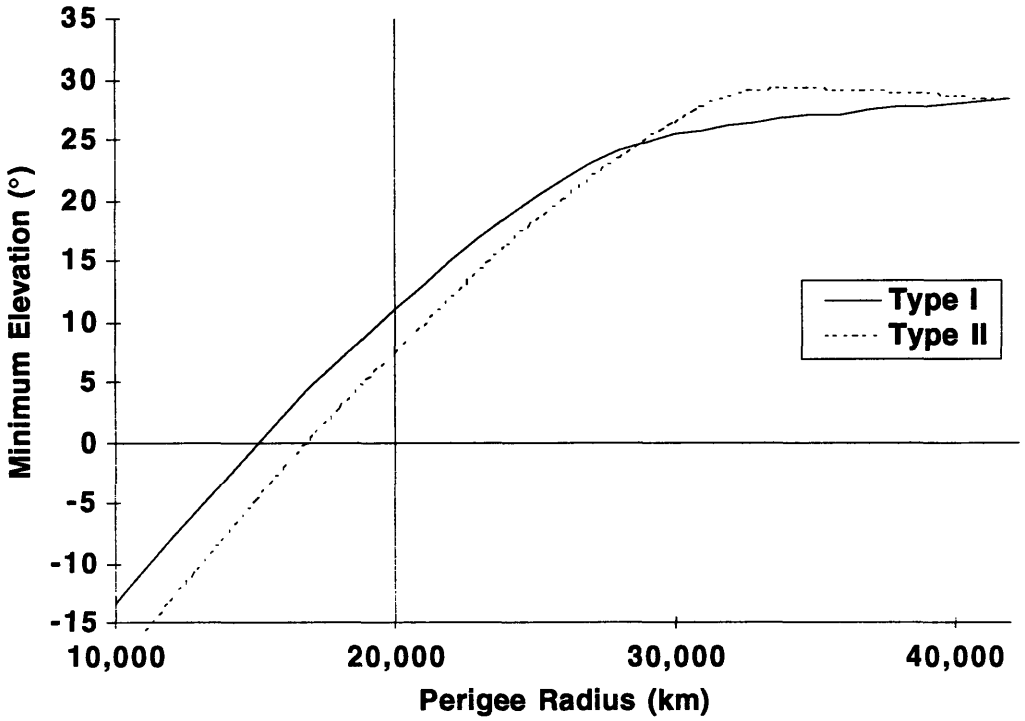

Fig. 4-30 Minimum elevation for type I and II orbits.

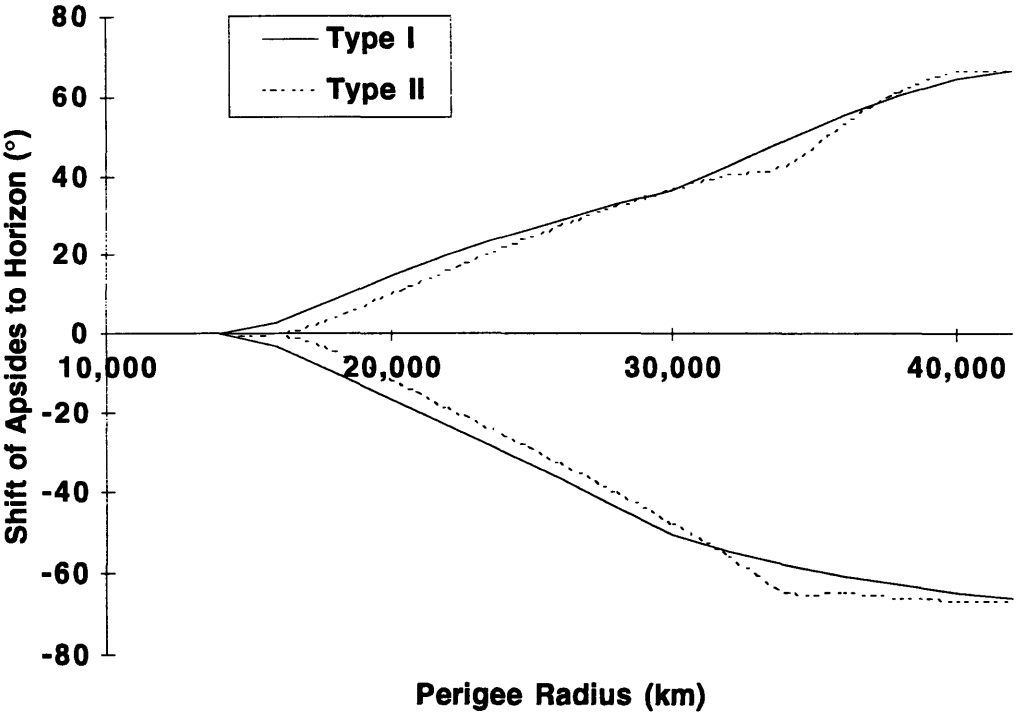

Fig. 4-31 The maximum change in the line of apsides from the optimal position to stay continuously above the horizon.

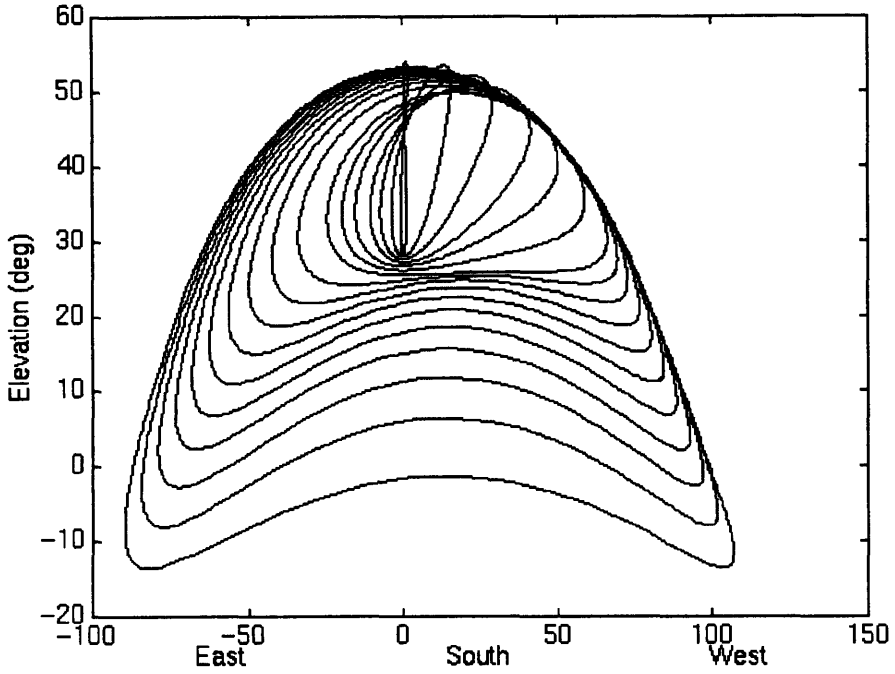

Fig. 4-32 Type I synchronous orbits with perigees from 10,000 km to 42,000 km every 2000 km.

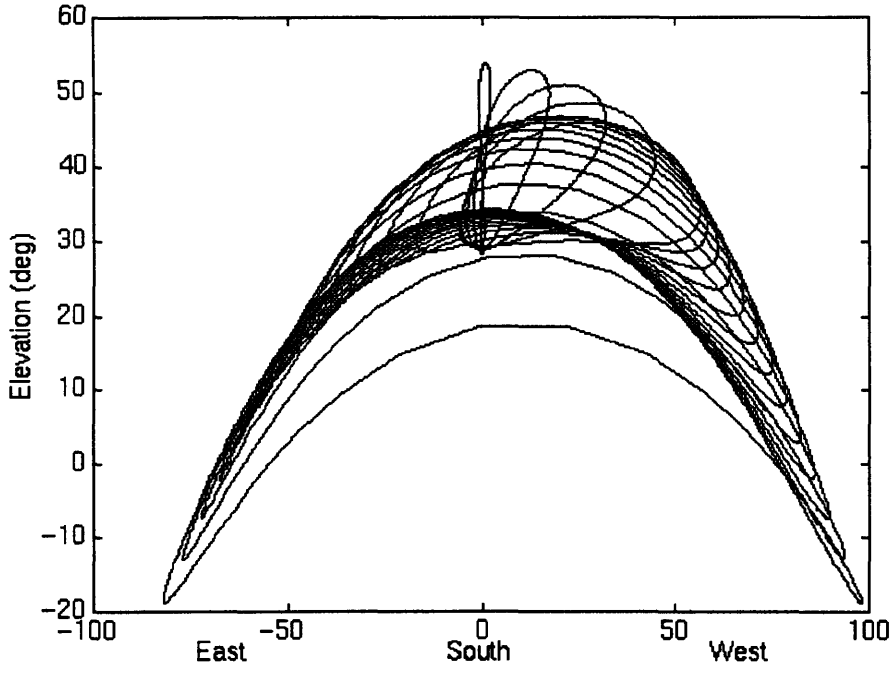

Fig. 4-33 Type II synchronous orbits with perigees from 10,000 km to 42,000 km every 2000 km.

4.6 Conclusion

The a 20,000 km × 64,330 km synchronous orbit was chosen as the trigger orbit for the following reasons:

- **Compatibility** -The single impulse 1247 m/s insertion is compatible with the secondary payload solid propulsion option.
- **Radiation** - The 20,000 km perigee is the minimum perigee radius acceptable to the science team.
- **Range** - The trigger satellites always have a range less than 0.214 light seconds.
- **Availability** - Each trigger satellite is continuously available and at least 7.6° above the horizon at all times.
- **Ground Stations** - Only one pair of ground stations at Haystack is necessary for continuous availability.
- **Reliability** - Continuous availability is not compromised even in the event of a launch failure provided that the two trigger satellites are distributed between two launches.

These reasons differ considerably from the reasons listed in section 4.2 for the selection of the original DRO trigger obit as a result of the continuous evolution in the trigger orbit requirements. While evolving requirements are not ideal, and can be frustrating to the engineering staff, they are a real part of most programs. If the evolution is managed it can result in a better design by producing the most achievable and relevant requirements possible. This flexibility can ultimately lead to lower costs and better data.

The next chapter discusses the operational and environmental details of the synchronous orbit selected in this chapter.

Chapter 5 Detailed Trigger Satellite Orbits

The purpose of this chapter is to develop the details of the trigger satellite orbits. This flows down from the trigger satellite deployment architecture determined in the last chapter and the requirements outlined in section 5.1 of this chapter. The insertion windows for centering the final orbit over Haystack are discussed in detail in section 5.2. Next, the selection of the insertion types to tailor the angle between the lines of apsides is described in section 5.3. The evolution of the trigger orbits over time and the corrections necessary to maintain continuous availability are discussed in section 5.4. Finally, the eclipsing environment of the trigger orbits is discussed in section 5.5.

5.1 Requirements and Basic Properties

The previous chapter, which described the selection of the trigger satellite deployment architecture, was a lesson in the evolution of requirements over the preliminary design process. However, once the synchronous orbit was selected the requirements solidified. The following requirements and constraints were used in the preparation of the detailed design:

- **Compatibility** - The trigger satellite shall be compatible with the helio satellites propulsion system, a Star 13A solid rocket motor.

- **Radiation** - The trigger orbit shall have a 20,000 km perigee to be acceptable to the science team in terms of data degradation and added cost for radiation hardening. A secondary requirement developed to have one trigger satellite out of the trapped radiation belts at all times in order to improve the data quality.

- **Eclipsing** - Since the trigger satellites are unable to transmit during eclipses, a secondary requirement developed to have only one trigger satellite eclipsing at a time.

- **Range** - The trigger satellites shall always have a range less than 1 light second.

- **Availability** - Each trigger satellite will be continuously available and at least 5° above the horizon at all times from Haystack.

- **Distributed Launches** - The trigger satellites will be divided into two launches in order to increases the probability of mission success.

- **GTO** - The GTO for Ariane 5 is 6,978 km × 42,165 km and the ASAP payload mass is 100 kg [7].

The basic properties of the trigger orbit that resulted from these requirements are listed in Table 5-1. The detailed properties of the trigger orbit are described in the following sections.

Table 5-1 Basic Trigger Orbit Properties

Characteristic	Value
Orbit	20,000 km × 64,335.78 km
a	42,167.89
e	0.5256
i	7.0°
Ω	Ω_{GTO} as generated in appendix C.1
ω	179.5°+$\Delta\omega$
Period (including J_2 correction of 11.4 sec)	24 hours 56 minutes 15.5 sec
Maximum Range	0.214 light seconds
Minimum Elevation	~5°
Pre and Post Insertion True Anomaly, f_{pre} and f_{post}	Type I 164.71° and 113.75°, Type II 195.29° and 246.25°
Change in Argument of Perigee, $\Delta\omega$	Type I +50.96°, Type II -50.96°
$\Delta long$	Type I 7.75°, Type II 6.0°
Continuous Visibility Tolerance in Longitude	Type I +14.75° to -15.50°, Type II 10.50° to -11.50°
Insertion ΔV	1247 m/s

5.2 Insertion Windows

The insertion window is the number of holding orbits in GTO that are necessary to insert the trigger satellite into an orbit that appears centered over (has the highest possible minimum elevation) a given point on the surface of the Earth. This section determines the windows for inserting into a trigger orbit that is centered over Haystack.

To understand what trigger insertion windows are it is useful to first consider how to insert into a geostationary orbit over a given point. All geostationary satellites trace out the same orbit over the course of a sidereal day. Different geostationary satellites are centered over different points on the

Earth because they are differently phased within the same orbit. The majority of this phasing is accomplished by holding in GTO for the correct insertion window. While holding in GTO a satellite passes through the insertion point to geostationary orbit, apogee of GTO, once every 10.647 hours. During this period the Earth rotates 160.1° so that at each successive apogee the satellite has an opportunity to insert into an obit over a point 160.1° west of the point reachable from the last apogee. By waiting long enough in GTO a phasing within a few degrees of the desired longitude can be achieved. Post insertion rephasing can then be used to refine the position. The idea of the insertion windows applies equally to synchronous orbits. All trigger satellites launched on the same date with the same insertion type will occupy approximately the same inertial orbit but will not necessarily have the same phasing depending on the number of holding orbits in GTO. Inserting at the first possible opportunity will not result in a sky track centered over Haystack. It is necessary to wait for specific insertion windows in order to center the trigger orbits over Haystack.

To determine the trigger orbit insertion windows, first consider locations that a type I and II orbit appear centered over if inserted at the first opportunity (just before or after the first apogee depending upon the type). As described in section 5.5.2, a synchronous orbit appears centered over a longitude *Δlong* away from the longitude directly below the perigee of the synchronous orbit. To find the longitude of the point directly below the perigee it is necessary to consider the geometry of the first perigee passage in the trigger orbit and the time of flight between the first perigee passage in GTO and the first perigee passage in the trigger orbit. The first perigee passage in GTO occurs at 15° W. In an inertial coordinate system the first perigee passage in the trigger orbit occurs at $\pm\Delta\omega$, equal to 50.96° as given in Figure 4-25, away from the first perigee passage in GTO as shown in Figure 5-1 and 5-2. Without the rotation of the Earth during the time of flight between the GTO perigee passage and the trigger orbit perigee passage, the first trigger orbit perigee in the would occur at 35.96° E for type I and 65.96° W for type II.

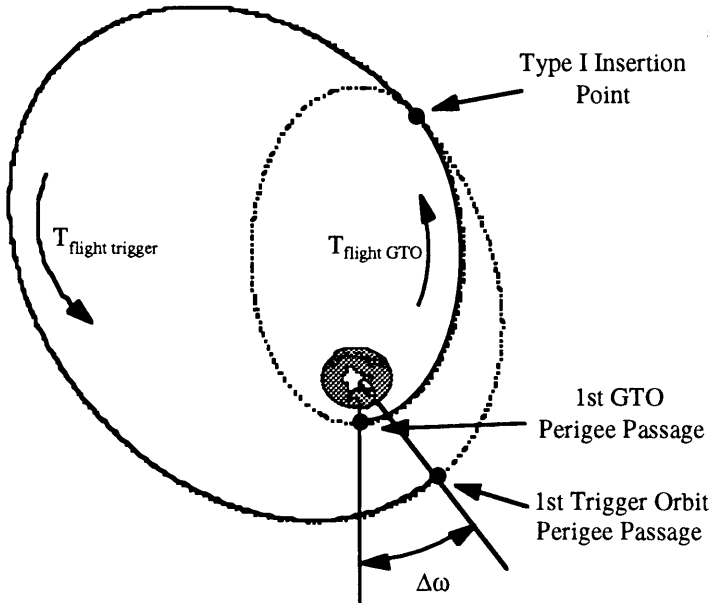

Fig. 5-1 1st GTO perigee passage to 1st type I trigger orbit perigee passage.

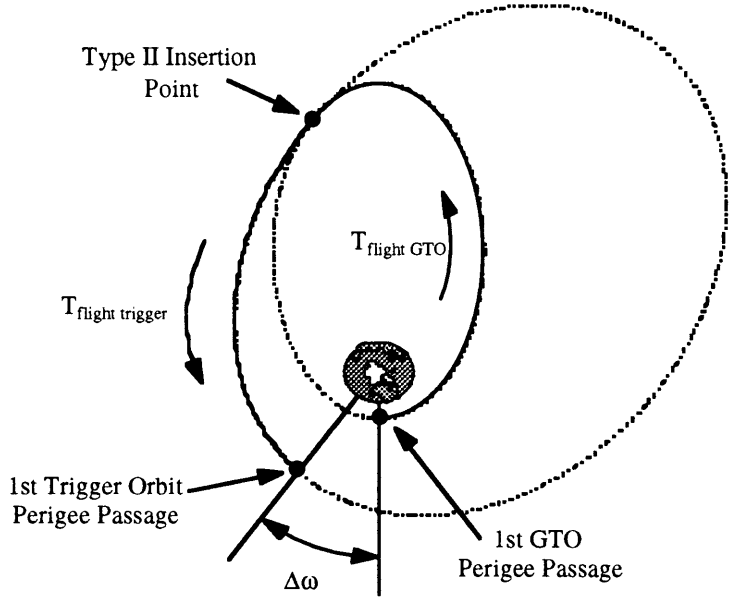

Fig. 5-2 1st GTO perigee passage to 1st type II trigger orbit perigee passage.

To account from the rotation of the Earth between the GTO perigee passage and the trigger orbit perigee passage it is necessary to compute the time of flight between the perigee passages, $T_{flight\ perigee\ to\ perigee}$. This can be done using the pre and post insertion true anomalies, f_{pre} and f_{post}, as given in Figure 4-24. First, the pre and post insertion eccentric anomalies, E_{pre} and E_{post}, are given by:

$$E = \cos^{-1}\left(\frac{e + \cos f}{1 + e\cos f}\right) \tag{5-1}$$

Where e is the eccentricity of the orbit equal to 0.7160 for GTO and 0.5256 for the 20,000 km perigee trigger orbit. The time of flight between perigee passages is equal to the time of flight from GTO perigee to the insertion point, $T_{flight\ GTO\ perigee\ to\ insertion}$, plus the time of flight from the insertion point to the trigger orbit perigee, $T_{flight\ insertion\ to\ trigger\ perigee}$, given by:

$$T_{flight\ perigee\ to\ perigee} = T_{flight\ GTO\ perigee\ to\ insertion} + T_{flight\ insertion\ to\ trigger\ perigee} \tag{5-2}$$

The time of flight from the insertion point to the trigger perigee is equal to the period of the trigger orbit, $P_{trigger}$, minus the time of flight from the trigger perigee to the insertion point, $T_{flight\ trigger\ perigee\ to\ insertion}$, so that equation 5-2 becomes:

$$T_{flight\ perigee\ to\ perigee} = T_{flight\ GTO\ perigee\ to\ insertion} + (P_{trigger} - T_{flight\ trigger\ perigee\ to\ insertion}) \tag{5-3}$$

Inserting Kepler's equation and the equation for the period of an orbit into equation 5-3 yields:

$$\begin{aligned} T_{flight\ perigee\ to\ perigee} = & \sqrt{\frac{a_{GTO}^2}{\mu}}(E_{pre} - e_{GTO}\sin E_{pre}) \\ & + \sqrt{\frac{a_{trigger}^2}{\mu}}(2\pi - E_{post} + e_{trigger}\sin E_{post}) \end{aligned} \tag{5-4}$$

Where a is the semi-major axis equal to 24,571 km for GTO and 42,165 km for the trigger orbit. The time of flight between perigee passages for type I and II synchronous orbits is shown in Figure 5-3 and 5-4. The time of flight is 24.0463 hours for type I trigger orbits and 10.5355 hours for type II trigger orbits so that the Earth rotates 361.68° by the time the type I trigger orbit perigee passage and 158.47° for the type II trigger orbit perigee passage.

Finally, the position over which the type I and II trigger orbits injected at the first opportunity will be centered is given by:

$$long = -15° \pm \Delta\omega - \theta + \Delta long \tag{5-5}$$

Where *long* is the east longitude of the centered point, $\Delta\omega$ is the change in argument of perigee equal to 50.96° as given by Figure 4-25 (positive for type I orbits and negative for type II orbits), θ is the rotation of the Earth as given above, and *Δlong* is the difference in longitude between the point directly below perigee and the point that the orbit appears centered over equal to 7.75° for type I orbits and 6° for type II orbits as given by 4-29. The centered point is 42.3° E for a type I orbit and 142.0° E for a type II orbit injected at the first opportunity.

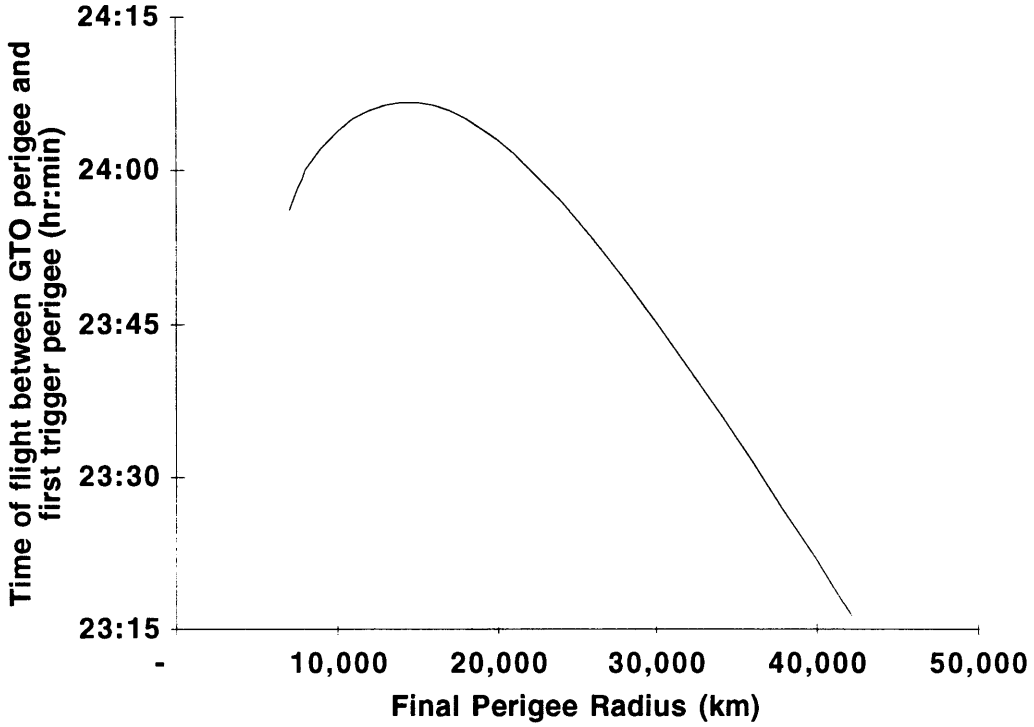

Fig. 5-3 Type I synchronous orbit time of flight between GTO perigee and the trigger orbit perigee.

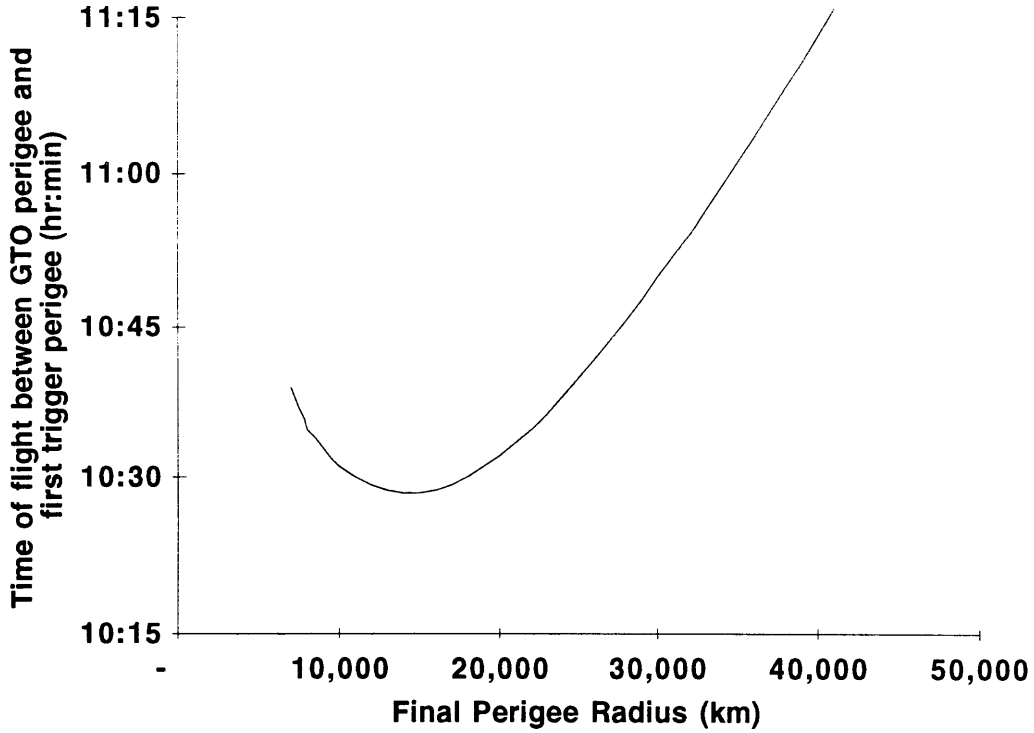

Fig. 5-4 Type II synchronous orbit time of flight between GTO perigee and the trigger orbit perigee.

After computing the centered point that results from inserting at the first possible opportunity the centered points produced by each following opportunity can be computed. Just as for geostationary orbits, for every successive holding orbit in GTO the first trigger satellite perigee passage occurs 10.647 hours latter and the Earth revolves another 160.1° so that for every successive holding orbit the centered point moves 160.1° westward. For type I the progression of centered points is 38.3° E, 238.2° E, 78.1° E, 278.0° E, etc.. For type II the progression of centered points is 139.5° E, 339.4° E, 179.3° E, 19.2° E, etc..

From the progression of centered points the insertion windows to appear centered above Haystack (285° E) can be found. Since the progression will never produce an orbit exactly centered over Haystack it is necessary to specify a tolerance around the longitude of Haystack. Figure 4-29 shows the maximum side to side deviation in the longitude of the centered point to remain continuously visible from a given point. The maximum allowable deviation is 14.75° for type I orbits and 10.50° for type II orbits. Using these tolerances the orbit will always start with continuous visibility but may not be centered over Haystack. The first five windows for type I and II are shown in table 5-2 along with their deviations from the ideal centered point. The data in table 5-1 includes the effect of the precession the trigger orbit caused by the J_2 perturbation which is described fully in section 5.4.1.1.

Table 5-2 Trigger orbit insertion windows.

Type I		Type II	
Holding Orbits	Deviation (°)	Holding Orbits	Deviation (°)
3	-3.8	26	7.2
12	-7.2	35	3.8
21	-10.6	44	0.4
30	-14.0	53	-3.0
68	11.6	62	-6.5

The initial deviation from the ideal centered orbit can be tolerated because trigger orbit will never be exactly centered over Haystack. The J_{22} perturbation, described fully in section 5.4.3, will cause drift east and west between corrections within east and west tolerances. If the initial deviation of the trigger orbit falls within the tolerance of the J_{22} correction cycle the first correction will be smaller than the normal. If the initial deviation of the trigger orbit falls outside of the positive (western) tolerance of the J_{22} correction cycle the first correction will need to be made immediately and will be up to 0.07 m/s larger than the normal J_{22} correction. If the initial deviation of the trigger orbit falls

outside of the negative (eastern) tolerance of the J_{22} correction cycle the first correction will not need to be made immediately but will still be up to 0.07 m/s larger than the normal J_{22} correction.

5.3 Line of Apsides

This section describes how widely separating the lines of apsides can be used to satisfy several secondary requirements concerning the radiation and eclipsing environment. By selecting the types of insertion it is possible to exert some control over the angle between the lines of apsides of the trigger orbits.

Several secondary requirements concerning the radiation and eclipsing environment were placed on the trigger satellite orbits in the time between the preliminary design work and the detailed work described in this chapter. First, it is desirable to have one trigger satellite outside of the radiation belts (near apogee) at all times in order to improve the quality of the data. Second, it is desirable to have only one trigger satellite eclipse at a given time. The trigger satellite can not transmit during eclipses because of power limitations so to maintain continuous burst warnings during the eclipse seasons only one trigger can eclipse at a given time. The secondary nature of these requirements means that they should only be meet if they do not drive the design.

Both of these secondary requirements can be meet by widely separating the lines of apsides. Consider two trigger orbits with lines of apsides 180° apart as shown in Figure 5-5. To remain continuously visible from the same ground station they must have phasing 180° apart so that one is at perigee while the other is at apogee. This means that when one is closest to Earth and in the worst radiation environment the other is farthest from Earth and in the best possible radiation environment. Further, the separation in line of apsides makes the probability of both eclipsing at the same time very low since the are both widely separated in distance and unlikely to enter the shadow of Earth at the same time. Unfortunately, no quantitiative analysis of this effect has been done.

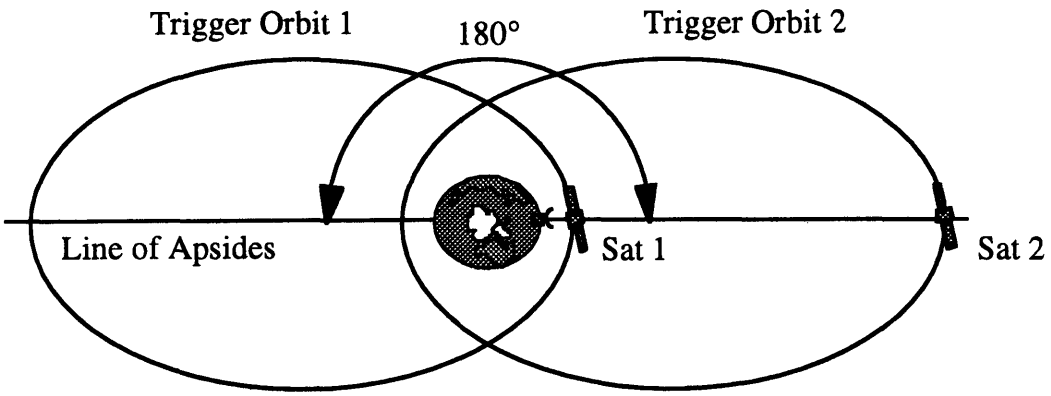

Fig. 5-5 Two trigger orbits with lines of apsides separated by 180°.

The angle between the line of apsides is determined by two sources: the insertion types, which are controllable, and the duration between trigger satellite launches which, while not controllable, is predictable within a range. To understand the effect of insertion type consider two trigger satellites launched at the same time. If both are inserted with the same type they will have the same line of apsides. However, if one is injected type I and the other type II the angle between the lines of apsides will be $2\Delta\omega$, as shown in Figure 5-6, where $\Delta\omega$ is the change in the argument of perigee as given in Figure 5-23. The choice of insertion type allows some degree of control to be exerted over the angle between the line of apsides. To understand the effect of the duration between trigger satellite launches consider two orbits of the same type with the same initial orientation relative to the Earth-Sun line but launched on different dates as shown in Figure 5-7. Once the first trigger satellite is inserted the first orbit will maintain its orientation in an inertial frame (with the exception of the slow drift caused by the perturbations discussed in section 6.4). When the second trigger satellite is inserted, the Earth-Sun line will have changed relative to an inertial frame, resulting in a difference in Longitude of the ascending node, $\Delta\Omega$, between the trigger orbits equal to the angle that the Earth traveled around the Sun between launches. While the ETA team does not control the duration between launches, the nominal duration between launches will be determined by how ETA is manifested by Arianespace which should be known well in advance. This can be used to plan insertion types. Short delays caused by weather and minor technical problems will have little effect on the insertion type planning. Launch failures and other catastrophic failures may cause long delays but are rare.

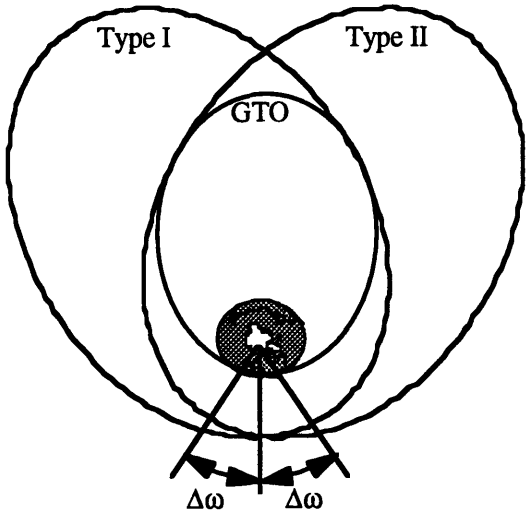

Fig. 5-6 Change in argument of perigee due to insertion type.

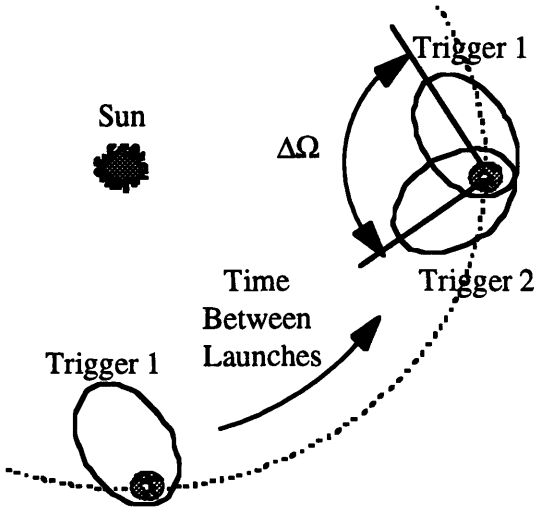

Fig. 5-7 Change in longitude of the ascending node due to difference in launch date.

The angle between the lines of apsides can be approximated by $\Delta apsides = \Delta\omega + \Delta\Omega$, where $\Delta apsides$ is the angle between the lines of apsides, $\Delta\omega$ is the change in argument of perigee caused by the insertion type given in Figure 5-23, and $\Delta\Omega$ is the change of the longitude of the ascending node caused by the duration between launches. This approximation is reasonable when the inclination of the trigger orbits to the ecliptic plane, as opposed to the equatorial plane, is small. The inclination to the ecliptic plane of the trigger orbits will vary between 16° to 30° depending on the time of year of launch, which is high enough to strain the validity of the approximation. While not useful for exact data, this approximation is useful for demonstrating what is possible by choosing the insertion types and planning on a nominal duration between launches as is shown in Figure 5-8.

Consider a nominal duration between launches of 60 days, the expected duration between Ariane 5 launches. If the first trigger is inserted type II, the second can be inserted type I and guarantee an angle between the lines of apsides of 100° for delays of up to 60 days. If the second launch is delayed for between 60 and 200 days the second trigger satellite can be injected type II and maintain an angle between the lines of apsides of at least 100°. For durations between launch dates know to within ±120 days the angle between the lines of apsides can always be kept at be more than 100° therefore meeting the secondary requirements.

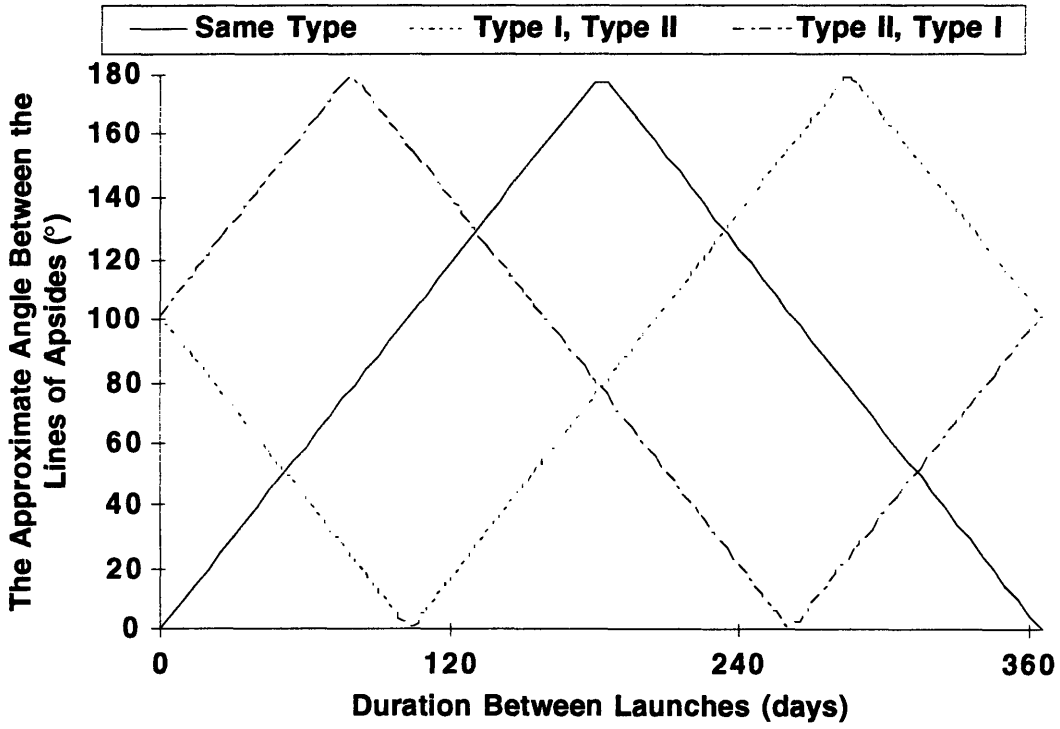

Fig. 5-8 Angle between the lines of apsides as a function of insertion type and duration between launches.

5.4 Orbit Evolution

In a perfectly Keplerian world, with point mass objects and no third body effects, a synchronous orbit that is continuously visible from a given point will remain continuously visible indefinitely. Unfortunately, the oblateness and elipticity of the Earth along with perturbations of the Sun and Moon will change the orbital elements of the synchronous orbit over time causing, if unchecked, the sky track of the orbit to drift and lose its continuous visibility from a given point. This section describes the sources of perturbation and how they can be counteracted by adjusting the final trigger orbit as described in section 5.4.1, correcting for insertion errors as described in section 5.4.2, and

making periodic corrections to the final orbit as described in section 5.4.3. Finally, the long term evolution of the sky track is described in section 5.4.4.

5.4.1 Adjustments to the Final Trigger Orbit

The oblateness of the Earth and the perturbations of the Sun and the Moon cause precession of the mean anomaly, M, the longitude of the ascending node, Ω, and the argument of perigee, ω, that can be corrected for by inserting into a final trigger orbit with a period a few seconds different from a true synchronous orbit. These perturbations and how they can be corrected by adjusting the period are described in the following subsections.

5.4.1.1 Oblateness of Earth

The oblateness of the Earth, an increase in the radius of the earth at the equator as shown in Figure 5-9, and also known as the J_2 harmonic, is the largest perturbation on the trigger satellites. The additional mass distributed around the equator causes orbits to precesses gyroscopically resulting in changes in ω, Ω, and M are given by [22]:

$$\dot{\Omega} = -1.5n(0.00108263)\left(\frac{r_{Earth}}{a}\right)^2 \frac{\cos i}{\left(1-e^2\right)^2}$$

$$\dot{\omega} = 0.75n(0.00108263)\left(\frac{r_{Earth}}{a}\right)^2 \frac{\left(4-5\sin^2 i\right)}{\left(1-e^2\right)^2} \qquad (5\text{-}6)$$

$$\dot{M} = n + \frac{-1.5n(0.00108263)}{\left(1-e^2\right)^2}\left(\frac{r_{Earth}}{a}\right)^2 \left(1-0.75\sin^2 i\right)$$

Where $\dot{\omega}$, $\dot{\Omega}$, and $\dot{M}$ are the rates of change in degrees per day, n = $\sqrt{\mu / a^3}$ is the mean motion of the orbit in degrees per day, i is the inclination of the orbit, e is the eccentricity of the orbit, a is the semi-major axis of the orbit, and r_{Earth} is the radius of the Earth.

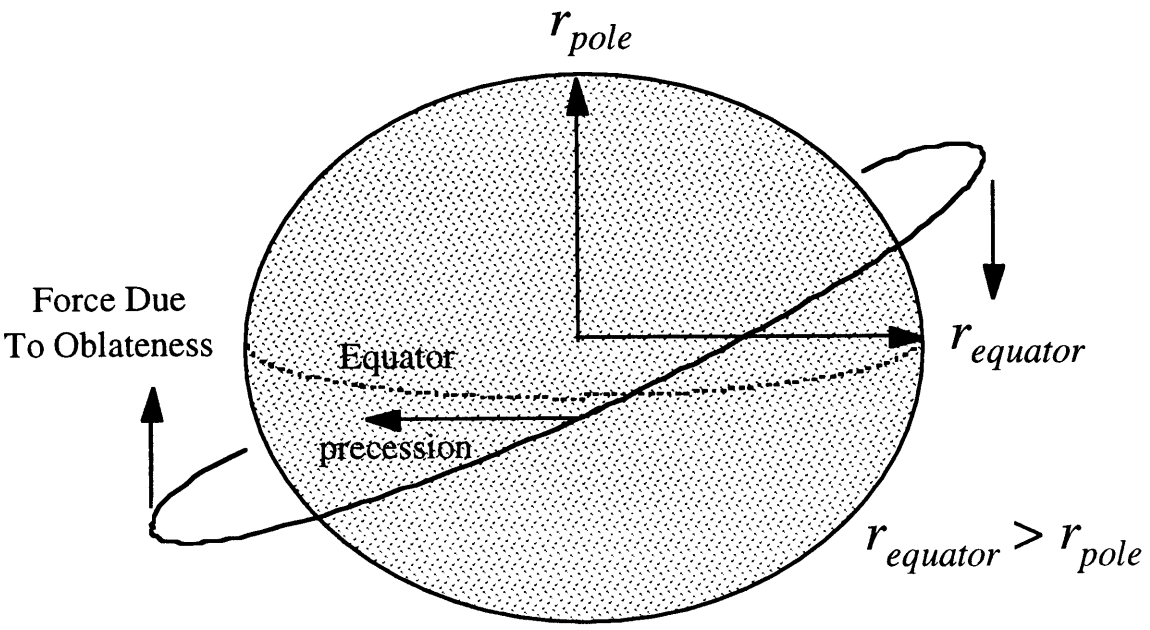

Fig. 5-9 The oblateness of the Earth.

5.4.1.2 Sun and Moon

The Sun and Moon also cause perturbations similar to, but much smaller than, those caused by the oblateness of the Earth. These perturbation are given by [23]:

$$\begin{aligned}
\dot{\Omega}_{Sun} &= -0.5544\frac{\cos i}{n} \\
\dot{\Omega}_{Moon} &= -1.2168\frac{\cos i}{n} \\
\dot{\omega}_{Sun} &= 0.2772\frac{\left(4-5\sin^2 i\right)}{n} \\
\dot{\omega}_{Moon} &= 0.6084\frac{\left(4-5\sin^2 i\right)}{n}
\end{aligned} \tag{5-7}$$

Where $\dot{\Omega}$, $\dot{\omega}$,and n are in degrees per day. In most cases the influence of the Sun and Moon on synchronous orbits is so small that it can be ignored, but is included here for completeness.

5.4.1.3 Period Correction

The perturbations of Ω, and ω cause a rotation of the line of apsides and the perturbation of M causes a re-phasing within the orbit. Since the orbit is low inclination the effects of Ω, ω, and M can be added together. The westward drift of the line of apsides and rephasing of M can be canceled out by rephasing the orbit to counteract the perturbations as is shown in Figure 5-10. Because the

perturbations are approximately time-constant, the rephasing can be made continuously by adjusting the initial period. The adjusted period, $P_{adjusted}$, and the new semi-major axis, $a_{adjusted}$, are given in terms of the sum of the perturbations $\dot{\omega}$, $\dot{\Omega}$, and $\dot{M}$ for each source by:

$$P_{adjusted} = \left(\frac{360 + \sum(\dot{M}_i + \dot{\Omega}_i + \dot{\omega}_i)}{360} \right) P_{Earth}$$

$$a_{adjusted} = \left(\frac{P_{adjusted}\sqrt{\mu}}{2\pi} \right)^{\frac{2}{3}} \tag{5-8}$$

Where P_{Earth} is the sidereal period of Earth (23 hrs 56 min 4.091 sec) and μ is the gravitational parameter. To sum the perturbations, as shown in Figure 5-11, it is assumed that the orbit lies in the equatorial plane which is a reasonable approximation for the 7° inclination trigger orbit. The required change in period and semi-major axis for the family of synchronous orbits reachable from GTO is shown in Figure 5-12. For the trigger orbit the required change in period is +11.4 sec and the change in semi-major axis is +3.73 km. The resulting change in insertion cost is ~+0.13 m/s. This sensitivity to insertion cost and semi-major axis points out the importance of insertion errors which will be dealt with in the next section.

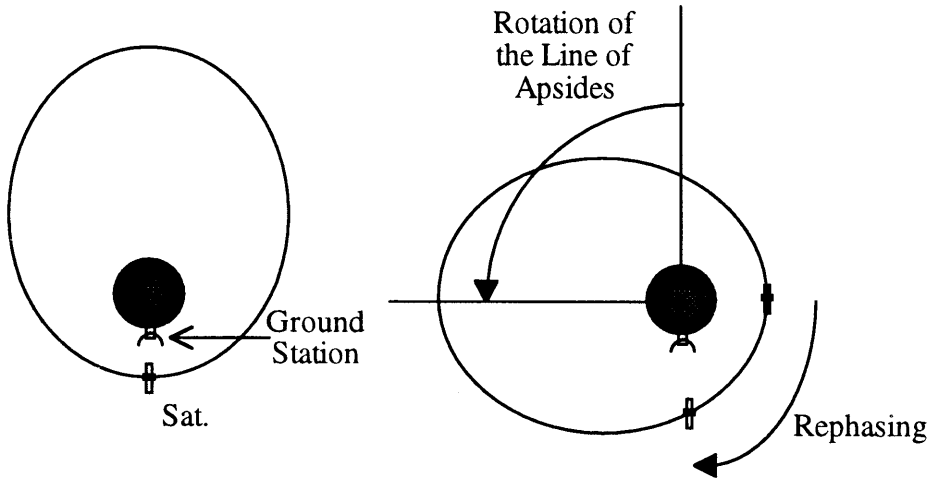

Fig. 5-10 The need for rephasing.

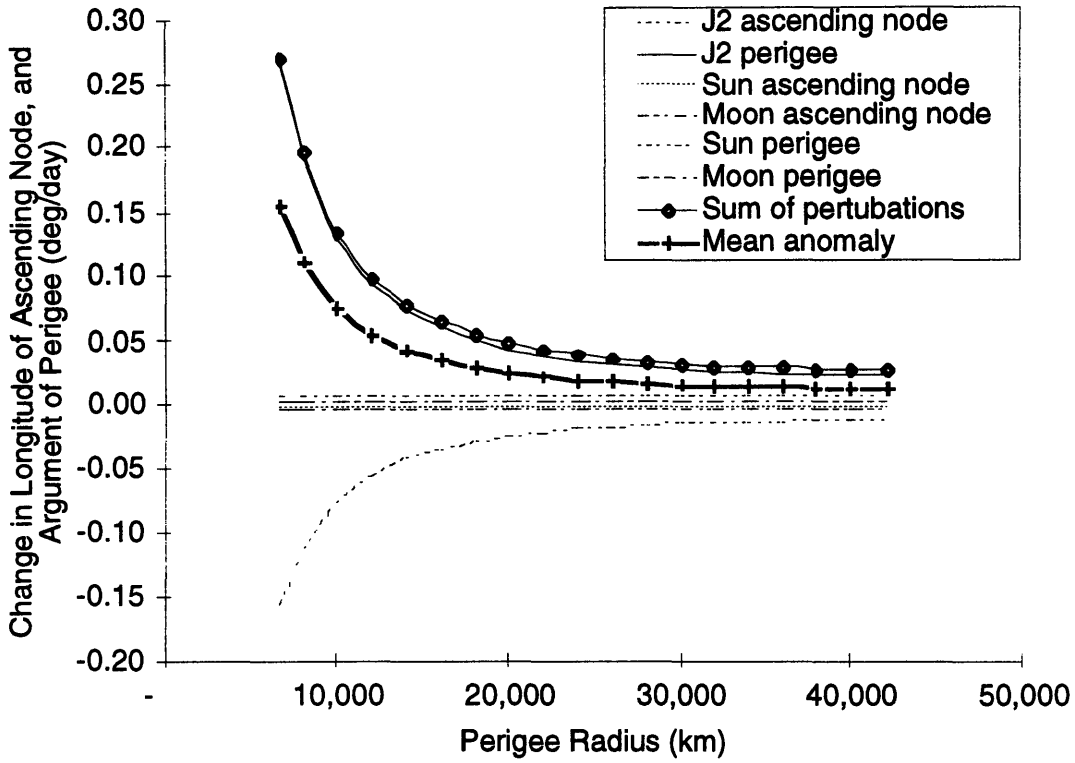

Fig. 5-11 Perturbation on longitude of ascending node, argument of perigee, and mean anomaly vs. perigee radius for synchronous orbits.

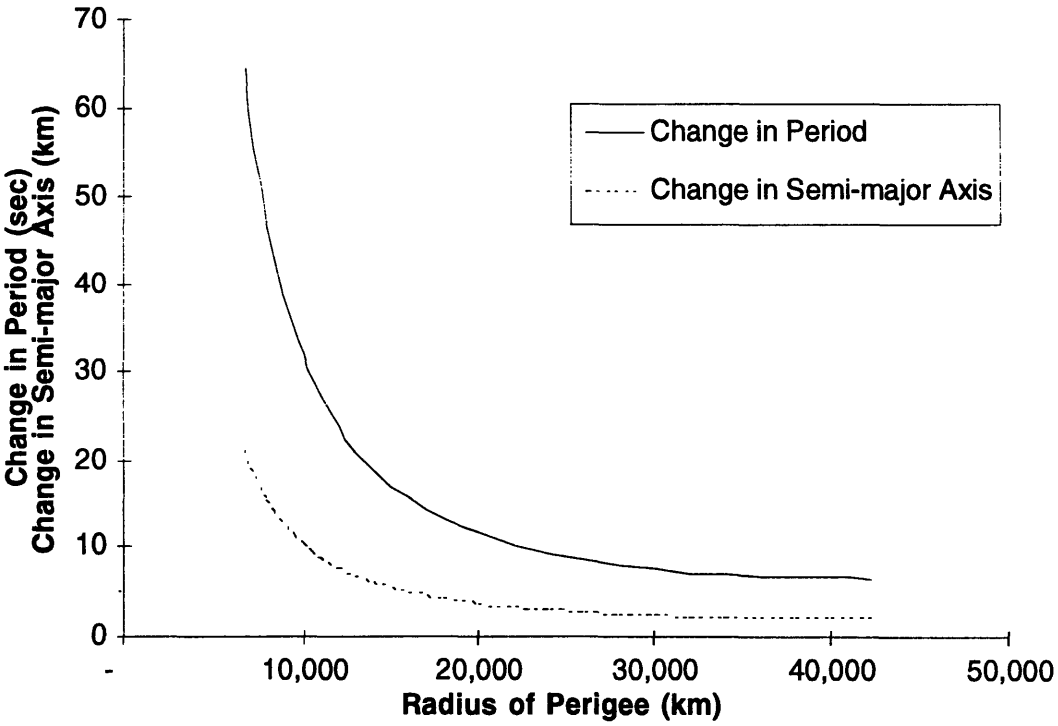

Fig. 5-12 Period and semi-major axis correction for perturbation vs. perigee radius for synchronous orbits.

5.4.2 Insertion Errors

Insertion errors due to errors in the total impulse provided by the solid rocket motor and in the pointing due to the guidance system result in errors in the semi-major axis and period of the trigger orbit. Variability in grain load, chemistry, and temperature results in a ±0.5% error in total impulse from the Star 13A which leads to an error in insertion ΔV of ~6.24 m/s. Inaccuracies in the guidance system and imbalance during the spin up result in an error in the pointing of the trigger satellites during the insertion burn. The loss in insertion ΔV is proportional to 1-cosϕ, where ϕ is the off pointing angle. The expected pointing error of 2° leads to an insertion ΔV error of ~0.76 m/s. The total ΔV error of ~7.00 m/s can be removed by making a correction at perigee using the cold gas system. Since the velocity of the trigger satellite is much higher at perigee than at the insertion point the correction can be made for less than the 7.00 m/s. The ratio of the error ΔV, ΔV_{error}, to the correction ΔV, $\Delta V_{correction}$, is approximated by the ratio of velocity in the synchronous orbit after insertion to the velocity at perigee so that $\Delta V_{correction}$ is given by:

$$\Delta V_{correction} \approx \Delta V_{error} \sqrt{\frac{\varepsilon_{Sync} + \frac{\mu}{r_{burn}}}{\varepsilon_{Sync} + \frac{\mu}{r_{Sync\ Peri}}}} \tag{5-9}$$

Where ε_{Sync} is the specific mechanical energy of a synchronous orbit (-4.72667 km^2/sec^2), $r_{Sync\ Peri}$ is the perigee radius of the synchronous orbit (20,000 km for the trigger orbit), and r_{burn} is the burn radius as computed by equation 5-6 and is shown in Figure 5-20 (38,710 km for trigger orbit). The required correction for the family of synchronous orbits reachable from GTO is shown in Figure 5-13. For the trigger orbit the $\Delta V_{correction}$ is 4.24 m/s. This correction is only made once immediately after the insertion; the following sections discuss perturbations that require periodic correction.

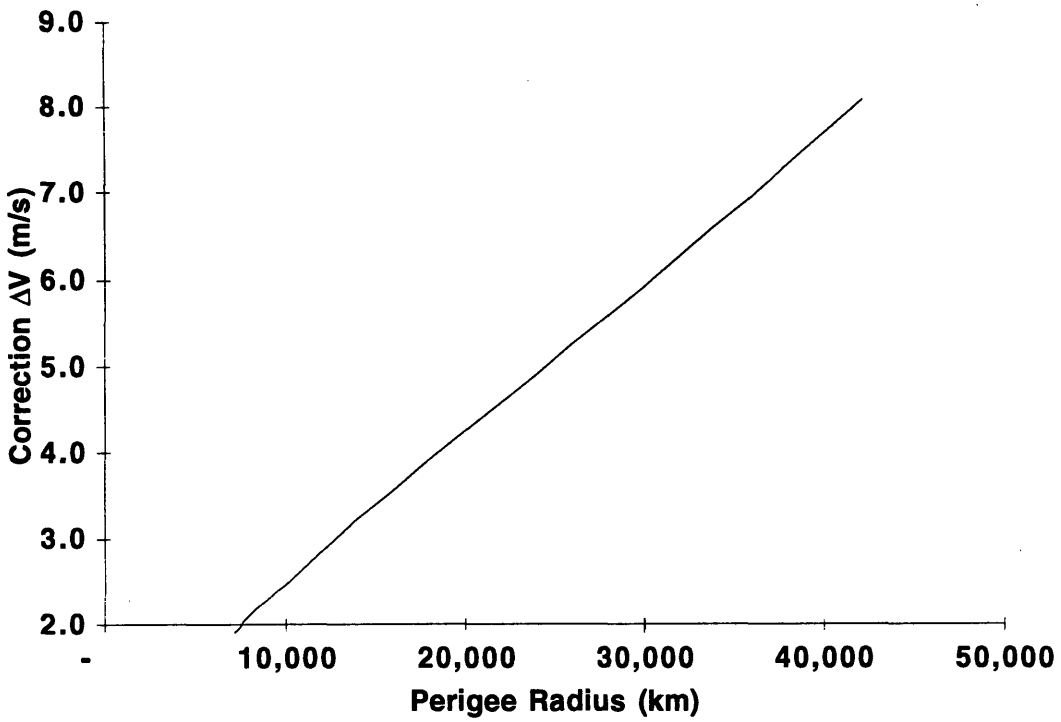

Fig. 5-13 Correction ΔV vs. perigee radius.

5.4.3 Periodic Corrections

The elipticity of the Earth's equator, also knows as the J_{22} harmonic, requires periodic corrections to be made in order to keep the trigger satellites in continuous view of the ground stations. The Earth, if cut in cross-section through the equatorial plane would be slightly elliptical as shown in Fig. 5-14. The semi-major axis of the ellipse runs from 166° E to 14° W and the semi-minor axis of the ellipse runs from 76° E to 104° W. This mass distribution creates a non-spherical gravity potential resulting in a radial force, F_r, (dotted lines in Figure 5-14) a tangential force, F_θ, (solid lines in Figure 5-14) and a force in the geocentric latitude direction, F_ϕ, (not shown) which are superimposed on the spherical gravity potential. These acceleration components are given by [24, pg. 57]:

$$F_r = -\frac{9\mu r_{Earth}^2 J_{22}}{r^4}\cos^2\phi\cos 2(\lambda-\lambda_{22})$$

$$F_\theta = \frac{6\mu r_{Earth}^2 J_{22}}{r^4}\cos^2\phi\sin 2(\lambda-\lambda_{22}) \qquad (5\text{-}10)$$

$$F_\phi = \frac{6\mu r_{Earth}^2 J_{22}}{r^4}\cos\phi\sin\phi$$

Where μ is the gravitational parameter, r_{Earth} is the radius of the Earth, J_{22} is -1.819×10^{-6}, λ_{22} is -14.918°. For the point in being considered r is the radius, ϕ is the geocentric latitude, and λ is the longitude. The orbits considered in this analysis are sufficiently close to equatorial that ϕ will be taken to be zero.

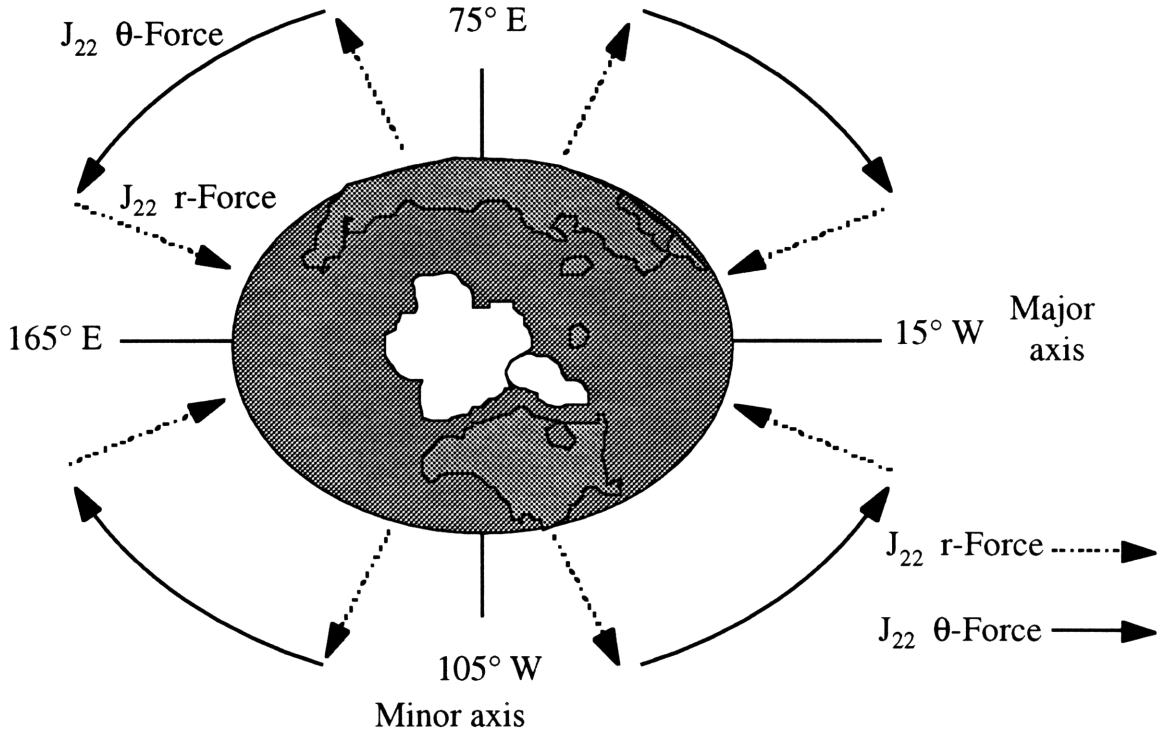

Fig. 5-14 Elipticity of the Earth's equator.

To understand what effect this perturbation has on the trigger orbit it is useful to start by considering the effect on a geostationary satellite in the quadrant between 15° W and 105° W or in the quadrant between 75° E and 165° E . The satellite begins in a ideal geostationary orbit with a period exactly equal to the sidereal period of the Earth. The radial J_{22} acceleration, F_r, is normal to the flight path and so produces no change in the semi-major axis, however, the tangential J_{22} acceleration, F_θ, is in the same direction as the flight path. Over time F_θ imparts a ΔV on the satellite that increases its semi-major axis and period. Since the satellite is now in an orbit with a period slightly longer than the sidereal period of Earth it begins to drift West relative to the Earth. The satellite continues to drift West aided by the J_{22} acceleration until it longitude exceeds 105° W or 75° E when the J_{22} acceleration will begin to oppose the westward drift, slowing the satellite and decreasing its period. The westward drift will eventual halt at an angle from the minor axis equal to the angle the satellite started at from the minor axis. After that the satellite will begin to drift Eastwards and will librate about the minor axis. While on any given day the satellite will occupy a point relative to the Earth,

this point will drift back and forth across the minor axis with a period of ~900 days as shown in Figure 5-15. To prevent this libration geostationary communications satellites must make small periodic ΔVs to counteract the F_θ acceleration. The cost of these ΔVs can be computed by simplifying equation 5-10 for geostationary orbit which yields $\Delta V = 1.7655\cos 2(\lambda - \lambda_{22})$ in m/s/yr., with a maximum of 1.7655 m/s/yr required.

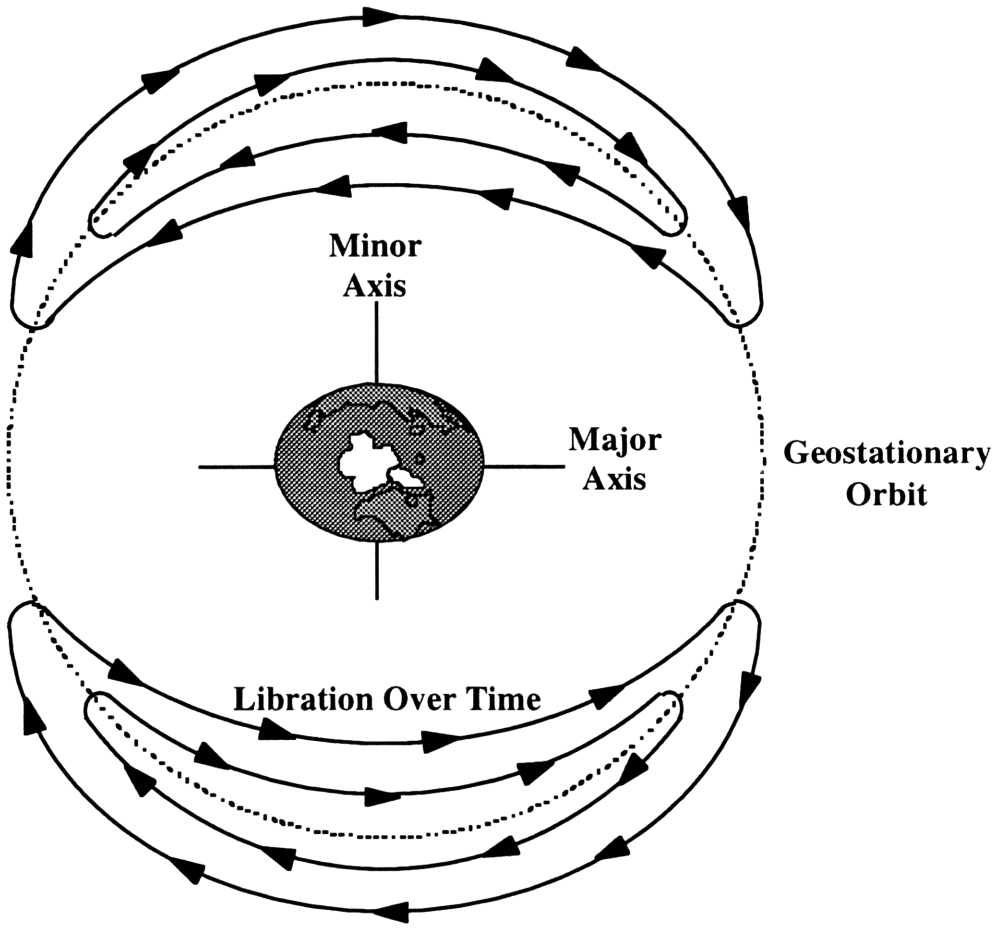

Fig. 5-15 Libration of a satellite in geostationary orbit about the minor axis of the Earth's equator (not to scale).

For general synchronous orbits with non-zero eccentricities like the trigger orbit the effect of J_{22} is similar to the effect of J_{22} on geostationary orbit. In a frame rotating with the Earth a non-zero eccentricity synchronous orbit traces out a closed figure over the course of a day rather than occupying a single point as shown in Figure 5-16. However, the effect of F_θ over time is the same, resulting in changes to the semi-major axis and period that cause the line of apsides of the orbit, relative to Earth, to librate about the minor axis of Earth. Again, this libration can be opposed by making small ΔVs to correct the changes to the semi-minor axis and period. The computation of the required ΔV is much more complicated because of the synchronous orbits daily movement relative to

the Earth. No analytical solution to 5-10 is obvious for a general synchronous orbit so the problem must be solved numerically.

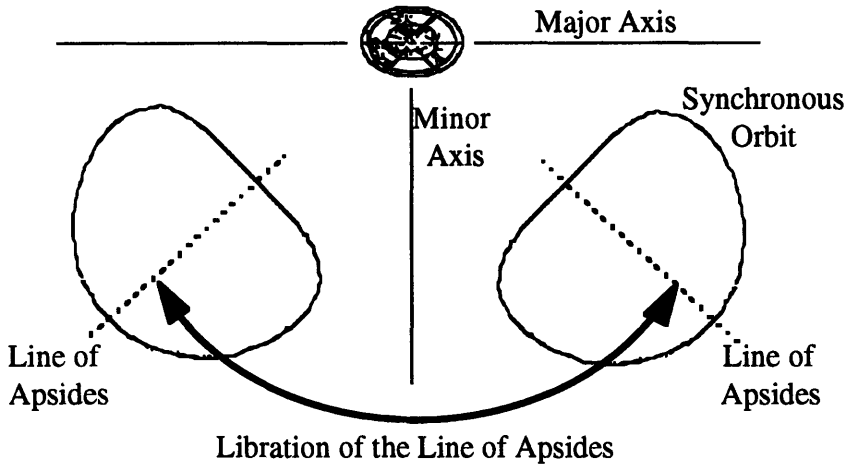

Fig. 5-16 Libration of the line of Apsides of a synchronous orbit about the minor axis of Earth's equator.

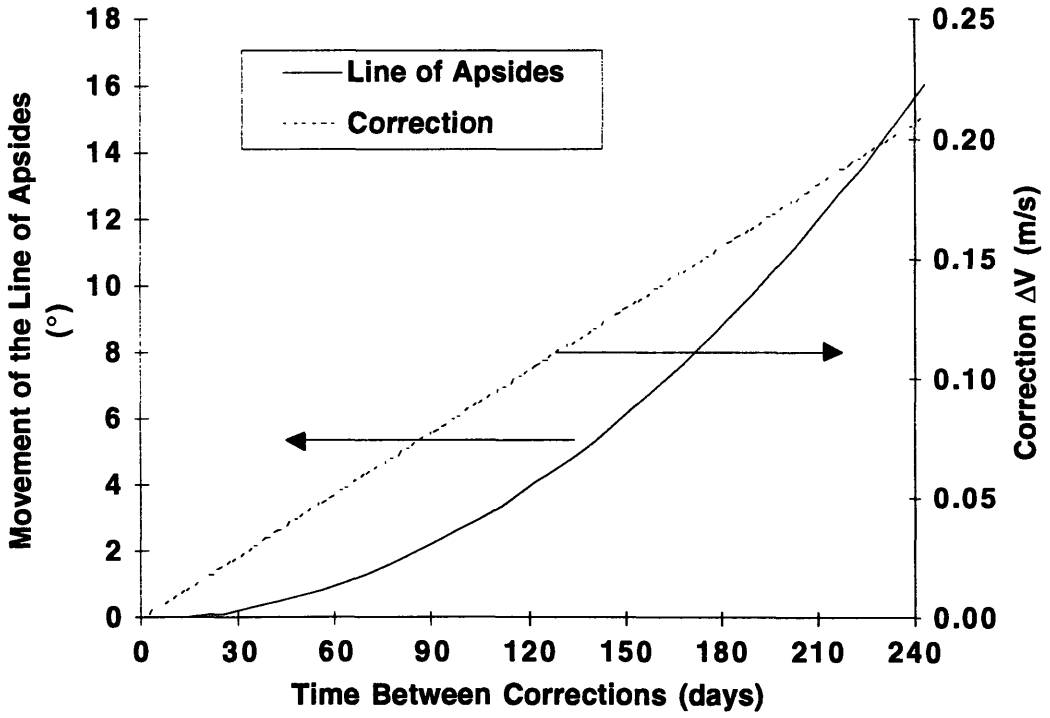

Fig. 5-17 J_{22} correction frequency and magnitude.

An Encke's method, described in appendix F, was used to integrate the J_{22} perturbation and find the daily change in semi-major axis. This was further checked by a Cowell's Method integration of the J_{22} perturbation. For the trigger orbit centered over Haystack (285° E) the daily change in the semi-

major axis was 42.5 m/day resulting in a change in the period of 0.130°/day or a rate of change in the line of apsides relative to the Earth of -5.44×10^{-4}°/day^2. This requires 0.315 m/s/yr of correction, or 1.58 m/s over the five year mission. Assuming that the rate of change in the line of apsides relative to the Earth remains approximately constant around 285° E, the deviation from the optimum position and the correction ΔV as a function of the time between corrections is shown in Figure 5-17. The allowable side to side deviations to remain continuously visible is shown in Figure 4-31. For type I orbits the allowable total side to side deviation is 31.25°. For type II orbits the allowable total side to side deviation is 22.0°. Keeping a ~5° margin between the lowest elevation and the horizon results in a minimum deviation of 12° for the type II orbit which requires a correction of 0.181 m/s every 210 days. The sky tracks of type I and II orbits at the beginning/end and middle (the farthest west and east points) of a 210 day correction cycle are shown if Figures 5-18 and 5-19. If the burn duration is limited by losses due to isentropic expansion in the cold gas reservoir, then burns can be made more frequently at a cost of more frequent corrections but with the benefit of less deviation in the sky track of the orbit.

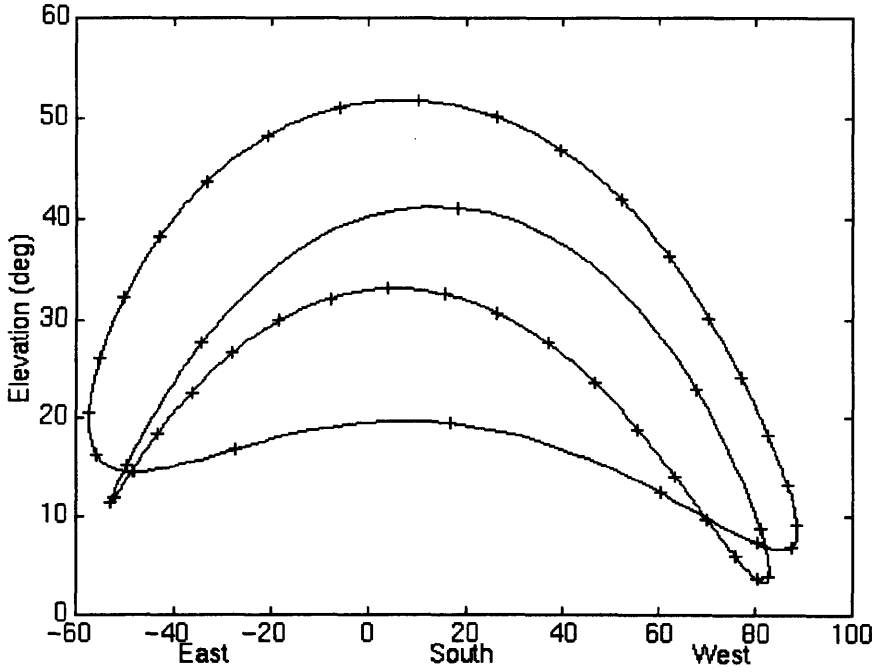

Fig. 5-18 Type I and II orbit tracks at the end / beginning (the farthest west points) of a 210 day correction cycle.

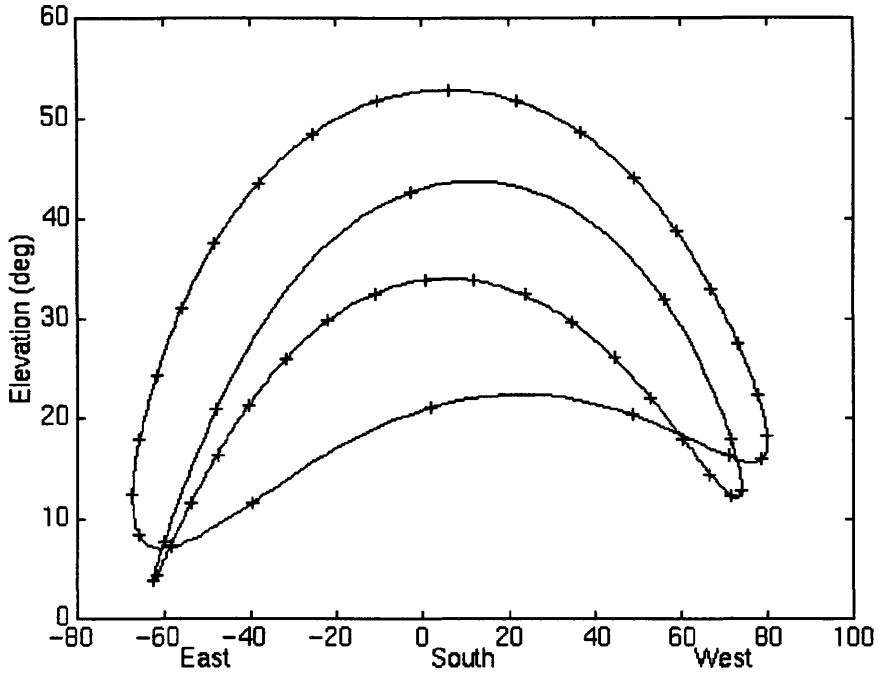

Fig. 5-19 Type I and II orbit tracks at the 115th day (the farthest east point) of a 210 day correction cycle.

5.4.4 Long Term Sky Track Evolution

Over the course of the mission the shape of the sky track will evolve due to the changes in argument of perigee caused by J_2 perturbation and changes in the inclination caused by the influence of the Sun and Moon. This topic has not been explored thoroughly, but test cases have been run to ensure that after the five year mission lifetime the sky tracks of the trigger orbits will still be continuously visible. The precession of the argument of perigee, caused by the J_2 perturbation, is given by equation 5-6 and is equal to 0.053°/day or 96.73° over five years. The type I and II orbits after five years accounting for the precession of the argument of perigee are shown in Figure 5-20. The change in inclination, caused by the perturbation of the Sun and Moon, results in the North-South station keeping required by geosynchronous communications satellites. The rate of change in inclination varies between ±0.9°/yr causing a maximum change in inclination of ±4.5° over the five year mission lifetime. The type I and II orbits after five years accounting for the precession of the argument of perigee and a ±4.5° change in inclination are shown in Figure 5-21 and Figure 5-22 respectively. To maintain the phasing so that the highest minimum elevation is maintained a small amount of rephasing may be needed over the mission lifetime. This can be folded into the J_{22} corrections and should cost less than 0.02 m/s over five years. In the future more detailed studies of the evolution of the sky track should be undertaken.

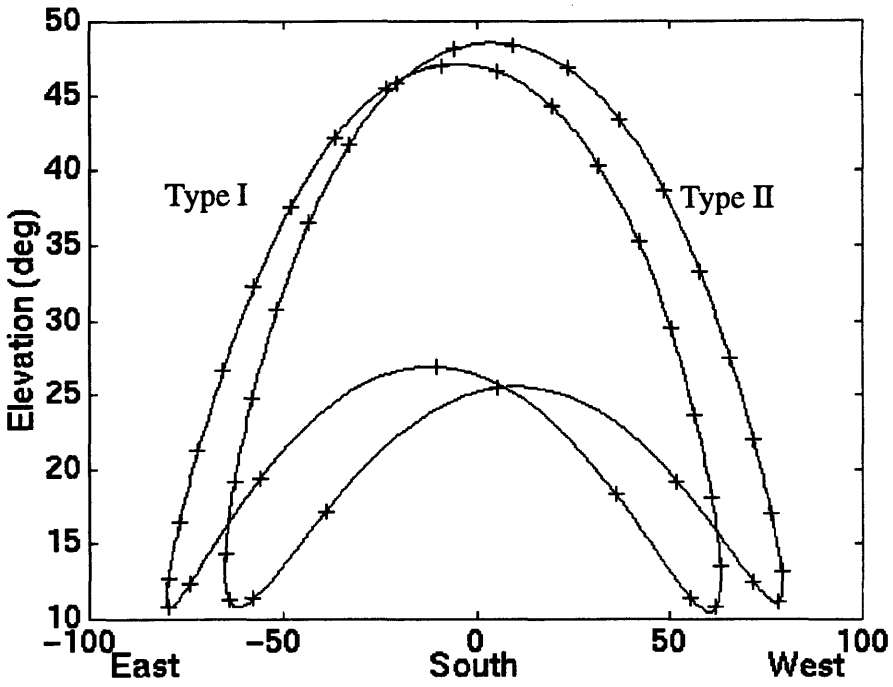

Fig. 5-20 Centered 7° inclination type I and II orbit tracks after five years.

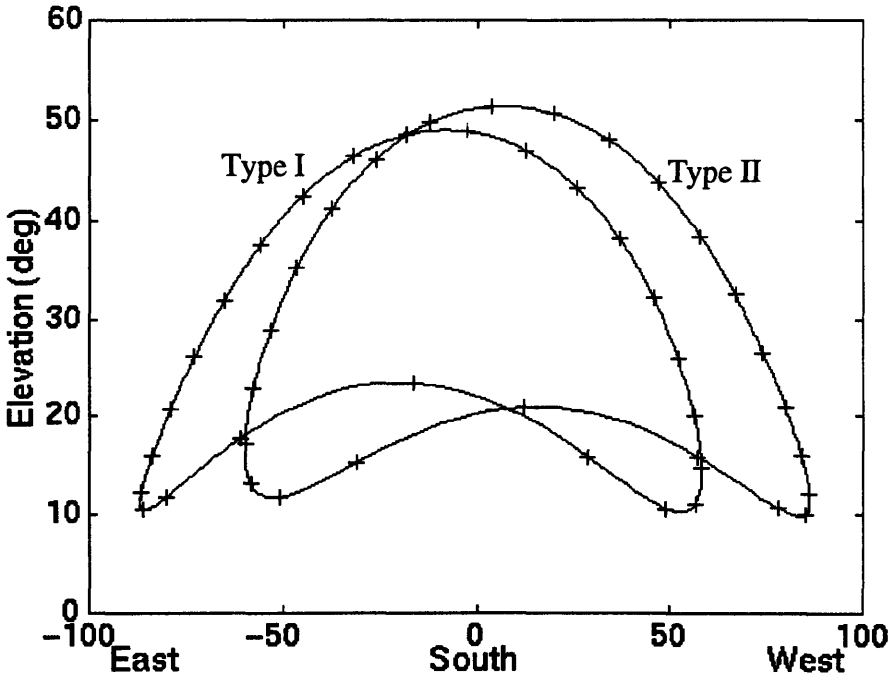

Fig. 5-21 Centered 11.5° inclination type I and II orbit tracks after five years.

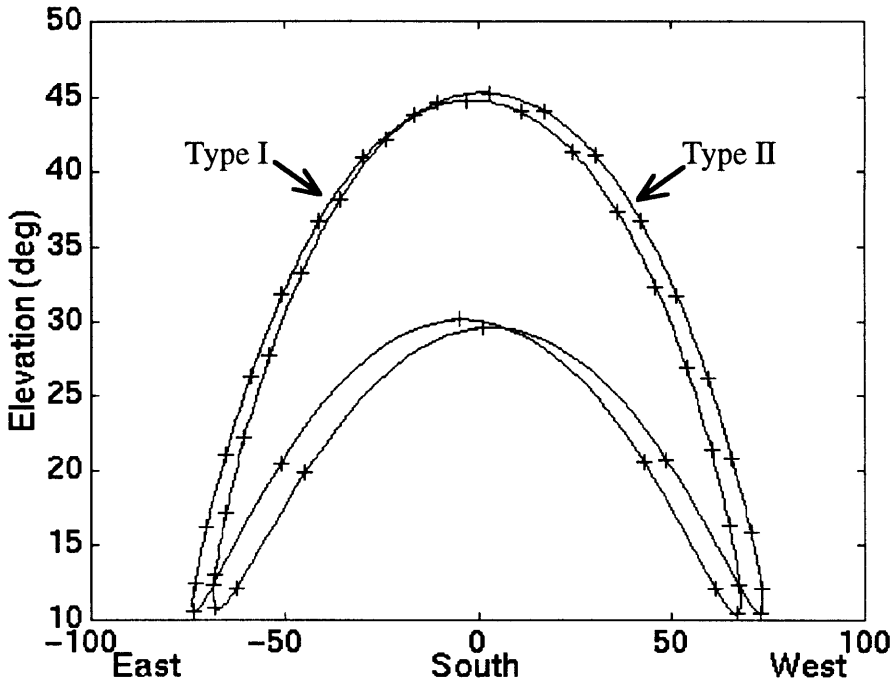

Fig. 5-22 Centered 2.5° inclination type I and II orbit tracks after five years.

5.5 Eclipsing Environment

This section describes the eclipsing environment of the trigger satellites which drives the mass of the batteries and power system. The existence and duration of a daily eclipse for a given trigger orbit is a function of two parameters. First, the time of year at launch determines the inclination of the orbit to the ecliptic and the orientation of the orbit in inertial coordinates. Second, the current time of year determines the orientation of the orbit relative to the Earth-Sun line. A code described in appendix G was used to determine penumbra and umbra eclipse durations as a function of time of year at launch and current time of year. Figures 5-23 and 5-24 show the umbra and penumbra eclipse times for the type I trigger orbit. Figures 5-25 and 5-26 show the umbra and penumbra eclipse times for the type I trigger orbit. The maximum penumbra duration is 136 minutes and the maximum umbra duration is 124 minutes. The small difference in umbra and penumbra duration is to be expected as their cone angles differ by only ~0.5°. Future work should account for the effect of orbit evolution on the eclipse duration.

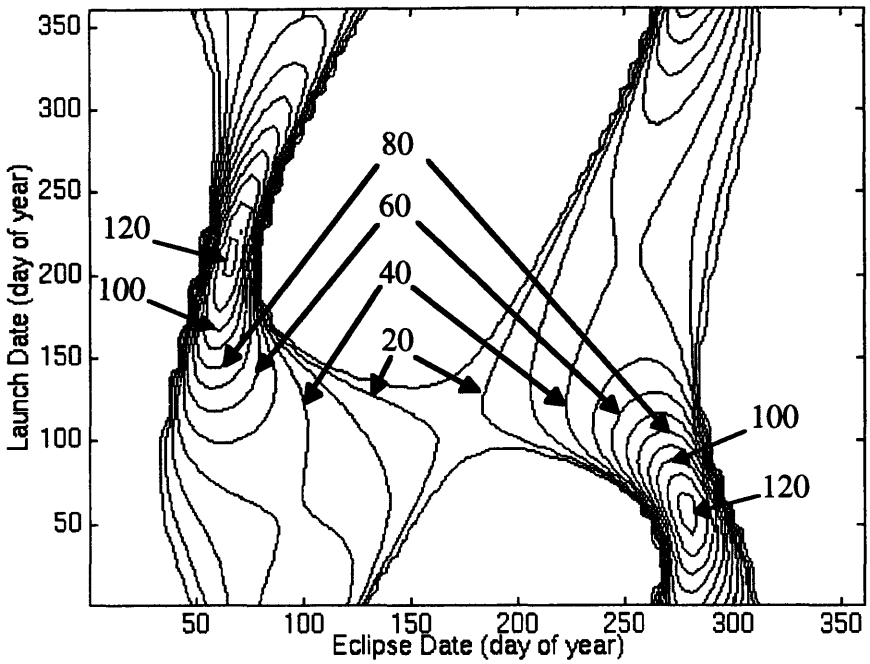

Fig. 5-23 Type I umbra eclipse duration (contours every 10 minutes).

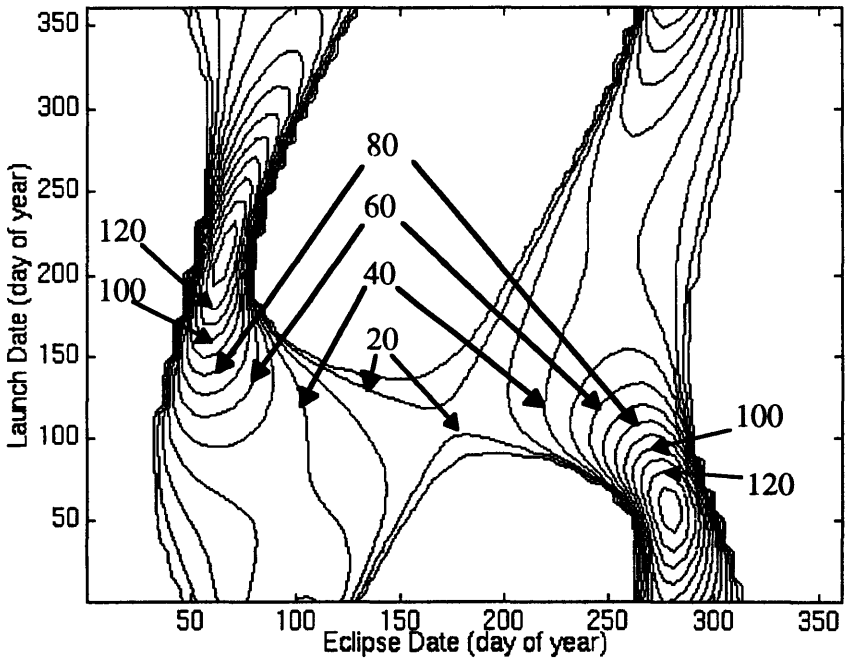

Fig. 5-24 Type I penumbra eclipse duration (contours every 10 minutes).

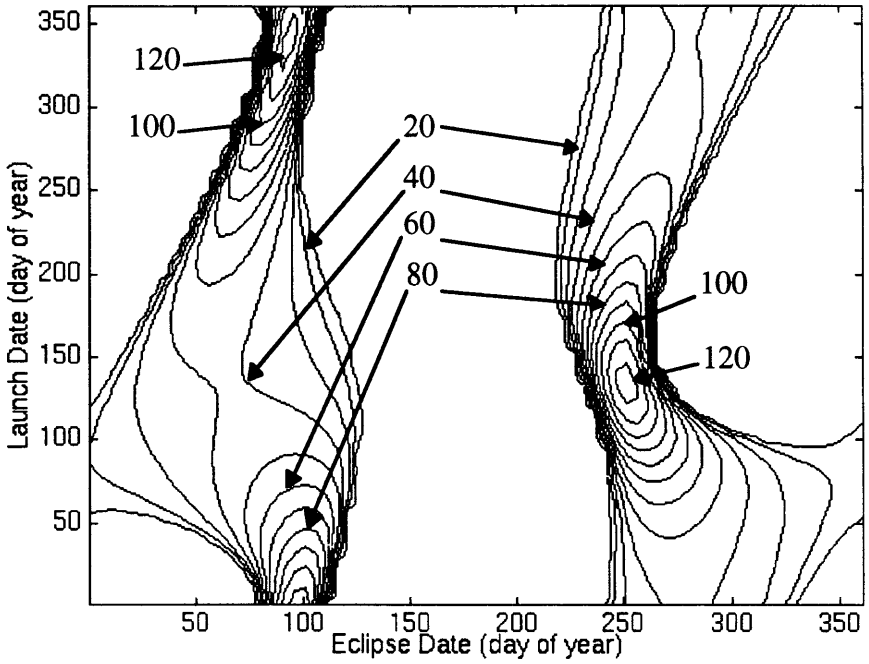

Fig. 5-25 Type II umbra eclipse duration (contours every 10 minutes).

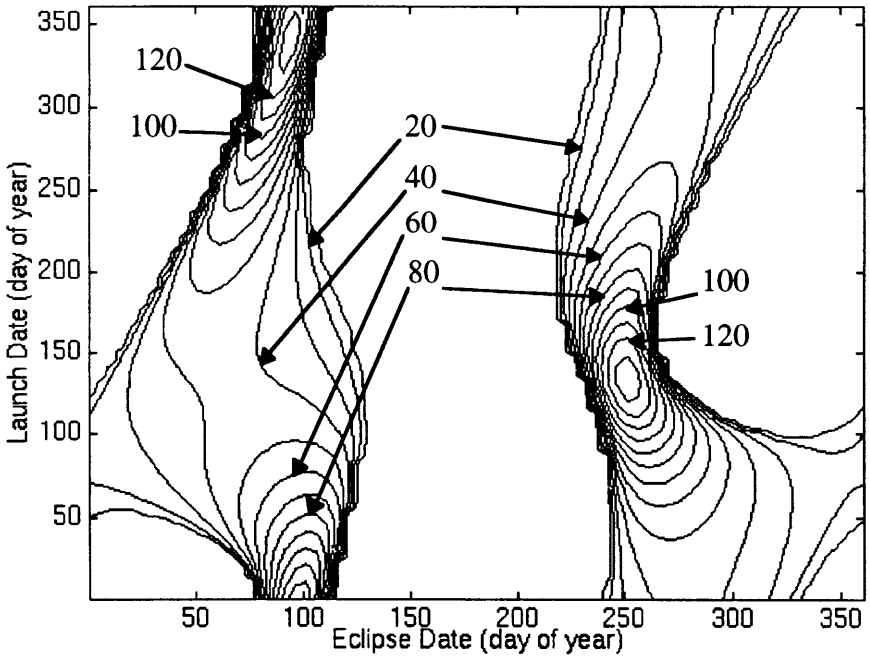

Fig. 5-26 Type II penumbra eclipse duration (contours every 10 minutes).

5.6 Conclusion

While the work in this chapter cannot be considered a comprehensive description of the details of the trigger orbits, it does explain many of the operational complexities of inserting and operating the trigger satellites. The items of most concern to other subsystems in this chapter are the cold gas corrections required and the eclipse duration. The required cold gas corrections consist of the insertion error correction, 4.24 m/s, the J_{22} corrections, 1.77 m/s, the re-phasing caused by the deviation of the insertion window, 0.07 m/s, and the re-phasing to account for the long term evolution of the sky tracks, 0.02 m/s for a total required cold gas ΔV of 6.10 m/s. The maximum penumbra duration is 136 minutes and the maximum umbra duration is 124 minutes.

Future work should concentrate on a more detailed examination of the trigger orbit evolution and the development of an operations plan and operations software. The perturbation analysis, while covering the most important effects, is somewhat piece-wise. An integrated examination of the trigger orbit evolution and its effects on other aspects of the trigger orbit such as the eclipse duration should be undertaken. Finally, as the design progresses, an operations plan and supporting software should be created.

Chapter 6 Conclusions

This chapter summarizes and concludes this thesis. The most important innovations in the ETA propulsion and trajectory design are listed. Future work is suggested and final comments are made.

6.1 Thesis Results

The three principal innovations to the ETA design introduced in this thesis are:

- **Impulsive Chemical Propulsion** - This first innovation led to the subsequent innovations. Using straight forward analytical techniques it is shown in section 2.5 that for the hyperbolic excess velocities, and hence spread rates, required by ETA making the spreading ΔVs near Earth, shortly after injection, when the velocity of the satellites is high, greatly reduced the total propulsive requirements. This both allows and requires the use of inherently high thrust, low cost, flight proven chemical propulsion. This greatly improves the technical feasibility of the mission and decreases its technical risk. After a comprehensive examination of different chemical propulsion types, the Star 13A solid rocket motor was selected. This work was closely linked to the innovations in launch mechanism described in the next item.

- **Ariane 5 ASAP Launch** - After examining multiple deployment strategies, launch on the Ariane 5 ASAP ring is selected in section 3.8. The ASAP ring allows for the launch of up to eight 100 kg 60 cm $\times$ 68 cm $\times$ 80 cm satellites to GTO simultaneously at very low cost [7]. Under an agreement with CNES the French will provide the Ariane slots for free. This low cost access to a high energy orbit allows ETA to fit the SMEX criteria, a far less expensive mission class the originally planned MIDEX class, without decreasing the scientific return. Further, at no extra cost, ETA can be launched in two batches of three satellites (two helio satellites and one trigger satellite) so that even in the event of a launch failure a minimal ETA constellation can be formed. This greatly increases the probability of mission success. The maximum ΔV required for providing a spread rate of 60°/yr is 1101 m/s.

- **The Synchronous Trigger Orbit** - In response to the selection of the solid rocket propulsion and Ariane 5 ASAP launch, relaxed radiation and Earth blockage requirements, and the requirement to rapidly provide continuous burst warnings to a single ground station at Haystack, even in the event of a satellite or launch failure, led to the adoption of a synchronous trigger orbit as described in chapter 4. This 20,000 km X 64,000 km, 7° inclined, one sidereal day orbit can be reached from GTO with a single burn, slightly off apogee, of 1247 m/s only

slightly more than required by the helio satellites. Being continuously visible from a single ground station will greatly reduce the cost and complexity of operating the trigger satellites over their lifetimes.

6.2 Future Work

As the ETA design progresses the following work should be undertaken:

Trigger Orbit Evolution - A significant effort is put into determining the major perturbations on the trigger orbits and determining the needed corrections in chapter 5. However, the nature of this work is that of a first order aproximation. Higher order models of the perturbations and their effects should be studied. Detailed operations plans should be developed for making corrections.

Constellation Analysis - The helio satellite deployment work in chapters 2 and 3 is geared towards achieving a constellation spread rate of 60°/yr. In fact, every helio satellite is capable of achieving a spread rate from 0°/yr to 60°/yr. No effort has been given to determining the optimum distribution of helio satellite spread rates. This optimization should be carried out in order to maximize the performance of ETA.

Detailed Design - The work contained in this thesis is a preliminary design. Work should be carried out to refine and confirm all of the interfaces between the propulsion and trajectory and the other components of ETA.

Operations Planning - The detailed design should culminate in an operations plan. The operations plan should be an extremely detailed step-by-step instruction for how to carry out the nominal mission and any likely contingencies both before and after launch. Pre-launch contingencies should include items such as mass growth and changes in the Ariane 5 launch window and GTO. Post-launch contingencies should include items such as restructuring the deployment in the event of the loss of satellites due to infant mortality or launch failure, injection to a lower energy orbit than planned due to partial launch vehicle failure, and lower than expected on orbit performance of the Star 13A.

Operations Software - To the degree possible, software corresponding to all aspects of the operations plan should be developed. This software would start with post launch elements for GTO, the constraints placed by the deployment of the primary payload, and operations concerns (crew

shifts, ground station availability), and compute the necessary burn parameters and windows. Finally, this software should perform automatic correction burn planning based on post injection date for the trigger satellites and data on long term evaluation. Automated software of this type should decrease the complexity and risk of error during the deployment sequence.

6.3 Final Comments

This thesis was successful in finding a helio satellite deployment architecture and trigger satellite orbits which meet more stringent requirements at lower cost than was done in the MIDEX ETA proposal. The SMEX ETA costs 46% less ($38M versus $70M) than the MIDEX ETA while increasing the scientific return. A significant fraction of this improvement can be attributed to the innovations in propulsion and trajectory introduced in this thesis. In addition, the propulsion technology used for the helio and trigger satellite deployment is simpler, more flight proven, and more reliable than the propulsion technology used in the MIDEX ETA. The author believes that the work described in this thesis has considerably improved the viability of the SMEX ETA.

Appendix A Cowell's Method Propagator

This appendix describes a generic modular Cowell's method orbit propagator developed by the author and used in several places in this thesis. Cowell's method refers to any method of propagating an orbit by direct integration in rectilinear coordinates. This code solves the initial value problem for up to ten massive or non-massive bodies by numerically integrating:

$$\begin{aligned} \frac{d\mathbf{v}}{dt} &= \mathbf{a} \\ \frac{d\mathbf{r}}{dt} &= \mathbf{v} \\ \frac{dm_{propellant}}{dt} &= -\frac{F_{thruster}}{gI_{sp}} \end{aligned} \tag{A-1}$$

Where **a** is the acceleration vector, **v** is the velocity vector, and **r** is the position vector. The operation of the code is summarized in Figure A-1. The details of the Cowell's code are described in the following sections

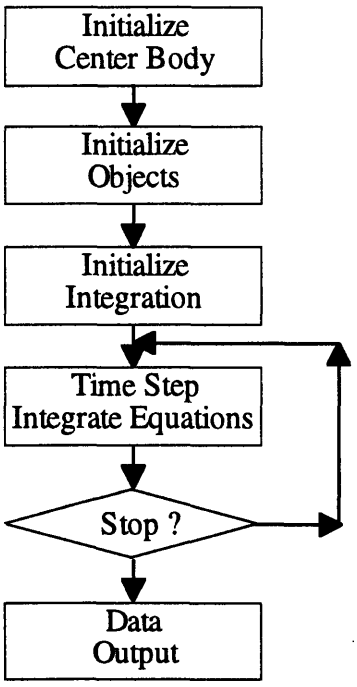

Fig. A-1 Cowell's method.

A.1 Initialization

Three items must be initialized: the center body, the objects being propagated, and the integration itself.

First, the center body, usually the Earth or the Sun, defines the coordinate system for the simulation. The mass of the center body, m_{center}, must be specified. If Hill accelerations are desired, the rotation rate, n, of the center body around another body must be specified. The Hill, or Clohessy-Wiltshire, equations are the linearized equations of motion for a body relative to a reference body (in this case the center body) which is in a circular orbit around another body. These equation can be used to model the perturbation of the Sun on bodies in orbit around the Earth. The Hill frame is defined in Figure A-2.

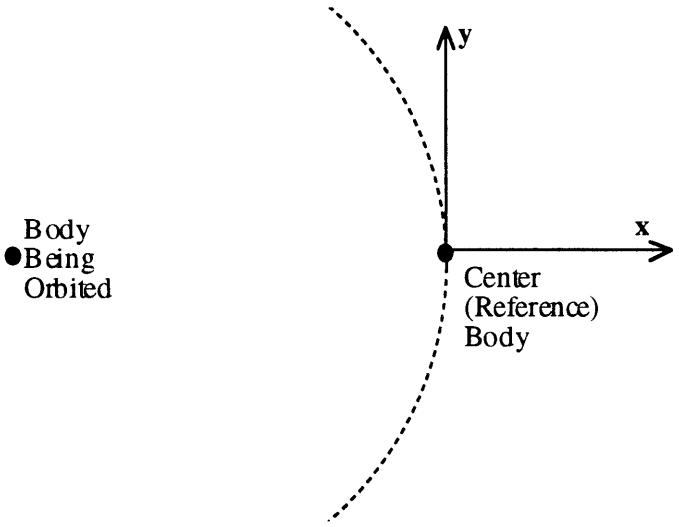

Fig. A-2 Hill frame.

Next, the bodies being propagated must be initialized. Each of up to ten bodies is defined by three vectors: position, **r**, velocity, **v**, and properties. The position and velocity are relative to the coordinate system defined about the center body. The properties vector consists of six components: type, dry mass, propellant mass, thrust, I_{sp}, and a control law. Two types of bodies exist. Type 1 "non-massive" bodies exert no gravitational force on other bodies while type 2 "massive" bodies do exert gravitational force on other bodies. Dry mass, propellant mass, thrust, and I_{sp} allow the propulsion system of a body to be specified. Finally, the control law variable determines how the trust is applied: 0 for no thrust, ±1 for parallel or opposite to the flight path, ±2 for prograde or retrograde (normal to the position vector in the **x**-plane rather than along the flight path) relative to the central body, etc..

Finally, the integration must be initialized. The start and end times for the integrator must be specified. While other criteria for halting the integration can be use, once a given ΔV is achieved for

example, duration is the default and must always be specified. In addition, the active position and velocity array must be initialized.

A.2 Accelerations

It is necessary to calculate the acceleration vector in equation A-1 for each time step. The acceleration vector is the sum of several components including: the gravitational attraction of the center body, the gravitational attraction of other massive bodies, the Hill accelerations, and thrust acceleration. The acceleration of a body by the center body is given by:

$$\mathbf{a}_i = \frac{Gm_{center}\mathbf{r}_i}{r_i^3} \tag{A-2}$$

Where G is the gravitational constant and i refers to the number of the body. Likewise, the acceleration due to massive bodies is:

$$\mathbf{a}_{ij} = \frac{Gm_j\mathbf{r}_{ij}}{r_{ij}^3} \tag{A-3}$$

Where j refers to the massive body and $\mathbf{r}_{ij}$ is the vector from body i to body j. The Hill acceleration, if present, is given by [20, pg. 142]:

$$\mathbf{a}_i = \begin{bmatrix} 3n^2 & 0 & 0 \\ 0 & 0 & 0 \\ 0 & 0 & -n^2 \end{bmatrix}\mathbf{r}_i + \begin{bmatrix} 0 & 2n & 0 \\ -2n & 0 & 0 \\ 0 & 0 & 0 \end{bmatrix}\mathbf{v}_i \tag{A-4}$$

Where n is the rotation rate of the center body around another body. Finally, the thrust acceleration is given by:

$$\mathbf{a}_{ij} = \mathbf{u}\frac{F_{thruster}}{m_{dry} + m_{propellant}} \tag{A-5}$$

Where $\mathbf{u}$ is a unit direction vector determined by the control law.

A.3 Integration

Equation A-1 is integrated using a modified version of the ODE45 Runge-Kutta integrator in MATLAB. The modifications allow changes to be made to the properties vectors between time steps and additional stop conditions to be added. The standard output for the Cowell's propagator is a matrix containing the time position history of the bodies being propagated. This can be used to produce snapshots of the constellations.

The Cowell's method propagator is useful when the traditional assumptions of Keplerian mission planning such as single massive center bodies, impulsive ΔVs, and patched conic motion break down. While the Cowell's method is slower than Keplerian methods it is more general and flexible than Keplerian methods.

Appendix B 2-D GTO Escape

This appendix describes how spread rate is generated from ΔV, position of perigee, and burn true anomaly, f_{burn}, using is a simplified Keplerian model. This process is summarized in Figure B-1. Two simplifications are introduced to increases the speed and generality of the code: First, the model used is 2-dimensional. All orbits are assumed to lie in the ecliptic plane. This significantly simplifies the code and eliminates the dependence on time of year increasing the generality of the code. Second, all burns are assumed to be parallel to the flight path also simplifying the code. While these simplification reduce the accuracy of the code, the quality is sufficient for use in the helio satellite deployment architecture study to gauge the effect of not having control over position of perigee. A considerably more accurate and complicated 3-D code was later developed and is described in Appendix C. Position of perigee, ω, is defined as the clockwise angle from the velocity vector of Earth to perigee of GTO as shown in Figure B-2. Position of perigee should not be confused with the Keplerian element argument of perigee wich is the angle between the ascending node and perigee. The details of generating the final spread rate is described in the following sections.

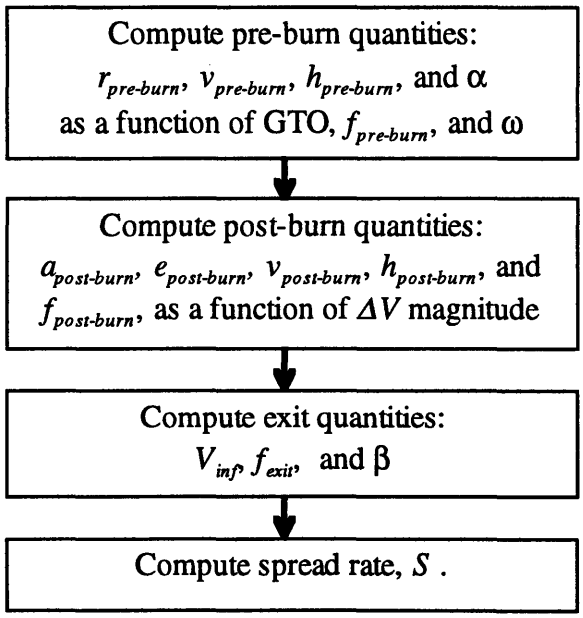

Fig. B-1 Generation of the spread rate

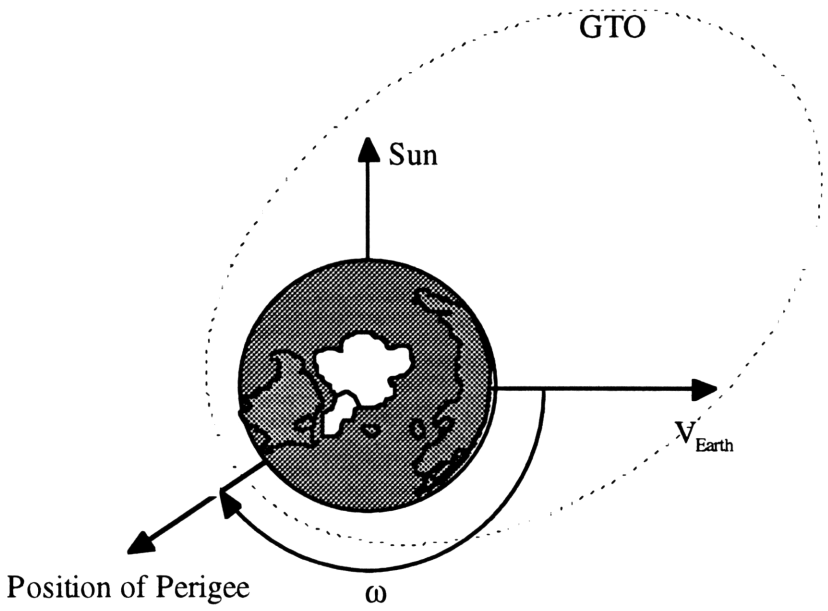

Fig. B-2 The definition of position of perigee used in this chapter.

B.1 Pre-Burn Quantities

From the elements of GTO, the position of perigee, ω, and burn true anomaly, $f_{pre\text{-}burn}$, the pre-burn orbital quantities can be computed. The relevant elements of GTO are: the semi-major axis, a_{GTO}, is 24571.5 km, and the eccentricity, e_{GTO}, is 0.716. The burn position, α, the clockwise angle between the velocity vector of Earth and the burn point, as shown in Figure B-3, is given by:

$$\alpha = \omega - f_{pre-burn} \tag{B-1}$$

The pre-burn radius, $r_{pre\text{-}burn}$, and velocity, $v_{pre\text{-}burn}$, can be computed by:

$$\begin{aligned} r_{pre-burn} &= \frac{a_{GTO}\left(1-e_{GTO}^2\right)}{1+e_{GTO}\cos f_{pre-burn}} \\ v_{pre-burn} &= \sqrt{\mu\left(\frac{2}{r_{pre-burn}}-\frac{1}{a_{GTO}}\right)} \end{aligned} \tag{B-2}$$

Where μ is the gravitational parameter. Finally, the specific angular momentum, $h_{pre\text{-}burn}$, is given by:

$$h_{pre-burn} = \sqrt{\mu a_{GTO}\left(1-e_{GTO}^2\right)} \tag{B-3}$$

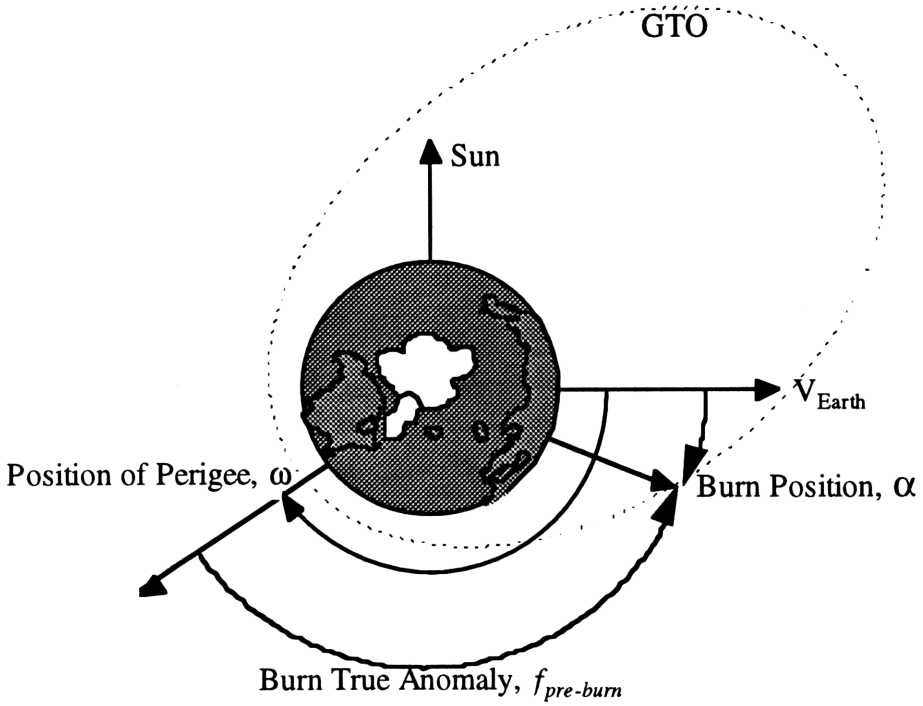

Fig. B-3 Burn position, α.

B.2 Post-Burn Quantities

The post-burn quantities can be computed with the ΔV and the pre-burn quantities computed above. The post-burn velocity, $v_{prost\text{-}burn}$, is given by:

$$v_{post-burn} = v_{pre-burn} + \Delta V \tag{B-4}$$

The post-burn specific angular momentum, $h_{prost\text{-}burn}$, is given by:

$$h_{post-burn} = \frac{v_{post-burn}}{v_{pre-burn}} h_{pre-burn} \tag{B-5}$$

The specific mechanical energy of the escape orbit, $\varepsilon_{prost\text{-}burn}$, is given by the Vis-Viva integral:

$$\varepsilon_{post-burn} = \frac{v^2_{post-burn}}{2} - \frac{\mu}{r_{pre-burn}} \tag{B-6}$$

With this the escape orbit eccentricity, $e_{prost\text{-}burn}$, can be computed by:

$$e_{post-burn} = \sqrt{1 + \frac{2\varepsilon_{post-burn} h^2_{post-burn}}{\mu^2}} \tag{B-7}$$

Finally, the post-burn true anomaly, $f_{prost\text{-}burn}$, is given by:

$$f_{post-burn} = \cos^{-1}\left(\frac{1}{e_{post-burn}}\left(\frac{h^2_{post-burn}}{\mu r_{post-burn}} - 1\right)\right) \text{sign}\, f_{pre-burn} \tag{B-8}$$

B.3 Exit Quantities

With the quantities determined in the last section it is now possible to propagate the orbits to escape. At an infinite distance the true anomaly, f_{xit}, of a hyperbolic escape orbit will be:

$$f_{exit} = \frac{\pi}{2} + \sin^{-1}\left(\frac{1}{e_{post-burn}}\right) \tag{B-9}$$

At an infinite distance the velocity vector will be parallel to the radius vector so that the exit direction, β, the angle between the velocity vector of Earth and the velocity vector of the satellite at infinity, as shown in Figure B-4, is given by:

$$\beta = f_{exit} - f_{post-burn} - \alpha \tag{B-10}$$

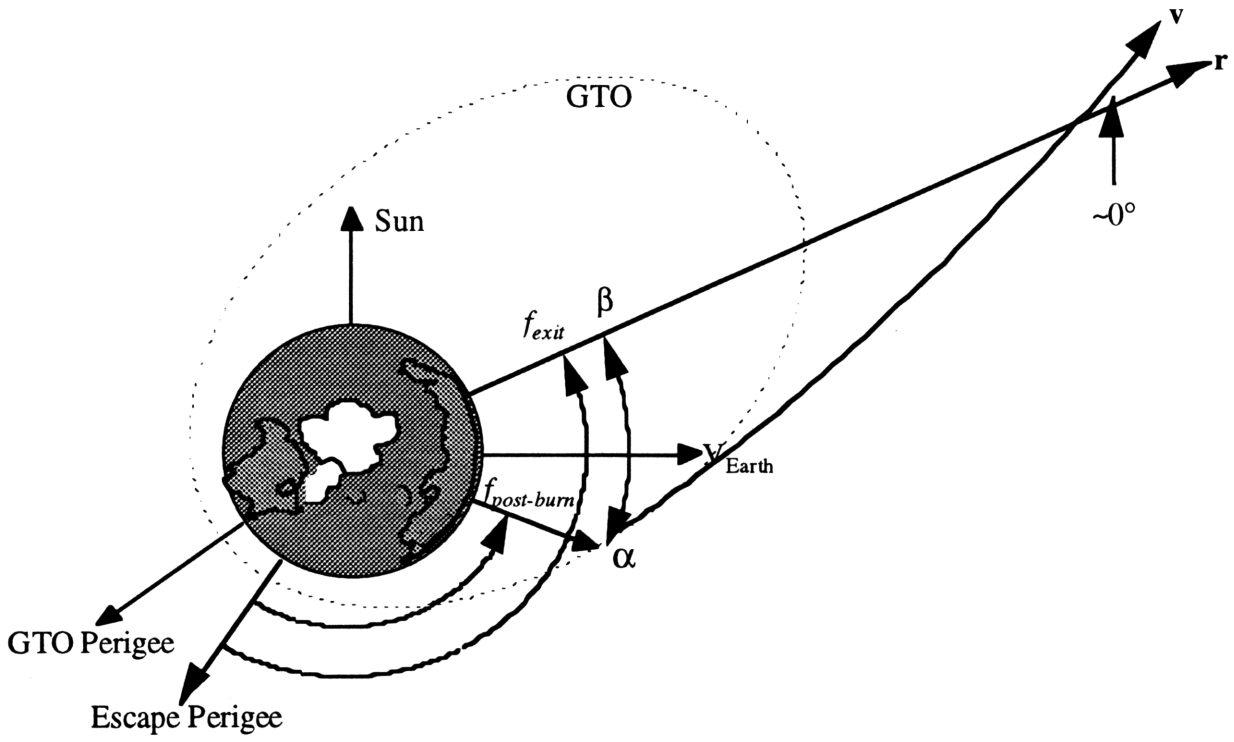

Fig. B-4 Exit direction.

The velocity at infinity, V_{inf}, is given by:

$$V_{inf} = \sqrt{2\varepsilon_{post-burn}} \tag{B-11}$$

Finally, the spread rate is estimated using equation 3-8:

$$S = \frac{V_{inf}}{27.5}\cos\beta \qquad \text{(B-12)}$$

Where spread rate, S, is in °/yr and V_{inf} is in m/sec.

Appendix C 3-D GTO Escape

This appendix describes how the final heliocentric elements and spread rate are generated from the burn parameters. This process is sumarized in Figure C-1. The following inputs are necessary: Launch date and time, ΔV, the escape burn true anomaly, and the burn direction angles. Launch date and time specify the position of Earth and the orientation of GTO in space. ΔV specifies the magnitude of the escape burn. Burn true anomaly specifies the position of the escape burn within GTO. Finally, the burn direction with respect to the flight path angle, given by the angles θ and ϕ shown in Figure C-2, specify the direction of the burn. The details of generating the final elements are described in the following sections.

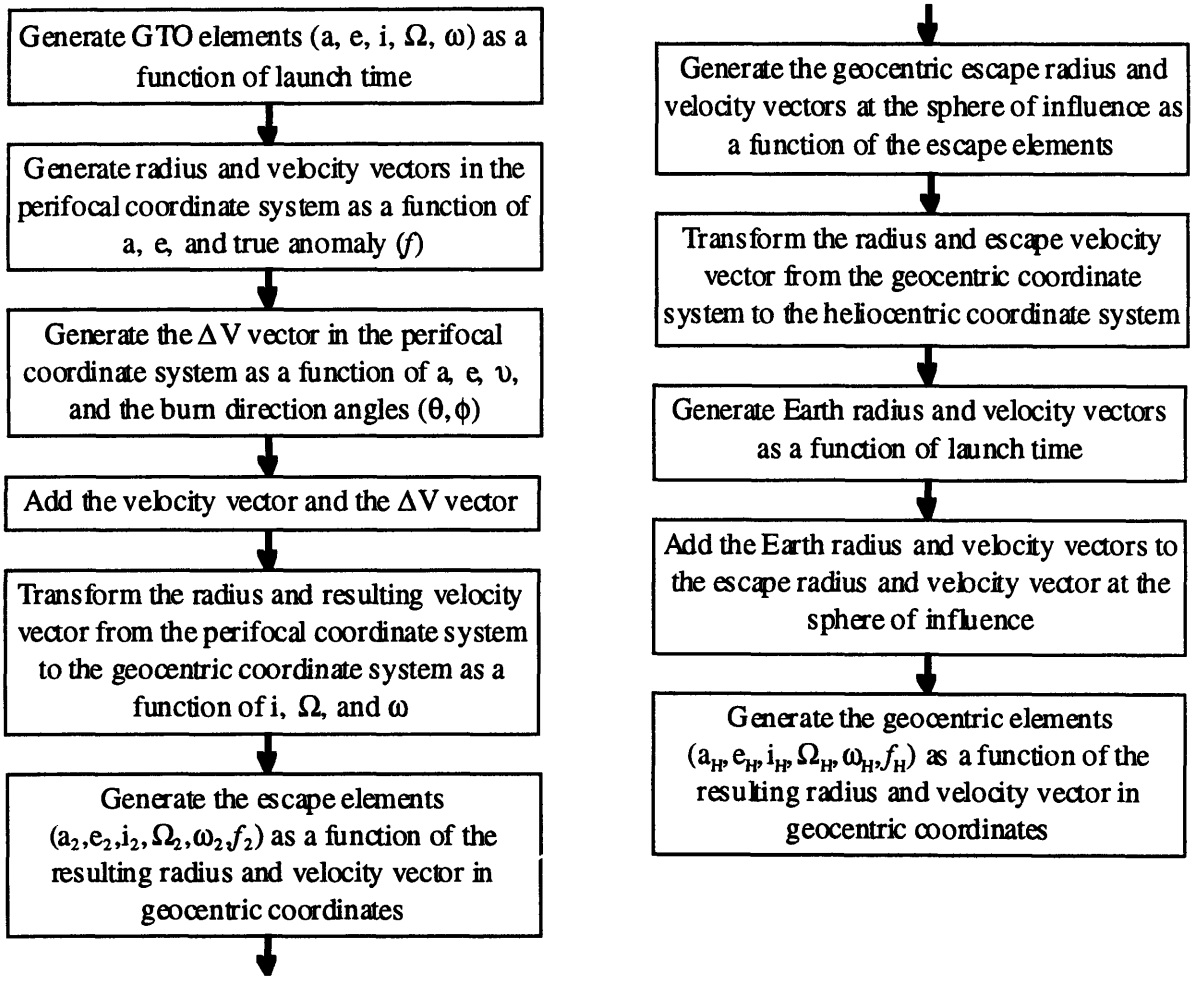

Fig. C-1 Generation of the Heliocentric Elements

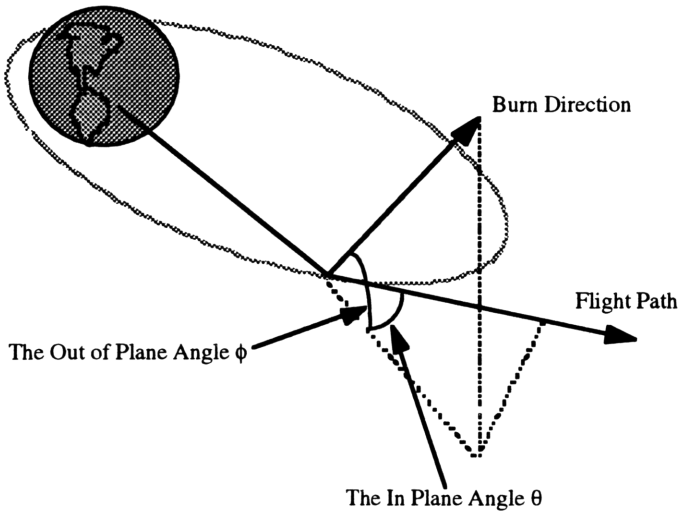

Fig. C-2 Burn direction angles

C.1 GTO Elements

All elements of the Ariane 5 GTO are constants with the exception of longitude of the ascending node, Ω, which is a function of launch date and time. The time invariant elements of GTO [15 pg. 3.2] are given in Table C-1.

Table C-1 Time Invariant Elements of GTO

Element	Value
a	24571.5 km
e	0.716
i	7°
ω	179.5°

The ascending node is at 165° east relative to the Earth at the time of launch. The longitude of the ascending node is the sum of 165° plus the Greenwich sidereal time, the angle between the Greenwich (prime) meridian and the vernal equinox direction at launch, as shown in Figure C-3. The Greenwich sidereal time is the Greenwich sidereal time at midnight GMT on the day of launch plus the angle the earth has rotated though between midnight and the launch time as shown in Figure C-4. The Greenwich sidereal time at midnight, θ_{g0}, is given by [25, pg. 20]:

$$\theta_{g0} = 99°.69009833 + 36000°.76989T_u + 0°.00038708T_u^2 \qquad \text{(C-1)}$$

where T_u the time in julian centruies since noon January 1st, 1900:

$$T_u = \frac{J.D. - 2451520.0}{36525} \qquad \text{(C-2)}$$

Where J.D. is the Julian Date.

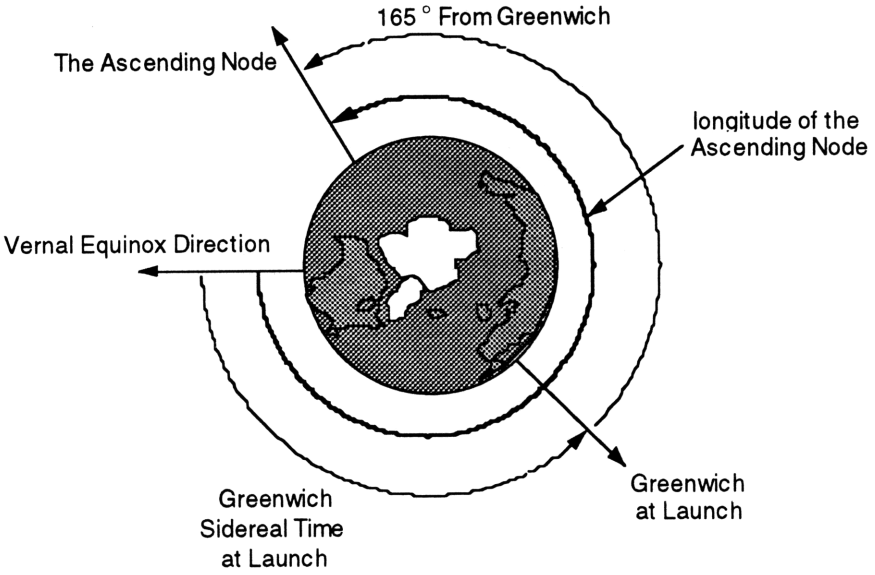

Fig. C-3 Longitude of the Ascending Node.

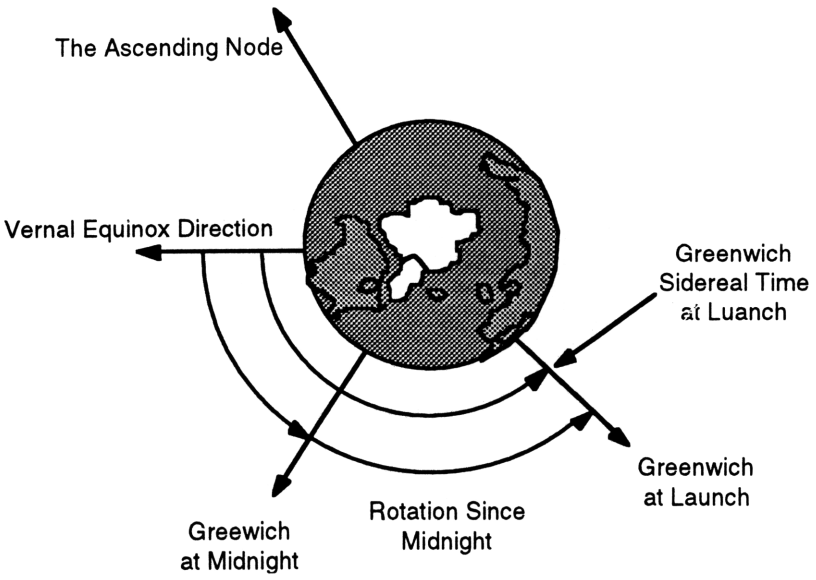

Fig. C-4 Greenwich Sidereal Time.

The Julian date, used commonly in the precision determination of orbits, is the decimal number of synotic (solar) days from noon December 31st, 4714 B.C. [25, pg. 17]. Therefore, Greenwich sidereal time is given by:

$$\theta_g = \theta_{g0} + (t - t_0)\frac{d\theta}{dt} \qquad \text{(C-3)}$$

Where t_0 is midnight and dθ/dt, the rotation rate of Earth, is 0.25068447 degrees/minute. While launch date may be considered a random variable (or at least beyond the control of the ETA team), launch time is constrained by the Ariane 5 GTO launch window. This 45 minute window is shown as a function of time of year in Figure C-5. It is very fortunate that this window falls near midnight as this is almost the ideal launch time for ETA [26, 8.30].

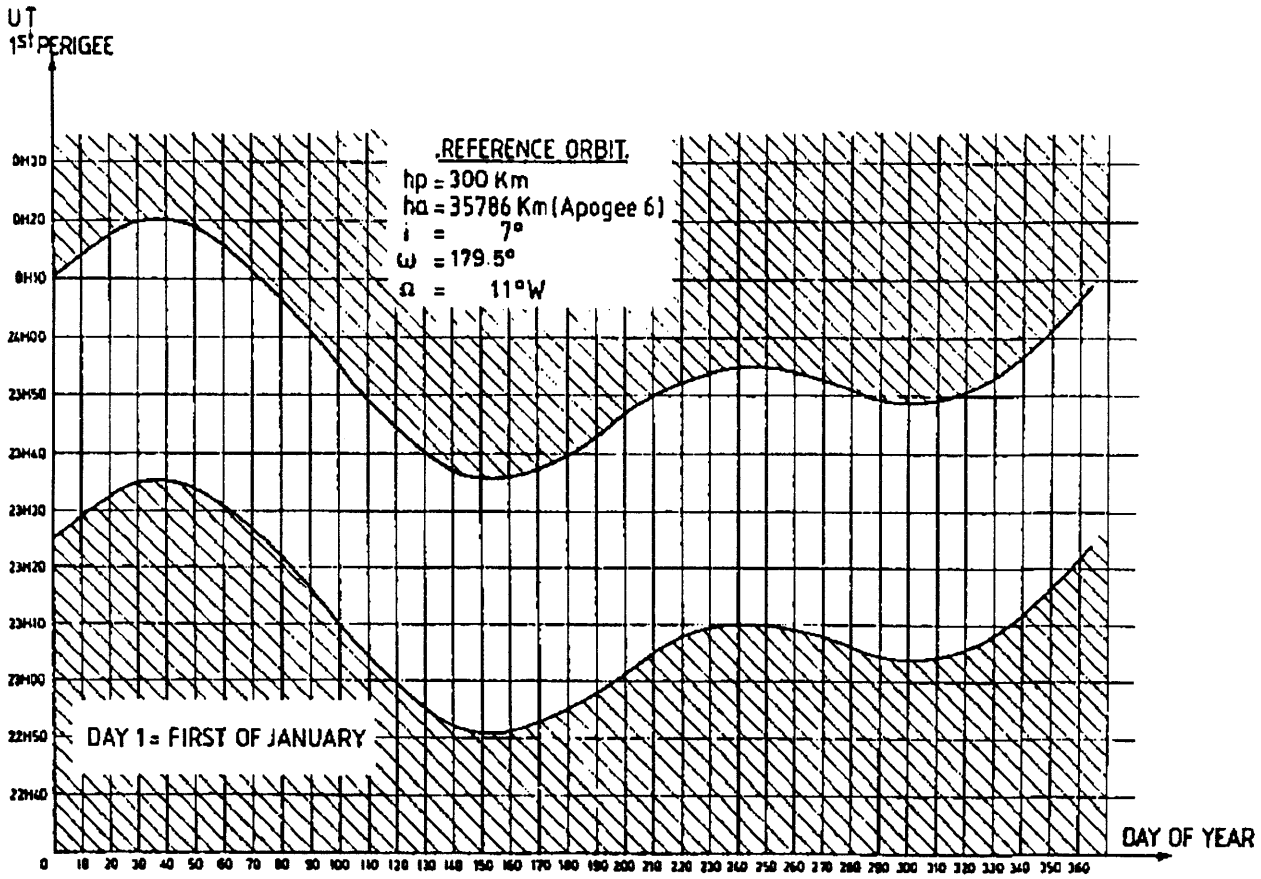

Fig. C-5 Ariane 5 GTO Launch Window [15].

C.2 Perifocal Radius and Velocity Vectors

With a and e as generated in section C.1, and the given burn true anomaly, f, the pre-burn radius and velocity vectors can be generated in perifocal coordinates. The perifocal coordinate system is centered on the focus of the orbit with the **x**-axis pointing towards perigee and the orbit lying in the **x**-**y** plane as shown in Figure C-6. The **z**-axis is parallel to the angular momentum vector, **h**, of the orbit.

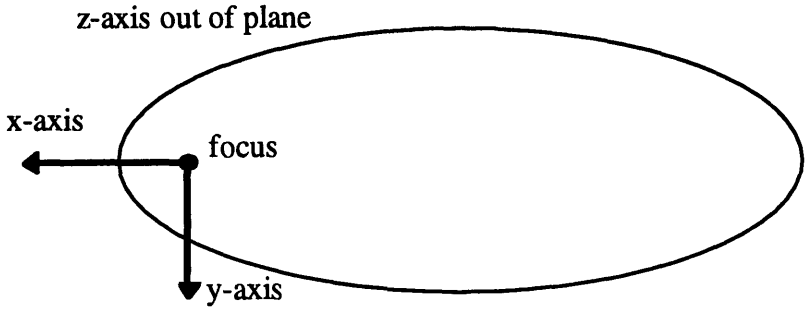

Fig. C-6 Perifocal Coordinates.

The radius and velocity vector of any object in perifocal coordinates is given by:

$$\mathbf{r} = \frac{a(1-e^2)}{1+e\cos f}[\cos f \quad \sin f \quad 0]$$
$$\mathbf{v} = \sqrt{\frac{\mu}{a(1-e^2)}}[-\sin f \quad e+\cos f \quad 0] \tag{C-4}$$

Where μ is the gravitational parameter.

C.3 Perifocal ΔV Vector

With a and e as generated in section C.1, the given burn true anomaly, and burn angles θ and ϕ the ΔV vector can be generated in perifocal coordinates. First, the radius and velocity are computed by:

$$r = \frac{a(1-e^2)}{1+e\cos f}$$
$$v = \sqrt{2\mu\left(\frac{1}{r} - \frac{1}{2a}\right)} \tag{C-5}$$

Next, flight path angle, α, the angle between the local horizontal and the velocity vector, can be computed by:

$$\alpha = \cos^{-1}\left(\frac{\sqrt{\mu a(1-e^2)}}{vr}\right) \quad \text{(positive when } 0 < f < \pi\text{)} \tag{C-6}$$

Finally, the $\Delta\mathbf{V}$ vector is given by:

$$\Delta\mathbf{V} = \Delta V\left[-\sin(f-\alpha-\theta)\cos\phi \quad \cos(f-\alpha-\theta)\cos\phi \quad \sin\phi\right] \tag{C-7}$$

C.4 Geocentric Resultant Vector

A resultant perifocal velocity vector is formed by adding the perifocal velocity and $\Delta\mathbf{V}$ vectors. Next, the perifocal radius vector and resultant velocity vector are transformed into geocentric coordinates. The geocentric coordinate system is centered upon Earth with the **x**-axis pointing in the vernal equinox direction and the **z**-axis parallel to the geographic north pole. The vectors are transformed by [27, pg. 82-83]:

$$\begin{aligned}\mathbf{r}_{geo} &= \mathbf{R}_{pf\,to\,geo}\mathbf{r}_{pf}\\ \mathbf{v}_{geo} &= \mathbf{R}_{pf\,to\,geo}\mathbf{v}_{pf}\end{aligned} \tag{C-8}$$

Where

$$\mathbf{R}_{pf\,to\,geo} = \begin{bmatrix} cl\cdot cw - sl\cdot sw\cdot ci & -cl\cdot sw - sl\cdot cw\cdot ci & sl\cdot si \\ sl\cdot cw + cl\cdot sw\cdot ci & -sl\cdot sw + cl\cdot cw\cdot ci & -cl\cdot ci \\ sw\cdot si & cw\cdot si & ci \end{bmatrix} \tag{C-9}$$

Where

$$\begin{aligned} cl &= \cos\Omega\\ sl &= \sin\Omega\\ cw &= \cos\omega\\ sw &= \sin\omega\\ ci &= \cos i\\ si &= \sin i\end{aligned} \tag{C-10}$$

Where Ω, ω, and i are the elements of the original GTO.

C.5 Generating Geocentric Elements

With the radius vector and resultant velocity vector in geocentric coordinates the elements of the escape trajectory can be determined. First, it is necessary to generate the angular momentum vector, **h**, the node vector, **n**, and the eccentricity vector, **e** as given by [27, pg. 61-63] in geocentric coordinates:

$$\begin{aligned}
\mathbf{h} &= \mathbf{r}\times\mathbf{v} \\
\mathbf{n} &= |0 \quad 0 \quad 1|\times\mathbf{h} \\
\mathbf{e} &= \frac{1}{\mu}\left[\left(v^2-\frac{\mu}{r}\right)\mathbf{r}-(\mathbf{r}\cdot\mathbf{v})\mathbf{v}\right]
\end{aligned} \tag{C-11}$$

The elements can then be generated by:

$$\begin{aligned}
a &= -\frac{\mu}{\left(v^2-\frac{2\mu}{r}\right)} \\
e &= |\mathbf{e}| \\
i &= \cos^{-1}\left(\frac{h_z}{h}\right) \\
\Omega &= \cos^{-1}\left(\frac{n_x}{n}\right)\text{sign}(n_y) \\
\omega &= \cos^{-1}\left(\frac{\mathbf{n}\cdot\mathbf{e}}{ne}\right)\text{sign}(e_z) \\
f &= \cos^{-1}\left(\frac{\mathbf{e}\cdot\mathbf{r}}{er}\right)\text{sign}(\mathbf{r}\cdot\mathbf{v})
\end{aligned} \tag{C-12}$$

C.6 Perifocal and Geocentric Escape Radius and Velocity Vectors

The radius and velocity vectors at the point where the orbit crosses the sphere of influence can now be computed. The sphere of influence is the imaginary boundary where the Sun's influence takes control of the motion of an object escaping Earth. This is assumed to occur at a radius of 1×10^6 km. First, it is necessary to calculate the true anomaly at the sphere of influence given by:

$$f = \cos^{-1}\left(\frac{1}{e}\left(\frac{a(1-e^2)}{r_{SOI}}-1\right)\right) \tag{C-13}$$

Where $\mathbf{r}_{SOI}$ is the radius of the sphere of influence. The geocentric radius and velocity vectors can now be generated by [28, pg. 5]:

$$\begin{aligned}
\mathbf{r} &= r\begin{bmatrix}\cos\Omega\cos\theta-\sin\Omega\sin\theta\cos i\\ \sin\Omega\cos\theta+\cos\Omega\sin\theta\cos i\\ \sin\theta\sin i\end{bmatrix} \\
\mathbf{v} &= -\sqrt{\frac{\mu}{a(1-e^2)}}\begin{bmatrix}\cos\Omega(\sin\theta+e\sin\omega)+\sin\Omega(\cos\theta+e\cos\omega)\cos i\\ \sin\Omega(\sin\theta+e\sin\omega)-\cos\Omega(\cos\theta+e\cos\omega)\cos i\\ -(\cos\theta+e\cos\omega)\sin i\end{bmatrix}
\end{aligned} \tag{C-14}$$

Where $\theta = \omega + f$ is the argument of latitude.

C.7 Earth Radius and Velocity Vectors

Before transforming the radius and velocity vectors into heliocentric coordinates it is necessary to compute the radius and velocity vectors of Earth. These can be computed using Earth's elements given by [29, pg. 8]:

Table C-2 Earth Orbital Elements

Element	Value
a	1.00000013
e	$0.01675104-0.00004180T_u-0.000000126T_u$
i	0°
Ω	0°
ϖ	$101°13'15".0 + 6189".03T_u + 1".63T_u^2 + 0".012T_u^3$
L	$99° + 12902768".13T_u + 1".089T_u^2$

Where T_u is calculated by equation C-2 and ϖ and L are given by:

$$\varpi = \Omega + \omega \tag{C-15}$$

$$L = \Omega + \omega + M$$

Where using M, the mean anomaly, E, the eccentric anomaly, can be computed using successive substitution as follows [28, pg. 4]:

$$\begin{aligned} E_0 &= 0 \\ E_1 &= M + e\sin E_0 \\ &\vdots \\ E_n &= M + e\sin E_{n-1} \end{aligned} \tag{C-16}$$

With E it is possible to calculate f by:

$$\begin{aligned} \cos f &= \frac{e - \cos E}{e\cos E - 1} \\ \sin f &= \frac{(1 + e\cos f)}{\sqrt{1-e^2}}\sin E \end{aligned} \tag{C-17}$$

With the standard six elements a, e, i, Ω, ω, and f the heliocentric radius and velocity vectors for Earth, $\mathbf{r}_{earth}$ and $\mathbf{v}_{Earth}$, are computed using equation C-14.

C.8 Heliocentric Radius and Velocity Vectors

The origin of the heliocentric coordinate system is the Sun, the **x**-axis points in the vernal equinox direction, and the **z**-axis is normal to the ecliptic plane. Two steps are required to produce the heliocentric radius and velocity vectors. First, the radius and velocity vectors at the sphere of influence must be transformed to heliocentric coordinates. Second, the radius and velocity vectors of earth must be added to the vectors at the sphere of influence. The transformation to heliocentric coordinates is given by:

$$\begin{aligned} \mathbf{r}_{heoSOI} &= \mathbf{R}_{geo\ to\ heo}\mathbf{r}_{SOI} \\ \mathbf{v}_{heoSOI} &= \mathbf{R}_{geo\ to\ heo}\mathbf{v}_{SOI} \end{aligned} \tag{C-18}$$

Where:

$$\mathbf{R}_{geo\ to\ heo} = \begin{bmatrix} 1 & & \\ & \cos(inc) & \sin(inc) \\ & -\sin(inc) & \cos(inc) \end{bmatrix} \tag{C-19}$$

Where *inc* is the tilt of the Earth, 23.5°. The final heliocentric radius and velocity vector are:

$$\begin{aligned} \mathbf{r}_{heo} &= \mathbf{r}_{Earth} + \mathbf{r}_{heoSOI} \\ \mathbf{v}_{heo} &= \mathbf{v}_{Earth} + \mathbf{v}_{heoSOI} \end{aligned} \tag{C-20}$$

C.9 Heliocentric Elements and Spread Rate

With the final heliocentric radius and velocity vector the heliocentric elements a_H, e_H, i_H, Ω_H, ω_H, and f_H can be computed using the same technique described in section C.5. The spread rate can be calculated by first calculating the period of the final orbit:

$$P = \frac{2\pi a_H^{\frac{3}{2}}}{\mu_{Sun}^{\frac{1}{2}}} \tag{C-21}$$

The average spread rate is then:

$$S = 2\pi\left(\frac{P_{Earth}}{P} - 1\right) \tag{C-22}$$

Where P_{earth} is the period of Earth, 1 year, and the spread rate is in radians per time unit.

Appendix D Keplerian Propagator

This appendix describes a general Keplerian orbit propagator used in this thesis for propagating the helio satellite constellations and investigating the trigger orbits [27, pg 177]. While less flexible than the Cowell's method propagator described in appendix A, this code is considerably faster. The operation of the code is summarized in Figure D-1. The Keplerian propagator requires as inputs the gravitational parameter, μ, of the center body and the six Keplerian elements, shown in Figure D-2, semi-major axis, a, eccentricity, e, inclination, i, longitude of ascending node, Ω, argument of perigee, ω, and true anomaly, f, for each object being propagated. The details of the code are described in the following sections.

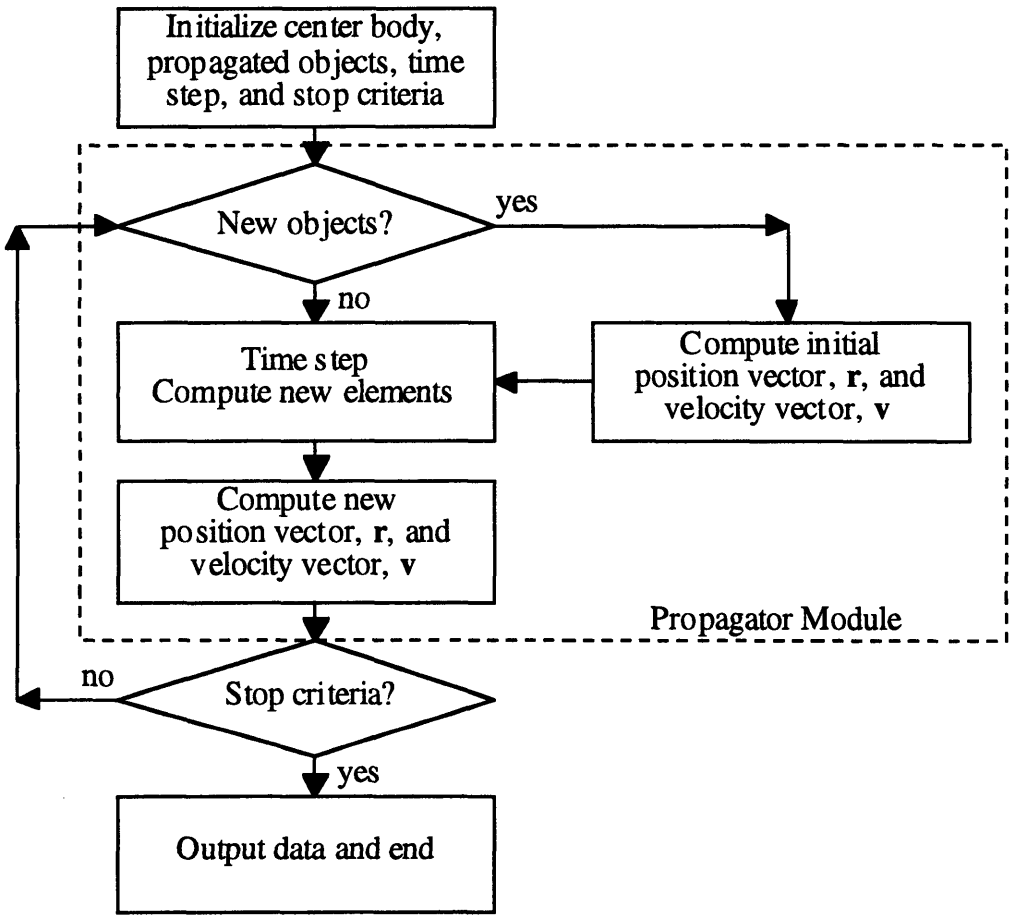

Fig. D-1 Keplerian propagator.

D.1 Initialization

The following items must be initialize before beginning the propagation: the center body, the objects being propagated, the time step, and stop criteria. The center body defines the origin of the

coordinate system and is specified by its gravitational parameter, μ. For each body being propagated a row vector containing the six initial elements for that body must be created and appended to the bottom of a matrix containing the elements for the other bodies. Additional bodies may be added during the propagation. The code propagates over a fixed time step which must be specified initially but can be varied during the propagation. Finally, the propagator module resides within a while loop which evaluates the stop criteria between time steps. Arbitrary stop criteria may be specified but fixed duration is the most common.

Once the objects, time step, and stop criteria are initialized the propagation is carried out by the propagator module. The next two sections describe the primary components of the propagator module.

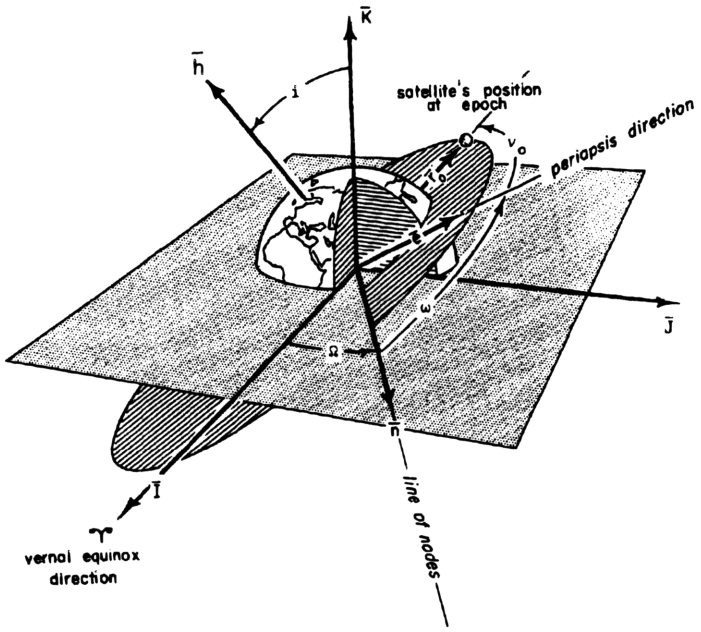

Fig. D-2 Keplerian Elements [27].

D.2 Propagating the Elements

This section describes how the Keplerian elements are propagated over each time step. Of the six Keplerian elements only true anomaly, f, is time dependent. To propagate the initial true anomaly, f_0, to the new true anomaly, f_1, as a function of the time step, dt , and the other elements it is first necessary to compute the initial radius, r_0, and the period of the orbit, P, given by:

$$r_0 = \frac{a\left(1-e^2\right)}{1+e\cos f_0} \tag{D-1}$$

$$P = 2\pi\sqrt{\frac{a^{3/2}}{\mu}} \tag{D-2}$$

Where a is the semi-major axis, e is the eccentricity, and μ is the gravitational parameter. With these it is now possible to compute the initial eccentric anomaly, E_0, given by:

$$\begin{aligned} \sin E_0 &= \frac{r_0 \sin f_0}{a\sqrt{1-e^2}} \\ \cos E_0 &= \frac{1}{e}\left(1-\frac{r_0}{a}\right) \end{aligned} \tag{D-3}$$

With the initial eccentric anomaly, E_0, it is possible to calculated the initial mean anomaly, M_0, given by:

$$M_0 = E_0 + \sin E_0 \tag{D-4}$$

With the initial mean anomaly, M_0, it is possible to compute the new mean anomaly, M_1, given by:

$$M_1 = M_0 + \frac{dt}{2\pi P} \tag{D-5}$$

Where dt is the time step and P is the period. Next, the new eccentric anomaly, E_1, is calculated by successive substitution given by:

$$\begin{aligned} E_0 &= 0 \\ E_1 &= M + e\sin E_0 \\ &\vdots \\ E_n &= M + e\sin E_{n-1} \end{aligned} \tag{D-6}$$

The iteration is continued until a specified tolerance is reached. The new eccentric anomaly, E_1, is equal to E_n. From the new eccentric anomaly the sines of the new true anomaly, f_1, are given by:

$$\begin{aligned} \cos f_1 &= \frac{e-\cos E_1}{e\cos E_1 - 1} \\ r_1 &= \frac{a\left(1-e^2\right)}{1+e\cos f_1} \\ \sin f_1 &= \frac{a\left(1-e^2\right)^{1/2}}{r_1 \sin E_1} \end{aligned} \tag{D-7}$$

Where r_1 is the new radius. Finally, the new true anomaly can be computed from the sines. With the new true anomaly it is possible to compute the new radius and velocity vectors wich is described in the next section.

D.3 Position and velocity vectors

Whenever a new set of elements is computed, a new object is added, or a simulation is begun, the position vector, **r**, and velocity vector, **v**, for each object is computed and stored. Position and velocity are given by:

$$\mathbf{r} = r\begin{bmatrix} \cos\Omega\cos\theta - \sin\Omega\sin\theta\cos i \\ \sin\Omega\cos\theta + \cos\Omega\sin\theta\cos i \\ \sin\theta\sin i \end{bmatrix}$$

$$\mathbf{v} = -\sqrt{\frac{\mu}{a(1-e^2)}}\begin{bmatrix} \cos\Omega(\sin\theta + e\sin\omega) + \sin\Omega(\cos\theta + e\cos\omega)\cos i \\ \sin\Omega(\sin\theta + e\sin\omega) - \cos\Omega(\cos\theta + e\cos\omega)\cos i \\ -(\cos\theta + e\cos\omega)\sin i \end{bmatrix} \qquad \text{(D-8)}$$

Where $\theta = \omega + f$ is the argument of latitude and r is the radius of the object as computed in D-1.

The position and velocity history produced by the code can be used to produce plots showing the orbit tracks of the bodies, instantaneous snapshots of their positions, or, as described in the next appendix, sky track plots of the orbit as seen from a given point on the surface of the Earth.

Appendix E Sky Track Plots

This appendix describes how sky tracks, plots of the motion of satellites in orbit around the Earth as viewed from the ground, are produced [27]. These sky tracks are used for analyzing the trigger orbits. The operation of the code is summarized in Figure E-1. Two inputs are required for the code: a position versus time history of the body being tracked, and the latitude and longitude of the viewing point relative to the coordinate system at the start of the time history. The details of the code are described in the following sections.

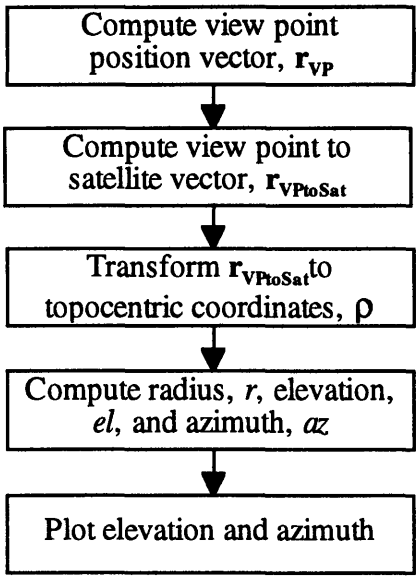

Fig. E-1 Sky track generator.

E.1 View Point Position

The coordinates of the view point are given by a longitude, *long*, a latitude, *lat* , at the start of the simulation as shown in Figure E-2. As the Earth rotates, the view point vector is rotated about the z-axis by an angle equal to the sidereal time elapsed, $\theta_{sidereal}$, given by:

$$\theta_{siderial} = (t - t_0)\frac{d\theta}{dt} \tag{E-1}$$

Where t_0 is the start time and $d\theta/dt$, the rotation rate of Earth, is 0.25068447 degrees/minute. The view point position vector is given in geocentric coordinates by:

$$\mathbf{r}_{VP} = r_{Earth}\left[\cos(long + \theta_{siderel})\cos(lat) \quad \sin(long + \theta_{siderel})\cos(lat) \quad \sin(lat)\right] \tag{E-2}$$

Where r_{Earth} is the radius of the Earth. The view point to satellite vector in geocentric coordinates, $\mathbf{r}_{VPtpsat}$, is given by:

$$\mathbf{r}_{\text{VPtoSat}} = \mathbf{r} - \mathbf{r}_{VP} \tag{E-3}$$

It is now possible to transform $\mathbf{r}_{\text{VPtosat}}$ to topocentric coordinates.

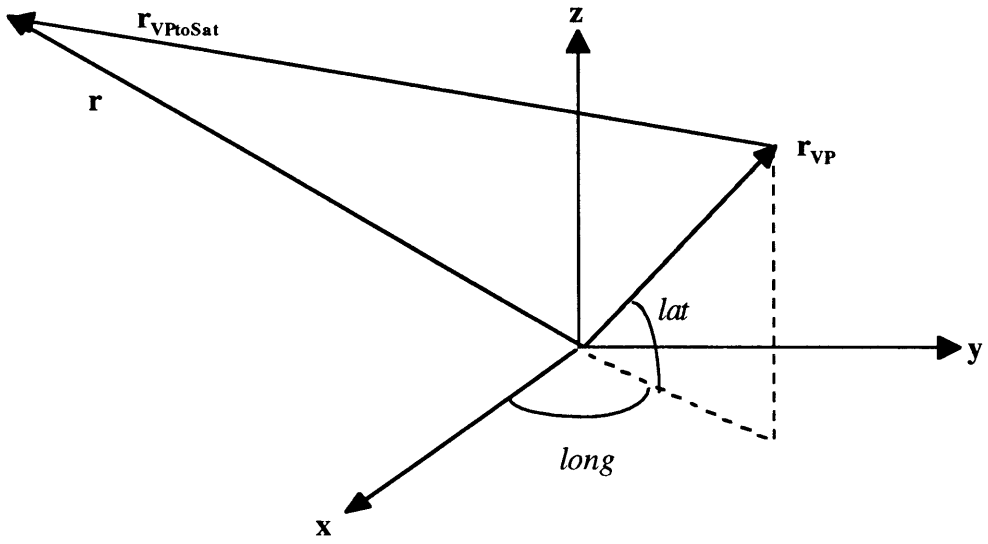

Fig. E-2 Initial view point position.

E.2 Topocentric Coordinates

This section describes how $\mathbf{r}_{\text{VPtoSat}}$ is transformed into the topocentric position vector, ρ. The topocentric , or **S-E-Z**, coordinate system is centered at any given point on the Earth with the **Z**-axis parallel to the local vertical, the **S**-axis parallel to the local horizontal pointing south, and the **E**-axis parallel to the local horizontal pointing east as shown in Figure E-3. The transformation from $\mathbf{r}_{\text{VPtpSat}}$ to ρ is given by:

$$\rho = \mathbf{R}_{\text{GeotoTopo}}\mathbf{r}_{\text{VPtoSat}} \tag{E-4}$$

Where

$$\mathbf{R}_{\text{GeotoTopo}} = \begin{bmatrix} sl \cdot co & sl \cdot so & -cl \\ -so & co & 0 \\ cl \cdot co & cl \cdot so & sl \end{bmatrix} \tag{E-5}$$

Where

$$\begin{aligned} sl &= \sin lat \\ cl &= \cos lat \\ so &= \sin(long + \theta_{sidereal}) \\ co &= \cos(long + \theta_{sidereal}) \end{aligned} \tag{E-6}$$

It is now possible to compute the elevation and azimuth angles.

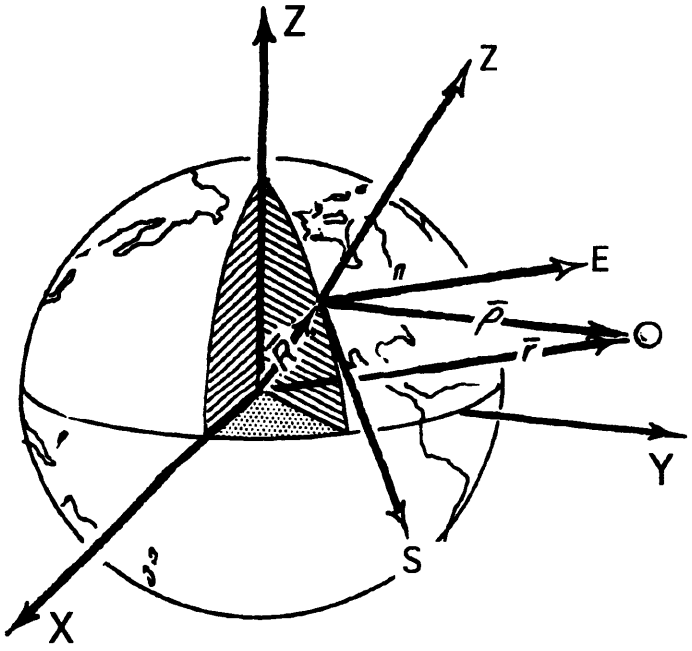

Fig. E-3 Topocentric coordinates [27].

E.3 Elevation and Azimuth

Elevation and azimuth are needed for producing an image of the motion of the satellites in the sky. Elevation, *el*, is the angle between the horizon and the satellite as shown in Figure E-4. Azimuth, *az*, is the angle between north (the negative **S**-axis in topocentric coordinates) and the projection of the topocentric position vector, ρ, in to the **S-E** plane as shown in Figure E-4. The elevation is given by:

$$el = \sin^{-1}\left(\frac{\rho_Z}{\rho}\right) \tag{E-7}$$

Where ρ_Z is the **z** component of ρ and ρ is the magnitude of ρ. Azimuth is given by:

$$az = \cos^{-1}\left(\frac{\rho_S}{-\rho \cos el}\right) \text{sign}\rho_E \tag{E-8}$$

Where ρ_S and ρ_E is the **x** and **y** component of ρ. Elevation and azimuth can now be plotted to form a sky track.

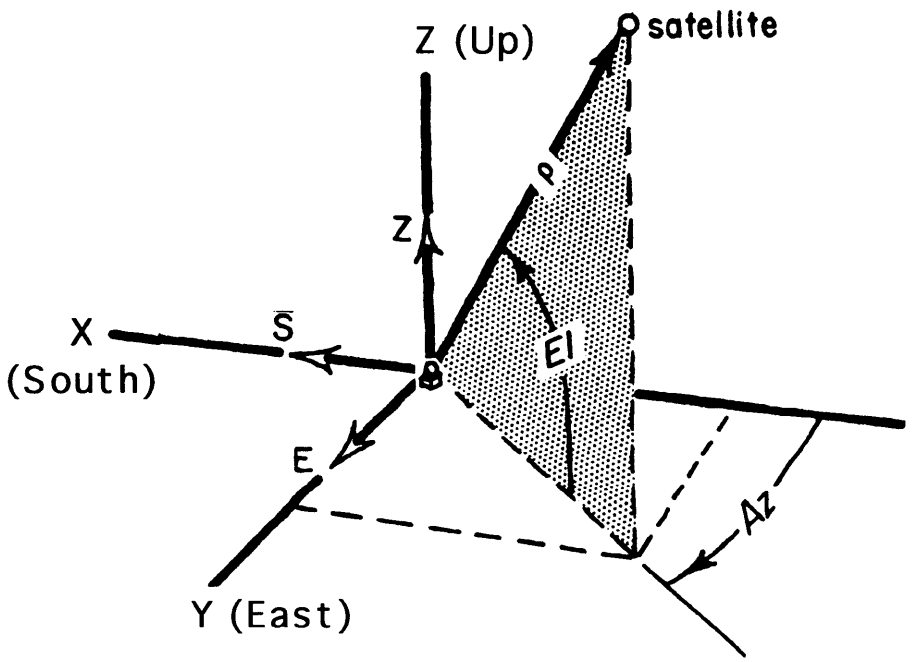

Fig. E-4 Elevation and azimuth [27].

Appendix F Encke's Method

This appendix describes a code which uses the universal variable formulation of the Encke's method of integrating the effects of small perturbations and was used in the analysis of the J_{22} perturbation described in chapter 5. The operation of the code is summarized in Figure F-1. Encke's method integrates the difference in position, δ, and the difference in velocity, ν, caused by a perturbation relative to a reference initially osculating Keplerian trajectory as shown in Figure F-2. The position and velocity at any given time are given by:

$$\begin{aligned} \mathbf{r} &= \mathbf{r}_{osc} + \delta \\ \mathbf{v} &= \mathbf{v}_{osc} + \nu \end{aligned} \tag{F-1}$$

Where $\mathbf{r}$ is the position, $\mathbf{r}_{osc}$ is the osculating position, $\mathbf{v}$ is the velocity, $\mathbf{v}_{osc}$ is the osculating velocity, and δ and ν are zero at time zero so that $\mathbf{r} = \mathbf{r}_{osc}$ and $\mathbf{v} = \mathbf{v}_{osc}$. By integrating only the perturbation the time steps can be larger and the results more accurate then those produced by a Cowell's Method code.

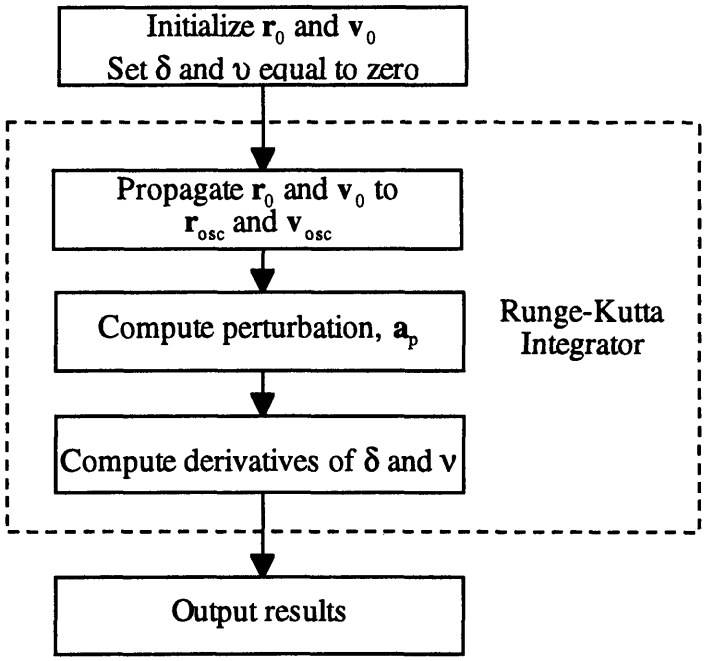

Fig. F-1 Encke's Method.

The Encke's method code is initialized with and initial position, $\mathbf{r}_0$, and velocity, $\mathbf{v}_0$. The principal module of the code produces the derivatives of δ and υ for integration using the ODE45 Runge-Kutta scheme in MATLAB. This module consists of three parts: a method for propagating $\mathbf{r}_0$ and $\mathbf{v}_0$ to $\mathbf{r}_{osc}$ and $\mathbf{v}_{osc}$ at each integration step, a routine for computing the perturbation acceleration $\mathbf{a}_p$ which is unique for each type of perturbation, and the differential equation for δ and υ. The

following sections describe universal variable formulation of the differential equation and the propagation method that supports it.

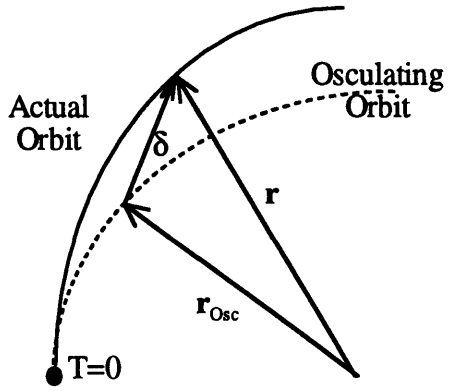

Fig. F-2 The osculating orbit.

F.1 The Differential Equation

The traditional formulation for the Encke's method is given as:

$$\frac{d^2\delta}{dt^2} + \frac{\mu}{r_{osc}^3}\delta = -\frac{\mu}{r_{osc}^3} f(q)\mathbf{r}(t) + \mathbf{a}_p \tag{F-2}$$

Where μ is the gravitational parameter, $\mathbf{a}_p$ is the perturbation acceleration, r_{osc} is the magnitude of $\mathbf{r}_{osc}$, and q and $f(g)$ are given by:

$$q = \frac{\delta \cdot (\delta - 2\mathbf{r})}{\mathbf{r} \cdot \mathbf{r}}$$
$$f(q) = q\frac{3 + 3q + q^2}{1 + (1+q)^{3/2}} \tag{F-3}$$

Equation F-2 can be broken into two sets of first order differential equations and integrated using a Runge-Kutta scheme. When δ and ν become sufficiently large Encke's method begins to lose its efficiency and the reference orbit should be rectified by selecting a new osculating orbit.

The traditional implementation of the Encke's method using Keplerian propagation has several disadvantages. At each time step $\mathbf{r}_{osc}$ must be propagated from the initial conditions requiring the computationally intensive iterative solution of Kepler's equation. The code must detect the type (ellipse, or hyperbola) of the osculating orbit and use the correct version of Kepler's equations. For orbits with eccentricities near one numerical accuracy is compromised. Partially to produce a more general code but mostly for the pedagogical value, a novel implementation of Encke's method [28, solutions 1] using universal variables was selected.

The universal variable formulation of the differential equation for Encke's method is given by:

$$\begin{aligned}\frac{d\delta}{d\chi} &= \frac{r}{\sqrt{\mu}}v \\ \frac{dv}{d\chi} &= -\frac{r\sqrt{\mu}}{r_{osc}^3}\delta - \frac{r\sqrt{\mu}}{r_{osc}^3}f(q)\mathbf{r}(\chi) + \frac{r}{\sqrt{\mu}}\mathbf{a}_d\end{aligned} \tag{F-4}$$

Where r is the magnitude of $\mathbf{r}$ and χ is the universal anomaly which is used to remove the singularity from Kepler's equation and is defined as $\dot{x} = \sqrt{\mu}/r$. In most applications equation F-4 is integrated over a single orbit ($\chi = 0$ to $\chi = 2\pi\sqrt{a}$) using a Runge-Kutta scheme.

F.2 The Propagator

At each time step it is necessary to determine $\mathbf{r}_{osc}$ and $\mathbf{v}_{osc}$ by propagating the initial conditions or the conditions after the last rectification. A traditional implementation of Encke's method would use a Keplerian propagator in time, like the one described in appendix D, but to make the universal variable formulation efficient a universal variable propagation method is used [30 pg. 464, 28]. The initial conditions in terms of $\mathbf{r}_0$ and $\mathbf{v}_0$ can be propagated to $\mathbf{r}$ and $\mathbf{v}$ by:

$$\begin{aligned}\mathbf{r} &= F\mathbf{r}_0 + G\mathbf{v}_0 \\ \mathbf{v} &= F_t\mathbf{r}_0 + G_t\mathbf{v}_0\end{aligned} \tag{F-5}$$

Where the functions F, G, F_t, and G_t can be given in terms of the universal functions U_1 and U_2 as given by:

$$\begin{aligned}F &= 1 - \frac{U_2}{r_0} \\ \sigma_0 &= \frac{\mathbf{r}_0'\mathbf{v}_0}{\sqrt{\mu}} \\ G &= \frac{rU_1}{\sqrt{\mu}} + \frac{\sigma_0 U_2}{\sqrt{\mu}} \\ F_t &= \frac{\sqrt{\mu}U_1}{rr_0} \\ G_t &= 1 - \frac{U_2}{r}\end{aligned} \tag{F-6}$$

Where r_0 is the magnitude of $\mathbf{r}_0$ and the universal functions are given by:

$$U_n = \chi^n \left[\frac{1}{n!} - \frac{\psi}{(n+2)!} + \frac{\psi^2}{(n+4)!} - \frac{\psi^3}{(n+6)!} + \cdots \right] \qquad \text{(F-7)}$$

$$\psi = \alpha\chi^2$$

Where α is $1/a$, and a is the semi-major axis of the orbit. Finally, it is often useful to know the time since χ=0 (usually perigee passage) which is given in terms χ by:

$$t = \frac{(\chi - \sigma + \sigma_0)}{\alpha\sqrt{\mu}} \qquad \text{(F-8)}$$

Note: Shortly before completing this thesis discrepancies were found between the Encke's method and Cowell's method for limiting cases of the J_{22} perturbation analysis. For synchronous orbit perigee radiuses above 15,000 km the Encke's and Cowell's Method results are nearly identical so that the analysis contained in chapter 5 is still valid. However, below 15,000 km the results diverge. Until this can be explained this code should be treated with caution.

Appendix G Eclipsing

This appendix describes a code for determining the eclipse duration for the trigger satellites as a function of launch date and day of year. This code is based on the work of Escobal [25, pg. 155]. The launch date determines the orientation of the trigger orbit in inertial coordinates. The day of year determines the orientation of the trigger orbit relative to the Earth-Sun line. The operation of the code is summarized in Figure G-1. The details of the code are contained in the following sections.

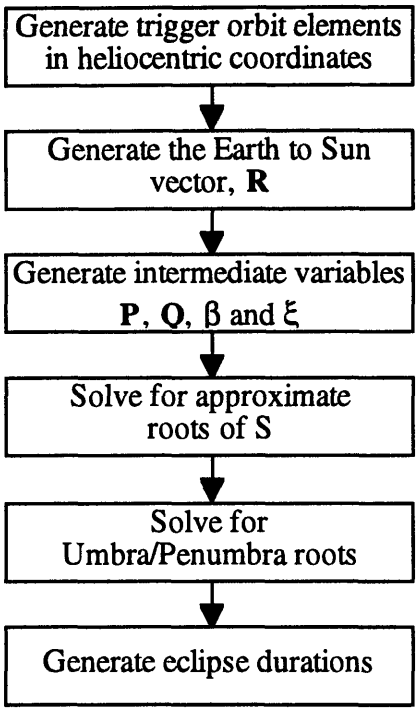

Fig. G-1 The eclipse code.

G.1 Trigger Elements and Earth to Sun Vector

This section describes how the ecliptic trigger orbit elements a, e, i, Ω, and ω, and the Earth to Sun vector, **R**, are generated. The ecliptic coordinate system is centered on Earth with the **z**-axis in the direction of the ecliptic north pole. Techniques described in appendix C are used heavily.

The geocentric trigger orbit elements are given in table G-1. Using equation C-14 a position, $\mathbf{r}_{geo}$, and velocity, $\mathbf{v}_{geo}$, can be generated for an arbitrary true anomaly. Using equations C-18 and C19 these vectors can be transformed to **r** and **v** in the ecliptic coordinate system. Heliocentric elements, i, Ω, and ω, can then be generated from **r** and **v** using the method described in C-5. The elements a and e will be the same as their geocentric counterparts.

The Earth to Sun vector, **R**, is the negative of the Earth radius vector generated in section C-7.

Table G-1 Trigger Orbit Elements

Element	Value
a	42,167.89
e	0.5256
i	7.0°
Ω	Ω_{GTO} as generated in appendix C.1
ω	179.5°±50.96° (type I positive, Type II negative)

G.2 Intermediate Variables

This section describes the generation of the intermediate variables P, Q, β, and ξ.

The P and Q vectors are unit vectors in the plane of the orbit. P points towards perigee and Q is 90° counter clockwise from P as shown in Figure G-2. P and Q are given as a function of the heliocentric elements by:

$$\mathbf{P} = \begin{bmatrix} \cos\omega\cos\Omega - \sin\omega\sin\Omega\cos i \\ \cos\omega\sin\Omega + \sin\omega\sin\Omega\cos i \\ \sin\omega\cos i \end{bmatrix}$$

$$\mathbf{Q} = \begin{bmatrix} -\sin\omega\cos\Omega - \cos\omega\sin\Omega\cos i \\ -\sin\omega\sin\Omega + \cos\omega\cos\Omega\cos i \\ \cos\omega\sin i \end{bmatrix} \qquad \text{(G-1)}$$

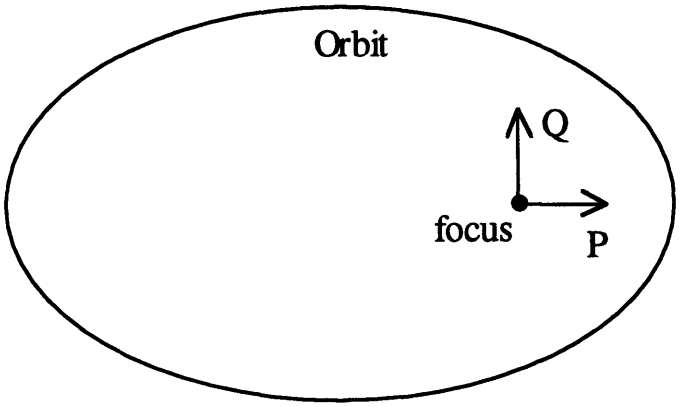

Fig. G-2 The P and Q unit vectors.

The variables β and ξ are given by:

$$\beta = \frac{\mathbf{P} \cdot \mathbf{R}}{R}$$
$$\xi = \frac{\mathbf{Q} \cdot \mathbf{R}}{R} \qquad \text{(G-2)}$$

Where R is the magnitude of **R**.

G.3 The Shadow Function S

This section describes the shadow function S and how it can be used to obtain the average eclipse entrance and exit true anomalies, *f*. The average eclipse, as opposed to the penumbra and umbra eclipse, is defined by a shadow cone of constant diameter equal to that of the Earth as shown in Figure G-3. For synchronous orbit radiuses the penumbra region is thin so that the average eclipse is a good approximation. The shadow function is given is given by:

$$S \equiv r_{Earth}^2(1+e\cos f)^2 + p^2(\beta\cos f + \xi\sin f)^2 - p^2 \qquad \text{(G-3)}$$

Where r_{Earth} is the radius of the Earth and $p = a(1-e^2)$. When S(*f*) is positive the *f* represents a point in the shadow of Earth subject to the constraint:

$$\beta\cos f + \xi\sin f < 0 \qquad \text{(G-4)}$$

For the purpose of solving for the roots of S it can be expressed as a polynomial function of cos*f* as given by:

$$S = A_0\cos^4 f + A_1\cos^3 f + A_2\cos^2 f + A_3\cos f + A_4 \qquad \text{(G-5)}$$

Where

$$
\begin{aligned}
A_0 &= [(r_{Earth}/p)^4 e^4 - 2(r_{Earth}/p)^2(\xi^2-\beta^2)e^2 + (\xi^2+\beta^2)^2] \\
A_1 &= [4(r_{Earth}/p)^4 e^3 - 4(r_{Earth}/p)^2(\xi^2-\beta^2)e] \\
A_2 &= [6(r_{Earth}/p)^4 e^2 - 2(r_{Earth}/p)^2(\xi^2-\beta^2) - 2(r_{Earth}/p)^2(1-\xi^2)e^2 \\
&\quad + 2(\xi^2-\beta^2)(1-\xi^2) - 4\beta^2\xi^2] \\
A_3 &= [4(r_{Earth}/p)^4 e - 4(r_{Earth}/p)^2(1-\xi^2)e] \\
A_4 &= [(r_{Earth}/p)^4 - 2(r_{Earth}/p)^2(1-\xi^2) + (1-\xi^2)^2]
\end{aligned}
\qquad \text{(G-6)}
$$

The roots of G-5 can be determined using the routine ROOTS in MATLAB. The valid true anomalies can be determined using G-3 and G-4.

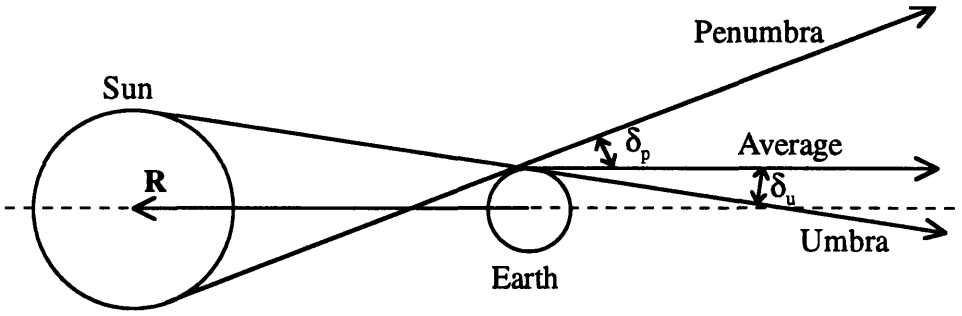

Fig. G-3 Eclipse geometry.

G.4 Umbra and Penumbra Eclipse

With the average entrance and exit eclipse true anomalies the umbra and penumbra entrance and exit true anomalies can be computed using a modified S function given by:

$$
\begin{aligned}
S \equiv\ & r_{Earth}^2(1+e\cos f)^2 + p^2(\beta\cos f + \xi\sin f)^2 - p^2 \\
& \mp 2pr_{Earth}(\beta\cos f + \xi\sin f)(1+e\cos f)\sin\delta_i
\end{aligned}
\qquad \text{(G-7)}
$$

Where δ_i is either the umbra cone angle, δ_u, equal to 0.264122° or the penumbra cone angle , δ_p, equal to 0.269007°. Using the average entrance and exit true anomalies as starting points, equation G-7 can be solved using Newton iteration.

G.5 Eclipse Duration

From the entrance and exit true anomalies, f_{enter} and f_{exit}, the eclipse duration can be computed. First, it is necessary to compute the entrance and exit eccentric anomalies, E_{enter} and E_{exit}, as given by:

$$\sin E = \frac{\sqrt{1-e^2}\sin f}{1+e\cos f}$$
$$\cos E = \frac{\cos f + e}{1+e\cos f} \qquad \text{(G-8)}$$

From the eccentric anomalies the eclipse duration, T, can be computed as given by:

$$T = \frac{a^{3/2}}{\sqrt{\mu}}\left[\sin E_{exit} - \sin E_{enter} + e(\sin E_{enter} - \sin E_{exit})\right] \qquad \text{(G-9)}$$

Where μ is the gravitational parameter.

References

[1] TRW Spacecraft Guide, TRW Space & Electronics Group, Redondo Beach, CA.

[2] Fishman, G.J., Meegan, C.A., "Gamma-Ray Bursts", Annual Revue of Astronomy and Astrophysics, 1995.

[3] Roth J., "Gamma-Ray Bursts: A Growing Enigma", Sky & Telescope, September 1996.

[4] Gehrels N. et al, "The BASIS Mission Concept For A Gamma-Ray Burst Imaging Spectrosopy", Gamma-Ray and Cosmic-Ray Detectors, Techniques, and Missions, Society of Photo-Optical Instrumentation Engineers, August 1996.

[5] Ricker, G.R., "The Energetic Transient Array (ETA): A Network of "Space Buoys" in Solar Orbit for Observations of Gamma-Ray Bursts", High Energy Astrophysics in the 21st Century, American Institute of Physics, 1990, pg. 357-387.

[6] Patel, B.T., Systems Analysis of an Astrophysics Mission Utilizing Electric Propulsion, MS Thesis, Massachusetts Institute of Technology, Boston, MA, September 1995.

[7] Maroquene, F., Arianespace, fax personal communication, 7 May 1997.

[8] Patel, B.T. et al, "Electric Propulsion for an Interplanetary Astrophysics Mission", 24th International Electric Propulsion Conference, IEPC-95-239, September 1995.

[9] Orbital Sciences Corporation, Commercial Pegasus Payload User's Guide, Orbital Sciences Corporation, Dulles, VA, 1993, Section 3.0.

[10] Orbital Sciences Corporation, Commercial Taurus Launch Vehicle Payload User's Guide, Orbital Sciences Corporation, Dulles, VA, 1996, Section 3.0.

[11] Lockheed Missiles & Space Company, Inc., Lockheed Launch Vehicle User's Guide, Lockheed Missiles & Space Company, Inc., Sunnyvale, CA, 1995, Section 2.5.

[12] Brown, C.D., Spacecraft Propulsion, American Institute of Aeronautics and Astronautics, Washington, DC, 1996, Chapter 4.

[13] Kaiser Marquardt, Rocket Engines And Propulsion Systems, Kaiser Marquardt, Van Nuys, CA, 1990.

[14] Martel, F., Personal communication, May-June 1996.

[15] Arianespace, Ariane 5 User's Manual, Arianespace, Every Cedex, France, 1991.

[16] Blamont, J., "Using Large Launchers for Small Satellites", JPL Publication 96-26, Jet Propulsion Laboratory, Pasadena, CA, December 1996.

[17] Star Solid Rocket Motor Data Sheets, Thiokol.

[18] Walstrom D, Engineer at Thiokol, Personal communication, June 1996 to May 1997.

[19] Fabas, N., Energetic Transient Array, Project Report, MIT Center for Space Research, Cambridge, MA, August 1996.

[20] Prussing, J.E., Conway, B.A., Orbital Mechanics, Oxford University Press Inc, New York, NY, 1993.

[21] Ocamp, C.A., Rosborough G.W., "Optimal low-thrust transfers between a class of restricted three-body trajectories", Proceedings of the AAS/AIAA Astrodynamics Conference, AAS 93-681, August 1993.

[22] Pisacane V.V., Moore, R.C., Fundamentals of Space Systems, Oxford University Press Inc., New York, NY, 1994.

[23] Larson, W.J., Wertz, J.R., Space Mission Analysis and Design, Microcosm Inc, Torrance, CA, 1992.

[24] Zee, C., Theory of Geostationary Satellites, Kluwer Academic Publishers, Dordrecht, Netherlands, 1988.

[25] Escobal, P.R., Methods of Orbit Determination, Wiley, New York, NY, 1965.

[26] McLain, C., Martinez-Sanchez, M., Ricker, G.R., "Creating Small Satellite Constellations Around the Sun", 10th Anual USU/AIAA Conference on Small Satellites Proceedings, September 1996.

[27] Bate, R.R., Mueller, D.D., White, J.E., Fundamentals of Astrodynamics, Dover, New York, NY, 1971.

[28] Battin, R.H., 16.346 Course Notes, MIT, Boston, MA, September 1996.

[29] Escobal, P.R., Methods of Astrodynamics,Wiley, New York, NY, 1968.

[30] Battin, R.H., An Introduction to the Mathematics and Methods of Astrodynamics, American Institute of Aeronautics and Astronautics, New York, NY, 1987.